Universidad de Oviedo
Departamento de Ingeniería Eléctrica, Electrónica,
de Computadores y Sistemas

Doctoral Thesis

Design, simulation and manufacturing techniques for fully textile integrated microwave circuits and antennas

---

Leticia Alonso González

Director: Samuel Ver Hoeye

Programa de Doctorado en Tecnologías de la Información y
Comunicaciones en Redes Móviles

2018

Presentación como
compendio de publicaciones

Justificación

El trabajo realizado por el autor de la tesis tiene gran calidad técnica y es altamente innovador, lo que está refrendado por diferentes publicaciones científicas tanto en revistas, como en congresos de ámbito internacional y nacional.

Revistas internacionales:

[1] L. Alonso-González, S. Ver Hoeye, C. Vázquez, M. Fernández, and F. Las-Heras, "On the techniques to develop millimetre-wave textile integrated waveguides using rigid warp threads", in IEEE Transactions on Microwave Theory Techniques, 66, no. 2, pp. 751-761, Feb. 2018.

[2] L. Alonso-González, S. Ver-Hoeye, M. Fernández-García, Y. Álvarez-López, C. Vázquez-Antuña, and F. L. H. Andrés, "Fully textile-integrated microstripf-ed slot antenna for dedicated short-range communications", in IEEE Transactions on Antennas and Propagation, vol. 66, no. 5, pp. 2262-2270, May 2018.

[3] L. Alonso-González, S. Ver-Hoeye, M. Fernández-García, and F. L. H. Andrés, "Three-dimensional fully interlaced woven microstrip-fed substrate integrated waveguide", in Progress In Electromagnetics Research, [accepted for publication].

Conferencias internacionales:

[1] European Microwave Week (EuMW), 6-11 septiembre 2015, Paris (Francia). "Millimetre wave transmitter based on a few-layer graphene frequency multiplier".
Coautora.

[2] Global Symposium on Millimeter Waves, 25-27 mayo 2015, Montreal (Canadá). "Millimetre wave textile integrated waveguide beamforming antenna for radar applications".
Primera autora y ponente.

[3] Global Symposium on Millimeter Waves, 25-27 mayo 2015, Montreal (Canadá). "Millimetre wave receiver based on a few-layer graphene WR-5 band subharmonic mixer".
Coautora.

[4] Global Symposium on Millimeter Waves, 25-27 mayo 2015, Montreal (Canadá). "3D printed millimeter wave receiver integrating a graphene subharmonic mixer and a diagonal horn antenna".
Coautora.

[5] Simposium Nacional de la Unión Científica de Radio. Septiembre 2016, Madrid (España). "Textile integrated waveguide cavity-backed slot antenna for 5G wearable applications".
Primer autor y ponente.
Premio a mejor contribución de jóvenes científicos.

Conferencias nacionales:

[1] IEEE MTT-S International Conference on Numerical Electromagnetic and Multiphysics Modeling and Optimization. Mayo 2017. Sevilla (España). "Novel parametric electromagnetic modelling to simulate textile integrated circuits".
Primer autor y ponente.

conclusiones generales y se proponen nuevas líneas de investigación.

RESUMEN (en Inglés)

This Doctoral Thesis presents novel results regarding the design, simulation and manufacturing techniques to develop microwave circuits and antennas in textile technology. For this purpose, Chapter 1 introduces the most employed techniques to develop textile integrated circuits and antennas, such as inkjet-printing over textile substrates, embroidery, *appliqué* processes or the use of non-woven materials or, simply, non-wovens. The beforementioned techniques present different problems, consequently, weaving has been found to be an alternative solution, becoming the basis of the Thesis.

With the aim of simplifying the simulation of the complex textile structures for their electromagnetic characterisation, Chapter 2presents a modelling technique based on three steps. These steps correspond to the translation between the different equivalent models of the same textile structure. The most complex model is based on the filaments which compose the employed multifilament threads, therefore, it is the model which requires more computational resources. The intermediate model emulates monofilament threads which are electromagnetically equivalent to the multifilaments and, consequently, reduces the computational complexity. Finally, the textile structure is translated into a third model based on homogeneous layers, which is analogous to the model employed in conventional simulations with rigid substrates. Eventually, the equivalent parameters which electromagnetically characterise both the dielectric and conductive materials from which the textile is composed, are obtained.

In order to validate the proposed simulation modelling, Chapter 3 presents different designs of structures based on substrate integrated waveguides implemented using weaving technology. The proposed designs differ in terms of the operating frequency, the design of the textile structure or in the level of integration of the transitions for the experimentally validation in the textile. In Chapter 3, two different filters are also proposed, which are based on the cosimulation between two different commercial electromagnetic simulator packages, in order to validate the simulation techniques already presented in the previous chapter.

With the aim of developing prototypes to be employed as a final application. Chapter 4 presents different designs of near-field and far-field tags and antennas. These prototypes, which are completely integrated in textile, are based on different technologies such as microstrip or substrate integrated waveguide, among others, and operate in different frequency bands.

The fabrication process using industrial weaving machines provides the enormous advantage of allowing the development of large prototypes as well as their large scale production. For this reason, Chapter 5 presents different types of frequency selective surfaces completely integrated in textile. Not only are these surfaces flexible, but also this characteristic provides them with different real applications. Finally, general conclusions and future lines of research are proposed.

Universidad de Oviedo

DEPARTAMENTO DE INGENIERÍA ELÉCTRICA, ELECTRÓNICA,
DE COMPUTADORES Y SISTEMAS

TESIS DOCTORAL

TÉCNICAS DE DISEÑO, SIMULACIÓN Y FABRICACIÓN DE CIRCUITOS Y ANTENAS DE MICROONDAS EN TECNOLOGÍA TEXTIL

LETICIA ALONSO GONZÁLEZ

DIRECTOR: SAMUEL VER HOEYE

Programa de Doctorado en Tecnologías de la Información y
Comunicaciones en Redes Móviles

2018

Universidad de Oviedo

Departamento de Ingeniería Eléctrica, Electrónica,
de Computadores y Sistemas

Doctoral Thesis

Design, simulation and manufacturing techniques for fully textile integrated microwave circuits and antennas

---

Leticia Alonso González

Director: Samuel Ver Hoeye

Programa de Doctorado en Tecnologías de la Información y
Comunicaciones en Redes Móviles

2018

Preliminary examiners:
Dr. Francisco Pelayo García de Arquer, University of Toronto
Dr. Jacobo Cal González, Medical University of Vienna

October 2018

A mis padres, a mi hermano
y a mis tíos Jose y Marisa.

Agradecimientos

Quisiera aprovechar esta oportunidad para agradecer a todas aquellas personas que, de un modo u otro, habéis contribuido a que el fin de esta etapa, que tanto me ha aportado, sea una realidad.

En primer lugar, me gustaría expresar mi más sincero agradecimiento a mi director, Samuel, por la oportunidad que me ha dado de realizar la Tesis Doctoral con él, por sus infinitas horas de dedicación y por su confianza depositada en mi. Sin sus ideas, su ayuda y su esfuerzo, este trabajo no sería el mismo.

En segundo lugar, quisiera agradecer a Fernando no solo la oportunidad de poder pertenecer al grupo TSC-UNIOVI, sino también su predisposición a ayudar y su eficiencia en la resolución de cualquier tipo de problema, sobre todo burocrático, incluso en las situaciones más adversas.

Son muchas las personas que, a lo largo de estos cuatro años, han formado parte del conocido como *Taburdiu*, siendo los verdaderos protagonistas de innumerables historias que se quedarán siempre para el recuerdo. Sin embargo, me gustaría mostrar mi agradecimiento de forma individual a algunas de estas personas. Quiero agradecer a Miguel su inestimable ayuda, sus consejos y el estar siempre disponible para compartir conmigo esos cinco minutos –que se convierten en dos horas– y buscar el lado positivo a todo. También quiero darle las gracias a María, sobre todo, por estar siempre dispuesta a resolver cualquier reto matemático, en tiempo récord. No puedo finalizar este apartado sin darle las gracias a Ana por todo lo que he aprendido gracias a ella, por tener siempre la palabra necesaria en el momento preciso, por sus consejos y por su confianza.

I would like to thank Dr. Steve Greedy for allowing me to spend three months at The University of Nottingham, and starting the collaboration with the Hub.

Y lo más importante: quiero agradecer a mis padres, a mi hermano y a mis tíos Jose y Marisa sus consejos, su apoyo y su paciencia durante estos años. Además, un agradecimiento adicional se merece mi hermano por contribuir con sus dotes artísticas en la portada de la Tesis. Sin vosotros, este trabajo sería imposible.

Resumen

En la presente Tesis Doctoral se presentan nuevos resultados en las técnicas de diseño, simulación y fabricación de circuitos y antenas en la banda de microondas implementados en tecnología textil. Para ello, en el Capítulo 1 se introducen las técnicas más utilizadas para el desarrollo de circuitos y antenas textiles, tales como la impresión por inyección de tinta sobre sustratos textiles, el bordado, el *appliqué* o el uso de materiales no tejidos, comúnmente conocidos como *non-wovens*. Las técnicas anteriormente mencionadas presentan diferentes desventajas, por lo que se propone el proceso de tejido como la solución alternativa sobre la que se fundamenta el resto de la Tesis.

Con el objetivo de simplificar la simulación de las complejas estructuras textiles para su caracterización electromagnética, en el Capítulo 2 se propone y presenta un modelado basado en tres pasos. Dichos pasos se corresponden con las traducciones entre los distintos modelos equivalentes de la misma estructura textil. El modelo más complejo está basado en los filamentos de los que se componen los hilos multifilamento empleados y es, por tanto, el modelo que mayores recursos computacionales requiere. El modelo intermedio simula hilos monofilamento electromagnéticamente equivalentes a los anteriores, reduciendo así la complejidad computacional. Finalmente, la estructura textil es traducida a un modelo de capas homogéneas, análogo al utilizado en las simulaciones convencionales con sustratos rígidos. Se obtienen así, los parámetros equivalentes que caracterizan tanto a los materiales dieléctricos, como a los conductores que conforman el tejido.

Para validar el modelado de simulación propuesto, en el Capítulo 3 se presentan diferentes diseños de estructuras basadas en tecnología de guía de ondas integrada en sustrato, implementadas mediante procesos de tejido. Los diseños propuestos difieren tanto en la frecuencia de operación, como en el diseño de la estructura textil o en el grado de integración en el tejido de sus transiciones para su posterior validación experimental.

Teniendo como objetivo el desarrollo de prototipos con aplicación real, en el Capítulo 4 se presentan diferentes diseños de etiquetas y antenas para su funcionamiento en campo cercano y lejano, respectivamente. Estos prototipos, también integrados completamente en textil, se corresponden con diferentes tecnologías como *microstrip* o guía de ondas integrada en sustrato, entre otras, y operan en diferentes bandas de frecuencias.

El proceso de fabricación utilizando telares industriales aporta la enorme ventaja de poder desarrollar prototipos de grandes dimensiones y a gran escala. Este hecho se aprovecha en el Capítulo 5, en el que se presentan distintos tipos de superficies selectivas en frecuencia completamente integradas en tejido. Estas superficies no sólo son flexibles, sino que además esta característica las provee de una gran aplicabilidad real. Finalmente, se presentan las conclusiones generales y se proponen nuevas líneas de investigación.

Conclusiones

En la presente Tesis Doctoral se han presentado las técnicas de diseño, simulación y fabricación de circuitos y antennas completamente integrados en textil que trabajan en el rango de frecuencias de microondas. Aunque ya se han propuesto en la literatura diferentes alternativas para la integración de circuitos y antennas en textil, ninguna de estas alternativas cumple simultáneamente tres características importantes: una integración completa en el tejido, la posibilidad de desarrollar diseños multicapa y la fabricación a gran escala. Por este motivo, se propone la tecnología basada en el tejido como la alternativa más apropiada.

En primer lugar, con el objetivo de simplificar el diseño y la simulación de estructuras tejidas, se ha desarrollado una técnica de modelado basada en tres etapas. Estas tres etapas corresponden, respectivamente, a tres modelos diferentes de la estructura tejida, aunque electromagnéticamente equivalentes. El primer modelo, denominado modelo multifilamento, emula la composición real de los materiales empleados –en este caso, hilos multifilamento–, mientras que el segundo y simplificado modelo, el modelo monofilamento, los transforma en monofilamentos. Finalmente, el modelo de capas emula la topología convencional empleada en la simulación de circuitos y antenas utilizando sustratos homogéneos. Como resultado, la traducción entre los distintos modelos permite reducir la complejidad computacional de las simulaciones.

Con el objetivo de demostrar la validez del modelado, se ha empleado esta técnica en el desarrollo de dos guías de onda integradas en textil que funcionan, respectivamente, en los rangos de frecuencias de ondas milimétricas y microondas. Como resultado, se ha obtenido una buena concordacia entre las simulaciones y los resultados experimentales, demostrando que es posible la propagación de una señal a través de una estructura tejida.

Una vez que el modelado ha sido validado experimentalmente, se han diseñado diferentes prototipos basados en esta técnica. En primer lugar se ha estudiado una etiqueta tejida de identificación por radiofrecuencia que opera en campo cercano y que está provista de un chip comercial. Además, se han propuesto diferentes alternativas para la integración del chip en la estructura tejida. Alternativamente, con el propósito de desarrollar estructuras radiantes tejidas capaces de funcionar en la región de campo lejano, también se han implementado dos antenas. Primero se ha desarrollado una antena de ranura alimentada por línea *microstrip*, sin embargo, con el objetivo de suprimir la radiación trasera, se ha propuesto una antena basada en una cavidad resonante alimentada por cable coaxial. Ambas antenas han sido experimentalmente validadas en cámara anecoica presentando una buena concordancia entre las simulaciones y las medidas.

Además, se han propuesto dos superficies selectivas en frecuencia aprovechando las capacidades de producción a gran escala que presenta la tecnología basada en tejido. Para ello, primero se ha desarrollado una superficie selectiva en frecuencia basada en una capa de resonadores periódicos en forma de cruz. Alternatively, con el objetivo de aumentar el ancho de banda, se ha desarrollado una nueva superficie selectiva en frecuencia basada en dos capas aisladas de resonadores en forma de anillos cuadrados. En consecuencia, no solo se han aprovechado las capacidades de producción a gran escala, sino que este último prototipo representa un ejemplo de integración completa en textil multicapa, satisfaciendo las tres características importantes previamente citadas que debería cumplir un circuito integrado en textil.

Abstract

This Doctoral Thesis presents novel results regarding the design, simulation and manufacturing techniques to develop microwave circuits and antennas in textile technology. For this purpose, Chapter 1 introduces the most employed techniques to develop textile integrated circuits and antennas, such as inkjet-printing over textile substrates, embroidery, *appliqué* processes or the use of non woven materials or, simply, non-wovens. The beforementioned techniques present different problems, consequently, weaving has been found to be an alternative solution, becoming the basis of the Thesis.

With the aim of simplifying the simulation of the complex textile structures for their electromagnetic characterisation, Chapter 2 presents a modelling technique based on three steps. These steps correspond to the translation between the different equivalent models of the same textile structure. The most complex model is based on the filaments which compose the employed multifilament threads, therefore, it is the model which requires more computational resources. The intermediate model emulates monofilament threads which are electromagnetically equivalent to the multifilaments and, consequently, reduces the computational complexity. Finally, the textile structure is translated into a third model based on homogeneous layers, which is analogous to the model employed in conventional simulations with rigid substrates. Eventually, the equivalent parameters which electromagnetically characterise both the dielectric and conductive materials from which the textile is composed, are obtained.

In order to validate the proposed simulation modelling, Chapter 3 presents different designs of structures based on substrate integrated waveguides implemented using weaving technology. The proposed designs differ in terms of the operating frequency, the design of the textile structure or in the level of integration of the transitions for the experimentally validation in the textile. In Chapter 3, two different filters are also proposed, which are based on the cosim-

ulation between two different commercial electromagnetic simulator packages, in order to validate the simulation techniques already presented in the previous chapter.

With the aim of developing prototypes to be employed as a final application. Chapter 4 presents different designs of near-field and far-field tags and antennas. These prototypes, which are completely integrated in textile, are based on different technologies such as microstrip or substrate integrated waveguide, among others, and operate in different frequency bands.

The fabrication process using industrial weaving machines provides the enormous advantage of allowing the development of large prototypes as well as their large scale production. For this reason, Chapter 5 presents different types of frequency selective surfaces completely integrated in textile. Not only are these surfaces flexible, but also this characteristic provides them with different real applications. Finally, general conclusions and future lines of research are proposed.

List of acronyms

ADS	Advanced Design System
AHMSIW	Arbitrarily Height-Modulated Substrate Integrated Waveguide
AHMTIW	Arbitrarily Height-Modulated Textile Integrated Waveguide
AUT	Antenna Under Test
BPAHMTIW	BandPass AHMTIW
BSAHMTIW	BandStop AHMTIW
CAD	Computer Aided Design
CP	CoPolar
DC	Direct Current
DSCR	Dedicated Short-Range Communications
EM	ElectroMagnetic
EVA	Ethylene Vinyl Acetate
FF	Far Field
FM	Filament Model
FSS	Frequency Selective Surface
HFSS	High Frequency Structure Simulator

IoT	Internet of Things
ISBN	International Standard Book Number
ISSN	International Standard Serial Number
ISO	International Standards Organisation
JCR	Journal Citation Reports
LM	Layers Model
MDIF	MultiDimensional File
MM	Monofilament Model
NP	Not Provided
PBC	Perfect Boundary Conditions
PEC	Perfect Electric Conductor
PES	PolyEtherSulfone
PET	PolyEthylene-Terephthalate
PIFA	Planar Inverted-F Antenna
RF	RadioFrequency
RFID	RadioFrequency IDentification
S2P	2-Port S-Parameter
SGH	Standard Gain Horn
SIW	Substrate Integrated Waveguide
SMA	SubMiniature version A
SRF	Self Resonance Frequency

TIC	Textile Integrated Circuit
TIW	Textile Integrated Waveguide
UV	Ultra-Violet
XP	CrossPolar

Definitions

- **Warp thread:** thread which is previously mounted in the weaving loom and, consequently, is parallel to the warp direction.

- **Weft thread:** thread which is successively inserted between the upper and the lower sheds and, consequently, is parallel to the weft direction.

- **dtex:** unit of measure for the linear mass density of fibres, yarns and threads which is defined as the mass in grams per 10 Km.

- **ply:** unit which indicates the number of components which are twisted together to form a thread. An n-ply thread is composed of n components.

- ***ppi*:** picks per inch, which indicates the number of weft threads per inch.

- ***epi*:** ends per inch, which indicates the number of warp threads per inch.

Table of contents

List of figures

List of tables

1

Introduction

Contents

1.1 Introduction

New approaches in the development of textile circuits and antennas are continually emerging to cope with the advances in flexible, lightweight and wearable applications [1, 2]. Therefore, multiple efforts are being made to achieve the full integration of these circuits and antennas in textile. As a result, during the last years, a wide variety of solutions have been developed to design, simulate and manufacture textile integrated circuits and antennas.

Nevertheless, in spite of the wide range of approaches presented in the literature, none of these circuits and antennas are, simultaneously, flexible, washable and completely integrated in textile, as will be explained in section 1.2. For this reason, their fabrication requires different processes, making the prototypes not appropriate for their large scale production using the available industrial machinery. Consequently, these textile prototypes cannot be as competitive as their analogous manfactured using conventional procedures.

For this reason, with the aim of achieving a complete integration in textile and, therefore, the possibility of producing flexible and washable circuits and antennas on a large scale, weaving technology is proposed. This technology not only fulfils all the beforementioned requirements, but also allows the possibility of implementing multilayered designs.

In order to facilitate the comprehension of the following chapters, in section 1.3, the fundamentals of the textile structures, the industrial looms operation and the characteristics and classifications of the different types of threads are presented.

1.2 State of the art: textile integration techniques

1.2.1 Ink-jet printing

Ink-jet printing is a type of computerised printing which recreates a digital image or pattern by propelling droplets of ink onto different kinds of substrates. For highly conductive inks, silver or copper nanoparticles in solution are the most employed alternatives, although carbon nanotube inks are also used in applications where the conductivity can be lower.

Before the development of the ink-jet printing technology, different alternatives have been employed, such as the traditional subtractive microfabrication technology or the screen printing procedure. The subtractive microfabrication technology requires a clear substrate in which two films, the ink and the photoresist, are deposited. By the exposition to ultra-violet radiation of the substrate through a mask, the leftover photoresist can be easily eliminated. After the etching procedure and corresponding photoresist removal, the ink pattern is printed over the substrate. This procedure is summarised in Figure 1.1.

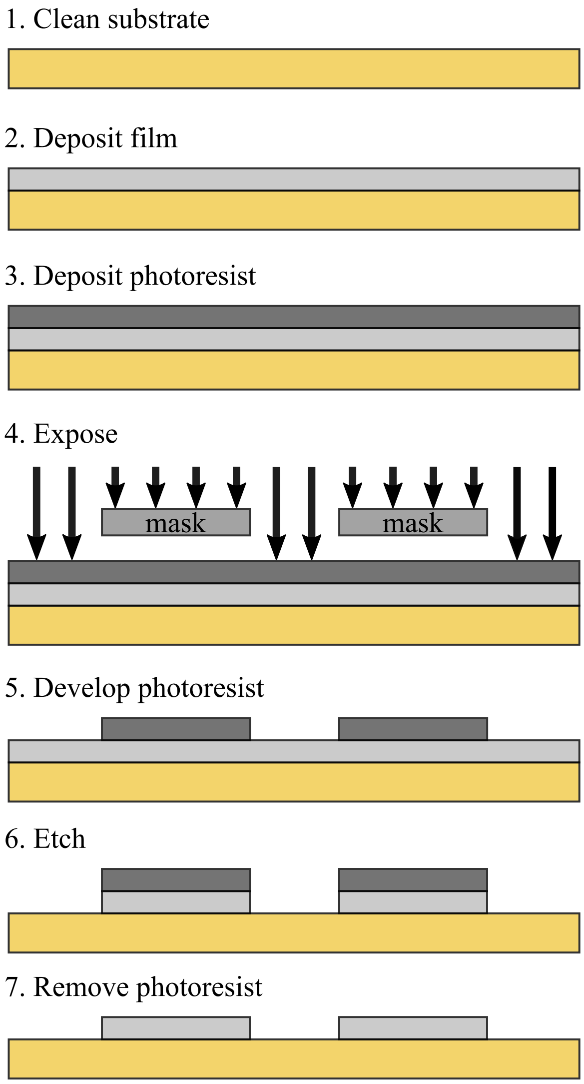

Figure 1.1: Traditional fabrication based on substrative microfabrication.

The screen printing procedure requires a screen frame mounted over the substrate. By the use of a squeegee, the active paste is spread over the frame and, consequently, over the substrate. After the curing process, the required pattern is printed over the substrate. This procedure is summarised in Figure 1.2.

The ink-jet printing procedure, as it has been previously mentioned, is based on the deposition of ink droplets onto a substrate and a posterior curing process, as depicted in Figure 1.3. In inkjet printing, a micrometer thick conductive layer or pattern is deposited on the desired substrate.

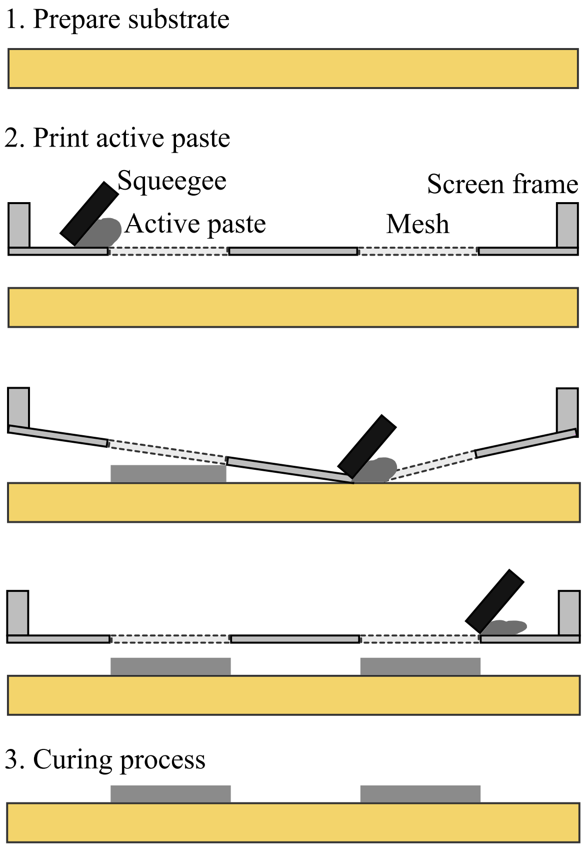

Figure 1.2: Screen printing technology.

Depending on the characteristics of the substrate, the ink-jet printing process implies different levels of difficulty. As a result, the ink-jet printing technique has been employed over flat and homogeneous substrates such as paper [3–5], Kapton [6–8] or flexible ceramic composites [9] to develop RF circuits and antennas.

Nevertheless, ink-jet printing over irregular, rough or porous surfaces, such as fabrics, becomes a challenging task due to the difficulty of achieving a highly conductive continuous track on the fabric with a thin ink-jet printed layer. As a result, ink-jet printed antennas over woven substrates present low values of efficiency. With the aim of solving these problems, two alternatives are proposed.

On the one hand, the performance of the ink-jet printed circuits can be improved by printing the conductive layer over an impermeable coated intermediate layer [10, 11]. On the other hand, printing multiple stacked conductive layers can also improve the performance of the prototype [12]. However, these options increase the manufacturing time and cost.

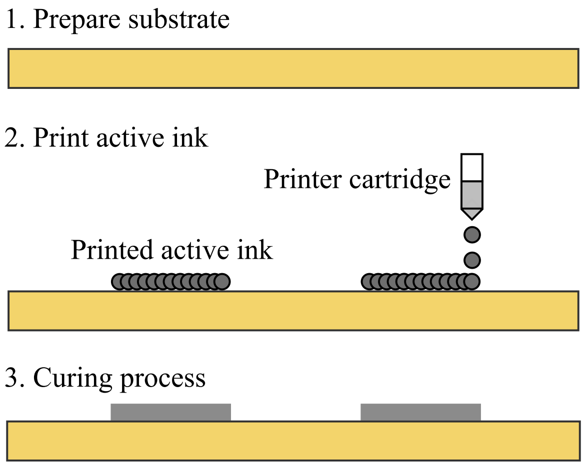

Figure 1.3: Direct writing based on inkjet printing technology.

The use of the ink-jet printing technique for the realisation of conductive patterns, specially over textile substrates, presents several advantages regarding the possibility of achieving complex details in the designs. Nevertheless, the requirement of an interface layer to deal with the uneven substrates represents an additional subprocess which supposes time during the manufacturing of the prototypes.

Furthermore, the impossibility of developing multilayered prototypes reduces the variety of implementable designs using this technique to dipole antennas [10], frequency selective surfaces (FSS) [11] or patch antennas [12]. Another disadvantage of this technique is that, although the technique can be employed in both sides of an existing substrate, the alignment of both patterns may become difficult to implement for large prototypes.

1.2.2 Embroidering

Embroidery is the art of realise patterns by means of stitches sewn directly onto an existing fabric. This technique used to be manual, however, with the development of the computerised embroidery machines, the patterns –previously designed using computer aided design (CAD) software packages– are automatically embroidered in the fabric. The patterns can be embroidered using electrically conductive threads, which provide a wide range of alternatives to develop RF circuits and antennas.

Depending on the density of the stitches, the embroidered pattern can be a line, a mesh or a surface. Conductive embroidered lines can be employed to develop contour antennas [13] or manufacturing rows of conductive vias for existing circuits [14], whereas conductive meshes can be employed in the development of planar inverted-F antennas (PIFA) [15].

Due to the possibility of manufacturing any embroidered pattern, the majority of the embroidered RF circuits or antennas are based on conductive surfaces [16–18]. Nevertheless, one of the disadvantages of embroidering, in comparison to ink-jet printing, is that embroidering does not allow the realisation of different patterns in both sides of an existing fabric, because the stitches completely cross the fabric from one side to the other. With the aim of finding a solution, in the bibliography, two individually embroidered fabrics are proposed and subsequently connected using *Velcros* to develop a reflectarray with a FSS [19].

Embroidery techniques present several advantages in terms of achieving complex designs of the conductive patterns due to the high resolution provided by the stitches. Furthermore, embroidering provides the possibility to easily manufacture lines and meshes, in contrast to ink-jet printing. This is due to the difficulty of printing very thin and continuous tracks on the fabric. Nevertheless, as also happened with the ink-jet printing procedures, the embroidery technique does not allow multilayered designs unless different fabrics are previously embroidered and, then, connected employing a different procedure such as using *Velcros* or weaving techniques. Furthermore, when connecting different layers is required to develop a whole design, aligning the different layers represents a problem.

1.2.3 Applique processes

Applique –or *appliqué*– processes consist of attaching various textile materials employing different alternatives such as sewing, adhesive or gluing procedures. Electrically conductive fabrics can be employed, leading to a wide variety of designs to develop RF circuits and antennas.

Different materials can be employed to implement the conductive elements of the circuits and antennas such as common woven copper plated or knitted silver fabrics [20], copper and nickel plated polyester fabrics [21], electrotextiles [22] or pure copper polyester taffeta [23]. However, specific commercial fabrics are also employed, such as *Less EMF* copper taffeta, *Less EMF* nickel-copper polyester ripstop, *Shieldex Nora Dell-CR* (nickel-copper-silver-plated nylon ripstop), *Shieldex* armor (nickel copper-silver nylon) [24], *ShieldIt Super* fabric [23] or *Zelt* conductive fabric [25].

The dielectric elements of the designs can be implemented using common nonconductive fabrics [20, 22], denim fabrics [21] or felt [23, 25]. Nevertheless, there are also commercial fabrics which are employed for this purpose, such as *Pellon Peltex 72F*, *Nomex* felt, *Creatology* stiffened felt or *Pellon Peltex 70* fabrics [24].

As previously mentioned, different procedures can be employed to attach the textile materials to conform the final design. Sewing procedures are employed in numerous designs in order to integrate the final prototypes into textile [20,23,26]. Nevertheless, adhesives are an interesting alternative to sewing because several commercial conductive fabrics are provided with the adhesive in one side [21]. When the conductive fabric is not provided with the adhesive, hold-melt adhesives can be employed, although the final prototype tends to stiff [24]. For this reason, spray adhesives are found more convenient, since they do not affect significantly the flexure nor electrical performance of the conductive materials, while allowing an homogeneous application [24, 25]. Another proposed alternative to connect the different materials of a prototype is through conductive vias implemented with eyelets [22].

Applique processes present various advantages in terms of developing RF antennas and circuits in textile, specially, due to the fact that using different separate structured layers allows a wide variety of designs, including multilayered prototypes [22, 25, 26]. Nevertheless, these techniques require several subprocesses to develop a final prototype, leading to a non-fully textile integrated circuit or antenna. In addition, the requirement of several subprocesses to implement a final design complicates a large scale production.

1.2.4 Non-woven based prototypes

Non-woven fabrics or simply, non-wovens, are fabric-like materials made from short staple fibres and continuous long fibres, bonded together by chemical, mechanical, heat or solvent treatments, leading to materials such as felt, which are neither woven nor knitted. Non-woven materials typically lack strength unless densified or reinforced. A non-woven itself is not a technique, but a material. However, non-wovens together with one of the previously presented techniques, can lead to the design of textile RF circuits or antennas.

Different materials can be employed as conductive non-woven fabrics to implement the conductive elements of RF circuits and antennas such as common carbon fibre non-woven fabric [27], copper, stainless or plated silver non-woven fabrics [28], polypyrrole-coated non-woven fabric [29], non-woven nanofibres [30] or copper-nickel coated non-woven fabrics [31]. Alternatively, dielectric non-woven fabrics can be employed such as the polypropylene based non-woven fabrics [32]. The different non-woven fabrics, as previously mentioned, are then attached using different techniques such as gluing [27] or sewing [29].

Non-wovens provide several advantages compared to the conventional fabrics. As an example, non-wovens provide higher levels of uniformity and consistency to high temperatures. Moreover, non-wovens are more stable regarding dimensionality. However, in order to develop a RF circuit or antenna using a non-woven, one or more of the before mentioned techniques must be applied. Consequently, every disadvantage previously mentioned can be extrapolated to the non-woven based prototype.

1.3 Weaving technology: fully textile integration

With the aim of achieving a fully textile integration of the RF circuits and antennas, the weaving technology is proposed in this Doctoral Thesis. For this purpose, the fundamentals of weaving and the classification of the threads will be presented throughout this section.

1.3.1 Textile structure overview

A textile structure can be divided into its composing threads, the warp threads and the weft threads, which are perpendicular to each other. The warp direction coincides with the length of the fabric, whereas the weft direction coincides with the width of the fabric and, consequently, with the width of the loom. For this purpose, the warp threads are previously assembled in the loom, whereas the weft threads are successively inserted in the woven structure during the fabrication process.

The primary motions required to weave a fabric are three. The first motion is called shedding. Shedding means the separation of the warp yarns, forming the lower and the upper sheds. This separation is made possible by the up and down movement of the frames in which the warp threads are assembled, leading to the aforementioned shedding movement. This movement is represented using red and green arrows, for the different sheds, in Figure 1.4.

The second motion needed is the filling insertion. Through the open shed of warp yarns, the filling weft yarn is inserted so that it interlaces with the warp yarns to produce a particular weave design. This movement is represented using a blue arrow in Figure 1.4. Beat-up is the third motion that the weaving loom performs. It is done with the aid of a reed, as it moves forward beating the filling

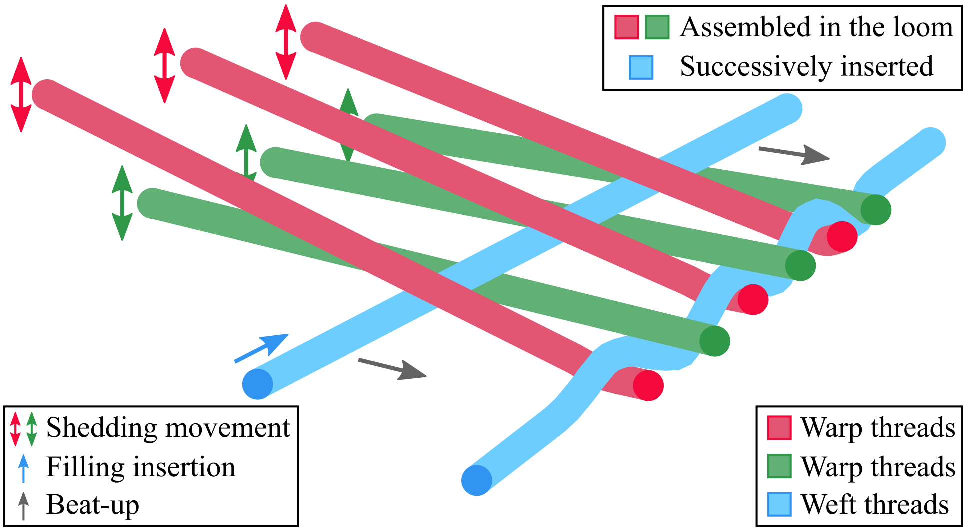

Figure 1.4: Simplified overview of the different threads in a generic loom.

yarn into the fabric to keep the threads from unraveling. This motion is depicted using grey arrows in Figure 1.4.

1.3.2 Modern industrial looms

In order to mass-produce a wide range of fabrics, thousands of different threads have to be organised in an industrial loom. For this reason, the warp threads must be organised in devices called heddles. Each heddle has an eye through which individual warp threads are threaded, as depicted in Figure 1.5. Heddles are suspended on the loom shafts, so that when a shaft is raised, the heddles go up, and the corresponding warp threads move with them. Although few hundreds of heddles and two shafts, moving up and down together, are required to create simple patterns, industrial looms have thousands of heddles and up to two dozens shafts moving independently. In other words, if an industrial loom is provided with twenty shafts, it is not mandatory that ten shafts are moving up when the other ten are moving down and vice versa.

To manufacture massive amounts of fabric in a cost-effective manner, the loom needs to move the weft through the warp threads as fast as possible. Old-style looms use a shuttle, which is a spool of thread that unravels as it is moved manually back and forth. With the aim of increasing the speed of the manufacturing process, shuttles have been substituted by different alternatives. One of the most efficient solution is the use of rapiers. One rapier picks up a piece of weft thread,

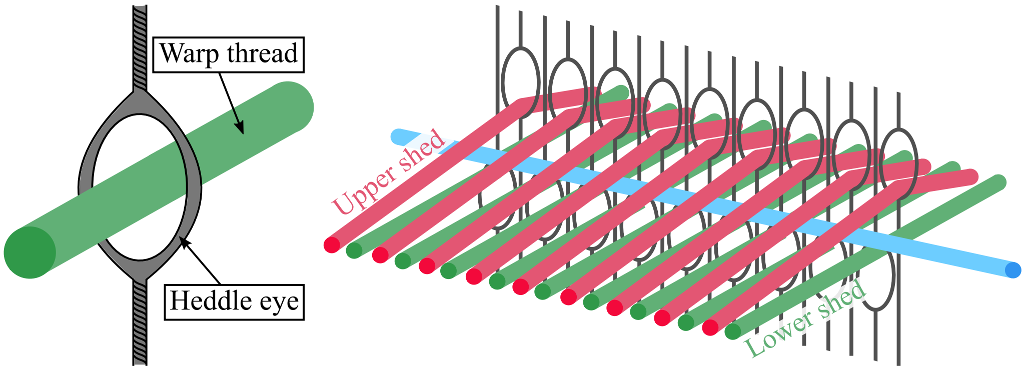

(a) (b)

Figure 1.5: Heddles mechanism overview. (a) Heddle magnification. (b) Distribution of the warp threads through the heddles.

pulls it to the middle of the loom width and passes the thread off to a second rapier. This second rapier pulls the thread the rest of the way across, while the first one goes back for another strand.

With the aim of manufacturing different, although simple, patterns and textures, different colored threads must be previously loaded on the loom. To achieve the different patterns, a weft presenter is required, which is a component that selects colors from different bobbins and gives them to the rapiers while they work. For complex patterns, a loom with a Jacquard attachment must be employed.

1.3.3 Jacquard looms

A Jacquard loom, also called Jacquard attachment, or Jacquard mechanism, is a loom with an incorporated special device to individually control the warp yarns. Therefore, this device controls all the threads loaded into the machine. Instead of combining the threads together onto the shafts of a standard loom, every strand has its own control system. Consequently, instructions are sent to each individual thread as it races through thousands of weaves to create a pattern.

As an example, in Figure 1.6a, the warp threads which are individually controlled are only two, whereas the rest of the warp threads work as if they were assembled in a standard loom, for simplification. As a result, Figure 1.6b depicts a hypothetical resultant fabric. Jacquard looms, together with the previously mentioned weft presenter, allow the fabrication of any pattern in the fabric.

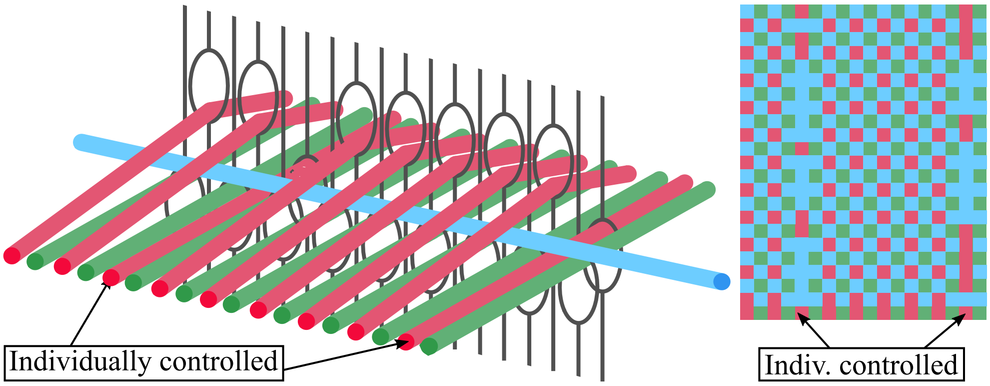

(a) (b)

Figure 1.6: Overview of the Jacquard mechanism and resultant fabric. (a) Distribution of the warp threads through the heddles. (b) Detailed resultant fabric.

1.3.4 Fundamentals of threads

Threads can be classified according to different factors such as the composition, texture, flexibility, among others. Regarding the composition, threads can be divided into two categories, monofilaments and multifilaments [33]. Monofilament threads are made from a single continuous fibre with a specified thickness. Although monofilament threads are strong, uniform and inexpensive to fabricate, they lack flexibility and are stiff in feel. As a result, usage is normally restricted to hems, draperies, and upholstered furniture.

Multifilament threads can also be classified into two categories [34]. On the one hand, smooth multifilament threads are usually made from nylon or polyester –or conductive materials– and are used where high strength is a primary requirement. These threads consist of two or more filaments twisted together. They are commonly used to sew shoes, leather garments and industrial products. On the other hand, textured filament threads are usually made from polyester –or conductive materials– and are used primarily as the looper thread for cover stitches. Texturing filaments gives the yarn more cover and high extensibility, although makes the thread more subject to snagging.

As an example, Figure 1.7a, depicts a fabric manufactured using monofilament threads [35], whereas Figure 1.7b represents a fabric which has been manufactured using multifilament threads [36]. The production cycle of every conventional thread begins as simple yarns. The basic yarns are produced by twisting

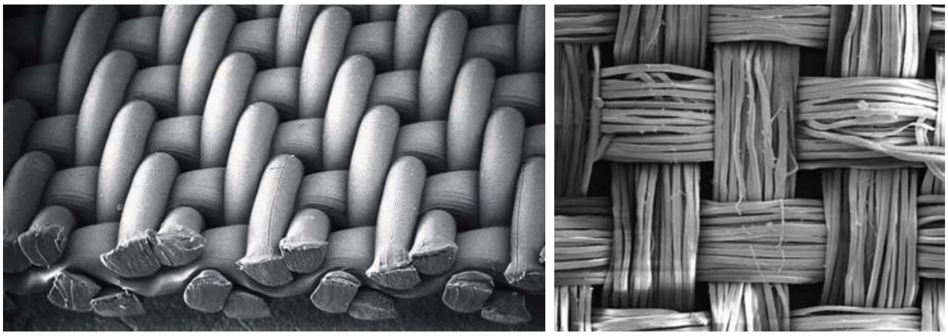

(a) (b)

Figure 1.7: Examples of fabrics. (a) Monofilament threads. (b) Multifilament threads.

together relatively short fibres or fine continuous filaments. For this purpose, two new concepts must be defined. A thread construction is defined in terms of the twist and twist direction.

Twist is the number of turns per unit length. A thread with too little twist may fray and break, whereas one with too much twist can cause snarling, looping and knotting. The direction of the finishing twist, or simply, the twist direction is very important. Twist can be inserted in either direction, consequently, this is described as either Z or S twist, as depicted in Figure 1.8a and Figure 1.8b, respectively. Most common machines use a Z twist thread. The direction of twist does not affect the strength of the thread, but it can seriously impair its performance when it is used on a machine for which it is not suited. Moreover, yarns with many components are twisted together to form an n-ply thread. The most commonly used are 2-, 3- or 4-ply threads. Figure 1.8c depicts an example of a 3-ply thread formation.

Another important characteristic of the threads is the textile measurement or linear density. Tex is a unit of measure for the linear mass density of fibres, yarns and threads and is defined as the mass in grams per 1000 meters. The most commonly used unit is actually the decitex –or dtex–, which is the mass in grams per 10 Km.

Depending on the characteristics of the threads, whether they are monofilaments or multifilaments, the twist, the linear mass density and, also, how they are assembled on the loom, the threads will tend to remain rigid or flexible. For this reason, the threads can present modifications in their cross section dimensions, as will be detailed in Chapter 2.

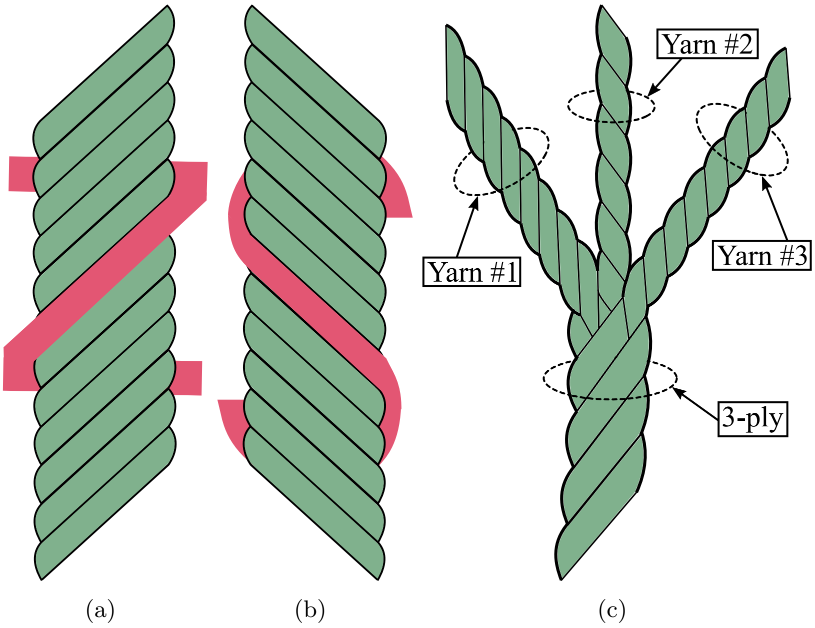

(a) (b) (c)

Figure 1.8: Twist direction and ply overview. (a) Z-twist example. (b) S-twist example. (c) 3-ply example.

Bibliography

[1] M. Sanchez-Fernandez, A. Tulino, E. Rajo-Iglesias, J. Llorca and A. G. Armada, “Blended antenna wearables for an unconstrained mobile experience,” in *IEEE Communications Mag.*, vol. 55, no. 4, pp. 160-168, April 2017. (Cited on page 2)

[2] D. Blanco and E. Rajo-Iglesias, “Wearable Fabry-Pérot antenna,” in *IEEE Antennas Wireless Propag. Lett.*, vol. 17, no. 1, pp. 106-109, Jan. 2018. (Cited on page 2)

[3] A. Rida *et al.*, “Design and integration of inkjet-printed paper-based UHF components for RFID and ubiquitous sensing applications,” presented in *European Microw. Conf.*, Munich, Oct. 9-12, 2007. (Cited on page 4)

[4] A. Rida *et al.*, “Conductive inkjet-printed antennas on flexible low-cost paper-based substrates for RFID and WSN applications,” in *IEEE Antennas Propag. Mag.*, vol. 51, no. 3, pp. 13-23, June 2009. (Cited on page 4)

[5] V. Lakafosis *et al.*, “Progress towards the first wireless sensor networks consisting on inkjet-printed, paper-based RFID-enabled sensor tags”, *Proceedings of the IEEE*, vol. 98, no. 9, pp. 1601-1609, Sep. 2010. (Cited on page 4)

[6] K. Kirschenmann *et al.*, “Inkjet printed microwave frequency multilayer antennas,” presented in *IEEE Antennas Propag. Society Int. Symp.*, Honolulu, HI, June 9-15, 2007. (Cited on page 4)

[7] J. Virtanen *et al.*, “The effect of conductor thickness in passive inkjet printed RFID tags,” presented in *IEEE Antennas Propag. Society Int. Symp.*, Toronto, ON, July 11-17, 2010. (Cited on page 4)

[8] A. Kanso *et al.*, “Inkjet printing of coplanar wire-patch antenna on a flexible substrate,” presented in *Int. Symp. on Antenna Technol. and Applied Electromagnetics*, Toulouse, France, June 25-28, 2012. (Cited on page 4)

[9] A. A. Babar *et al.*, “Inkjet-printable UHF RFID tag antenna on a flexible ceramic- polymer composite substrate,” presented in *IEEE/MTT-S Int. Microw. Symp. Digest*, Montreal, QC, Canada, June 17-22, 2012. (Cited on page 4)

[10] A. Chauraya *et al.*, “Inkjet printed dipole antennas on textiles for wearable communications,” in *IET Microw. Antennas Propag.*, vol. 7, no. 9, pp. 760-767, June 2013. (Cited on pages 4 and 5)

[11] W. G. Whittow *et al.*, “Printed frequency selective surfaces on textiles”, in *Electron. Lett.*, vol. 50, no. 13, pp. 916-917, June 2014. (Cited on pages 4 and 5)

[12] W. G. Whittow *et al.*, “Inkjet-printed microstrip patch antennas realized on textile for wearable applications”, in *IEEE Antennas and Wireless Propag. Lett.*, vol. 13, pp. 71-74, 2014. (Cited on pages 4 and 5)

[13] G. Ginestet *et al.*, “Embroidered antenna-microchip interconnections and contour antennas in passive UHF RFID textile tags”, in *IEEE Antennas and Wireless Propag. Lett.*, vol. 16, pp. 1205-1208, 2017. (Cited on page 6)

[14] A. Paraskevopoulos *et al.*, “Higher-mode textile patch antenna with embroidered vias for on-body communication”, in *IET Microw. Antennas and Propag.*, vol. 10, no. 7, pp. 802-807, May 2016. (Cited on page 6)

[15] B. Ivsic, D. Bonefacic and J. Bartolic, “Considerations on embroidered textile antennas for wearable applications”, in *IEEE Antennas Wireless Propag. Lett.*, vol. 12, pp. 1708-1711, 2013. (Cited on page 6)

[16] S. Zhang *et al.*, “Broad-band embroidered spiral antenna for off-body communications”, in *IET Microw. Antennas Propag.*, vol. 10, no. 13, pp. 1395-1401, Oct. 2016. (Cited on page 6)

[17] T. Acti *et al.*, “Embroidered wire dipole antennas using novel copper yarns”, in *IEEE Antennas Wireless Propag. Lett.*, vol. 14, pp. 638-641, Nov. 2015. (Cited on page 6)

[18] Z. Wang *et al.*, “Embroidered multiband body-worn antenna for GSM/PCS/WLAN communications”, in *IEEE Trans. Antennas Propag.*, vol. 62, no. 6, pp. 3321-3329, June 2014. (Cited on page 6)

[19] M. M. Tahseen and A. A. Kishk, “Flexible and portable textile-reflectarray backed by frequency selective surface”, in *IEEE Antennas Wireless Propag. Lett.*, vol. 17, no. 1, pp. 46-49, Jan. 2018. (Cited on page 6)

[20] R. R. G. Perron, G. C. Huang and M. F. Iskander, “Textile electromagnetic coupler for monitoring vital signs and changes in lung water content”, in *IEEE Antennas Wireless Propag. Lett.*, vol. 14, pp. 151-154, 2015. (Cited on pages 6 and 7)

[21] D. Ferreira *et al.*, “Wearable textile antennas: examining the effect of bending on their performance”, in *IEEE Antennas Propag. Mag.*, vol. 59, no. 3, pp. 54-59, June 2017. (Cited on pages 6 and 7)

, “Design and implementation of electro-textile ground planes for wearable UHF RFID patch tag antennas”, in *IEEE Antennas Wireless Propag. Lett.*, vol. 12, pp. 964-967, 2013.

[22] R. Moro *et al.*, “Textile microwave components in substrate integrated waveguide technology,” *IEEE Trans. Microw. Theory and Techn.*, vol. 63, no. 2, pp. 422-432, Feb. 2015. (Cited on pages 6 and 7)

[23] P. J. Soh *et al.*, “Design of a broadband all-textile slotted PIFA”, in *IEEE Trans. Antenna Propag.*, vol. 60, no. 1, pp. 379-384, Jan. 2012. (Cited on pages 6 and 7)

[24] T. Haagenson *et al.*, “Textile antennas for spacesuit applications: design, simulation, manufacturing, and testing of textile patch antennas for spacesuit applications”, in *IEEE Antennas Propag. Mag.*, vol. 57, no. 4, pp. 64-73, Aug. 2015. (Cited on pages 6 and 7)

[25] S. Zhu and R. Langley, “Dual-band wearable textile antenna on an EBG substrate”, in *IEEE Trans. Antenna Propag.*, vol. 57, no. 4, pp. 926-935, April 2009. (Cited on pages 6 and 7)

[26] J. Lilja *et al.*, “Design and manufacturing of robust textile antennas for harsh environments”, in *IEEE Trans. Antenna Propag.*, vol. 60, no. 9, pp. 4130-4140, Sept. 2012. (Cited on page 7)

[27] T. C. Baum *et al.*, “Investigations of a load-bearing composite electrically small Egyptian axe dipole antenna”, in *IEEE Trans. Antenna Propag.*, vol. 65, no. 8, pp. 3827-3837, Aug. 2017. (Cited on pages 7 and 8)

[28] Y. Senbokuya and H. Tsunoda, "A study on the circular patch antennas using conductive non-woven fiber fabrics", presented in *IEEE Antennas Propag. Soc. Int. Symp.*, San Antonio, TX, June 16-21, 2002. (Cited on page 7)

[29] Y. Jiang *et al.*, "A highly usable and customizable sEMG sensor for prosthetic limb control using polypyrrole-coated nonwoven fabric sheet", presented in *IEEE SENSORS*, Busan, South Korea, Nov. 1-4, 2015. (Cited on pages 7 and 8)

[30] R. Polansky *et al.*, "A study on the usage of nonwoven nanofibers in electrical insulating materials", presented in *IEEE Conf. on Electrical Insulation and Dielectric Phenomena*, Ann Arbor, MI, Oct. 18-21, 2015. (Cited on page 7)

[31] A. N. Austin *et al.*, "Analysis of the shielding properties of metalised nonwoven materials", presented in *International Symposium on Electromagnetic Compatibility*, Brugge, Belgium, Sep. 2-6, 2013. (Cited on page 7)

[32] S. Gangopadhyay *et al.*, "Design and development of electro-conductive rectangular textile antenna using polypropylene fabrics", presented in *IEEE Uttar Pradesh Section Int. Conf. Electrical, Computer and Electronics*, Mathura, India, Jan 26-28, 2017. (Cited on page 8)

[33] COATS, "All about sewing threads". [Online]. Available: www.coatsindustrial.com/en/information-hub/apparel-expertise/sewing-threads. (Cited on page 11)

[34] R. Sinclair, "Textile and fashion", in *Woodhead Publishing Series in Textile*, Elsevier Ltd, 2015, pp. 213-253. (Cited on page 11)

[35] Boegger Industrial Limited, "Filter cloth-selection an important role of filtration". [Online]. Available: www.filtercloths.org/technology/select-filter-cloth.html. (Cited on page 11)

[36] National Museums Liverpool, "Scanning electron microscopy". [Online]. Available: www.liverpoolmuseums.org.uk/conservation/departments/science/scanning-electron-microscopy.aspx. (Cited on page 11)

2

Modelling techniques

Contents

The aim of this chapter is to describe the modelling technique employed to electromagnetically simulate complex textile structures. First, a description of a three-step modelling to characterise both dielectric and electrically conductive textile materials is presented. Secondly, a technique to design arbitrarily height-modulated textile integrated waveguide filters is discussed.

The modelling techniques presented in this chapter are then employed and experimentally verified in the different circuits and antennas presented in the following chapters.

2.1 Three-step modelling

The herein presented technique is a parametric modelling based on three steps, the filament model (FM), the monofilament model (MM) and the layers model (LM). Each model represents, equivalently, the electromagnetic (EM) behaviour of the same woven structure, nevertheless, the computational complexity is successively reduced from the FM to the MM, and the LM. Therefore, the aim of this modelling is to electromagnetically characterise a woven structure before its fabrication.

The different modelling steps and the most important parameters required to translate between modellings are summarised in Figure 2.1 and will be described in detail in the following subsections. This parametric modelling will then be applied to different microwave circuits and antennas in the following chapters. Therefore, this modelling is employed with the aim of predicting the EM behaviour of the textile structure and subsequently compare these predictions with the measurements for its experimentally validation.

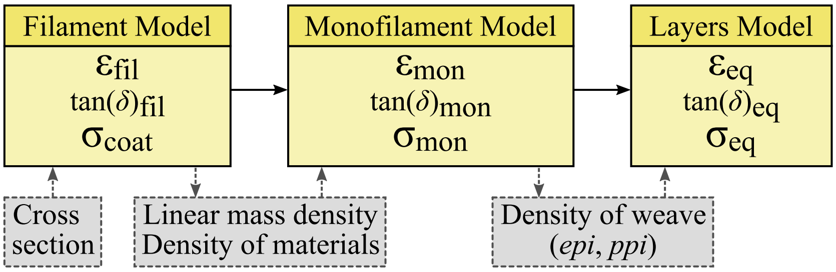

Figure 2.1: Three-step characterisation model, corresponding relative permittivities, loss tangents and electrical conductivities and required parameters for translation between models.

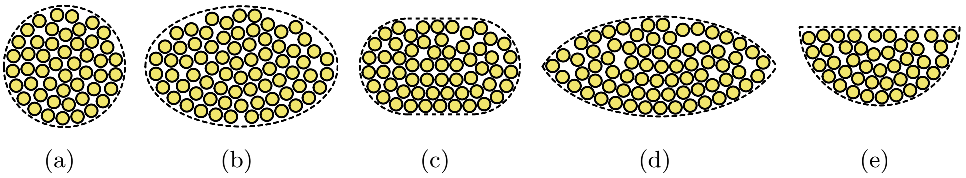

(a) (b) (c) (d) (e)

Figure 2.2: Different distributions of the filaments in the cross section of a multifilament thread. (a) Circular. (b) Pierce's elliptic. (c) Kemp's racetrack. (d) Hearle. (e) Bowshaped.

2.1.1 Filament model

The FM emulates the real composition of the thread and represents the most computationally complex problem. It takes into account the number of filaments which compose the thread, the dimensions of each filament and the characteristic parameters of the material from which the filaments have been extruded, which are the relative dielectric permittivity, $\varepsilon_{\mathrm{fil}}$, and the loss tangent, $\tan(\delta)_{\mathrm{fil}}$.

During the fabrication process of the multifilament threads, the different filaments tend to be packed adopting a circularly-shaped cross section, as generically depicted in Figure 2.2a. However, this cross section tends to deform when the threads are in a woven structure, due to the forces they experiment. Some approaches to characterise the deformed cross section of these threads have been widely used such as the Pierce's elliptic cross section (Figure 2.2b), the Kemp's racetrack section (Figure 2.2c), the Hearle's section (Figure 2.2d) or the Bowshaped geometry (Figure 2.2e) [1].

The circular cross section consists of a circumference whose diameter is given by D_{C} as it is represented in Figure 2.3a. The Pierce's elliptic cross section, which is the most used one, consists of an ellipse whose axes are D_{W} and D_{H}, respectively, as depicted in Figure 2.3b. The Kemp's racetrack cross section consists of a rectangle enclosed by two semicircular ends and is fully defined using two parameters, its width, D_{W}, and its height, D_{H}, as it can be seen in Figure 2.3c. The Hearle's cross section consists of two identical arcs of a circumference, together, leading to an eye-shaped structure, which can be described from the radius of the circumference, R_{H}, and the semiangle of the arc, θ_{H}, as depicted in Figure 2.3d. The bowshaped cross section consists of a semi-circumference, which can be defined using its radius, R_{B}, as it can be seen in Figure 2.3e.

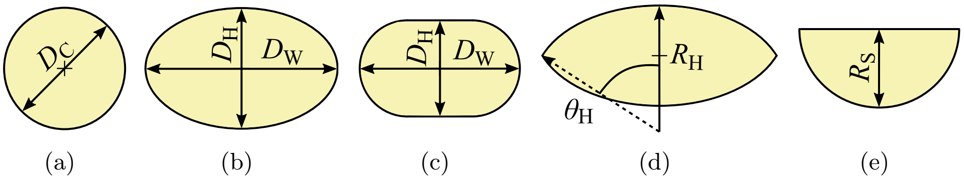

Figure 2.3: Dimensions of the cross sections for the different distributions of the filaments in a multifilament thread. (a) Circular. (b) Pierce's elliptic. (c) Kemp's racetrack. (d) Hearle. (e) Bowshaped.

2.1.2 Monofilament model

The MM represents an electromagnetically equivalent textile structure by replacing the multifilament threads with monofilament threads, and reducing the computational complexity. Depending on the EM behaviour of the thread, electrically conductive or dielectric, a different procedure to translate from the FM to the MM is required.

2.1.2.1 Dielectric materials

Due to the air gaps between the filaments that are forming the thread, the relative permittivity of its equivalent dielectric monofilament is reduced and denoted by ε_{mon}. A new loss tangent can be defined and denoted by $\tan(\delta)_{\text{mon}}$.

To translate the FM into the MM, a theoretical method has been used. For this purpose, the linear mass density of the thread, L_{dtex}, the density of the material from which the filaments have been extruded, δ_{fil}, and the geometric parameters of the thread (cross section dimensions and length: W, H and L, respectively, as depicted in Figure 2.4a) must be taken into account. The linear mass density of the threads is commonly measured using the dtex unit.

Given a generic thread with an elliptic cross section, its volume is given by $V_o = \pi WHL/2$. The linear mass density per unit length represents the weight of the thread per unit length, including the air gaps. If it is specified using dtex, then it is defined for $L = 10$ Km. The density parameter represents the weight of the material per unit volume. Therefore, given a thread whose volume is V_o, if the value of its linear mass density is compared to the value of its weight, the proportion of air inside the thread can be calculated as summarised in Figure 2.4a.

Simulating a rectangular waveguide which has been filled with filaments (ε_{fil} and $\tan(\delta)_{\text{fil}}$), using the same proportion of air as there is inside the thread, and

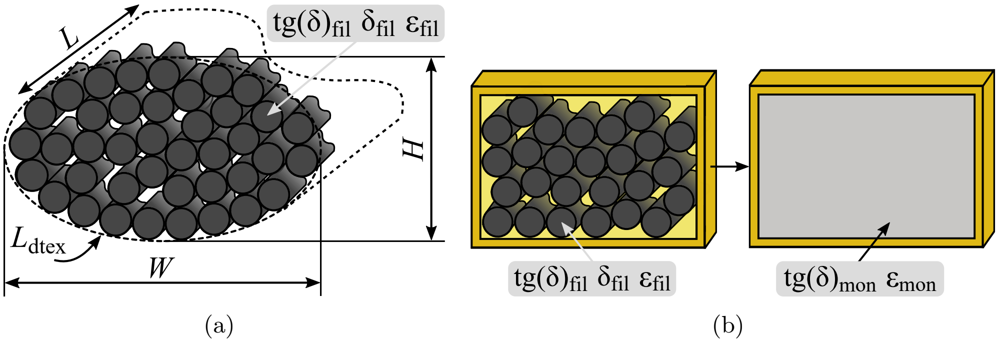

(a) (b)

Figure 2.4: Translation from FM to MM. (a) Parameters involved in the translation from the FM into the MM using dielectric materials. (b) Overview of the waveguide procedure.

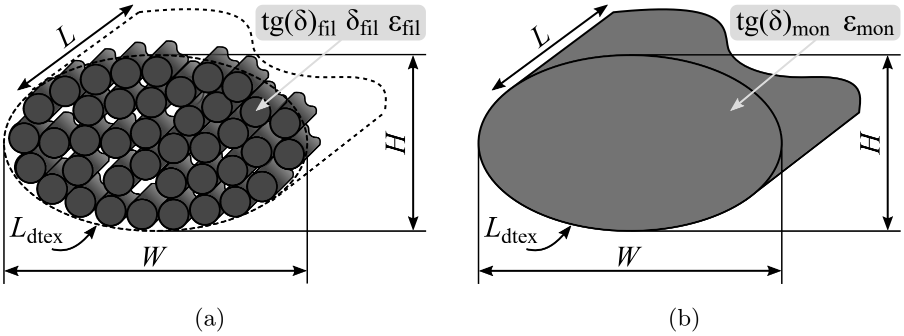

(a) (b)

Figure 2.5: Translation from the FM into the MM outline applied to dielectric threads. (a) FM applied to a thread. (b) MM applied to a thread.

comparing its EM behaviour with another rectangular waveguide which has been homogeneously filled, the corresponding $\varepsilon_{\mathrm{mon}}$ and $\tan(\delta)_{\mathrm{mon}}$ parameters can be easily extracted from the cut-off frequency and the insertion losses as summarised in Figure 2.4b. Therefore, a dielectric multifilament thread can be translated into its equivalent monofilament thread as depicted in Figure 2.5.

2.1.2.2 Conductive materials

Conductive threads can be manufactured from a conductive material, or can be made from dielectric materials and subsequently coated with conductive material. The coating procedure includes three steps. First, the non-coated threads are knitted into a fabric. Secondly, the fabric is plated with the conductive

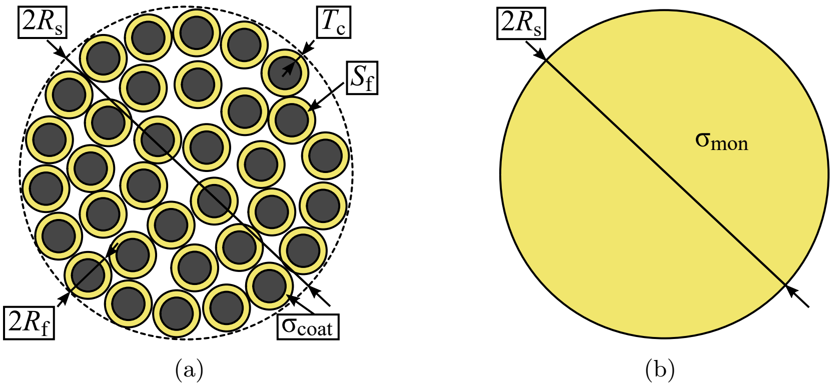

Figure 2.6: Translation from a conductive multifilament thread into a conductive monofilament thread. (a) Conductive multifilament thread cross section. (b) Equivalent conductive monofilament thread cross section.

material by an electrolysis process. Finally, the fabric is de-knitted and it can be guaranteed that every thread has been completely plated. Consequently, the thickness of the coating and its composition become relevant, then, the skin effect has to be analysed.

Figure 2.6a depicts an example of a multifilament thread, whereas Figure 2.6b represents its electromagnetically equivalent monofilaments. The aim of this section is to calculate the electrical conductivity of the equivalent monofilament, σ_mon.

The skin depth can be calculated from the expression (2.1), where δ is the skin effect depth, ρ_coat is the resistivity of the material employed for the coating, f is the operating frequency and μ is the magnetic permeability. The first step in the characterisation of the conductive materials is the comparison between the calculated skin depth, δ, and the thickness of the conductive coating which has been applied to each filament, T_c. Two different procedures have to be taken into account to translate the multifilament thread into its analogous monofilament, depending on the fact that the skin depth is less or equal than the thickness of the conductive coating applied to each filament. Both cases are schematically represented in Figure 2.7.

$$\delta = \sqrt{\frac{\rho_\mathrm{coat}}{\pi f \mu}} \tag{2.1}$$

If the skin depth is less or equal than the thickness of the conductive coating applied to each filament, $\delta \leqslant T_\mathrm{c}$, the resistance per unit length of each filament

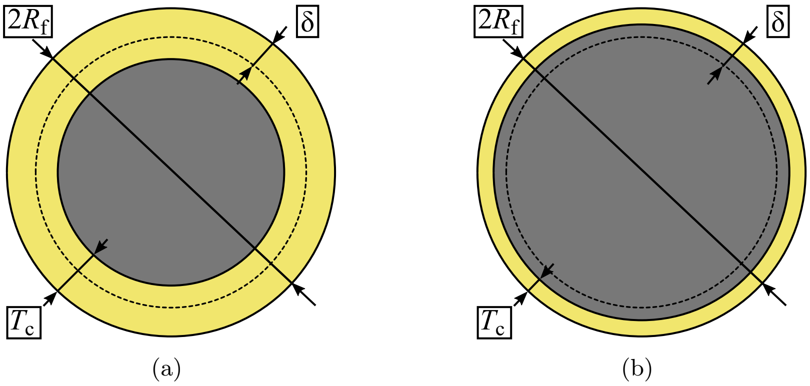

Figure 2.7: Different cases in the translation from the multifilament thread into the analogous monofilament thread, using the magnification of a single filament. (a) $\delta \leqslant T_\mathrm{c}$. (b) $\delta > T_\mathrm{c}$.

can be calculated using (2.2), where $(R/l)_\mathrm{f}$ denotes the resistance per unit length of each filament, ρ_coat and σ_coat are, respectively, the resistivity and conductivity of the material employed for the coating, and S_f represents the area of the effective conductive cross section of each filament.

$$(R/l)_\mathrm{f} = \frac{\rho_\mathrm{coat}}{S_\mathrm{f}} = \frac{1}{\sigma_\mathrm{coat} \cdot S_\mathrm{f}} \tag{2.2}$$

In order to calculate the effective conductive cross section of each filament, as the δ is less or equal than T_c, the δ parameter has to be taken into account instead of T_c. Consequently, the S_f associated to a single filament whose external radius (including the coating) is R_f is given by (2.3).

$$S_\mathrm{f} = \pi \cdot {R_\mathrm{f}}^2 - \pi \cdot (R_\mathrm{f} - \delta)^2 = \pi \cdot (2 \cdot R_\mathrm{f} \cdot \delta - \delta^2) \tag{2.3}$$

Substituting (2.3) in (2.2), the resistance per unit length of a single filament is given by (2.4). Consequently, the resistance per unit length of a multifilament thread, (R/l), composed of N_fil filaments is given by (2.5).

$$(R/l)_\mathrm{f} = \frac{1}{\sigma_\mathrm{coat} \cdot \pi \cdot (2 \cdot R_\mathrm{f} \cdot \delta - \delta^2)} \tag{2.4}$$

$$(R/l) = \frac{(R/l)_\mathrm{f}}{N_\mathrm{fil}} = \frac{1}{N_\mathrm{fil} \cdot \sigma_\mathrm{coat} \cdot \pi \cdot (2 \cdot R_\mathrm{f} \cdot \delta - \delta^2)} \tag{2.5}$$

With the aim of substituting the multifilament thread by an electromagnetically equivalent monofilamente thread, the effective radius of the multifilament thread, R_S, must be taken into account. Therefore, the electromagnetically equivalent monofilament thread must have the same radius, R_S, in order to keep the same woven structure.

The monofilament thread is provided with a conductive coating (σ_mon) whose thickness is given by T_R, leading to a corresponding area of the conductive cross section denoted by S_mon. The S_mon can be calculated using (2.6).

$$S_\mathrm{mon} = \pi \cdot {R_\mathrm{S}}^2 - \pi \cdot (R_\mathrm{S} - T_\mathrm{R})^2 = \pi \cdot (2 \cdot R_\mathrm{S} \cdot T_\mathrm{R} - {T_\mathrm{R}}^2) \tag{2.6}$$

In order to guarantee the electromagnetic equivalence between the multifilament thread and the proposed monofilament thread, the resistances per unit length must be the identical. For this purpose, the resistance per unit length of the monofilament thread, $(R/l)_\mathrm{mon}$, can be calculated using (2.7). Alternatively, the resistance per unit length of the multifilament thread, (R/l), has been previously calculated in (2.5).

$$(R/l)_\mathrm{mon} = \frac{1}{\sigma_\mathrm{mon} \cdot \pi \cdot (2 \cdot R_\mathrm{S} \cdot T_\mathrm{R} - {T_\mathrm{R}}^2)} \tag{2.7}$$

The condition of achieving the same resistance per unit length with both threads, leads to the equation presented in (2.8).

$$\frac{1}{\sigma_\mathrm{mon} \cdot (2 \cdot R_\mathrm{S} \cdot T_\mathrm{R} - {T_\mathrm{R}}^2)} = \frac{1}{N_\mathrm{fil} \cdot \sigma_\mathrm{coat} \cdot (2 \cdot R_\mathrm{f} \cdot \delta - \delta^2)} \tag{2.8}$$

Nevertheless, the electromagnetic field penetrates a distance given by the skin depth in the monofilament, therefore, it must be calculated. The skin depth in the monofilament thread is denoted by δ_mon and can be calculated using (2.9). Consequently, $T_\mathrm{R} = \delta_\mathrm{mon}$.

$$\delta_\mathrm{mon} = \sqrt{\frac{1}{\sigma_\mathrm{mon} \pi f \mu}} \tag{2.9}$$

Substituting the expressions (2.1) and (2.9) in (2.8) and simplifying, the value of the electrical conductivity of the equivalent monofilament, σ_mon, can be calculated using (2.10), where σ_mon depends on the cross section of the equivalent monofilament (R_S), the frequency (f), the number of filaments which compose each multifilament thread (N_fil), the magnetic permeability (μ) and the electrical conductivity of the coating (σ_coat).

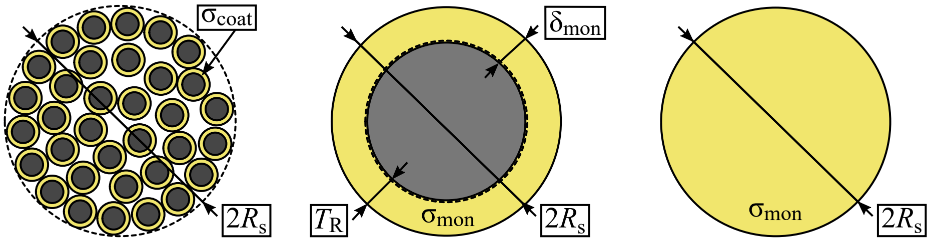

(a) (b) (c)

Figure 2.8: Translation from the multifilament thread into the analogous monofilament thread overview ($\delta \leqslant T_{\mathrm{c}}$). (a) Multifilament thread. (b) Equivalent monofilament thread provided with the conductive coating. (c) Equivalent monofilament thread.

$$\begin{aligned} &\sigma_{\mathrm{mon}} \cdot (2 \cdot R_{\mathrm{S}} \cdot \sqrt{\frac{1}{\pi f \mu \sigma_{\mathrm{mon}}}} - \frac{1}{\pi f \mu \sigma_{\mathrm{mon}}}) = \\ &= N_{\mathrm{fil}} \cdot \sigma_{\mathrm{coat}} \cdot (2 \cdot R_{\mathrm{f}} \cdot \sqrt{\frac{1}{\pi f \sigma_{\mathrm{coat}}}} - \frac{1}{\pi f \mu \sigma_{\mathrm{coat}}}) \end{aligned} \tag{2.10}$$

Once the σ_{mon} is calculated, the electromagnetically equivalent monofilament threads can be simulated using the same radius, R_{S}, and the σ_{mon}. The beforementioned translation procedure from the multifilament conductive thread into its equivalent monofilament thread is summarised in Figure 2.8.

Nevertheless, the calculated skin depth in (2.1) may have been greater than the thickness of the conductive coating applied to each filament, $\delta > T_{\mathrm{c}}$. In this case, the resistance per unit length of the multifilament thread can be calculated using (2.11), where the parameter δ has been substituted with T_{c} in comparison to the expression in (2.5).

$$(R/l) = \frac{1}{N_{\mathrm{fil}} \cdot \sigma_{\mathrm{coat}} \cdot \pi \cdot (2 \cdot R_{\mathrm{f}} \cdot T_{\mathrm{c}} - {T_{\mathrm{c}}}^2)} \tag{2.11}$$

As a result, the value of the electrical conductivity of the equivalent monofilament, σ_{mon}, can be calculated using (2.12), where σ_{mon} depends on the cross section of the equivalent monofilament (R_{S}), the frequency (f), the number of filaments which compose each multifilament thread (N_{fil}), the magnetic permeability (μ), the electrical conductivity of the coating (σ_{coat}) and the thickness

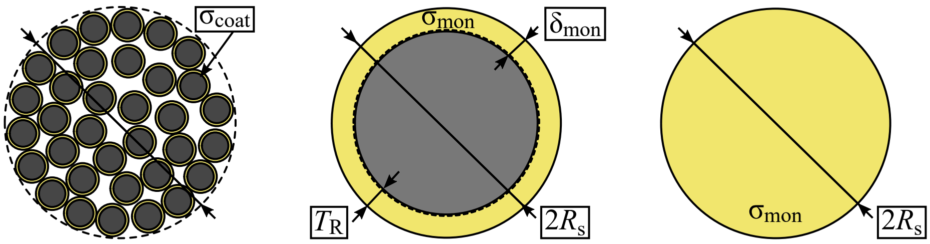

(a) (b) (c)

Figure 2.9: Translation from the multifilament thread into the analogous monofilament thread overview ($\delta > T_\mathrm{c}$). (a) Multifilament thread. (b) Equivalent monofilament thread provided with the conductive coating. (c) Equivalent monofilament thread.

of the conductive coating applied to each filament (T_c). The beforementioned translation procedure from the multifilament conductive thread into its equivalent monofilament thread is summarised in Figure 2.9.

$$\begin{aligned}\sigma_\mathrm{mon} \cdot (2 \cdot R_\mathrm{S} \cdot \sqrt{\frac{1}{\pi f \mu \sigma_\mathrm{mon}}} - \frac{1}{\pi f \mu \sigma_\mathrm{mon}}) &= \\ = N_\mathrm{fil} \cdot \sigma_\mathrm{coat} \cdot (2 \cdot R_\mathrm{f} \cdot T_\mathrm{c} - {T_\mathrm{c}}^2)&\end{aligned} \tag{2.12}$$

Comparing the expression in (2.10) with the expression in (2.12), there is an important difference. While in (2.10) the thickness of the conductive coating does not appear in the equation due to the fact that it is sufficiently thick, in (2.12), this thickness, T_c, is determinant in order to calculate the equivalent electrical conductivity, σ_mon. With the aim of summarising the employed notation in the previous paragraphs, Table 2.1 presents the parameters and their corresponding meanings.

The aforementioned methodology to obtain the equivalent conductive monofilament has been first validated in simulations. For this purpose, a multifilament thread has been introduced in a rectangular waveguide, parallel to the orientation of the electric field, $\vec{E}$, and the scattering parameters have been calculated. The simulated thread is composed of $N_\mathrm{fil} = 19$ filaments, whose radius –including the coating– is $R_\mathrm{f} = 31$ µm. The employed thickness of the silver coating of each filament is $T_\mathrm{c} = 0.5$ µm. These filaments compose a multifilament thread whose equivalent radius is $R_\mathrm{S} = 0.075$ mm.

Table 2.1: Notation employed for the translation from conductive multifilament threads to monofilament threads.

Parameter	Meaning
σ_{coat}	Electrical conductivity of the coating
σ_{mon}	Electrical conductivity of the equivalent monofilament
δ	Calculated skin depth using σ_{coat}
δ_{mon}	Calculated skin depth using σ_{mon}
N_{fil}	Number of filaments which compose the multifilament thread
R_{S}	Equivalent radius of the multifilament (and monofilament)
R_{f}	Radius of one filament which composes the multifilament thread
T_{c}	Thickness of the coating of each filament
T_{R}	Thickness of the coating of the equivalent monofilament
S_{f}	Conductive area of the cross section of each filament
S_{mon}	Conductive area of the cross section of the monofilament
$(R/l)_{\mathrm{f}}$	Resistance per unit length of each filament
(R/l)	Resistance per unit length of the complete multifilament thread
$(R/l)_{\mathrm{mon}}$	Resistance per unit length of the equivalent monofilament

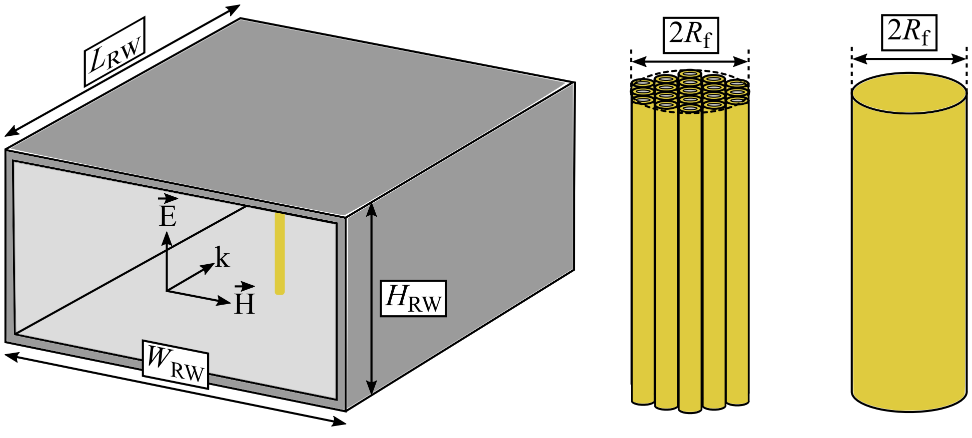

(a) (b) (c)

Figure 2.10: Simulated set-up for the translation between conductive multifilament and monofilament threads. (a) Set-up overview. (b) Magnification of the multifilament thread. (c) Magnification of the monofilament thread.

The ideal air-filled rectangular waveguide employed in this validation has been simulated using a perfect electric conductor (PEC). The dimensions of the waveguide are its width, height and length, which correspond to $W_{\mathrm{RW}} = 20$ mm, $H_{\mathrm{RW}} = 10$ mm and $L_{\mathrm{RW}} = 25$ mm, respectively. The length of the thread is, also, H_{RW}. Figure 2.10 depicts the simulation set-up and the corresponding magnifications of the multifilament and monofilament threads.

Applying the methodology described in the previous paragraphs and using $\sigma_{\mathrm{coat}} = 6.28 \cdot 10^7$ S/m, which is the electrical conductivity of the silver, the skin depth is $\delta = 0.7328$ µm. The skin depth has been found to be greater than the thickness of the silver coating, consequently the second part of the procedure, summarised in the expression (2.12), must be employed. As a result, the equivalent conductivity of the monofilament thread has been found to be $\sigma_{\mathrm{mon}} = 4.3863 \cdot 10^8$ S/m. Due to the fact that the skin depth is greater than T_{c}, the multifilament thread must be simulated as a dielectric thread with a silver coating.

Therefore, the scattering parameters have been calculated in the range of frequencies in which the waveguide presents its single-mode operation, $f \in [7.5, 15]$ GHz. Figure 2.11 depicts the simulated scattering parameters for both cases: using the multifilament thread and using the equivalent monofilament thread with σ_{mon}. A good agreement between both simulations has been obtained.

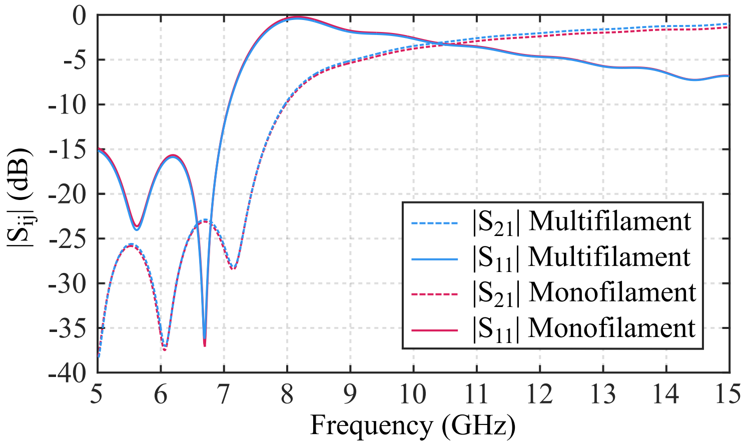

Figure 2.11: Comparison of the simulated scattering parameters of the equivalence between conductive multifilament and monofilament threads.

2.1.2.3 Woven structures using the monofilament model

Once the multifilament threads have been translated into their equivalent monofilaments, a woven structure can be designed. This woven structure will coincide with the real structure during the fabrication process. As it has been previously explained in Chapter 1, a woven structure is composed of two types of threads, the warp threads and the weft threads, respectively, as generically depicted in Figure 2.12.

Two different parameters, closely related to the density of the woven structure, can be defined for its accurate characterisation. These parameters are the number of ends per inch, *epi*, and the number of picks per inch, *ppi*. The *epi* parameter represents the number of warp ends per inch, as depicted in Figure 2.13, whereas the *ppi* parameter represents the number of weft threads per inch, as represented in Figure 2.14.

In order to design a woven structure using the MM, several factors have to be taken into account. First, depending on the dimensions of the cross section and rigidity of the different employed materials, a woven structure can adopt one of the following two approaches. Either the warp threads are more rigid and the weft threads tend to conform the woven structure around the warp threads, while the warp threads remain straight, as depicted in Figure 2.12, or vice versa. Secondly, the *epi* and *ppi* parameters, which will depend on the characteristics of the industrial loom and the procedure employed to manufacture the woven structure, must be known. Figure 2.15 summarises the procedure to design a woven structure.

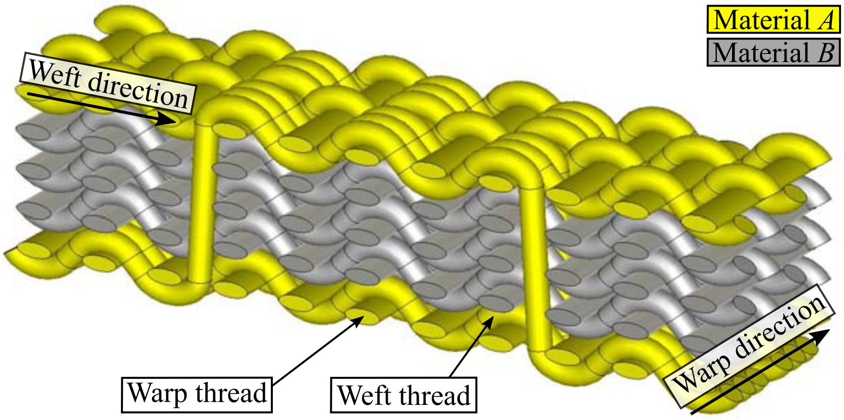

Figure 2.12: Generic multilayered woven structure using the MM and two different materials, material *A* (yellow) and material *B* (grey).

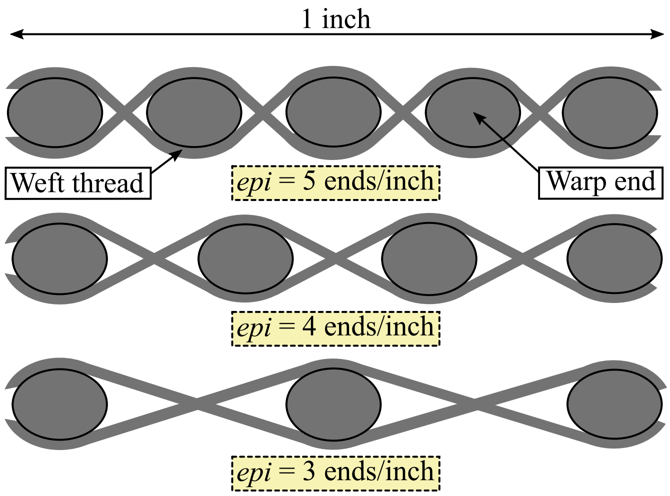

Figure 2.13: Schematic representation of the *epi* parameter (front view of the woven structure).

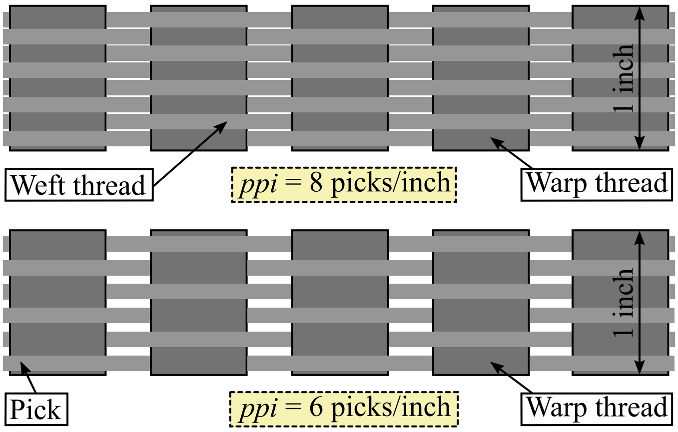

Figure 2.14: Schematic representation of the *ppi* parameter (side view of the woven structure).

Although different approaches to characterise the deformed cross section of the threads have been used, as explained in section 2.1.2, the most employed one is the Pierce's elliptic cross section. For this reason, the herein presented parametrisation of a woven structure will be described assuming that all the cross sections have been modelled with the Pierce's elliptic approximation, therefore, as ellipses. Moreover, a mathematical modelling of the paths of the non–rigid threads in the structure is required. Consequently, these paths have been mathematically modelled as ellipse arcs and tangent lines.

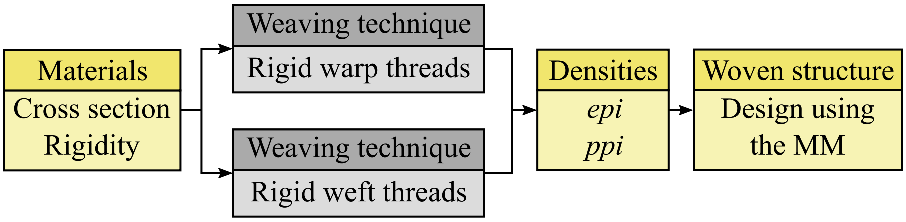

Figure 2.15: Block diagram to summarise the procedure of designing a woven structure.

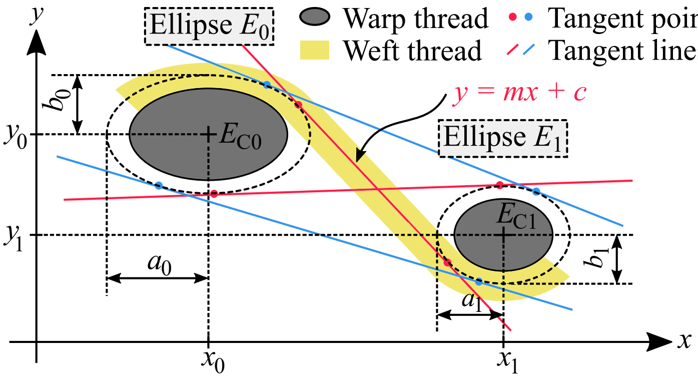

Figure 2.16: Generic mathematical modelling based on ellipses and tangents.

Assuming that the threads which remain straight are the warp threads, and the weft threads conform the woven structure, finding the tangent points given a pair of ellipses is required. Given two generic ellipses, E_0 and E_1, as depicted in Figure 2.16, they represent the cross-sections of two consecutive warp threads. Nevertheless, an analogous modelling can be employed if the threads which remain straight are the weft threads.

As these warp threads may belong to different layers of the woven structure or be composed of different materials, the corresponding ellipses are defined by the coordinates of their centres, $E_{C0} = (x_0, y_0)$ and $E_{C1} = (x_1, y_1)$, and the dimensions of their semiaxes, $\{a_0, b_0\}$ and $\{a_1, b_1\}$, respectively, and consequently a generic mathematical modelling is presented. The parametric equations to define either ellipse, with $\theta \in [0, 2\pi)$, are given by (2.13) and (2.14).

$$E_{x0} = a_0 cos(\theta) + x_0 \tag{2.13a}$$

$$E_{y0} = b_0 sin(\theta) + y_0 \tag{2.13b}$$

$$E_{x1} = a_1 cos(\theta) + x_1 \tag{2.14a}$$

$$E_{y1} = b_1 sin(\theta) + y_1 \tag{2.14b}$$

If a solution exists, then, four different lines are tangent to both ellipses. A line can be defined by two parameters, its slope, m, and its y-axis intercept, c. Thus, the generic line is defined by $y = mx+c$. By setting the equation of the line equal to (2.13) and (2.14), or to their equivalent cartesian mathematical expressions, and imposing on the line the condition of being tangent to both ellipses, only a point of each ellipse must coincide with a point of the line. For this purpose, the discriminant functions of the resultant expressions must be equal to zero. Therefore, the second order system of equations in (2.15) is generated.

$$\begin{cases} -2b_0^2x_0 - 2ma_0^2(y_0 - c))^2 + (-4(b_0^2 + a_0^2m^2) \\ \qquad (x_0^2b_0^2 + a_0^2(y_0 - c)^2 - a_0^2b_0^2)) = 0 \\ \\ -2b_1^2x_1 - 2ma_1^2(y_1 - c))^2 + (-4(b_1^2 + a_1^2m^2) \\ \qquad (x_1^2b_1^2 + a_1^2(y_1 - c)^2 - a_1^2b_1^2)) = 0 \end{cases} \tag{2.15}$$

The solution of (2.15) returns the slopes and the intercepts of the four different lines that are tangent to the ellipses, which are denoted by m_i and c_i, with $i \in [1, 4]$. From the slopes and the intercepts, the tangent points (x_{p0_i}, y_{p0_i}) and (x_{p1_i}, y_{p1_i}), for E_0 and E_1 respectively, can be worked out as shown in (2.16) and (2.17).

$$x_{p0\_i} = -(-2b_0^2x_0 - 2m_ia_0^2(y_0 - c_i))/(2(b_0^2 + a_0^2m_i^2)) \tag{2.16a}$$

$$y_{p0\_i} = m_ix_{p0\_i} + c_i \tag{2.16b}$$

$$x_{p1\_i} = -(-2b_1^2x_1 - 2m_ia_1^2(y_1 - c_i))/(2(b_1^2 + a_1^2m_i^2)) \tag{2.17a}$$

$$y_{p1\_i} = m_ix_{p1\_i} + c_i \tag{2.17b}$$

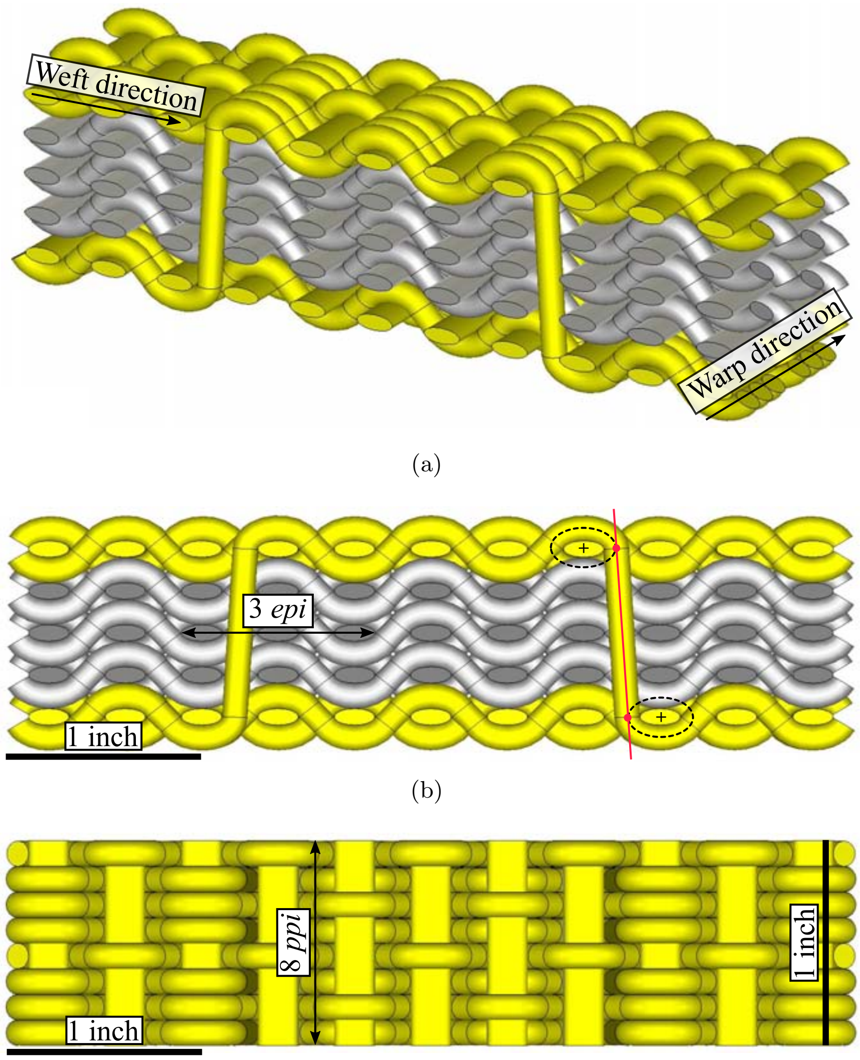

(a)

(b)

(c)

Figure 2.17: Generic multilayered woven structure using rigid warp threads and two materials, conductive (yellow) and dielectric (grey). (a) Woven structure overview. (b) Front view and *epi* parameter. (c) Top view and *ppi* parameter.

Once the tangent points have been worked out, the paths of the weft threads are defined and the woven structure is completely characterised. Figure 2.17 depicts a generic multilayered woven structure, where an example of the ellipses, the tangent points and the tangent line is indicated.

2.1.3 Layers model

As it has been mentioned before, a woven structure designed using the MM is directly translatable into a manufactured prototype. Nevertheless, finding a computationally simpler modelling is required in order to simulate larger and more complex structures. For this reason, the LM is proposed.

The LM is defined using an homogeneous dielectric substrate whose relative pemittivity and loss tangent are denoted by $\varepsilon_{\mathrm{eq}}$ and $\tan(\delta)_{\mathrm{eq}}$, respectively, and a conductivity denoted by σ_{eq}. Depending on the electromagnetic behaviour of the thread, electrically conductive or dielectric, a different procedure to translate from the MM to the LM is required.

2.1.3.1 Dielectric materials

Due to the air gaps between the dielectric monofilaments which form the woven structure, the relative permittivity of the equivalent dielectric substrate is reduced and denoted by $\varepsilon_{\mathrm{eq}}$. A new loss tangent can be defined and denoted by $\tan(\delta)_{\mathrm{eq}}$.

To translate the MM into the LM, a theoretical method has been used. For this purpose, the $\varepsilon_{\mathrm{mon}}$ and $\tan(\delta)_{\mathrm{mon}}$, as well as the *epi* and *ppi* parameters must be taken into account. Simulating a rectangular waveguide which has been filled with monofilaments ($\varepsilon_{\mathrm{mon}}$ and $\tan(\delta)_{\mathrm{mon}}$), using the same *epi* and *ppi* densities as the dielectric substrate has in the woven structure, and comparing its electromagnetic behaviour with another rectangular waveguide which has been homogeneously filled, the corresponding $\varepsilon_{\mathrm{eq}}$ and $\tan(\delta)_{\mathrm{eq}}$ parameters can be easily extracted from the cut-off frequency and the insertion losses as summarised in Figure 2.18. Therefore, the dielectric parameters of the MM can be translated into their corresponding of the LM.

Consequently, the relative dielectric permittivity is first reduced from the FM to the MM due to the air gaps between the filaments which conform the thread, transforming $\varepsilon_{\mathrm{fil}}$ into $\varepsilon_{\mathrm{mon}}$. Analogously, the relative dielectric permittivity is then reduced again from the MM to the LM due to the air gaps between the monofilaments which conform the equivalent woven structure, transforming $\varepsilon_{\mathrm{mon}}$ into $\varepsilon_{\mathrm{eq}}$.

2.1.3.2 Conductive materials

To translate the conductive monofilaments, σ_{mon}, from the MM into a homogeneous conductive material, σ_{eq}, for the LM, a square-shaped woven MM

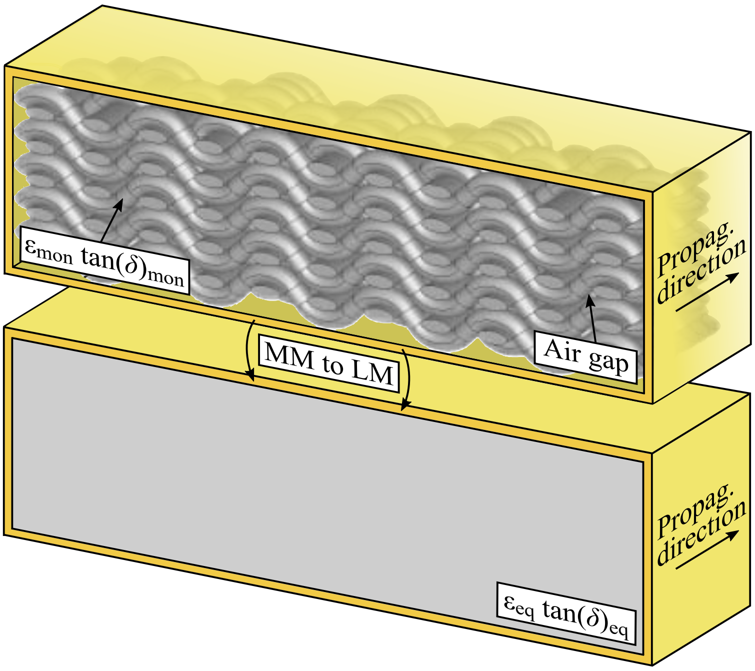

Figure 2.18: Translation from the MM into the LM outline applied to dielectric monofilaments using the waveguide based methodology

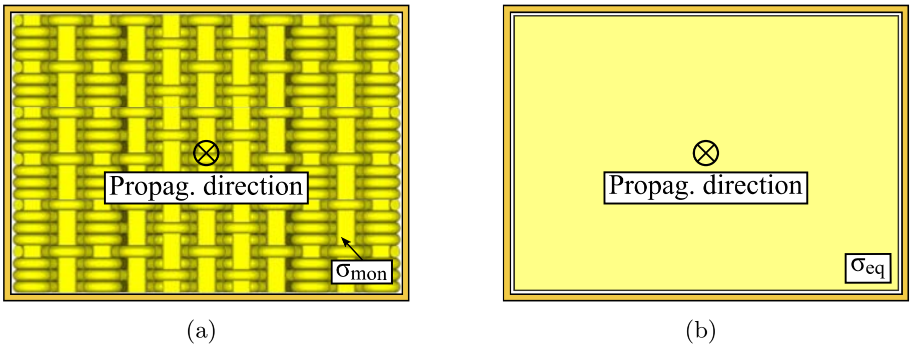

Figure 2.19: Translation from the MM into the LM outline applied to conductive monofilaments using a rectangular waveguide. (a) MM applied to the threads. (b) LM applied to the threads.

structure is simulated inside a rectangular waveguide, perpendicular to its propagation direction. Its EM behaviour, in terms of the scattering parameters is, then, compared to a homogeneous conductive square-shaped sheet, using the same dimensions and a conductivity given by σ_{eq} as summarised in Figure 2.19.

2.1.3.3 Deformation of woven structures

As it has been previously explained, the woven structure depends not only on the employed materials, but also on the *epi* and *ppi* parameters. For this reason, the same materials may present different cross sections depending on the woven structure in which they are employed. As a consequence, the translation between the different models may lead to different results.

Figure 2.20 depicts an overview of the deformation of the woven structures. Figure 2.20a represents a hypothetical translation of a SIW (substrate integrated waveguide) into a woven structure, using rigid warp threads. Although the following chapter is focused on SIW structures, this is an example whose aim is to clarify the deformation of the woven structures and the corresponding effect in the three-step modelling. For this reason, in Figure 2.20, dielectric materials are green colored, whereas conductive materials are grey colored and the electromagnetic field propagates in the direction parallel to the warp direction.

Figure 2.20a represents a woven structure whose threads are provided with circular cross sections, consequently with circumferences whose diameter is denoted d_{W}. These threads are composed of filaments whose diameter are denoted by d_{fil}. Besides, the distance between the conductive vias of the woven SIW is d_{V}. Analogously, Figure 2.20b depicts a similar structure, nevertheless, the cross sections of the threads have been modified and are ellipses whose horizontal and vertical axes are d_{wX} and d_{wY}, respectively. Figure 2.20c also depicts a similar structure, although the ellipses present a bigger eccentricity compared to the ellipses in Figure 2.20b.

The different buckling effects the circumference and the ellipses experiment in the representations of Figure 2.20 leads to two consequences. First, the bigger the eccentricity of the ellipses, the bigger the distance between the conductive vias. Secondly, the modification of the eccentricity of the ellipses and the corresponding variation of the distance d_{V}, lead to the modification of the air gaps between the threads.

As a result, the equivalent relative permittivity of the woven structure inside the SIW is modified, even though the materials remain being the same. For example, if the following relation is made between the beforementioned parameters: $d_{\mathrm{wY}} = d_{\mathrm{W}} - 4 \cdot n \cdot d_{\mathrm{fil}}$, being d_{wX} the corresponding so that the perimeter of the cross section remains constant, and n a variable to control the eccentricity (deformation index), a relation between the cut-off frequency of the structure and n, as well as between the equivalent relative permittivity $\varepsilon_{\mathrm{eq}}$ of the structure and n can be worked out.

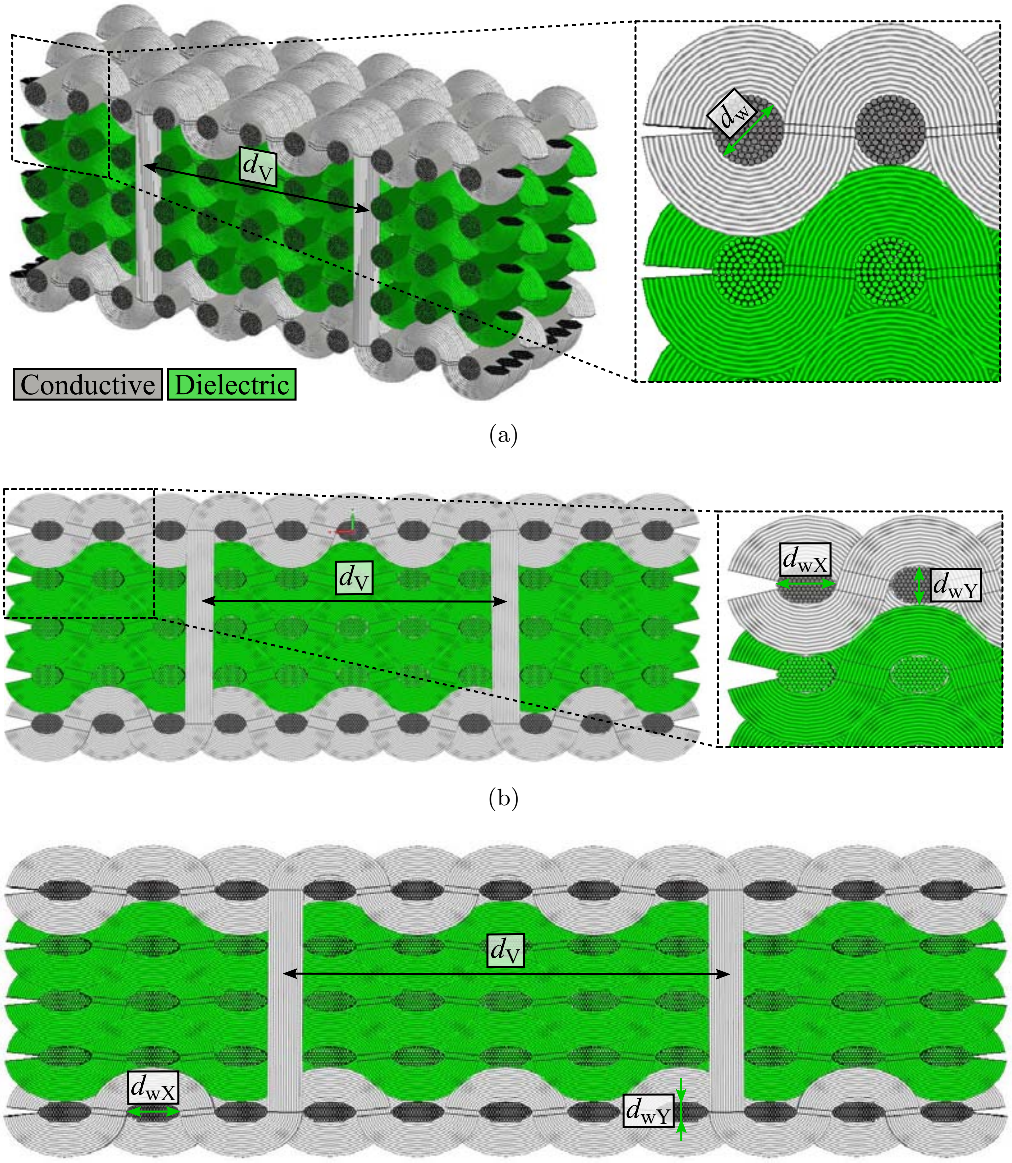

(a)

(b)

(c)

Figure 2.20: Deformation of the woven structures overview. (a) Initial circular cross section overview and corresponding magnification. (b) Elliptic cross section (smaller eccentricity) and corresponding magnification. (c) Elliptic cross section (bigger eccentricity).

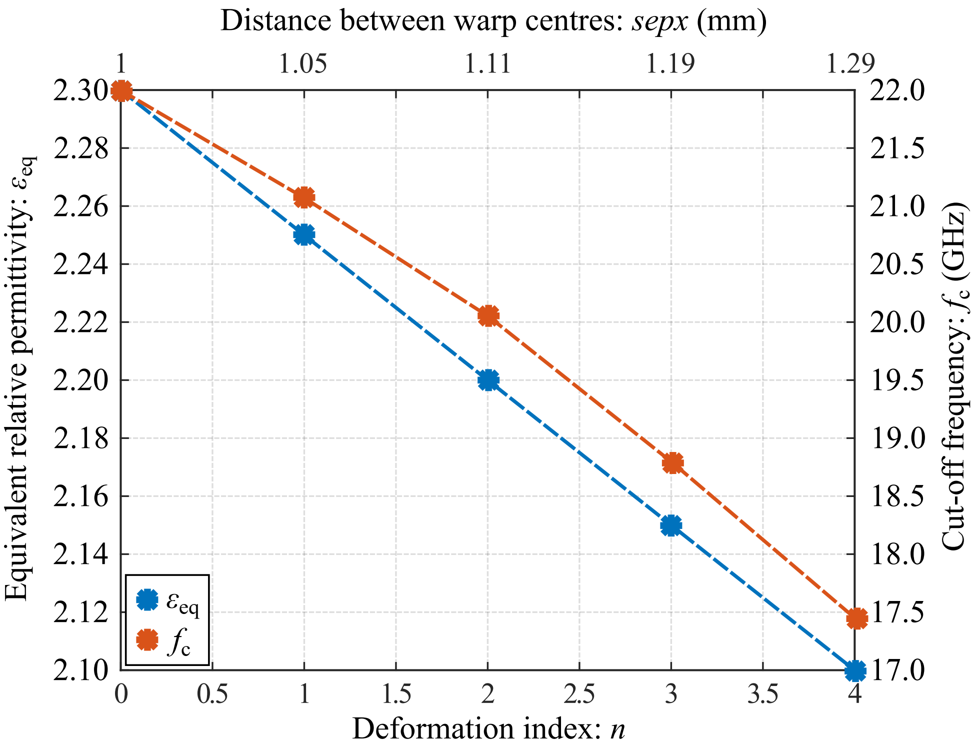

Figure 2.21: Modification of the equivalent relative permittivity and the cut-off frequency of a woven SIW depending on the deformation index and corresponding distance between warp centres.

Figure 2.21 depicts the dependence between the equivalent permittivity of the woven structure and the deformation index. The green colored filaments have been simulated using a relative permittivity of $\varepsilon_{fil} = 3.5$. As a result, the relation between the cut-off frequency of the woven SIW and n is also represented. As previously mentioned, the bigger the eccentricity of the ellipses, the bigger the distance between the conductive vias. This is due to the distance between the centres of two consecutive warp threads, *sepx*, increases.

2.1.4 Conclusions

A three-step modelling has been explained to electromagnetically simulate woven structures. First, a FM has been defined to characterise the different threads, dielectric or conductive, employed in the woven structure. For both, the dielectric and conductive materials, the deformed cross section of the threads and the number of filaments which form each thread have been taken into account.

Then, a reduction of the computational complexity of the problem is achieved by defining the MM, which substitutes the multifilament threads by electromagnetically equivalent monofilament threads. To translate the FM into the MM for the dielectric threads, the FM and the EM characteristics of the materials from which the filaments have been extruded are taken into account. In addition, in order to rigorously translate the FM into the MM, the skin depth effect has been taken into account for the conductive materials.

A new model, the LM, has been defined in order to obtain a homogeneous relative permittivity and electrical conductivity, reducing the complexity of the woven structure to a conventional substrate integrated structure.

Using the beforementioned three-step modelling, a designed woven structure can be electromagnetically characterised before its fabrication. Therefore, fully textile integrated circuits and antennas can be easily designed and simulated using the LM, which is equivalent to the conventional method to simulate standard circuits and antennas. Moreover, the LM reduces the computational complexity of the original EM problem and, therefore, reduces the simulation times, avoiding the simulation of the complete MM of the circuit or antenna.

This modelling will be particularised and employed in the development of different microwave circuits and antennas in the following chapters in order to demonstrate its validity.

2.2 Modelling of arbitrarily height–modulated textile integrated waveguide filters

The herein presented technique is a parametric modelling to develop arbitrarily height-modulated textile integrated waveguide (AHMTIW) filters. This modelling is based on the before mentioned LM, and applied to substrate integrated waveguides (SIW). Although the fabrication of a height-modulated SIW using standard prototyping machinery represents a complex problem, its analogous textile integrated waveguide (TIW) allows its large-scale manufacturing using industrial looms.

2.2.1 Description of the modelling

An AHMTIW filter is an arbitrarily height-modulated standard substrate integrated waveguide (AHMSIW) filter which has been translated into a fully textile integrated structure. In other words, an AHMTIW is the textile version of a SIW structure whose height discretely changes along its propagation direction in

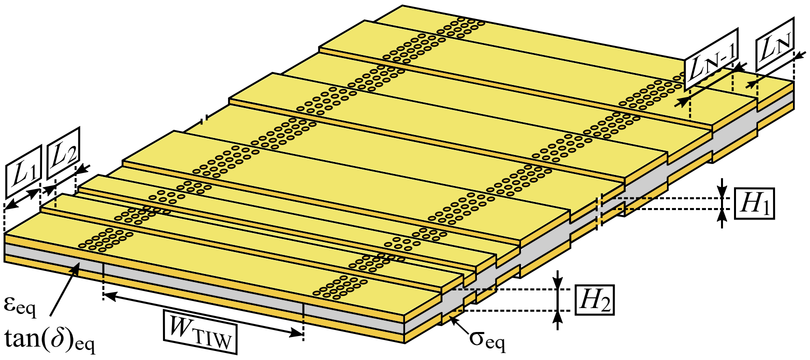

Figure 2.22: LM associated to a generic AHMTIW filter.

order to obtain a certain frequency response. Due to the fact that the translation between woven structures and their EM equivalent LM has been presented in section 2.1, this section will only be focused on the development of AHMTIW filters from the LM or, equivalently, the development of AHMSIW filters.

In order to develop bandstop or bandpass AHMTIW filters, a novel technique based on arbitrarily modulating the height of the TIW along its propagation direction is presented. For this purpose, the length of the TIW has been divided into N segments and two different heights, H_1 and H_2, have been defined. The separation between the conductive vias of the TIW has been denoted by W_{TIW}, as depicted in Figure 2.22.

The length of each segment in which the TIW has been divided is denoted by L_i, with $i \in [1, N]$. Each length, L_i, can be optimised in order to achieve a required bandstop or bandpass response of the filter.

2.2.2 Implementation

In order to implement the filters, four different blocks have been defined for their posterior EM simulation. These blocks are a H_1-height TIW segment, a H_2-height TIW segment, a stepped TIW segment whose height is modified along its propagation direction from H_1 to H_2, and a stepped TIW segment whose height is modified from H_2 to H_1, respectively, as depicted in Figure 2.23.

Figure 2.23a and Figure 2.23b represent two TIW segments whose heights and lengths are H_1 and $L1_i$, and H_2 and $L2_i$, respectively. These blocks are denoted by $H_{1\_\text{Block}\_i}$ and $H_{2\_\text{Block}\_i}$, respectively.

Figure 2.23c represents a TIW segment whose height discretely changes along its length. The first half presents a height of H_1, whereas the second one is equal

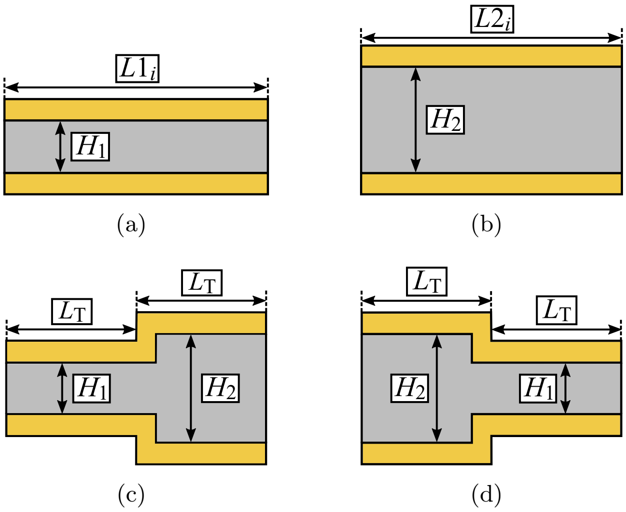

Figure 2.23: Side view of the different blocks to develop AHMTIW filters. (a) H_{1_Block}. (b) H_{2_Block}. (c) $H_{1\_2\_\mathrm{Block}}$. (d) $H_{2\_1\_\mathrm{Block}}$.

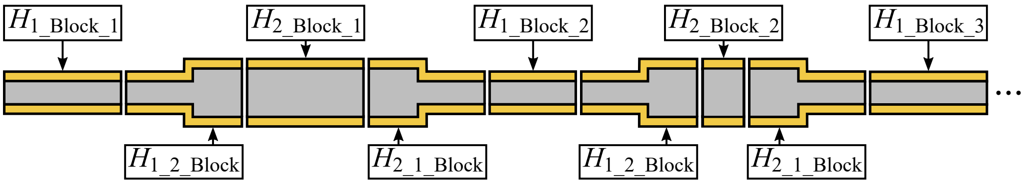

Figure 2.24: Side view of the connection between the blocks to achieve bandstop or bandpass AHMTIW filters.

to H_2. This block is denoted by $H_{1\_2\_\mathrm{Block}}$. Equivalently, Figure 2.23d depicts a TIW segment whose height changes along its length from H_2 to H_1. This block is denoted by $H_{2\_1\_\mathrm{Block}}$.

In order to achieve a structure as the one depicted in Figure 2.22, the different blocks have to be connected in a precise order, the $H_{1\_\mathrm{Block}\_1}$ block, the $H_{1\_2\_\mathrm{Block}}$ block, the $H_{2\_\mathrm{Block}\_1}$ block, the $H_{2\_1\_\mathrm{Block}}$ block, the $H_{1\_\mathrm{Block}\_2}$ block, and so on, as represented in Figure 2.24.

The blocks denoted by $H_{1\_2\_\mathrm{Block}}$ and $H_{2\_1\_\mathrm{Block}}$ can be electromagnetically simulated given their dielectric parameters, $\varepsilon_{\mathrm{eq}}$ and $\tan(\delta)_{\mathrm{eq}}$, conductivity, σ_{eq}, and dimensions, using the 3-D full-wave simulation software ANSYS HFSS, *High Frequency Structure Simulator*, and obtaining their scattering parameters (S-parameters).

Likewise, H_{1_Block} and H_{2_Block} blocks are simulated using HFSS given their

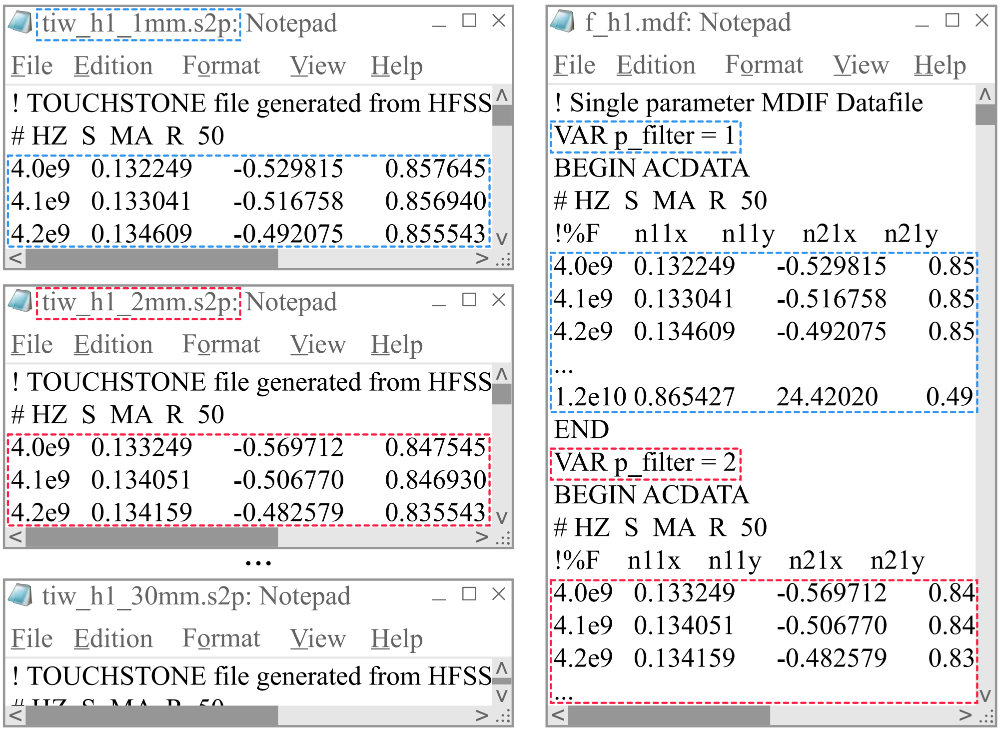

```
! TOUCHSTONE file generated from HFSS
# HZ  S  MA  R  50
4.0e9  0.132249    -0.529815    0.857645
4.1e9  0.133041    -0.516758    0.856940
4.2e9  0.134609    -0.492075    0.855543
```

```
! TOUCHSTONE file generated from HFSS
# HZ  S  MA  R  50
4.0e9  0.133249    -0.569712    0.847545
4.1e9  0.134051    -0.506770    0.846930
4.2e9  0.134159    -0.482579    0.835543
```

```
! TOUCHSTONE file generated from HFSS
```

(a)

```
! Single parameter MDIF Datafile
VAR p_filter = 1
BEGIN ACDATA
# HZ  S  MA  R  50
!%F    n11x    n11y    n21x    n21y
4.0e9  0.132249    -0.529815    0.85
4.1e9  0.133041    -0.516758    0.85
4.2e9  0.134609    -0.492075    0.85
...
1.2e10 0.865427    24.42020     0.49
END
VAR p_filter = 2
BEGIN ACDATA
# HZ  S  MA  R  50
!%F    n11x    n11y    n21x    n21y
4.0e9  0.133249    -0.569712    0.84
4.1e9  0.134051    -0.506770    0.84
4.2e9  0.134159    -0.482579    0.83
...
```

(b)

Figure 2.25: Simulated S-parameters and corresponding files. (a) Different Touchstone S2P files for each length sweep. (b) Generated MDIF file.

dielectric parameters, conductivity, dimensions, and sweeping their length parameters, $L1$ and $L2$, in order to obtain the different S-parameters datasets as a function of the length.

As an example, H_{1_Block} block is simulated for different values of its length, $L1 \in [1, 30]$ mm. As a result of each simulation, the S-parameters are exported into a Touchstone S2P, *2-port S-parameter*, file as depicted in Figure 2.25a. Once every dataset of S-parameters has been exported, then a *MultiDimensional File*, MDIF file, can be generated by defining the sweep variable before the corresponding S-parameters. In Figure 2.25b, the variable *p_filter* has been defined, whose value corresponds to the length of the TIW segment in millimetres.

Two MDIF files, associated to the S-parameters of the H_{1_Block} and H_{2_Block} blocks, have been generated and named *f_h1.mdf* and *f_h2.mdf*, respectively. Similarly, another MDIF file, associated to the S-parameters of both, the $H_{1\_2\_\mathrm{Block}}$ and $H_{2\_1\_\mathrm{Block}}$ blocks, has been generated and named *f_h12.mdf*.

A schematic model of the AHMTIW filter can be designed using *Advanced Design System*, ADS, once the three MDIF files have been created, as summarised in Figure 2.26. Figure 2.26a depicts the concatenation of the different defined blocks. Connected to the first and last block of the concatenation, there are two identical terminals whose characteristic impedance, Z_{in}, is given by (2.18) [2], where D and S are the diameter and the separation between two consecutive conductive vias of the SIW, respectively.

$$Z_{\text{in}} = \frac{2\pi f \mu_0}{\sqrt{\left(\frac{2\pi f}{c/\sqrt{\varepsilon_{\text{eq}}}}\right)^2 - \left(\frac{\pi}{W_{TIW} - \frac{S^2}{0.95S}}\right)^2}} \tag{2.18}$$

Figure 2.26b depicts i-th H_{1_Block} block associated to the *f_h1.mdf* file. Therefore, the value of *p_filter* is equal to v1_i, being v1_i a variable to optimise. Figure 2.26c depicts the $H_{1\_2\_\text{Block}}$ block associated to the *f_h12.mdf* file. Consequently, the value of *p_filter* is 1, due to the fact that in this file, there are only the datasets associated to the $H_{1\_2\_\text{Block}}$ and $H_{2\_1\_\text{Block}}$ blocks.

Figure 2.26d depicts i-th H_{2_Block} block associated to the *f_h2.mdf* file. Therefore, the value of *p_filter* is equal to v2_i, being v2_i a variable to optimise. Figure 2.26e depicts the $H_{2\_1\_\text{Block}}$ block associated to the *f_h12.mdf* file. Consequently, the value of *p_filter* is 2. In other words, the variable *p_filter* indicates the value of the corresponding optimised variable for the blocks $H_{1\_\text{Block}\_i}$ or $H_{2\_\text{Block}\_i}$, whereas it indicates 1 or 2 for the transition blocks $H_{1\_2\_\text{Block}}$ or $H_{2\_1\_\text{Block}}$, respectively.

Once the schematic model is configured in ADS, an optimisation of the v1_i and v2_i variables can be carried out in order to obtain the required response of the filter. An optimisation based on the gradient can be used, although at the end of the optimisation, the values of v1_i and v2_i are not integers, leading to the interpolation of the S-parameters. For this reason, the values of v1_i and v2_i must be truncated and a tuning process is required, as summarised in Figure 2.27. Although ADS implements a discrete optimiser, it cannot be applied to such a complex optimisation problem, due to the associated difficulty to converge.

2.2.3 Conclusions

A modelling technique to develop AHMTIW filters from the LM has been explained. The filters are based on the arbitrarily modulation of their height along their propagation direction.

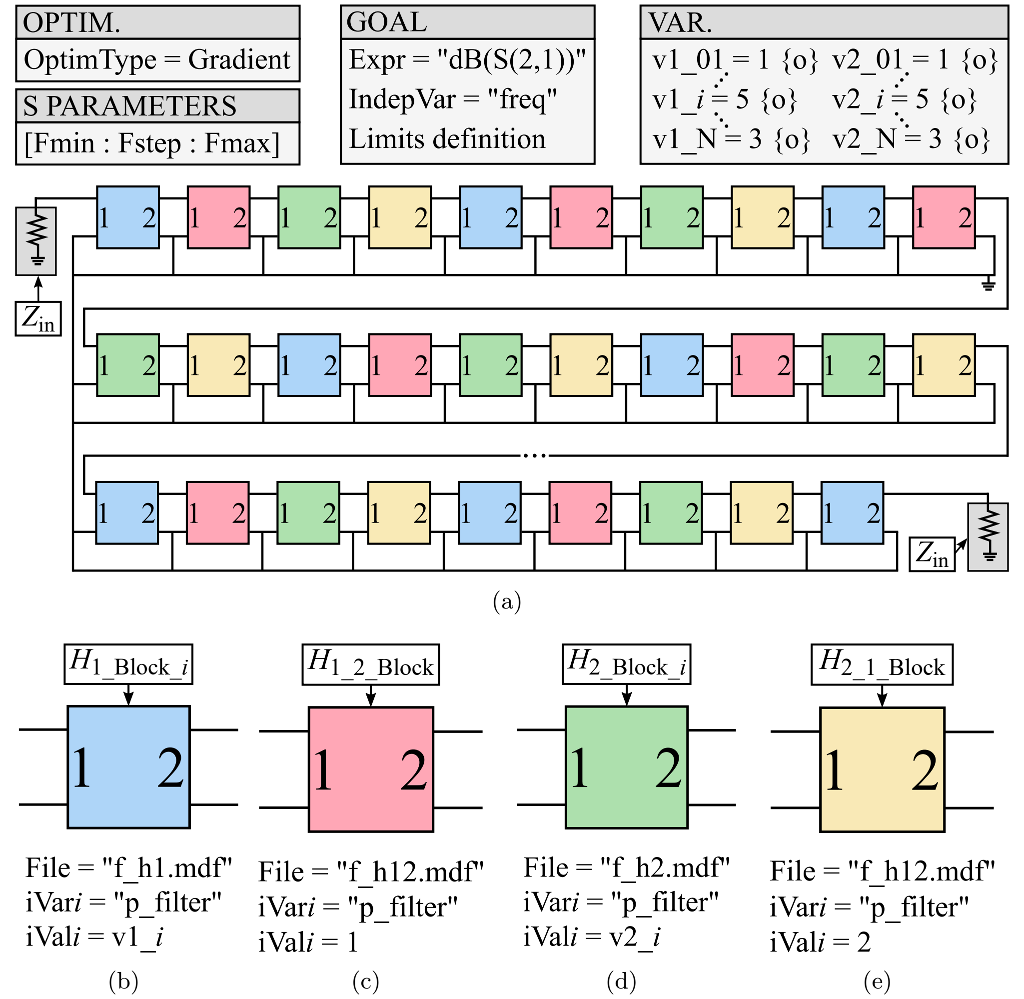

Figure 2.26: Schematic model of the AHMTIW filter optimisation using ADS. (a) Schematic model outline. (b) Generic H_{1_Block} block. (c) Generic $H_{1\_2\_\mathrm{Block}}$ block. (d) Generic H_{2_Block} block. (e) Generic $H_{2\_1\_\mathrm{Block}}$ block.

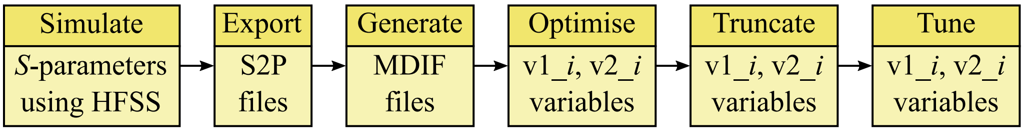

Figure 2.27: Block diagram to summarise the AHMTIW design.

First, the generic structure is divided into four different types of blocks and each of them is simulated using HFSS. The blocks associated to constant heights along the propagation direction are simulated for different values of their lengths.

Then, the S-parameter datasets of the simulations are exported to different S2P files. Once all the S2P files are generated, three MDIF file can be created for its use in the schematic model of the filter in ADS. Once the ADS schematic model has been configured, an optimisation of the v1_i and v2_i parameters can be carried out, to achieve the required response of the filter. After a process of truncation and tuning, the filter is designed.

The procedure to design arbitrarily height-modulated filters can be generalised using m different heights, instead of two as is the case. Although for their application in woven structures, and the complexity of their manufacturing, two heights have been considered optimal.

This modelling technique will be validated. For this purpose, in Chapter 3, two different filters, a bandstop and a bandpass filter, respectively, will be presented.

Bibliography

[1] H. U. Jinlian, “Structure and mechnics of woven fabrics”, in *Woodhead Publishing in Textiles, The Textile Institute*, New York, NY, USA, 2004, pp. 63-66. (Cited on page 21)

[2] K. Rabaani and N. Boulejfen, “Characteristic impedance and propagation constant assessment of Substrate Integrated Waveguide transmission line,” presented in *11th Int. Design & Test Symp. (IDT)*, Hammamet, Tunisia, Dec. 18–20, 2016. (Cited on page 45)

3

Fully woven textile integrated waveguides and filters

Contents

The aim of this chapter is to describe the design, simulation and experimental validation of millimetre-wave and microwave textile integrated waveguides (TIW), and validate the modelling of arbitrarily height-modulated textile integrated waveguide (AHMTIW) filters using the techniques presented in Chapter 2.

3.1 TIW with a WR-28 transition using rigid warp threads

3.1.1 Introduction

During the last few years, there has been an increasing interest in the development of microwave and millimetre-wave textile integrated circuits (TIC) based on substrate integrated waveguide (SIW) technology. In the literature, different approaches have been developed to translate into textile the, generally, three layers in which a SIW can be separated and its corresponding electrically conductive vias.

A conventional SIW is composed of three layers, a substrate layer between two conductive plates. The dielectric substrate can be translated into textile by the use of standard dielectric fabrics [1–4] or dielectric non-wovens such as felt [5–8]. Alternatively, the conductive plates can be translated into their textile analogous using conventional conductive fabrics [5, 7, 8], copper-coated nylon taffeta [9], electrotextiles [1–4] or commercial super-conductive textiles such as *ShieldIt* [6]. The conductive vias, which connect the conductive plates through the dielectric substrate, can be emulated in the textile structures by the use of conductive threads [5, 7, 8], eyelets [1–4, 9] or conductive cylindrical wires [6]. However, in order to achieve a compact prototype, whose layers are connected not only through the vias, the techniques already presented in Chapter 1 must be employed.

The aforementioned alternatives are not fully integrated in textile and require several processes to be manufactured, such as sewing, coating or gluing. For these reasons, a fully TIW for its operation in the millimetre-wave range of frequencies is presented in this section [10].

3.1.2 Structure of the TIW

Two TIW, denoted by $dsgn_1$ and $dsgn_2$ respectively, using rigid warp threads are proposed to operate at a range of frequencies between 34 and 37 GHz. The TIW have been designed using the procedure described in section 2.1. Figure 3.1a represents an overview of the layers model (LM) associated to the proposed TIW, the coordinate system, the orientation of the EM field and the propagation direction. The TIW are based on a standard SIW, consequently, a TIW can be divided into three different layers, a dielectric layer (whose height is given by H_{SIW}) between two conductive plates, as depicted in Figure 3.1b. The separation

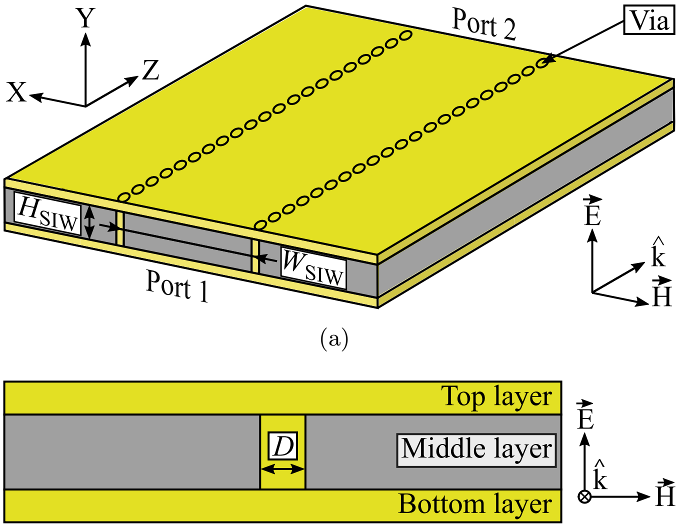

(a)

(b)

Figure 3.1: Schematic drawing of the proposed TIW, conductive materials (yellow) and dielectric materials (grey). (a) TIW outline. (b) Front view magnification and layers.

between the two rows of conductive vias is given by W_{SIW}, whereas the diameter of each via is denoted by D.

The proposed TIW are fully integrated in textile, therefore, the conductive and dielectric parts are manufactured using different types of threads. Consequently, different materials have been employed for the design of the TIW, for both the weft and warp directions. In the proposed TIW, the warp direction coincides with the propagation direction, whereas the weft direction is parallel to the orientation of the magnetic field.

3.1.3 Characterisation of the conductive materials

Electrically conductive *Shieldex 117f17 2-ply* yarns, with 17 filaments per ply and a density of 117 dtex have been used for the weft threads. For simplification, this material will be denoted by *Shx2p*. These threads adopt a Pierce's elliptic cross section when they are in the woven structure. In addition, electrically conductive *Shieldex 117f17 1-ply* yarns, with 17 filaments per ply and a density of 117 dtex have been used for the warp threads. These threads have been modelled using the Kemp's racetrack cross section. For simplification, this material will be denoted by *Shx1p*. The cross section approaches and corresponding dimensions

Table 3.1: Cross section dimensions of the employed conductive materials.

Material	Thread direction	Cross section	Dimension	Notation	Value (mm)
Shx2p	Weft	Kemp	Rectangle length	R_{L}	0.2
			Circumference radius	C_{R}	0.075
Shx1p	Warp	Pierce	Horizontal semi-axis	H_{S}	0.13
			Vertical semi-axis	V_{S}	0.065

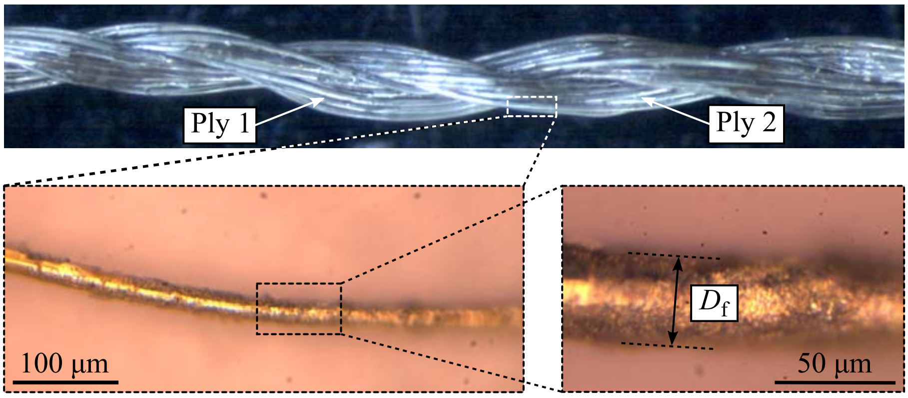

Figure 3.2: *Shx2p* thread sample and magnifications of one filament.

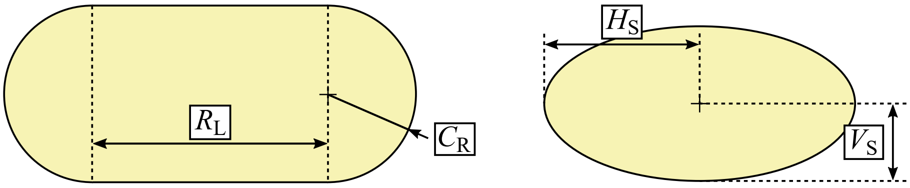

(a)

(b)

Figure 3.3: Cross section dimensions of the monofilament threads. (a) *Shx2p* threads. (b) *Shx1p* threads.

of the different conductive threads are summarised in Table 3.1. The thickness of the silver coating of each filament, for both types of threads, is given by $T_{\mathrm{c}} = 0.5$ µm, whereas the total diameter of each filament is given by $D_{\mathrm{f}} = 2 \cdot R_{\mathrm{f}} = 31$ µm, as depicted in Figure 3.2.

Following the procedure described in section 2.1.2.2, both conductive threads must be translated into their analogous monofilaments. For this purpose, the analysis of the skin depth effect is discussed in this section. First, using the expression described in (2.1), where $\rho_{\mathrm{coat}} = 1.59 \cdot 10^{-8}$ (Ωm) is the resistivity of the silver and f is the minimum operating frequency of the design, $f = 34$ GHz, the skin depth is $\delta = 0.3442$ µm. As the thickness of the conductive coating of the filaments is greater than the skin depth, the first part of the procedure is followed.

Nevertheless, the procedure already described in section 2.1.2.2 employed a circumference as the equivalent cross section of the multifilament thread, for simplification. For this reason, some expressions must be particularised to the different cross sections of the *Shieldex* yarns. Using the expression (2.4), the resistance per unit length of each filament is $(R/l)_{\mathrm{f}} = 479.6838$ Ω/m. As the *Shx2p* and the *Shx1p* threads present a different number of filaments, the resistance per unit length of each type of thread will be different.

The *Shx2p* threads are composed of $N_{\mathrm{fil}} = 34$ filaments, therefore, using the expression in (2.5), $(R/l)_{\mathrm{Shx2p}} = 14.1083$ Ω/m. Alternatively, the *Shx1p* threads are composed of $N_{\mathrm{fil}} = 17$ filaments and, consequently, $(R/l)_{\mathrm{Shx1p}} = 28.2167$ Ω/m.

Particularising the expression in (2.6) for the Kemp's racetrack and the Pierce's elliptic cross sections, the areas of the equivalent conductive cross sections of the monofilament threads for the *Shx2p* and the *Shx1p* threads, S_{mon2} and S_{mon1}, can be expressed using, respectively, (3.1) and (3.2).

$$S_{\mathrm{mon2}} = \pi \cdot {C_{\mathrm{R}}}^2 - \pi \cdot (C_{\mathrm{R}} - T_{\mathrm{R}})^2 + 2 \cdot C_{\mathrm{R}} \cdot R_{\mathrm{L}} - 2 \cdot (C_{\mathrm{R}} - T_{\mathrm{R}}) \cdot R_{\mathrm{L}} \tag{3.1}$$

$$S_{\mathrm{mon1}} = \pi \cdot H_{\mathrm{S}} \cdot V_{\mathrm{S}} - \pi \cdot (H_{\mathrm{S}} - T_{\mathrm{R}}) \cdot (V_{\mathrm{S}} - T_{\mathrm{R}}) \tag{3.2}$$

Once the expressions of the $S_{\mathrm{mon}i}$ are obtained, the resistances per unit length of the monofilament can be expressed particularising (2.7) for the Kemp's racetrack and the Pierce's elliptic cross sections, as generically indicated in (3.3).

$$(R/l)_{\mathrm{mon}i} = \frac{1}{\sigma_{\mathrm{mon}i} \cdot \pi \cdot S_{\mathrm{mon}i}} \tag{3.3}$$

With the aim of achieving the same resistance per unit length in both the multifilament and the monofilamente threads, $(R/l)_{\mathrm{Shx2p}}$ must be equal to $(R/l)_{\mathrm{mon2}}$ and, equivalently, $(R/l)_{\mathrm{Shx1p}}$ must be equal to $(R/l)_{\mathrm{mon1}}$. As it has been thoroughly explained in section 2.1.2.2, the parameter T_{R} coincides with the skin depths, δ_{mon2} and δ_{mon1}, calculated using the equivalent electrical conductivi-

Table 3.2: Cross section dimensions of the employed dielectric materials ($dsgn_1$).

Material	Thread direction	Cross section	Dimension	Value (mm)
PET_{warp}	Warp	Pierce	Horizontal semi-axis	0.075
			Vertical semi-axis	0.055
$PES_{\mathrm{weft\_dsgn1}}$	Weft	Kemp	Rectangle length	0.2
			Circumference radius	0.075

ties of the monofilaments, σ_{mon2} and σ_{mon1}, respectively, as expressed in (2.9). Solving the corresponding equations using numeric methods, the solutions have been found to be $\sigma_{\mathrm{mon2}} = 2.0326 \cdot 10^{35}$ Ω/m and $\sigma_{\mathrm{mon1}} = 1.5557 \cdot 10^{35}$ Ω/m, respectively.

3.1.4 Characterisation of the dielectric materials

For the dielectric parts of the prototypes, three different materials have been employed. For the dielectric warp threads in both $dsgn_1$ and $dsgn_2$, polyethylene-terephthalate (commonly known as PET or polyester) with a density of 50 dtex and composed of 18 filaments has been used. For the dielectric weft threads in $dsgn_1$ high tenacity polyethersulfone (commonly known as PES) with a density of 550 dtex and composed of 80 filaments has been used. Alternatively, in $dsgn_2$, PET threads with a density of 167 dtex and composed of 36 filaments have been employed.

For simplification, the PET warp threads for both designs, the PES weft threads for $dsgn_1$ and the PET weft threads for $dsgn_2$ will be denoted by PET_{warp}, $PES_{\mathrm{weft\_dsgn1}}$ and $PET_{\mathrm{weft\_dsgn2}}$, respectively. A sample of each dielectric material is depicted in Figure 3.4.

Different cross section approximations have been used to characterise the dielectric materials. For PET_{warp} threads, the Pierce's elliptic cross section has been employed, whereas for $PES_{\mathrm{weft\_dsgn1}}$ and $PET_{\mathrm{weft\_dsgn2}}$, the Kemp's racetrack section and the circular cross section have been chosen, respectively. The dimensions of the cross sections are summarised in Table 3.2 and Table 3.3, respectively.

Each filament of PET belonging to the employed dielectric threads has a relative permittivity of $\varepsilon_{\mathrm{fil\_PET}} = 3.7$, a loss tangent of $\tan(\delta)_{\mathrm{fil\_PET}} = 0.001$ and a density of $\delta_{\mathrm{fil\_PET}} = 1.5$ g/cm^3. Alternatively, each filament of PES belonging

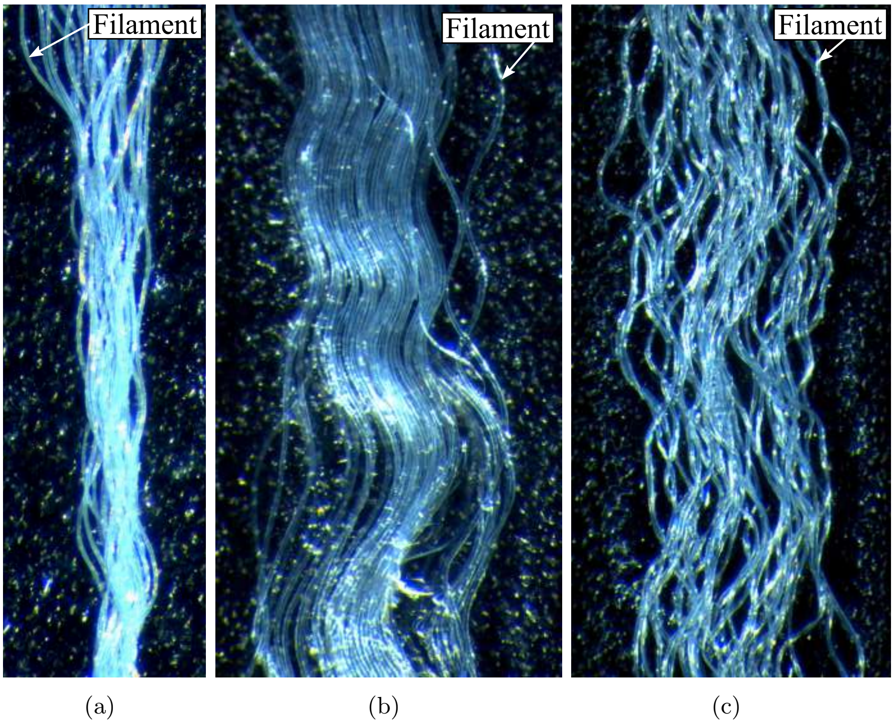

(a) (b) (c)

Figure 3.4: Dielectric materials with their unraveled filaments. (a) PET_{warp} thread sample. (b) $PES_{\text{weft\_dsgn1}}$ thread sample. (c) $PET_{\text{weft\_dsgn2}}$ thread sample.

Table 3.3: Cross section dimensions of the employed dielectric materials ($dsgn_2$).

Material	Thread direction	Cross section	Dimension	Value (mm)
PET_{warp}	Warp	Pierce	Horizontal semi-axis	0.075
			Vertical semi-axis	0.055
$PET_{\text{weft\_dsgn2}}$	Weft	Circular	Circumference radius	0.075

to the employed dielectric threads has a relative permittivity of $\varepsilon_{\text{fil\_PES}} = 3.5$, a loss tangent of $\tan(\delta)_{\text{fil\_PES}} = 0.001$ and a density of $\delta_{\text{fil\_PES}} = 1.5$ g/cm^3 [11–18]. The previously mentioned dielectric parameters are summarised in Table 3.4.

In order to translate the dielectric threads from the filament model (FM) into the monofilament model (MM), the procedure explained in section 2.1.2.1 has been followed. As a result, the equivalent dielectric parameters of the monofilaments are summarised in Table 3.5. The loss tangents have not been significantly

Table 3.4: Characteristic parameters of the employed dielectric materials.

Parameter	PET	PES
Relative permittivity	$\varepsilon_{\text{fil\_PET}} = 3.7$	$\varepsilon_{\text{fil\_PES}} = 3.5$
Loss tangent	$\tan(\delta)_{\text{fil\_PET}} = 0.001$	$\tan(\delta)_{\text{fil\_PES}} = 0.001$
Density (g/cm^3)	$\delta_{\text{fil\_PET}} = 1.5$	$\delta_{\text{fil\_PES}} = 1.5$

Table 3.5: Parameters of the equivalent monofilaments

Monofilament	% of air	Relative Permittivity	Loss Tangent
PET_{warp}	75%	$\varepsilon_{\text{mon\_PET}} = 1.72$	$\tan(\delta)_{\text{mon\_PET}} = 0.001$
$PES_{\text{weft\_dsgn1}}$	24%	$\varepsilon_{\text{mon\_PES\_dsgn1}} = 2.83$	$\tan(\delta)_{\text{mon\_PES\_dsgn1}} = 0.001$
$PET_{\text{weft\_dsgn2}}$	37%	$\varepsilon_{\text{mon\_PET\_dsgn2}} = 2.11$	$\tan(\delta)_{\text{mon\_PES\_dsgn2}} = 0.001$

modified from the FM to the MM due to the resolution of the method employed.

According to the procedure referenced in section 2.1.2.3, and due to the fact that the PET_{warp} threads remain straight, the different weft threads, in both designs, will conform the woven structure around the warp threads. The *epi* and *ppi* parameters employed in both designs are 59 and 79, respectively, leading to woven structures which will be explained in detail in section 3.1.5.

Nevertheless, for clarification, the parameters which describe the LM are calculated and presented in this subsubsection. Given the *epi* and *ppi* parameters and the dielectric characteristics of the employed materials, and following the procedure explained in section 2.1.3, the equivalent relative permittivities, $\varepsilon_{\text{eq\_dsgn1}}$ and $\varepsilon_{\text{eq\_dsgn2}}$, have been found to be 1.55 in both cases. Even though the composition of the weft threads in both designs is different, the difference between the $\varepsilon_{\text{mon\_PES\_dsgn1}}$ and the $\varepsilon_{\text{mon\_PET\_dsgn2}}$, and the dimensions of their different cross sections have lead to the same result. In $dsgn_1$, the amount of dielectric material different from air in the substrate is lower than in $dsgn_2$, whereas $\varepsilon_{\text{mon\_PES\_dsgn1}}$ is greater than $\varepsilon_{\text{mon\_PET\_dsgn2}}$. Analogously, the equivalent loss tangents, $\tan(\delta)_{\text{eq\_dsgn1}}$ and $\tan(\delta)_{\text{eq\_dsgn2}}$, have been found to be 0.001, and the calculated equivalent electrical conductivity $\sigma_{\text{eq}} = 5 \cdot 10^4$ S/m. The low value of the conductivity is due to the separation between the threads which compose the woven structure.

3.1.5 Design of the woven prototype

Once the materials have been characterised and the densities of the woven structure, *epi* and *ppi* parameters, have been defined, a woven design which emulates the structure of a SIW is required. For the conductive plates of the SIW, top and bottom layers, two layers composed of warp and weft conductive threads have been used. The dielectric layer has been realised using a single layer of dielectric material composed of warp and weft threads. The conductive vias have been emulated using conductive weft threads crossing the prototype from the top to the bottom layer. For this reason, different weft patterns have been designed to create the SIW structure, while connecting the different layers of the prototype generalising the equations described in section 2.1.2.3 for the different cross sections.

Once the equivalent monofilaments are calculated, a MM structure can be developed to emulate a SIW, as depicted in Figure 3.5. Figure 3.5a shows a conventional SIW or, equivalently, the LM associated to a TIW. The electric field is vertically oriented, therefore, parallel to the Y-axis, whereas the magnetic field is parallel to the X-axis. Consequently, the EM field propagates in $\hat{\text{k}}$ direction from port 1 to port 2. Figure 3.5b represents the woven translation of the SIW, in which the conductive materials are yellow colored, and the dielectric materials are gray colored. The woven MM structure is composed of three layers of warp threads, a layer of dielectric threads between two layers of conductive materials. The warp threads are parallel to the propagation direction. Then, the woven structure is achieved by weaving different weft patters around the warp threads.

Figure 3.6 depicts different views of the proposed woven structure and detailed weft patterns. Figure 3.6a represents the front view of the proposed MM structure and a magnification where the equivalent substrate height, H_{SIW}, has been indicated. Figure 3.6b and Figure 3.6c depict the conductive weft patterns, I and II, required to emulate the vias by connecting the top layer with the bottom layer. With the aim of achieving a compact structure, two different weft patterns for the vias are required. In other words, if only one of the patterns were employed, half of the warp conductive threads in both the top and bottom layers would not be woven and, therefore, they would be loose. Figure 3.6d depicts the non conductive weft pattern which represents the substrate of the SIW.

A general top view of the woven structure is shown in Figure 3.7a, where the separation between the conductive vias is also detailed, whereas Figure 3.7b represents the top view of the woven structure without the conductive threads which conform the vias. Combining the different weft patterns with the warp threads, the beforementioned woven structure presented in Figure 3.5b can be achieved.

3.1.6 Design of the TIW to WR-28 transition

For the posterior experimental validation of the prototypes, a TIW to WR-28 waveguide transition has been designed. The transition is based on an air-filled stepped rectangular waveguide with six sections, which have been optimised for maximum coupling between the WR-28 waveguide and the textile prototypes [19].

The transition is not symmetrical in the H-plane: it consists of a stepped part schematically depicted in Figure 3.8a and Figure 3.8c, and a flat cover represented

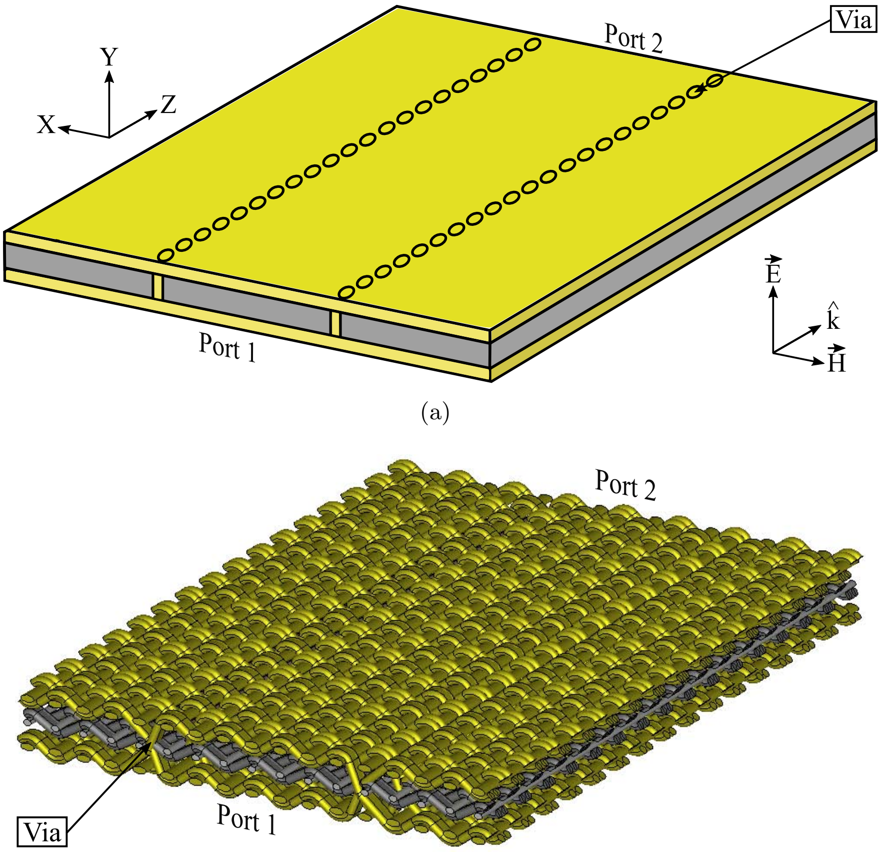

Figure 3.5: General overview of the proposed design. (a) Conventional SIW equivalent to the LM. (b) Proposed woven structure of the TIW.

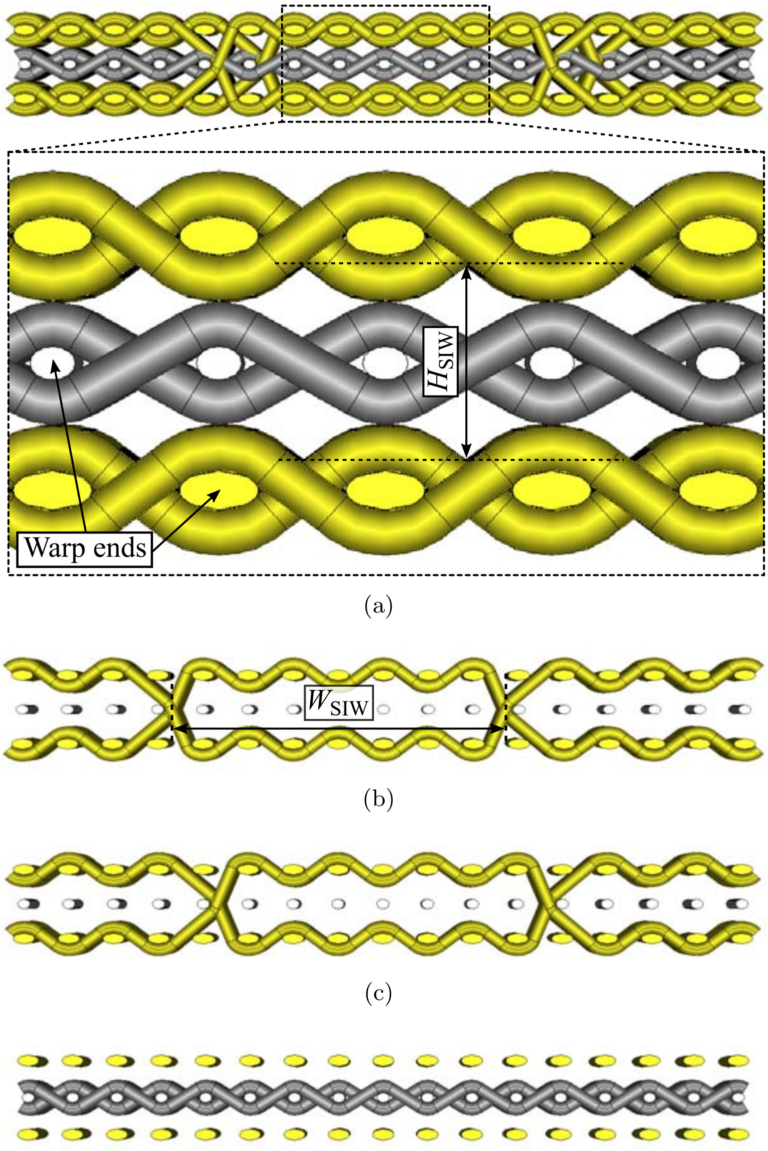

(a)

(b)

(c)

(d)

Figure 3.6: MM of the TIW (conductive material is yellow colored and dielectric materials are gray colored). (a) General front view and magnification. (b) Front view of vias pattern I. (c) Front view of vias pattern II. (d) Front view of substrate pattern.

in Figure 3.8b, which are fabricated separately. The TIW port of the transition has been designed to compress the textile structure between these two parts. The dimensions of the optimised design are summarised in Table 3.6.

3.1.7 Simulations

The proposed woven structures have been electromagnetically analysed using a commercial 3D high frequency simulator. Therefore, the MM has been analysed for both designs, using their corresponding dielectric parameters, and compared with the behaviour of the corresponding LM, using a 10 mm length TIW, as depicted in Figure 3.9.

The different behaviour of the scattering parameters near the cut-off frequency of the TIW is due to the different solvers employed in the simulations. While the

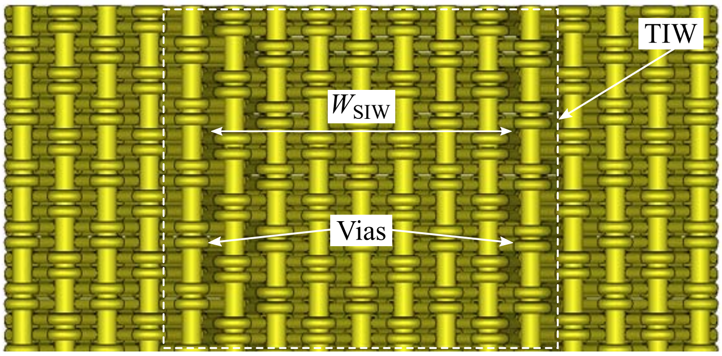

(a)

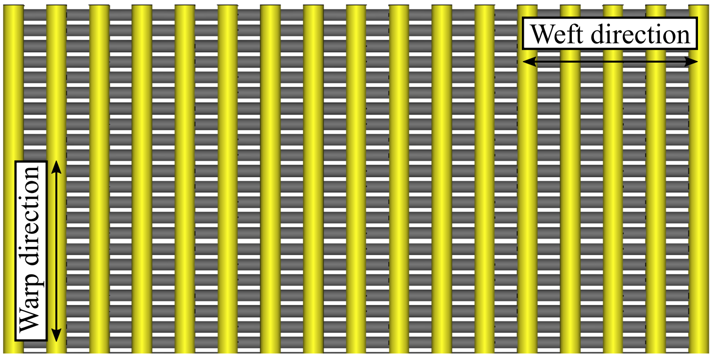

(b)

Figure 3.7: MM of the TIW. (a) General top view. (b) Top view without the conductive threads which emulate the vias.

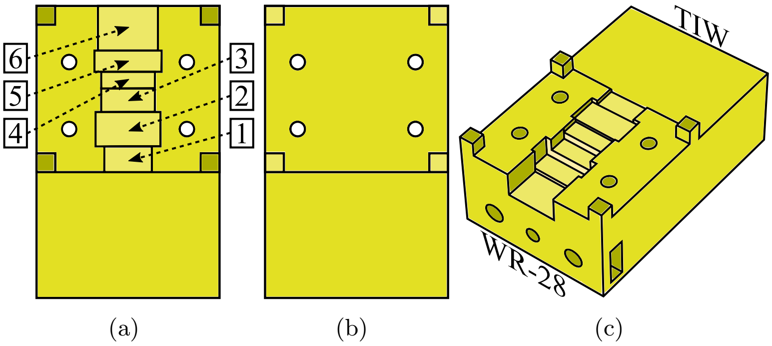

(a) (b) (c)

Figure 3.8: Design of the proposed TIW to WR-28 transition. (a) Stepped part inner view. (b) Flat cover inner view. (c) Stepped part overview.

Table 3.6: Dimensions of the TIW to WR-28 waveguide transition

Step	1	2	3	4	5	6
Width (mm)	5.76	7.48	6.39	6.31	7.88	7.11
Length (mm)	2.72	4.26	2.24	2.49	2.89	3
Height (mm)	0.36	0.26	0.69	1.78	2.97	3.56

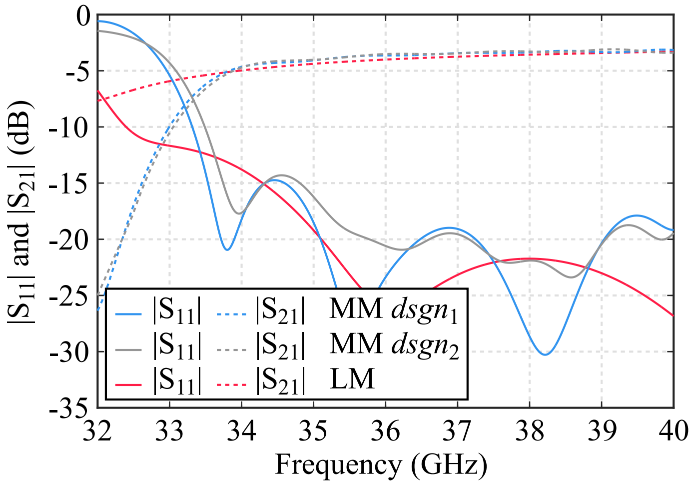

Figure 3.9: Comparison between the simulated scattering parameters of the LM and the MM for both designs using a 10 mm long TIW.

MM has been simulated using an hexahedral mesh and a Transient Solver, due to the complexity of the structure, the LM had to be simulated using a Frequency

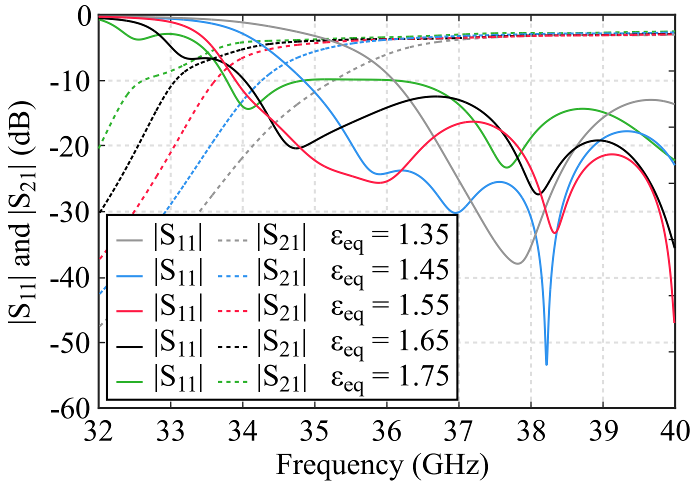

Figure 3.10: Simulated scattering parameters of a 10 mm long TIW section terminated with two WR-28 waveguide to TIW transitions, using the LM.

Domain Solver with a tetrahedral mesh.

The transition from TIW to WR-28 waveguide has also been simulated. Although it has been optimised for the calculated equivalent relative dielectric permittivity of the dielectric layer $\varepsilon_{eq} = 1.55$, its behaviour has also been evaluated for different values. The simulated scattering parameters of a 10 mm long TIW section connected to a TIW to WR-28 waveguide transition in both ports are presented in Figure 3.10, where the cut-off frequency is modified as follows: the lower the equivalent relative permittivity, the higher the cut-off frequency.

3.1.8 Fabrication process

Two millimetre-wave TIW sections have been manufactured using an industrial MüGrip loom with a maximum $epi = 106$ ends/inch, to validate the proposed TIW. Figure 3.11 represents the top view of the TIW prototype ($dsgn_1$ or $dsgn_2$ indistinctively) and detailed magnifications, where the different weft patterns can be identified. The front views and corresponding magnifications of the prototypes associated to $dsgn_1$ and $dsgn_2$ are depicted in Figure 3.12. These magnifications exhibit the elliptic cross section of the warp threads, specially in the conductive materials. Moreover, the paths of the weft threads can be easily identified as ellipse arcs and tangent lines as modelled, specially in $dsgn_1$, due to the higher warp thread rigidity.

In order to experimentally evaluate the textile prototypes, a pair of TIW to

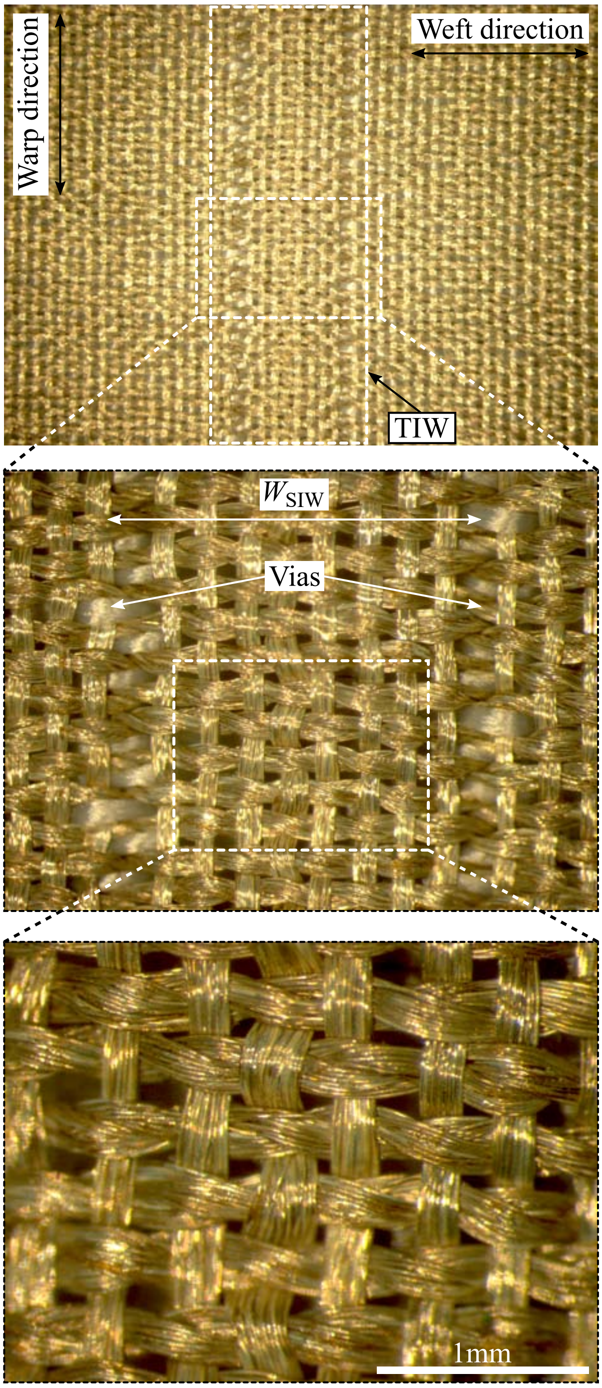

Figure 3.11: Top view of the TIW prototype using rigid warp threads ($dsgn_1$ or $dsgn_2$ indistinctly) and detailed magnifications.

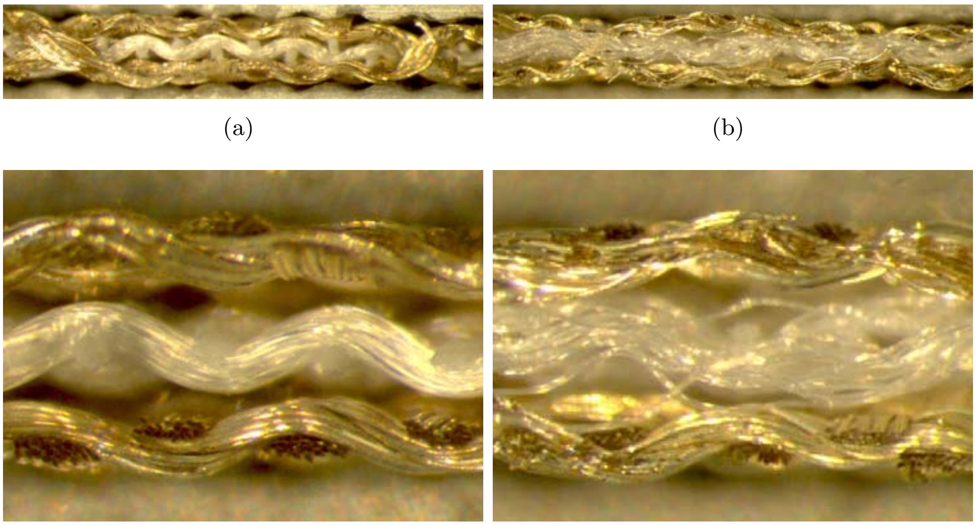

(a) (b) (c) (d)

Figure 3.12: Proposed TIW prototype. (a) Front view of $dsgn_1$. (b) Front view of $dsgn_2$. (c) Magnification of $dsgn_1$. (d) Magnification of $dsgn_2$.

WR-28 waveguide transitions have been fabricated. Each transition has been manufactured in two different pieces: a stepped part and a flat cover, as depicted in Figure 3.13a. Both parts have been manufactured using a high precision stereolithography process in which a photopolymer resin is progressively cured, layer by layer, with ultra-violet (UV) radiation exposure, as the solidified part is lifted out of the resin tank. The inner parts of the transition and the connecting flanges are provided with the required electrical conductivity through the deposition of a thin gold layer using a sputtering process. The manufactured transition is presented in Figure 3.13b.

3.1.9 Experimental validation

The prototypes have been characterised using the experimental set-up presented in Figure 3.14. The two ports of the TIW section are connected to the TIW to WR-28 waveguide transitions. A pair of Agilent R281B WR-28 waveguide coaxial adapters are required to connect the prototypes to an Agilent N5247A PNA-X vector network analyser.

Figure 3.15a represents a comparison between the simulated and measured insertion losses of the TIW ($dsgn_1$) for three different lengths, 30, 40 and 55 mm,

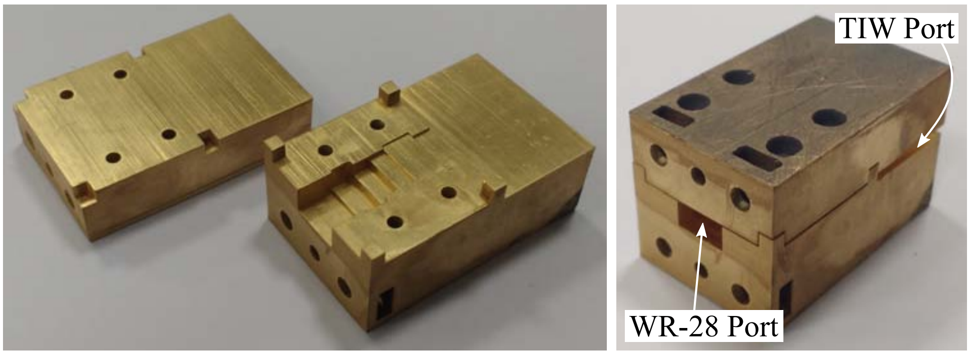

(a) (b)

Figure 3.13: Proposed WR-28 waveguide to TIW manufactured transition. (a) Flat and stepped parts. (b) Transition overview.

respectively. Three different lengths have been employed in order to consider the R281B WR-28 waveguide to coaxial adapters and the TIW to WR-28 waveguide transitions frequency responses and, therefore, normalise the measured results. For the simulations, the results from the MM have been considered. Figure 3.15b depicts a comparison between the simulated and measured return losses of the TIW ($dsgn_1$) for the three before mentioned lengths. The corresponding results for $dsgn_2$ are shown in Figure 3.16, where three different lengths, 40, 50 and 60 mm, have been employed.

As predicted by the simulations, both prototypes present an insertion loss value of 3 dB/cm. This insertion loss may be reduced by using threads with a higher conductivity such as silver or copper yarn instead of silver coated *Shieldex*. In other words, although the skin depth effect has been previously studied, concluding that the silver coating thickness has been sufficient to consider the conductive thread as completely conductive, the wear out of the thread in the loom may decrease this thickness, leading to a decrease of its conductivity. Moreover, the behaviour of the prototypes can be improved by using a greater *epi* parameter, due to the fact that the fabrication of a tighter structure reduces the gaps between conductive warp and weft threads, limiting the radiative losses.

The agreement between simulated data and measurements demonstrates the validity of the TIW as a fully woven guiding structure, even though an improvement in the conductivity of the materials is required. However, the differences between the simulated data and the measured results are due to the following discrepancies between the simulated model and the measured prototype. Although

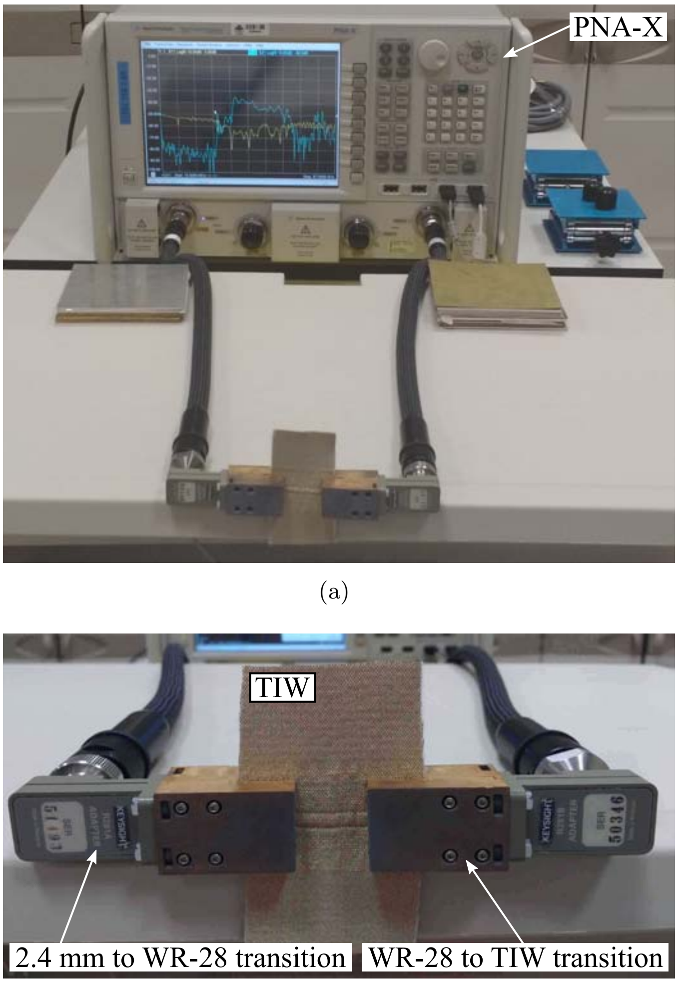

(a)

(b)

Figure 3.14: Set-up for the TIW experimental validation. (a) General overview. (b) Magnification of the TIW and the transitions.

a fully automated industrial weaving loom has been used for the manufacturing of the prototypes, the height of the woven dielectric substrate layer is not uniform along the propagation direction. This leads to a band-pass frequency response instead of the expected flat frequency response of the waveguide. Other differences between the simulated and measured frequency response can be due to the mathematical approximations which have been used in the model, such as the cross sections of the threads, or the curves described by the different weft patterns.

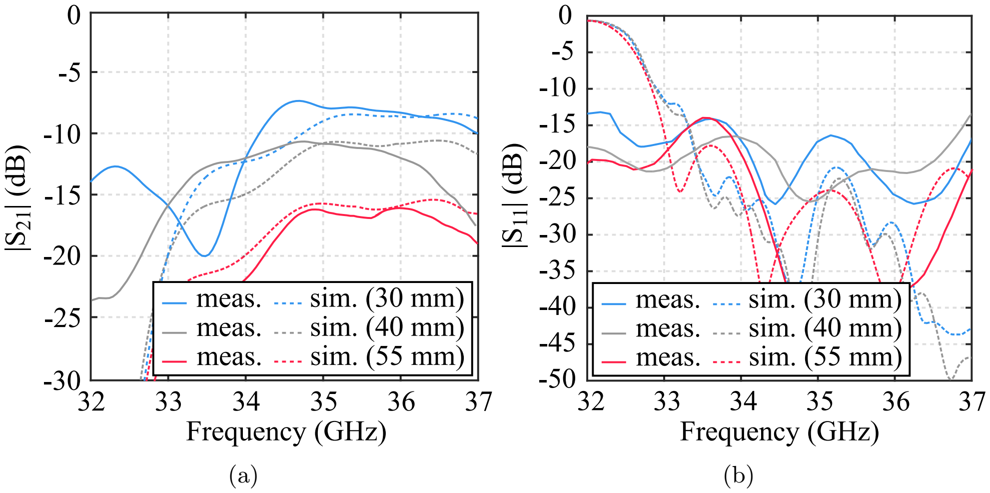

(a) (b)

Figure 3.15: Simulated and measured scattering parameters of the TIW ($dsgn_1$). (a) $|S_{21}|$. (b) $|S_{11}|$.

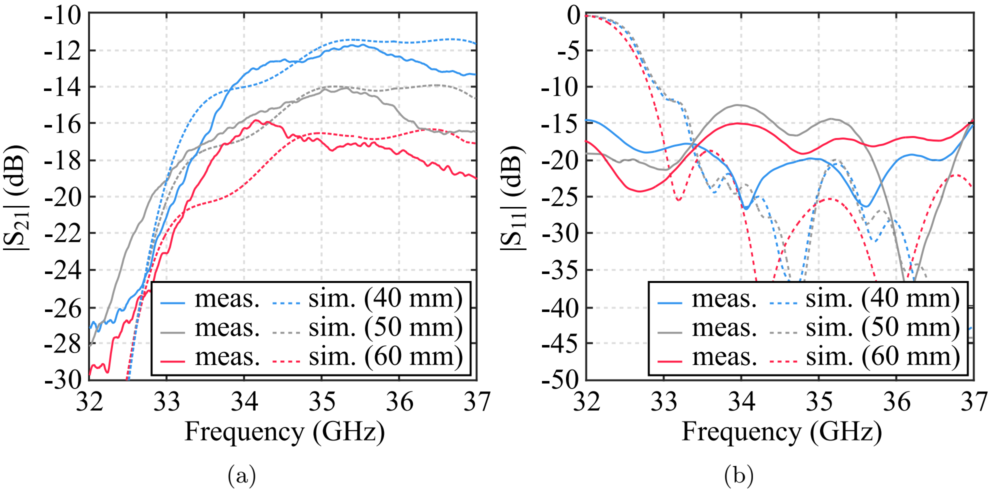

(a) (b)

Figure 3.16: Simulated and measured scattering parameters of the TIW ($dsgn_2$). (a) $|S_{21}|$. (b) $|S_{11}|$.

3.1.10 Conclusions

A novel technique to develop millimetre-wave TIW using rigid warp threads has been presented. The three-step parametric modelling to simulate textile structures based on the reduction of the computational complexity of the problem has been implemented. To validate the modelling, two TIW, which use different dielectric threads, have been manufactured and experimentally characterised. The theoretically predicted behaviour of the textile structures has been experimentally verified. Nevertheless, in order to reduce the insertion losses it is proposed to use conductive threads with a lower resistance. Besides, the theoretical resistance calculated from the information provided by *Shieldex* does not match the measured resistance and consequently, does not fulfil the requirements to develop the desired prototypes.

The manufactured prototypes reveal the potential of the textile technology applied to waveguide based designs working at the millimetre-wave range frequency, opening a new field of research. These prototypes represent a first step in TIW technology and demonstrate the possibility of guiding a RF signal along textile structures.

3.2 TIW with a microstrip transition using rigid weft threads

3.2.1 Introduction

With the aim of enhacing the design presented in the previous subsection, a microwave TIW to microstrip transition is proposed, integrating the transitions for the experimental validation into the textile [20]. This design implements the modelling technique already described in Chapter 2, although simplified, due to the use of monofilaments, instead of multifilament threads, consequently reducing the three steps into two.

Moreover, in contrast to the TIW presented in the previous subsection, the warp threads employed in this design are more flexible than the weft threads. This modification allows the possibility of creating different warp patterns, as well as achieving a constant height of the textile substrate. Consequently, this leads to the implementation of a TIW to microstrip woven transition, avoiding the fabrication of the 3D-printed transitions and achieving a complete integration of the prototype in the textile.

3.2.2 Structure of the TIW

A TIW using rigid weft threads is proposed to work at a range of frequencies between 7.5 and 12 GHz and has been designed using the procedure described in section 2.1 and particularised to two steps. Figure 3.17 represents an overview of

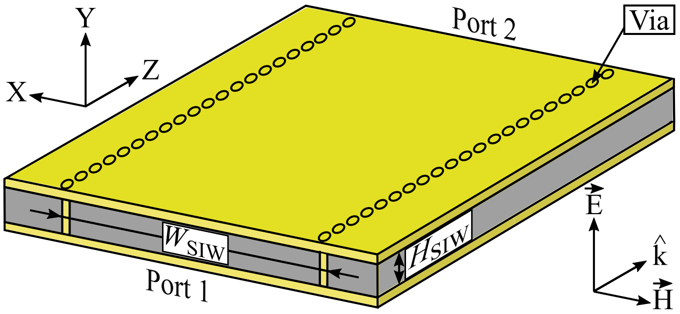

Figure 3.17: Schematic drawing of the proposed TIW, conductive materials (yellow) and dielectric materials (grey).

the LM associated to the proposed TIW, the coordinate system, the orientation of the EM field and the propagation direction.

The TIW is based on a SIW, then, the TIW can be divided into three different layers, a dielectric layer (whose height is denoted by H_{SIW}) between two conductive plates. The separation between the two rows of conductive vias is given by W_{SIW}, whereas the diameter of each via and the separation between two consecutive vias are given by D and S, respectively. The parametric length of the TIW is given by L_{SIW}.

The proposed TIW is fully integrated in textile, therefore, the conductive and dielectric parts are manufactured using different types of threads. In the proposed TIW, the warp direction coincides with the propagation direction, whereas the weft direction is parallel to the orientation of the magnetic field. Unlike in the case of the TIW presented in section 3.1, where the warp threads remain straight, in the present TIW, the weft threads are the ones which remain straight. The employed materials will be explained in section 3.2.3 and section 3.2.4.

3.2.3 Characterisation of the conductive materials

Electrically conductive *Shieldex 117f17 2-ply* yarns, with 17 filaments per ply and a density of 117 dtex have been used for the weft threads. For simplification, this material will be denoted by *Shx2p*. These threads adopt the Pierce's elliptic cross section when they are in the woven structure. In addition, electrically conductive *Shieldex 117f17 1-ply* yarns, with 17 filaments per ply and a density of 117 dtex have been used for the warp threads. These threads adopt the circularly cross section, since they are not deformed when they are in the woven structure. The cross section approaches and corresponding dimensions of the

Table 3.7: Cross section dimensions of the employed conductive materials.

Material	Thread direction	Cross section	Dimension	Notation	Value (mm)
Shx2p	Weft	Pierce	Horizontal semi-axis	H_S	0.1
			Vertical semi-axis	V_S	0.05
Shx1p	Warp	Circularly	Circumference radius	C_R	0.075

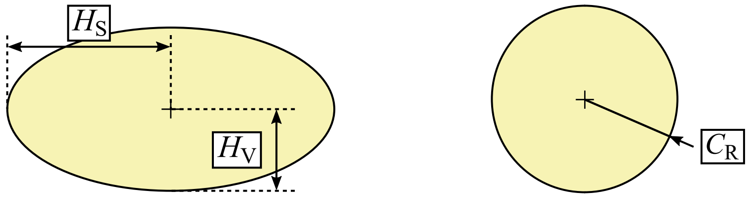

(a) (b)

Figure 3.18: Cross section dimensions of the monofilament threads. (a) *Shx2p* threads. (b) *Shx1p* threads.

different conductive threads are summarised in Table 3.7. The thickness of the silver coating of each filament, for both types of threads, is given by $T_\mathrm{c} = 0.5$ µm, whereas the total diameter of each filament is given by $D_\mathrm{f} = 31$ µm, as it has been previously depicted in Figure 3.2.

Following the procedure described in section 2.1.2.2, both conductive threads must be translated into their analogous monofilaments. For this purpose, the analysis of the skin depth effect is discussed in this section. First, using the expression described in (2.1), where $\rho_\mathrm{coat} = 1.59 \cdot 10^{-8}$ (Ωm) is the resistivity of the silver and f is the minimum operating frequency of the design, $f = 7.5$ GHz, the skin depth is $\delta = 0.7328$ µm. As the thickness of the conductive coating of the filaments is less than the skin depth, the second part of the procedure is followed.

In order to employ the procedure described in section 2.1.2.2, some expressions must be particularised to the different cross sections of the *Shieldex* yarns. Using the expression (2.4), and substituting δ by T_c, the resistance per unit length of each filament is $(R/l)_\mathrm{f} = (\pi \cdot \sigma_\mathrm{coat} \cdot (2 \cdot R_\mathrm{f} \cdot T_\mathrm{c} - {T_\mathrm{c}}^2))^{-1} = 331.8772$ Ω/m. As the *Shx2p* and the *Shx1p* threads present a different number of filaments, the resistance per unit length of each type of thread will be different.

The *Shx2p* threads are composed of $N_\mathrm{fil} = 34$ filaments, therefore, $(R/l)_\mathrm{Shx2p} =$

9.7611 Ω/m. Alternatively, the *Shx1p* threads are composed of $N_{\text{fil}} = 17$ filaments and, consequently, $(R/l)_{\text{Shx1p}} = 19.5222\ \Omega/\text{m}$. The equivalent cross sections of the threads have been modified due to the forces the threads experiment in the different woven structure in comparison to the previous section.

Particularising the expression in (2.6) for the Pierce's elliptic cross section, the areas of the equivalent conductive cross sections of the monofilament threads for the *Shx2p* and the *Shx1p* threads, S_{mon2} and S_{mon1}, can be expressed using, respectively, (3.4) and (3.5).

$$S_{\text{mon2}} = \pi \cdot H_{\text{S}} \cdot V_{\text{S}} - \pi \cdot (H_{\text{S}} - T_{\text{R}}) \cdot (V_{\text{S}} - T_{\text{R}}) \tag{3.4}$$

$$S_{\text{mon1}} = \pi \cdot {C_{\text{R}}}^2 - \pi \cdot (C_{\text{R}} - T_{\text{R}})^2 \tag{3.5}$$

Once the expressions of the $S_{\text{mon}i}$ are obtained, the resistances per unit length of the monofilament can be expressed particularising (2.7) for the Pierce's elliptic cross sections, as generically indicated in (3.6).

$$(R/l)_{\text{mon}i} = \frac{1}{\sigma_{\text{mon}i} \cdot \pi \cdot S_{\text{mon}i}} \tag{3.6}$$

With the aim of achieving the same resistance per unit length in both the multifilament and the monofilamente threads, $(R/l)_{\text{Shx2p}}$ must be equal to $(R/l)_{\text{mon2}}$ and, equivalently, $(R/l)_{\text{Shx1p}}$ must be equal to $(R/l)_{\text{mon1}}$. As it has been thoroughly explained in section 2.1.2.2, the parameter T_{R} coincides with the skin depths, δ_{mon2} and δ_{mon1}, calculated using the equivalent electrical conductivities of the monofilaments, σ_{mon2} and σ_{mon1}, respectively, as previously expressed in (2.9). Solving the corresponding equations using numeric methods, the solutions have been found to be $\sigma_{\text{mon2}} = 1.4023 \cdot 10^9\ \Omega/\text{m}$ and $\sigma_{\text{mon1}} = 3.5130 \cdot 10^8\ \Omega/\text{m}$, respectively.

3.2.4 Characterisation of the dielectric materials

For the dielectric parts of the prototype, two different types of thread have been employed. For the warp threads, uncoated polyethersulfone (PES) monofilament has been used. For the weft threads, uncoated polyethylene-terephthalate (PET) monofilament has been employed. For simplification, the PES warp threads and the PET weft threads will be denoted by PES_{warp} and PET_{weft}, respectively.

The characteristic parameters of the employed materials in the operation frequency band are defined for the MM, as the threads are monofilaments, and are

Table 3.8: Characteristic parameters of the employed dielectric materials.

Parameter	PES	PET
Relative permittivity	$\varepsilon_{\text{mon\_PES}} = 3.4$	$\varepsilon_{\text{mon\_PET}} = 3.7$
Loss tangent	$\tan(\delta)_{\text{mon\_PES}} = 0.01$	$\tan(\delta)_{\text{mon\_PET}} = 0.001$

Table 3.9: Cross section dimensions of the employed dielectric materials.

Material	Thread direction	Cross section	Dimension	Value (mm)
PES_{warp}	Warp	Circularly	Radius	0.075
PET_{weft}	Weft	Circularly	Radius	0.5

the following. The relative permittivities of the PET and the PES are $\varepsilon_{\text{mon\_PES}} = 3.4$ and $\varepsilon_{\text{mon\_PET}} = 3.7$, respectively. The loss tangents associated to the PES and the PET are $\tan(\delta)_{\text{mon\_PES}} = 0.01$ and $\tan(\delta)_{\text{mon\_PET}} = 0.001$, respectively [15, 18]. The before mentioned characteristic parameters are summarised in Table 3.8.

For both, the PES_{warp} and the PET_{weft} threads, the circularly cross section was found to be the best approximation. The dimensions of the cross section of each type of dielectric thread are indicated in Table 3.9.

According to the procedure referenced in section 2.1.2.3, and due to the fact that the PES_{weft} threads remain straight, the different warp threads will conform the woven structure around the weft threads. The *epi* and *ppi* parameters employed in both designs are 169.3 and 16.9, respectively, leading to woven structures which will be explained in detail in section 3.2.5.

Nevertheless, for clarification, the parameters which describe the LM are calculated and presented in this subsubsection. Given the *epi* and *ppi* parameters and the dielectric characteristics of the employed materials, and following the procedure explained in section 2.1.3, the equivalent relative permittivity, ε_{eq} has been found to be very close to 1. This means that, even though the woven substrate is composed of materials whose relative permittivities are different from the vacuum relative dielectric permittivity, $\varepsilon_{\text{r0}} = 1$, the existence of thick dielectric yarns placed perpendicularly aligned with the propagation direction, leads to the existence of big air gaps, consequently reducing the value of the equivalent relative permittivity. Using this procedure no more precision can be achieved to calculate ε_{eq}, however, the design will not be affected by the use of $\varepsilon_{\text{eq}} = \varepsilon_{\text{r0}}$. Analogously, the equivalent loss tangent has been calculated and found to be $\tan(\delta)_{\text{eq}} = 0.01$ due to the influence of the *PES*. The calculated equivalent electrical conductivity has also been calculated has found to be $\sigma_{\text{eq}} = 5 \cdot 10^5$ S/m.

3.2.5 Design of the woven prototype

After the characterisation of the materials and the definition of the densities of the woven structure, *epi* and *ppi* parameters, a woven design which emulates the structure of a SIW is required. For the top and bottom layers of the SIW, which correspond to the conductive plates, two layers of warp and weft conductive threads have been employed. Analogously, the dielectric layer has been realised using one layer of dielectric material in both the warp and the weft directions. The conductive vias which connect the top and bottom layers of the SIW have been emulated using warp threads which cross the prototype from the top layer, to the bottom. In the proposed textile structure, the effective diameter of the vias is closely related to the diameter of the conductive warp threads employed to implement the top and bottom conductive layers of the TIW structure. The diameter of these conductive warp threads not only restricts the effective diameter of vias, but also the separation between two consecutive vias, S, which is also restricted by the diameter of the dielectric weft threads.

The distance between the two rows of conductive vias has been designed to be $W_{\text{SIW}} = 25$ mm, in order to achieve the required cut-off frequency. The separation between two consecutive vias belonging to the same row has been designed to be $S = 1.5$ mm, whereas the diameter of the conductive vias is $D = 0.15$ mm. For this reason, different warp patterns have been designed to create the SIW structure, while connecting the different layers of the prototype generalising the equations described in section 2.1.2.3 for the different cross sections.

The design of conventional SIW, manufacturable using standard prototyping machines, presents an important difference compared with the design of their analogous TIW. In a SIW, the diameter of the vias can be increased while keeping the distance between the centres of the via holes as a constant, up to a certain limit. By doing this, the non-conductive space between two consecutive vias is reduced. However, increasing the effective diameter of the vias in a TIW can only be achieved by using thicker conductive warp threads, which leads to the deterioration of the TIW performance. In other words, when the effective diameter of the vias increases, the conductive warp threads tend to decrease their flexibility due to the thickness. Consequently, the separation between the vias does not remain constant, but increases, as well as the non-conductive spaces between vias, which lead to the increase of the losses.

For this reason, in order to reduce the losses of the woven structure, a possible solution is proposed. The diameter of the thick dielectric weft threads can be reduced, consequently, the vias would keep the same diameter while the distance between two consecutive vias would be reduced. However, the thickness of the woven structure would also be reduced. This consequence could also be solved by employing more interwoven layers of dielectric thinner threads, however, a more complex weaving loom would be required. For the aforementioned reasons, the dimensions of the threads employed to develop the proposed TIW have been chosen in order to achieve a balance between the losses and the required thickness of the structure.

A MM woven structure can be developed to emulate a SIW, as depicted in Figure 3.19. Figure 3.19a shows a conventional SIW or, equivalently, the LM associated to a TIW. The electric field is vertically oriented, therefore, parallel to the Y-axis, whereas the magnetic field is parallel to the X-axis. Consequently, the EM field propagates in $\hat{k}$ direction from port 1 to port 2. Figure 3.19b depicts the woven translation of the SIW, in which the conductive and dielectric materials are yellow and gray colored, respectively. The woven MM structure is composed of three layers of warp threads, a layer of dielectric threads between two layers of conductive materials. The warp threads are parallel to the propagation direction. Then, the woven structure is achieved by weaving different warp patterns around the rigid weft threads. A magnification of the TIW is also shown in Figure 3.19.

Figure 3.20 depicts different side views of the proposed woven structure and detailed warp patterns. Figure 3.20a represents a general side view of the woven structure in which the height of the woven dielectric layer, H_{SIW}, is indicated. In this representation, the weft ends and the warp threads which conform the woven structure are depicted. Consequently, the conductive warp patterns which generate the conductive plates and the dielectric warp patterns required to connect the woven substrate are represented.

Figure 3.20b depicts the side view of the auxiliary substrate patterns, which are called binders and are required to connect the three layers of the woven structure with the aim of implementing a compact structure. If dielectric binders were not employed, the woven structure would only be completely connected through the conductive vias and, therefore, only in the positions where the vias are required. As a result, except from the positions were the vias are implemented, the woven structure would be composed of three independent woven layers. Figure 3.20c represents the side view of the vias patterns to electrically connect the top and bottom conductive layers.

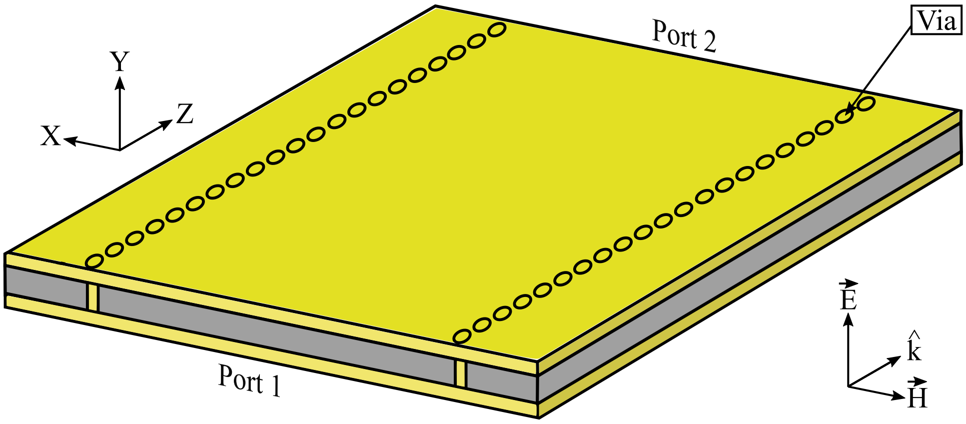

(a)

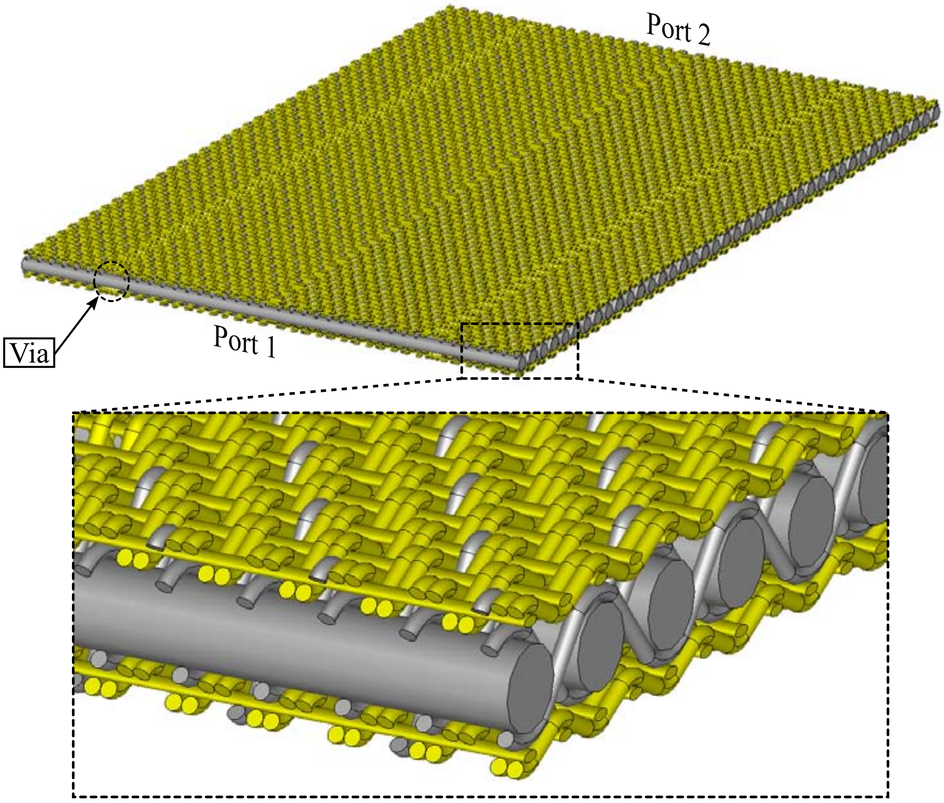

(b)

Figure 3.19: General overview of the proposed design. (a) Conventional SIW equivalent to the LM. (b) Proposed woven structure of the TIW and magnification.

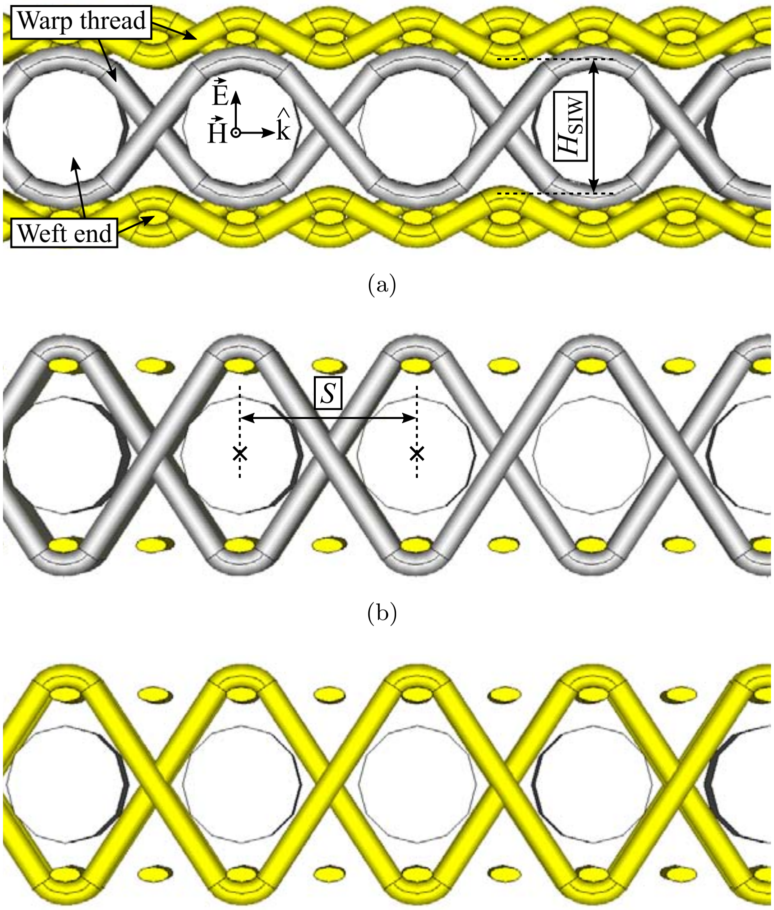

(a)

(b)

(c)

Figure 3.20: MM of the TIW (conductive material is yellow colored and dielectric materials are gray colored). (a) General side view. (b) Side view of the substrate patterns to connect the three layers. (c) Side view of the vias patterns.

A general top view and magnification of the woven structure is depicted in Figure 3.21a, in which the separation between the conductive vias is also detailed. Figure 3.21b represents the front view, or view from the port of the woven structure. Combining the different warp patterns with the weft threads, the aforementioned woven structure presented in Figure 3.19b can be achieved.

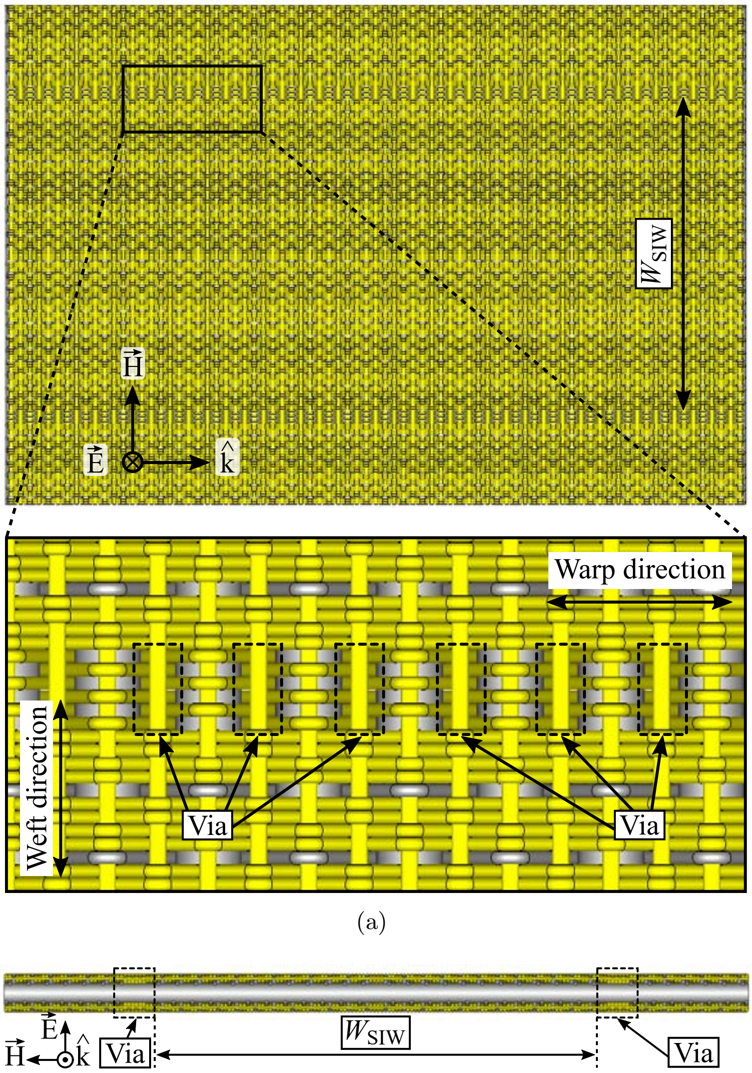

(a)

(b)

Figure 3.21: MM of the TIW (conductive material is yellow colored and dielectric materials are gray colored). (a) General top view and magnification. (b) General front view (port view).

3.2.6 Design of the TIW to microstrip transition

For the experimental validation of the prototype, a TIW to microstrip line transition has been designed. As the height of the prototype is given by the diameter of the dielectric weft threads, then $H_{\mathrm{SIW}} = 1$ mm. Given the height

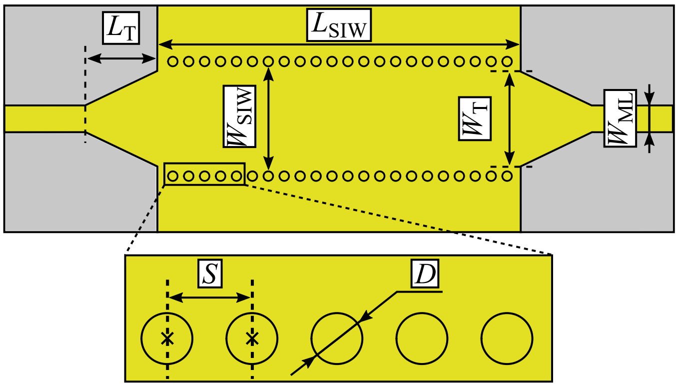

Figure 3.22: Schematic top view of the back to back TIW to microstrip transition and magnification.

of the substrate and its equivalent relative permittivity, $\varepsilon_{eq} = 1$, then the width, W_{ML}, of a microstrip line, whose characteristic impedance is equal to 50 Ω, can be worked out [21]. Consequently, $W_{ML} = 5$ mm.

The transition is based on a tapered transmission line, as depicted in Figure 3.22, whose dimensions have been optimised for maximum coupling between the TIW and the microstrip line. Consequently, the dimensions of the taper have been found to be $W_T = 22$ mm and $L_T = 20$ mm.

3.2.7 Simulations

The proposed prototype has been electromagnetically analysed using a 3D high frequency simulator with a tetrahedral mesh. Figure 3.23 represents the simulated magnitude of the scattering parameters of the equivalent LM (including the transitions) for three different length, L_{SIW}, of the prototype corresponding to 10, 15 and 20 mm, respectively. The simulated magnitude of the return losses is 0.6 dB/cm. The MM has not been completely simulated for the aforementioned lengths due to the computational resources required for this purpose.

3.2.8 Fabrication process

Different TIW have been manufactured using an industrial MüGrip loom, corresponding to different lengths, to validate the proposed TIW. In order to manufacture the woven TIW to microstrip transitions, not only three layers of warp and weft threads are required, but also an auxiliary fourth layer of weft threads. The purpose of this extra layer is weaving the leftover conductive warp

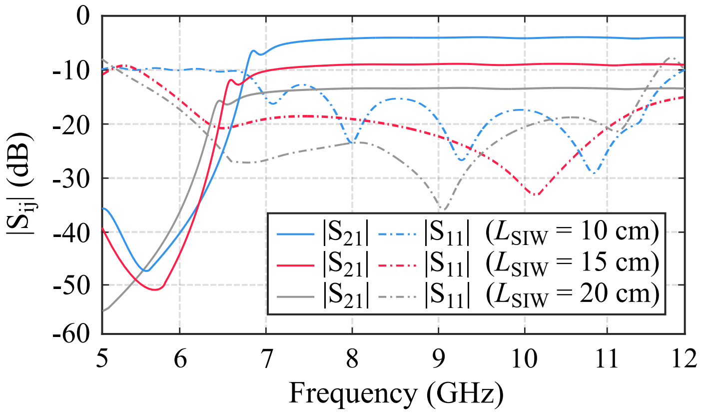

Figure 3.23: Simulated scattering parameters of the LM for the three different lengths.

threads which are not required in the top layer of the tapered microstrip line. Once these conductive warp threads are woven in the auxiliary layer, a cutting process automatically cuts and removes this layer, leading to loose weft threads in the top layer. To avoid this problem, a warp pattern composed of dielectric threads (binders) connect all the layers achieving a compact structure. The aforementioned process is summarised in Figure 3.24.

With the aim of achieving the tapered structure for the TIW to microstrip transitions, the conductive warp threads of the top layer must be interrupted. Although this prototype has been manufactured using a LPKF ProtoLaser S prototyping machine to structure the top layer of the woven structure and removing the leftover material, the fabrication process can be improved by using an auxiliary layer of weft threads as follows.

Figure 3.24a and Figure 3.24d depict the auxiliary layer corresponding to two different positions in the X–axis of the taper, respectively, as indicated in Figure 3.24g. Likewise, Figure 3.24b and Figure 3.24e represent the loose threads after the cutting process for the two different positions of the taper. Figure 3.24c and Figure 3.24f depicts the dielectric binders required to connect the three layers achieving a compact woven structure. Consequently, the taper becomes a stepped structure as depicted in Figure 3.24g.

Once the auxiliary layer is removed, the prototype manufacturing is finished. Figure 3.25 represents the top view of the manufactured TIW and magnification where a row of vias can be identified. Figure 3.26 depicts a side view of the proposed TIW and a magnification. The width of the woven structure, H_{SIW}

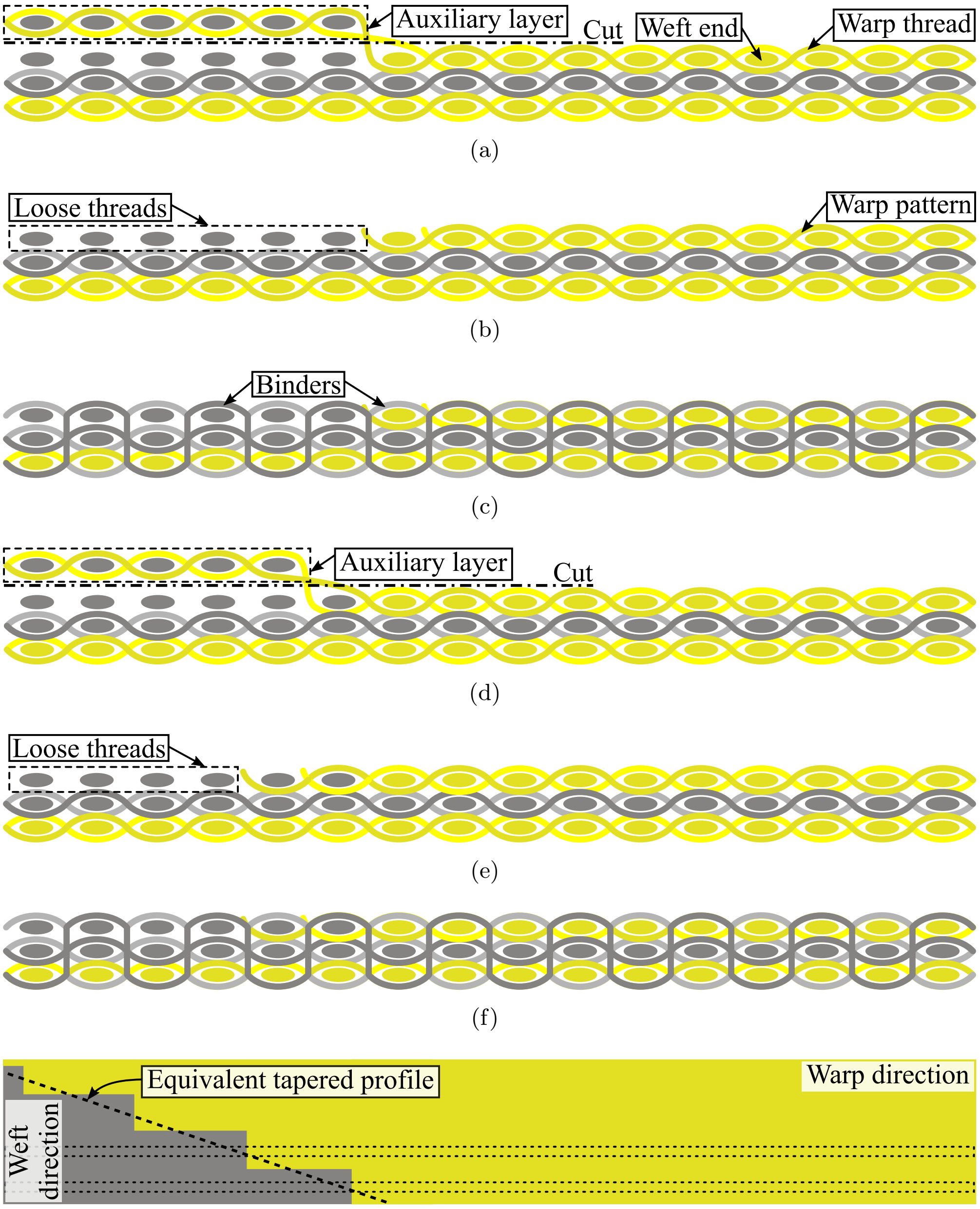

(a) (b) (c) (d) (e) (f) (g)

Figure 3.24: Schematic drawing of the woven structure. (a) Side view with the auxiliary layer. (b) Loose threads, after cutting. (c) Binders to avoid the loose threads. (d) Side view with the auxiliary layer (different part). (e) Loose threads, after cutting in (d). (f) Binders to avoid the loose threads in (e). (g) Top view equivalence and details of the tapered profile and the two different parts of the taper.

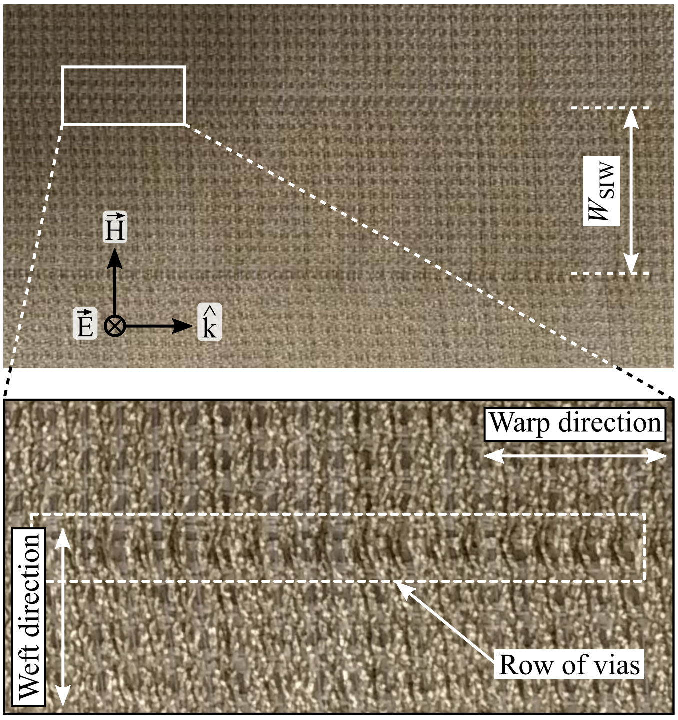

Figure 3.25: Top view of the manufactured TIW prototype and magnification.

can be identified, as well as the separation between two consecutive dielectric weft threads, therefore, the separation between two adjacent conductive vias, S. Figure 3.27 represents the top view of the complete TIW, including the transitions to microstrip lines.

Once the woven prototypes has been manufactured and, with the aim of performing its experimental validation, two subminiature version A (SMA) connectors must be mounted in the structure. Both connectors have been glued to the prototype using conductive epoxy.

3.2.9 Experimental validation

The prototype has been validated using the experimental set-up presented in Figure 3.28. The two ports of the TIW section are connected to an Agilent N5247A PNA-X vector network analyser. Figure 3.29a represents a comparison between the simulated and measured insertion losses of the TIW for three different values of L_{SIW}, 10, 15 and 20 cm, respectively. For the simulations, the data associated to the LM has been considered. Figure 3.29b depicts a comparison

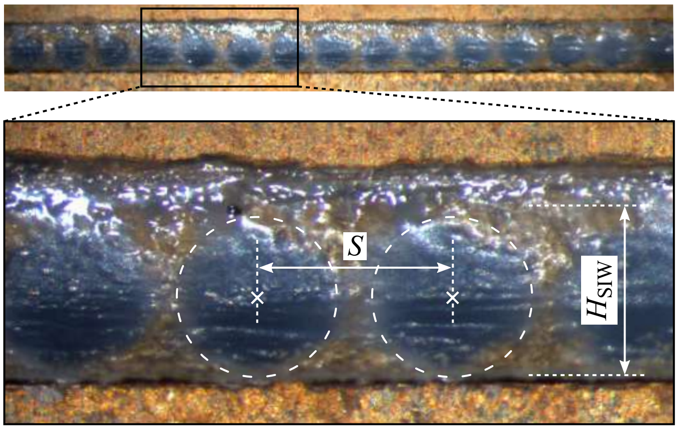

Figure 3.26: Side view of the manufactured TIW prototype and magnification.

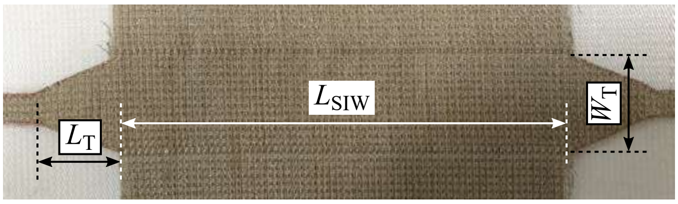

Figure 3.27: Top view of the manufactured back to back microstrip to TIW transition.

between the simulated and measured return losses of the TIW.

As predicted by the simulations, the prototype presents a minimum insertion loss of 0.35 dB/cm, although it also presents a maximum insertion loss of 0.7 dB/cm, due to the ohmic losses of the conductive materials and the intrinsic radiative losses of the microstrip line. As it has been previously explained in section 3.1.9, regarding the millimetre-wave TIW using rigid warp threads, the insertion loss may be reduced using threads with higher conductivity. The use of coated threads may also lead to the deterioration of the conductive coating, due to the wear out, consequently decreasing the thickness of the coating. For this reason, monofilament silver threads are proposed to achieve a higher conductivity while avoiding the uncoating problem due to the wear out.

The agreement between simulated data and measurements demonstrates the validity of the TIW as a fully woven guiding structure. However, the differences between the simulated data and the measured results may be due to manufacturing errors as well as the difficulty of fixing the connector in the textile structure.

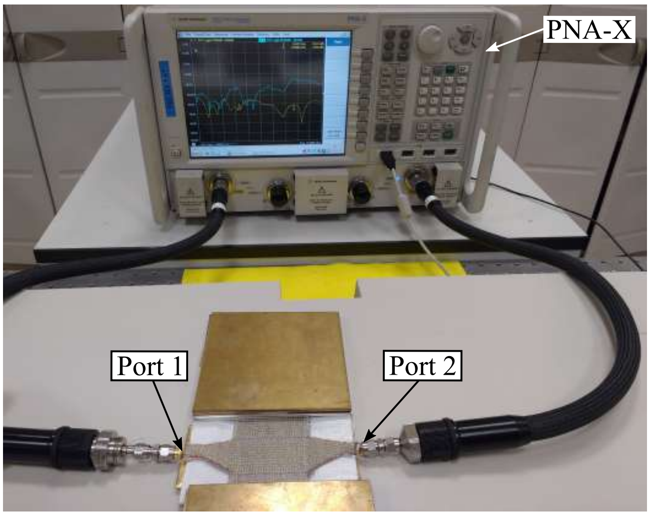

Figure 3.28: Set-up for the experimental validation of the TIW.

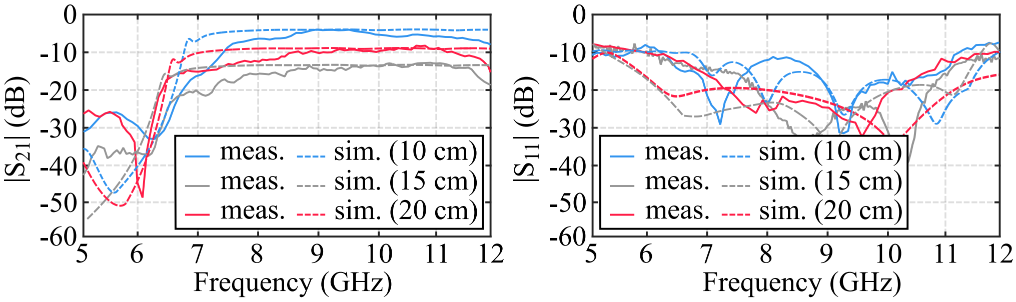

(a)

(b)

Figure 3.29: Simulated and measured scattering parameters. (a) $|S_{21}|$. (b) $|S_{11}|$.

3.2.10 Conclusions

A novel technique to develop microwave TIW using rigid weft threads has been presented. The general procedure based on the three-step parametric modelling to simulate woven structures presented in section 2.1 has been particularised to monofilaments, leading to a simplified two-step modelling. This two-step modelling has been applied to the design of the TIW. With the aim of achieving a complete integration of the prototype in textile for its experimental validation, a pair of tapered TIW to microstrip transitions have been designed and manufactured using an extra layer of textile materials.

To validate the design, three prototypes with different lengths have been experimentally characterised. The theoretically predicted behaviour of the textile structure has been experimentally verified. However, in order to reduce the insertion losses, it is proposed to use conductive threads with a lower resistance, such as silver monofilaments.

3.3 Bandpass arbitrarily height-modulated textile integrated waveguide filter

3.3.1 Introduction

With the aim of demonstrating the validity of the modelling already presented in section 2.2, a bandpass arbitrarily height-modulated textile integrated waveguide filter is presented in this section. Due to the fact that the modelling technique is based on the discrete modulation of the height of a SIW structure, the fabrication of a filter using the conventional procedures would be very complicated. In other words, a height-modulated SIW filter could be manufactured by the use of a previously modified substrate layer –using a milling machine to modulate its height– and subsequently providing the substrate with the conductive vias and the required electrical conductivity through the deposition of a thin gold layer using a sputtering process.

Alternatively, the height-modulated SIW filter could be also manufactured using various stacked layers of substrate segments to achieve the different heights, avoiding the use of a milling machine. In order to connect the different layers, a gluing procedure could be employed, although the alignment of the different segments which compose the multilayered substrate and corresponding vias represents a difficulty.

In this section, a fully textile integrated filter is presented, with the aim of demonstrating the diverse possibilities achievable with the woven technology. For this purpose, the modification of the number of layers of weft threads along a woven structure is employed, in order to achieve the different heights and, therefore, the required height-modulation.

3.3.2 Structure of the filter and corresponding blocks

A bandpass arbitrarily height-modulated textile integrated waveguide filter, denoted by BPAHMTIW filter, whose passband belongs to the range of frequencies between 8 and 9 GHz, is proposed. The filter has been designed using the procedure thoroughly explained in section 2.2 and, for this purpose, the filter is composed of 61 blocks.

The blocks employed for the development of the BPAMHTIW filter are four and are based on a SIW structure whose separation between the inner the rows of vias is W_{TIW}. Moreover, three rows of vias have been employed in each side of the SIW structure, and these rows are separated a distance S from each other. The distance between two consecutive vias is also denoted by S. The conductive vias have been modelled by cylinders whose diameter is given by D. The total width of the SIW structure is W and the thickness of the conductive layers has been denoted by T.

In order to discretely modulate the height of the SIW, two different values for the height are defined, H_1 and H_2, respectively. The four different blocks are depicted in Figure 3.30, whereas the aforementioned dimensions are summarised in Table 3.10.

3.3.3 Simulation of the blocks

The blocks which will conform the BPAMHTIW filter have been simulated using HFSS obtaining the corresponding Touchstone S2P files. For this purpose, a substrate has been previously defined in the simulation environment, using the dielectric parameters obtained from a manufactured woven sample with the same structure.

These parameters, which correspond to the LM of the woven structure, have been measured using an Agilent Technologies 85072A Split Cylinder Resonator and have been found to be the relative permittivity $\varepsilon_{\text{eq}} = 1.7$ and the loss tangent $\tan(\delta)_{\text{eq}} = 0.00362$. Alternatively, an equivalent electrical conductivity of $\sigma_{\text{eq}} = 5 \cdot 10^5$ S/m has been employed for the simulations.

Figure 3.31 depicts the $|S_{11}|$ parameters, and detailed magnifications, corresponding to different lengths of the H_{1_Block} block. Figure 3.32 represents the corresponding $|S_{21}|$ parameters associated to the same lengths, for the H_{1_Block} blocks. Analogously, Figure 3.33 and Figure 3.34 represent the beforementioned data, but associated to the H_{2_Block} blocks.

Table 3.10: Dimensions of the SIW structure of the blocks.

Dimension	W_{TIW}	S	D	W	T	H_1	H_2
Value (mm)	20	0.5	0.25	40	0.25	1	2

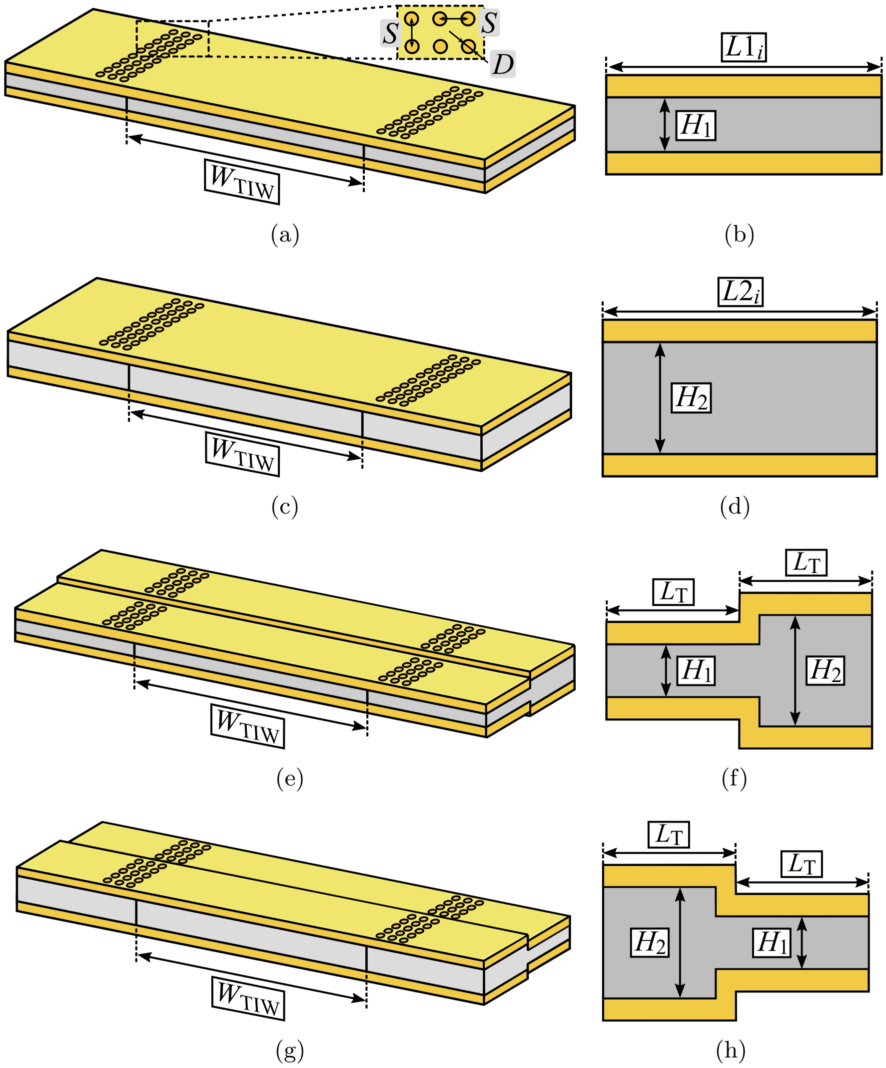

(a) (b) (c) (d) (e) (f) (g) (h)

Figure 3.30: Different blocks involved in the filter design. (a) Overview of the H_{1_Block} block. (b) Side view of the H_{1_Block} block. (c) Overview of the H_{2_Block} block. (d) Side view of the H_{2_Block} block. (e) Overview of the $H_{1\_2\_\mathrm{Block}}$ block. (f) Side view of the $H_{1\_2\_\mathrm{Block}}$ block. (g) Overview of the $H_{2\_1\_\mathrm{Block}}$ block. (h) Side view of the $H_{2\_1\_\mathrm{Block}}$ block.

Although the H_{1_Block} and H_{2_Block} blocks have been simulated using lengths from 0.5 mm to 15 mm with a step length of 0.5 mm, in the graphics only half of the simulations have been included for simplifications. The transition blocks have also been simulated as depicted in Figure 3.35.

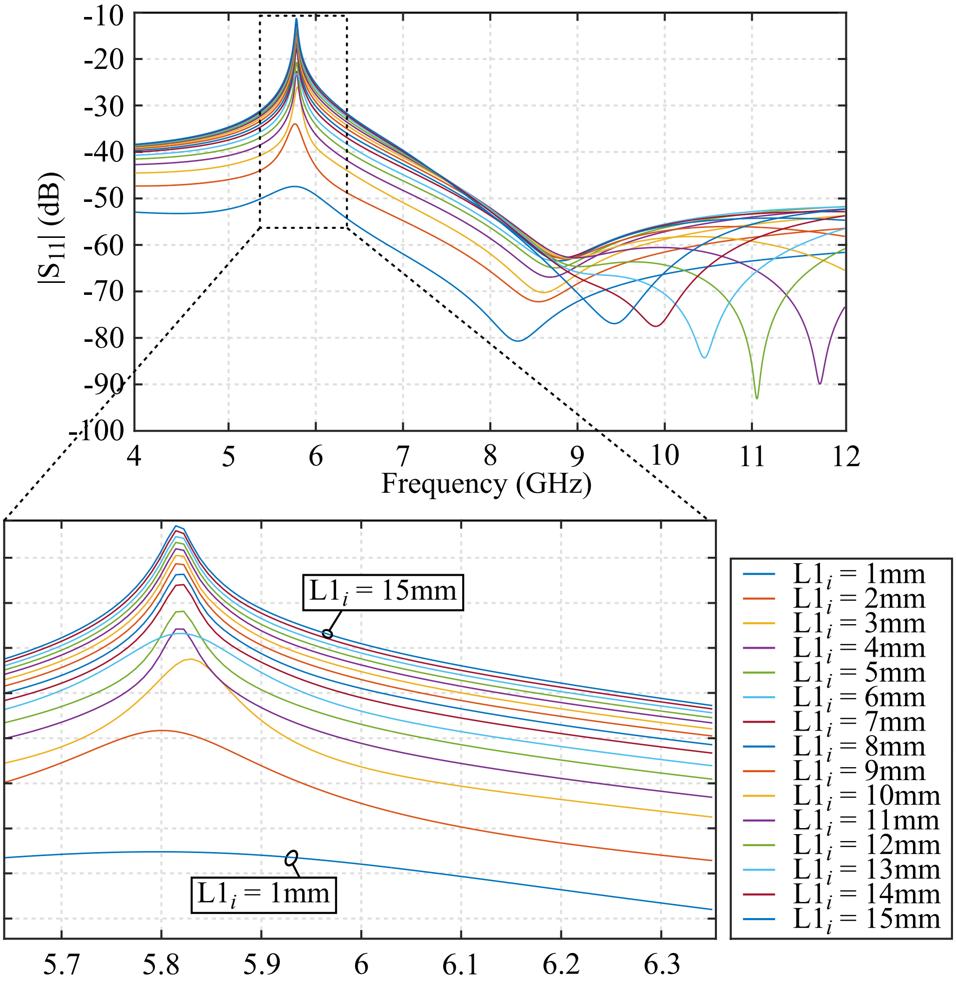

Figure 3.31: Simulated $|S_{11}|$ parameter corresponding to the H_{1_Block} block, for different lengths, and detailed magnification.

3.3.4 Design and implementation of the filter

Once the different blocks have been simulated and the Touchstone S2P files are obtained, the three MDIF files are generated as previously explained in Figure 2.25. These MDIF files are, respectively, the *f_h1.mdf*, *f_h12.mdf* and *f_h2.mdf* files. The *f_h1.mdf* file contains the data corresponding to the scattering parameters of the different H_{1_Block} blocks, depending on the length of the structure. Analogously, *f_h1.mdf* file contains the same information although corresponding to the H_{2_Block} blocks. The *f_h12.mdf* file only contains the scattering parameters corresponding to the $H_{1\_2\_\text{Block}}$ and $H_{2\_1\_\text{Block}}$ blocks.

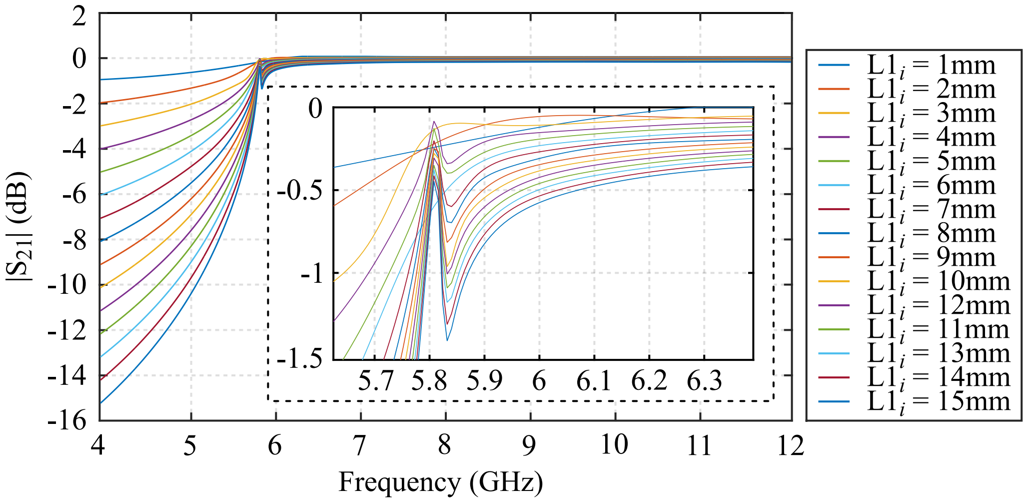

Figure 3.32: Simulated $|S_{21}|$ parameter corresponding to the H_{1_Block} block, for different lengths, and detailed magnification.

The schematic model in ADS can be implemented once the MDIF files have been generated. For this purpose, a model similar to the one previously presented in Figure 2.26a has been implemented as shown in Figure 3.36a. Figure 3.36b and Figure 3.36d depict, respectively, a generic blue colored block and a generic green colored block, which are provided with the optimal values for their parameters. These optimal values are related to the length of the corresponding segments in the SIW structure: each optimal value corresponds to half the length of the segment in millimetres.

Alternatively, Figure 3.36c and Figure 3.36e represent, respectively, a generic red colored block and a generic yellow colored block, which represent the transition blocks. These two blocks do not require a parameter to be optimised because their parameters are predefined, respectively, to 1 or 2, indicating whether the scattering parameters associated to these blocks are written in the first or second half of the *f_h12.mdf* file.

3.3.5 Optimisation of the filter

The optimisation has been configured using a solver which implements a method based on the gradient function. The goal of the optimisation has been defined in order to obtain a frequency response with the following requirements: a passband in a frequency range between 8 and 9 GHz and a $|\mathrm{S}_{21}| < -25$ dB for the frequencies below and above the passband.

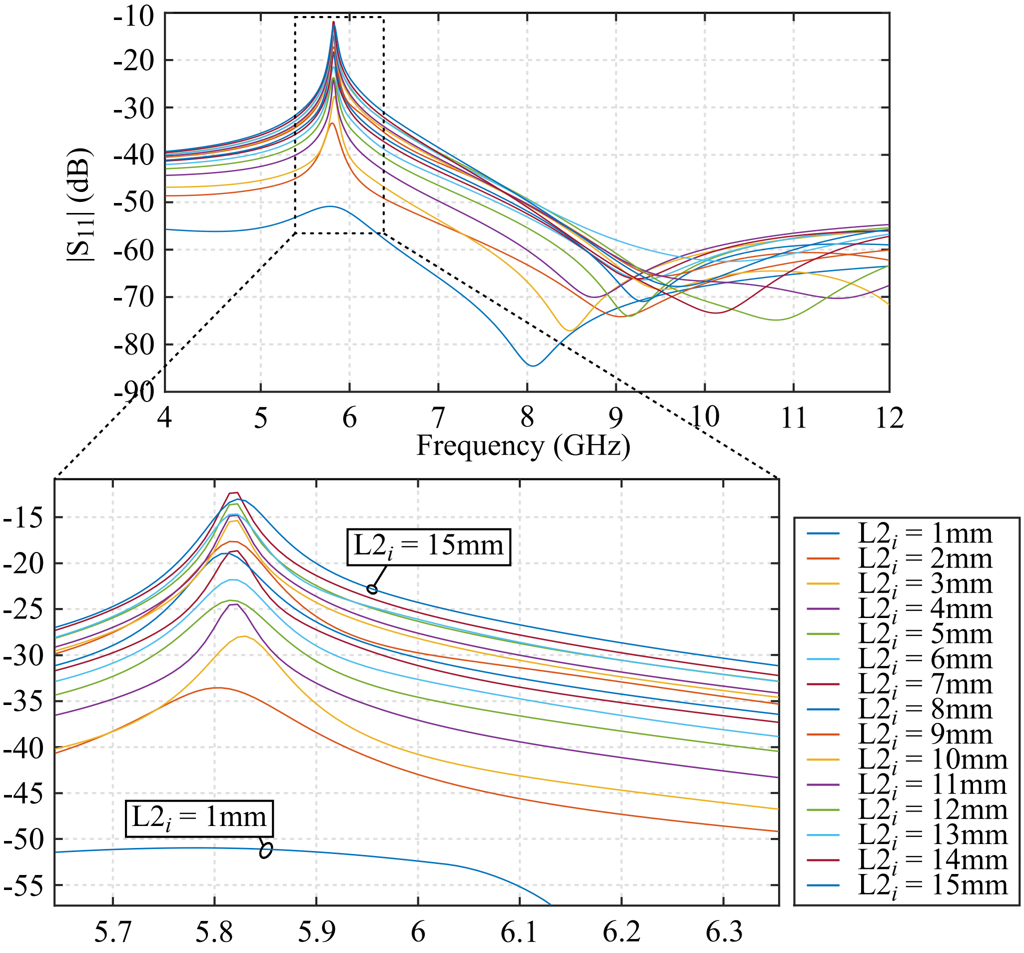

Figure 3.33: Simulated $|S_{11}|$ parameter corresponding to the H_{2_Block} block, for different lengths, and detailed magnification.

Once the optimisation has converged, the resulting variables v1_i and v2_i does not present integer values due to the interpolation between non previously calculated scattering parameters. Due to the fact that the variables v1_i and v2_i are related to the lengths of the segments of the SIW structure which will be translated into a woven prototype, integer values are required. For this purpose, the optimal values of the variables v1_i and v2_i have been truncated.

A tuning process has not been required due to the results fulfilled the requirements after truncating the variables. Table 3.11 summarises the truncated optimal values for the variables v1_i and v2_i.

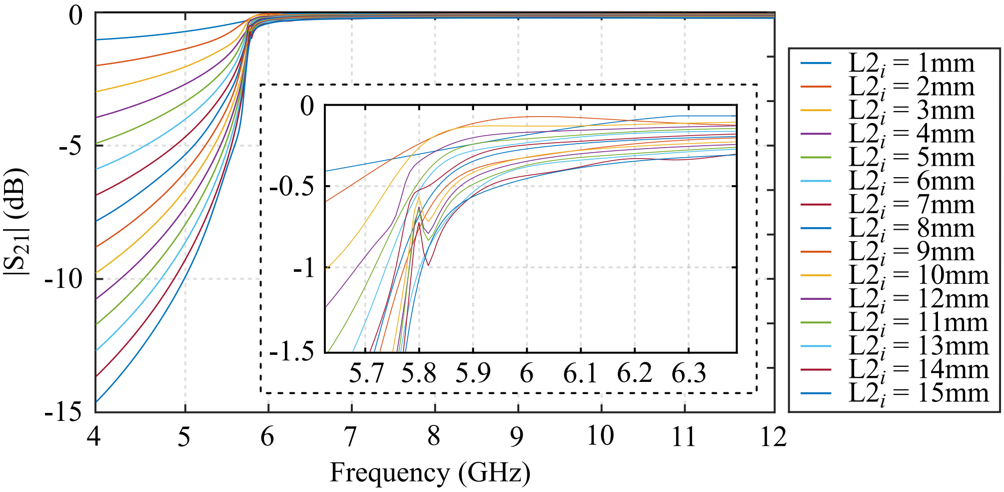

Figure 3.34: Simulated $|S_{21}|$ parameter corresponding to the H_{2_Block} block, for different lengths, and detailed magnification.

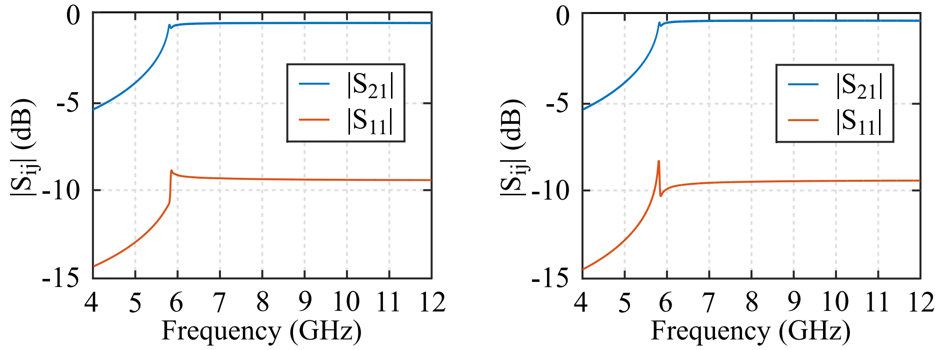

(a)

(b)

Figure 3.35: Simulated $|S_{\text{ij}}|$ parameters corresponding to the transition blocks. (a) $H_{1\_2\_\text{Block}}$. (b) $H_{2\_1\_\text{Block}}$.

Table 3.11: Truncated optimal values for the BPAHMTIW filter.

v1_i

i	1	2	3	4	5	6	7	8	9	10	11	12	13	14
Value	1	1	1	1	2	1	20	20	20	20	20	20	20	20

v2_i

i	1	2	3	4	5	6	7	8	9	10	11	12	13	14	15
Value	1	1	4	4	1	1	19	15	19	16	19	19	18	19	19

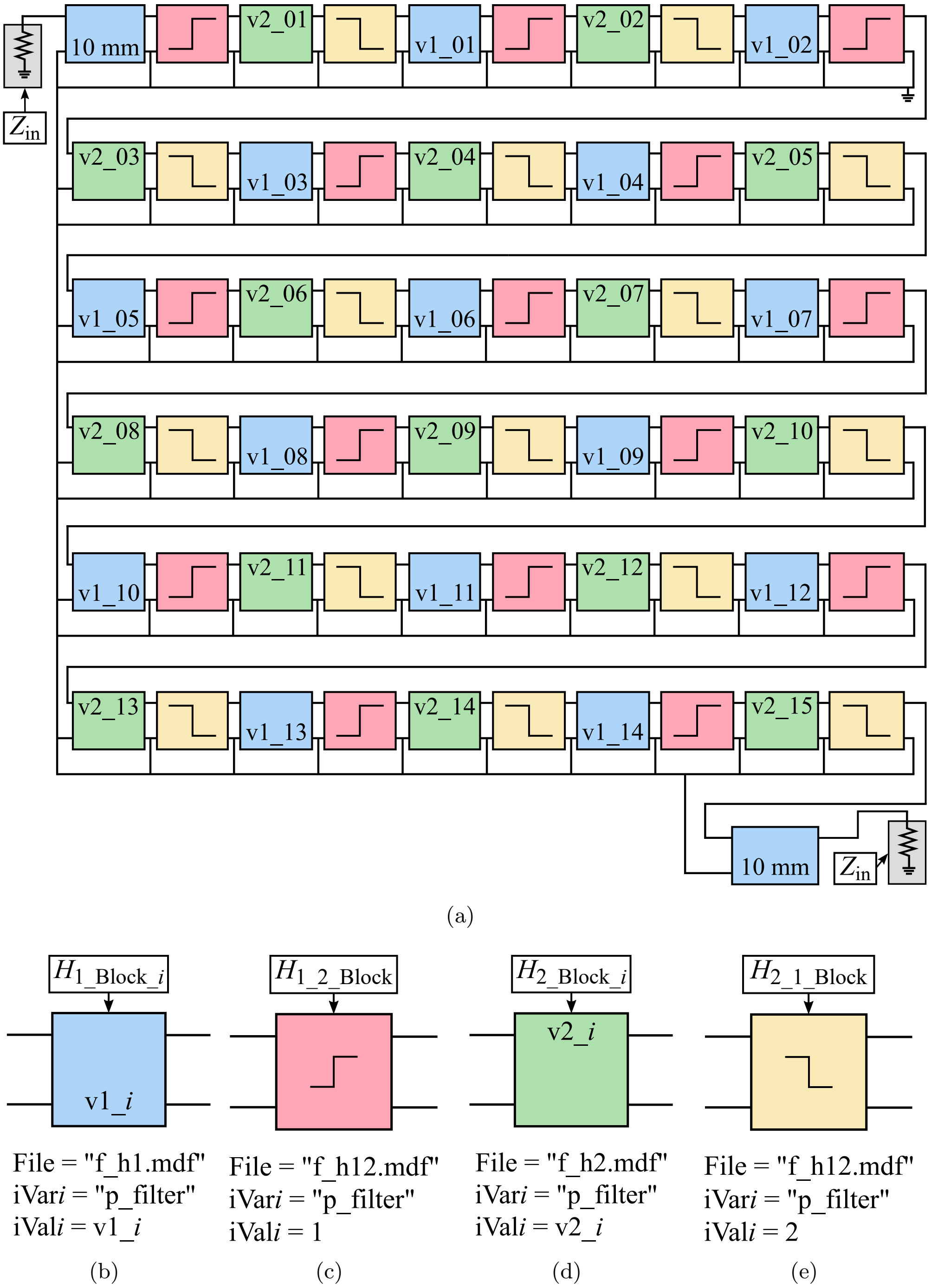

Figure 3.36: Schematic model of the BPAHMTIW filter optimisation using ADS. (a) Schematic model outline. (b) Generic H_{1_Block} block. (c) Generic $H_{1\_2\_\text{Block}}$ block. (d) Generic H_{2_Block} block. (e) Generic $H_{2\_1\_\text{Block}}$ block.

Table 3.12: Lengths of the different segments of the BPAHMTIW filter.

Length (mm) of the i-th segment whose height is H_1											
i		1	2	3	4	5	6	7	8	9	10
Length		5.5	5.5	5.5	5.5	6	5.5	15	15	15	15
i	11	12	13	14							
Length	15	15	15	15							
Length (mm) of the i-th segment whose height is H_2											
i	1	2	3	4	5	6	7	8	9	10	11
Length	5.5	5.5	7	7	5.5	5.5	14.5	12.5	14.5	13	14.5
i	12	13	14	15							
Length	14.5	14	14.5	14.5							

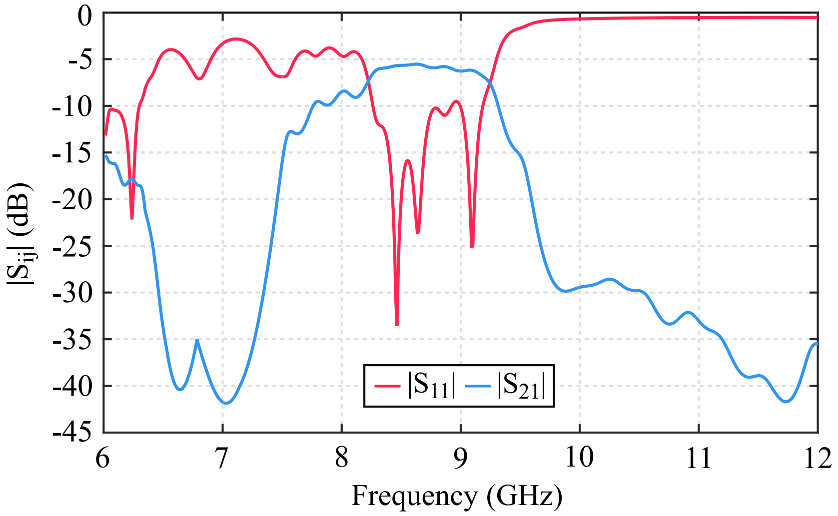

Figure 3.37: Simulated S–parameters of the optimised BPAHMTIW filter.

As previously mentioned, in order to translate the values summarised in Table 3.11 into the lengths of the different blocks which conform the filter (in millimetres), multiplying by two the optimal values is required. Once the physical lengths of the blocks are calculated, a simplified notation to define the filter can be employed, which corresponds to the one already used in Figure 2.22. In this figure, instead of using the lengths of the H_{1_Block} and H_{2_Block} blocks, the lengths of the segments corresponding to the different heights, H_1 and H_2, are employed. For this purpose, the parameter L_T, previously defined, is required.

As a result, the lengths of the segments whose heights are H_1 = 1 mm and H_2 = 2 mm, respectively, are summarised in Table 3.12. Consequently, taking into account the first and last blocks in Figure 3.36, whose lengths have been fixed to 10 mm, and the values shown in Table 3.12, the BPAHMTIW is completely characterised.

The resulting filter, whose total length is L_{total} = 341 mm, presents the frequency response depicted in Figure 3.37. A $|\mathrm{S}_{21}|$ = −6 dB is achieved in the passband of the filter due to its length.

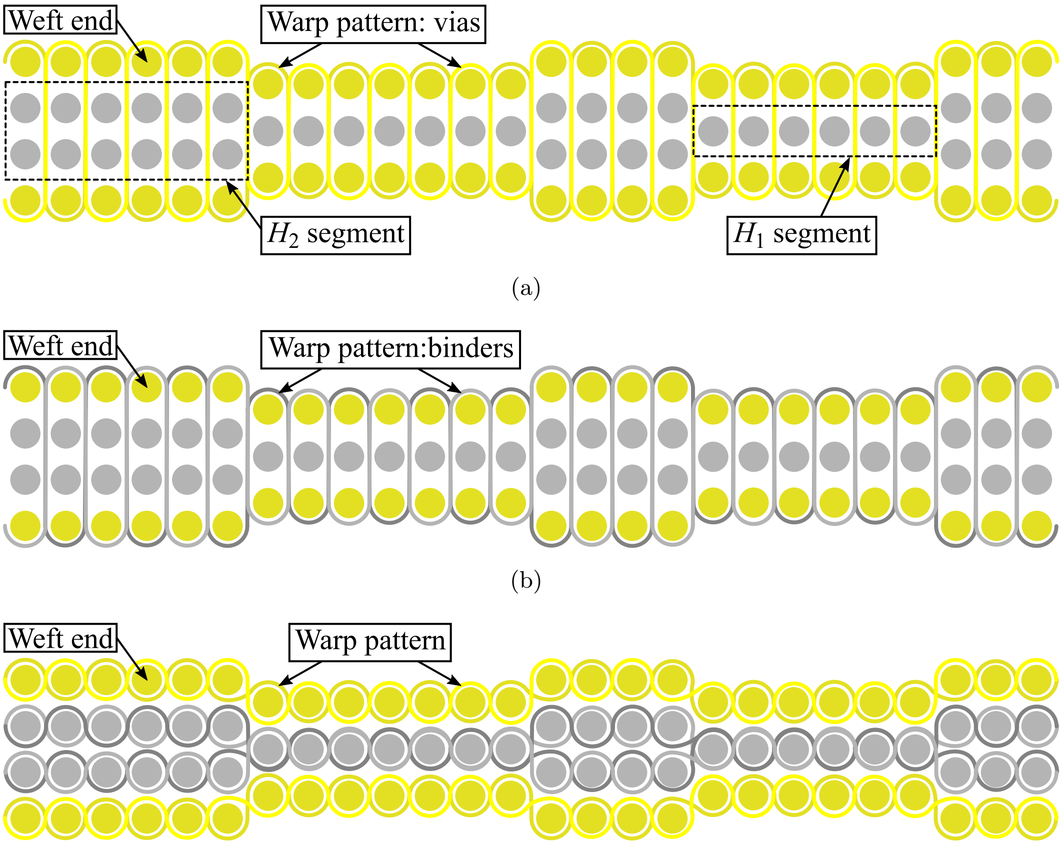

(a)

(b)

(c)

Figure 3.38: Translation into a woven prototype. (a) Proposed warp patterns for the conductive vias. (b) Proposed warp patterns for the dielectric binders. (c) Proposed general warp patterns for the TIW structure.

3.3.6 Translation into a woven prototype

Once the filter has been designed, it has to be translated into a woven prototype. For this purpose, Figure 3.38 depicts the different woven patterns required to manufacture it. Figure 3.38a represents the side view of the weft threads, in other words, the weft ends. Moreover, this figure depicts the warp patterns which emulate the conductive vias of the structure, connecting the top and bottom layers of the TIW structure through the dielectric layers.

The segments with different heights, H_1 and H_2, can also be seen in Figure 3.38a. Alternatively, Figure 3.38b represents the warp patterns corresponding to the dielectric binders. The binders are required in order to achieve a compact structure connected not only from the conductive vias. Figure 3.38c depicts the general warp patterns required to implement the different layers of the TIW structure: the conductive plates and the dielectric layers.

3.3.7 Conclusion

A bandpass AHMTIW filter has been proposed in this section in order to validate the modelling technique already presented in section 2.2. Different segments of a SIW structure have been electromagnetically simulated in order to generate the S2P Touchtone files with the scattering parameters. The S2P Touchtone files have been subsequently combined in three different MDIF files.

The bandpass AHMTIW filter has been composed of 61 different blocks: 31 blocks have been predefined, whereas 29 blocks have been optimised in order to obtain the desired frequency response. As a result, the simulated scattering parameters fulfil the requirements.

3.4 Bandstop arbitrarily height-modulated textile integrated waveguide filter

3.4.1 Introduction

In order to demonstrate the validity of the modelling previously explained in section 2.2 not only for bandpass filters, but also for bandstop filters, the methodology has been applied for the design and optimisation of a bandstop filter. Nevertheless, with the aim of reducing the value of the $|S_{21}|$ parameter in the passband, the number of blocks to optimise has been reduce from 61 to 37.

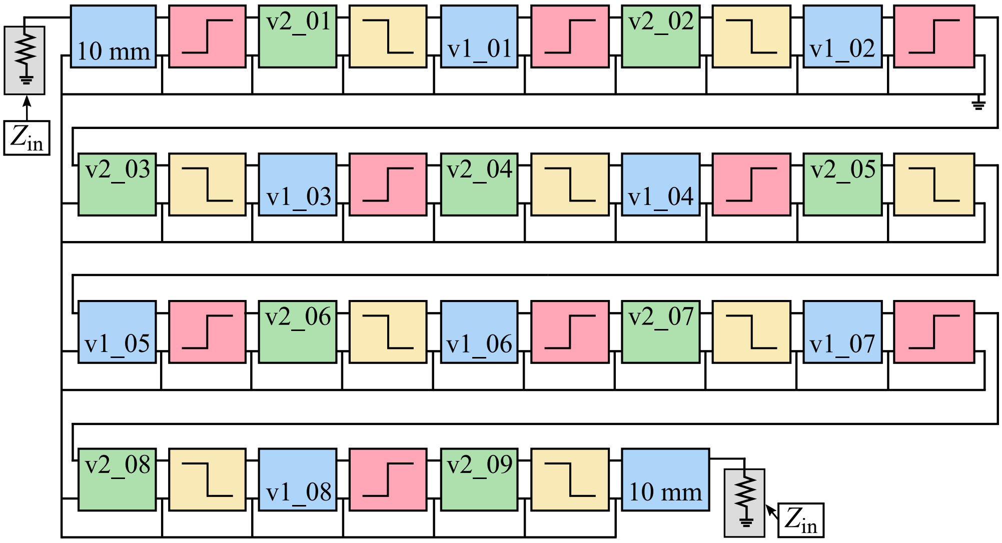

Figure 3.39: Schematic model of the BSAHMTIW filter optimisation using ADS.

3.4.2 Structure of the filter and corresponding blocks

A bandstop arbitrarily height-modulated textile integrated waveguide filter, denoted by BSAHMTIW filter, whose stopband belongs to the range of frequencies between 7.5 and 9 GHz, is proposed. The filter has been designed using the methodology already explained in section 2.2 and, for this purpose, the filter is composed of 37 blocks. The blocks employed for the development of the BSAMHTIW filter are the ones already thoroughly explained for the BPAMHTIW in section 3.3.

3.4.3 Design and implementation of the filter

As the blocks employed for the design of the BSAMHTIW filter are the same already employed for the BPAMHTIW filter, the MDIF files have not been modified. For this reason, the new schematic model in ADS is similar to the one previously presented for the bandpass filter. This new schematic model is composed of the 37 blocks shown in Figure 3.39.

3.4.4 Optimisation of the filter

The optimisation has been configured using the same solver which implements a method based on the gradient function. The goal of the optimisation has been

Table 3.13: Truncated optimal values for the BSAHMTIW filter.

v1_i									
i		1	2	3	4	5	6	7	8
Value		10	10	10	10	10	10	10	10
v2_i									
i	1	2	3	4	5	6	7	8	9
Value	10	10	10	10	10	10	10	10	10

Table 3.14: Lengths of the different segments of the BSAHMTIW filter.

Length (mm) of the i-th segment whose height is H_1										
i		1	2	3	4	5	6	7	8	9
Length		10	10	10	10	10	10	10	10	10
Length (mm) of the i-th segment whose height is H_2										
i	1	2	3	4	5	6	7	8	9	10
Length	10	10	10	10	10	10	10	10	10	10

defined in order to obtain a frequency response with the following requirements: a stopband in a frequency range between 7.5 and 9 GHz and a $|S_{21}| > -6$ dB for the frequencies below and above the stopband.

Once the optimisation has converged, the resulting variables v1_i and v2_i does not present the desired integer values. For this purpose, the optimal values of the variables v1_i and v2_i have been truncated and the tuning process has not been required due to the results fulfilled the requirements after truncating the variables. Table 3.13 summarises the truncated optimal values for the variables v1_i and v2_i.

As previously mentioned, in order to translate the values summarised in Table 3.13 into the lengths of the different blocks which conform the filter (in millimetres), multiplying by two the optimal values is required. Once the physical lengths of the blocks are calculated and taking into account the previously defined value of the L_T parameter, the lengths of the segments whose heights are $H_1 = 1$ mm and $H_2 = 2$ mm, respectively, can be calculated as summarised in Table 3.14.

Taking into account the first and last blocks in Figure 3.39, whose lengths have been fixed to 10 mm, and the values shown in Table 3.14, the BSAHMTIW is

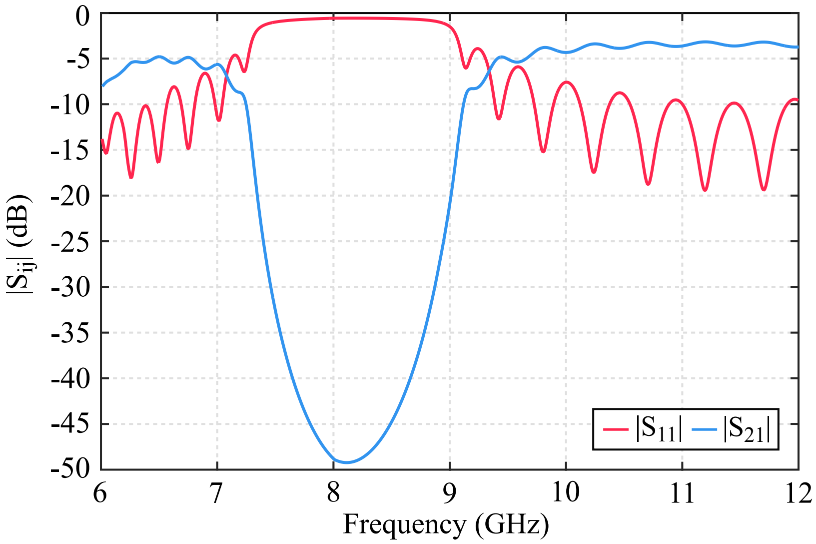

Figure 3.40: Simulated scattering parameters of the optimised BSAHMTIW filter.

completely characterised. The resulting filter, whose total length is $L_{\text{total}} = 204$ mm, presents the frequency response depicted in Figure 3.40.

3.4.5 Translation into a woven prototype

As the BSAHMTIW filter presents the same topology as the BPAHMTIW filter already explained in the previous section, the translation into a woven prototype is completely analogous. One or two layers of dielectric threads are required in order to generate the height modulation and two layers of conductive weft threads are employed to achieve the conductive plates of the SIW structure.

Moreover, conductive warp threads are employed in order to connect the weft threads which individually compose the top and bottom conductive layers, and to implement the conductive vias. Dielectric warp threads are required to create a compact height-modulated dielectric layer and the binders.

3.4.6 Conclusion

The modelling technique previously explained in section 2.2 has been applied to create a bandstop AHMTIW filter. The number of blocks employed in the design of the filter has been reduced in comparison to the filter already proposed in the previous section. As a consequence, the time required in the optimisation has been notably decreased.

The simualted frequency response of the BSAHMTIW filter fulfils the desired requirements and, therefore, it has been demonstrated the validity of the modelling in the development of bandstop filters.

Bibliography

[1] R. Moro *et al.*, "Textile microwave components in substrate integrated waveguide technology," *IEEE Trans. Microw. Theory and Techn.*, vol. 63, no. 2, pp. 422-432, Feb. 2015. (Cited on page 53)

[2] M. Bozzi *et al.*, "Innovative SIW components on paper, textile, and 3D-printed substrates for the Internet of Things," presented in *Asia-Pacific Microw. Conf. (APMC)*, Nanjing, China, Dec. 6-9, 2015. (Cited on page 53)

[3] R. Moro *et al.*, "Compact cavity-backed antenna on textile in substrate integrated waveguide (SIW) technology," 2013 European Microwave Conference, Nuremberg, 2013, pp. 1007-1010. (Cited on page 53)

[4] R. Moro *et al.*, "Circularly-polarised cavity-backed wearable antenna in SIW technology," *IET Microw. Antennas Propag.*, vol. 12, no. 1, pp. 127-131, Oct. 2018. (Cited on page 53)

[5] Y. Hong, J. Tak and J. Choi, "An all-textile SIW cavity-backed circular ring-slot antenna for WBAN applications," *IEEE Antennas Wireless Propag. Lett.*, vol. 15, pp. 1995-1999, 2016. (Cited on page 53)

[6] S. Yan, P. J. Soh and G. A. E. Vandenbosch, "Dual-band textile MIMO antenna based on substrate-integrated waveguide (SIW) technology," *IEEE Trans. Antennas Propag.*, vol. 63, no. 11, pp. 4640-4647, Nov. 2015. (Cited on page 53)

[7] S. Yoon and J. Choi, "H-plane SIW horn antenna made of textile for millimeter-wave WBAN application," presented in *Int. Symp. on Antennas and Propag. (ISAP)*, Phuket, Thailand, Oct. 30 - Nov. 2, 2017. (Cited on page 53)

[8] S. Lee and J. Choi, "An all textile H-plane SIW horn antenna with metamaterial absorber for millimeter-wave WBAN applications," presented in *IEEE*

Int. Symp. on Antennas and Propag. & USNC/URSI National Radio Science Meeting, San Diego, CA, July 9-14, 2017. (Cited on page 53)

[9] T. Castel *et al.*, "Capacity of broadband body-to-body channels between firefighters wearing textile SIW antennas," *IEEE Trans. Antennas Propag.*, vol. 64, no. 5, pp. 1918-1931, May 2016. (Cited on page 53)

[10] L. Alonso-González *et al.*, "On the techniques to develop millimeter-wave textile integrated waveguides using rigid warp threads," *IEEE Trans. Microw. Theory and Techn.*, vol. 66, no. 2, pp. 751-761, Feb. 2018. (Cited on page 53)

[11] MakeItFrom.com database, "PET vs. PES". [Online]. Available: www.makeitfrom.com/compare/Polyethylene-Terephthalate-PET-PETE/Polyethersulfone-PES. (Cited on page 58)

[12] Plastics international, "PES (Polyethersulfone)", Plastics international datasheet. [Online]. Available: www.plasticsintl.com/datasheets/Radel_A_PES.pdf. (Cited on page 58)

[13] PHT Plastiques Hautes Technologies, "Range polyethersulfone - PES", PHT Manufacturer of semicompressed platic products. [Online]. Available: www.pht-plastic.com/choice-of-materials/pes-polyethersulfone-1/. (Cited on page 58)

[14] G. Wypych, *Handbook of fillers (4th edition)*, in ChemTech Publishing, Toronto, Canada, 2016, pp. 264-265. (Cited on page 58)

[15] L. Chao *et al.*, "Dielectric permittivity measurements of thin films at microwave and terahertz frequencies", presented in *European Microw. Conf.*, Manchester, UK, Oct. 10–13, 2011. (Cited on pages 58 and 75)

[16] O. Sushko *et al.*, "Comparative study of sub-THz FSS filters fabricated by inkjet printing, microprecision material printing, and photolithography", *IEEE Trans. THz Sci. Technol.*, vol. 7, no. 2, pp. 184-190, Mar., 2017. (Cited on page 58)

[17] S. Khanal *et al.*, "Towards printed millimeter-wave components: material characterization", presented in *Global Symp. on Millimetre-Waves (GSMM)*, Espoo, Finland, June 6–8, 2016. (Cited on page 58)

[18] B. C. Steele, “Electronic ceramics”, *Elsevier Applied Science*, London, UK, USA, 1991, pp. 140. (Cited on pages 58 and 75)

[19] J. L. Cano, A. Mediavilla and A. R. Perez, “Full-band air-filled waveguide-to-substrate integrated waveguide (SIW) direct transition”, *IEEE Antennas Wireless Propag. Lett.*, vol. 25, no. 2, pp. 79-81, Feb. 2015. (Cited on page 61)

[20] L. Alonso-González *et al.*, “Three-dimensional fully interlaced woven microstrip-fed substrate integrated waveguide”, in *Progress In Electromagnetics Research*, [accepted for publication.] (Cited on page 71)

[21] D. M. Pozar, “Microwave Engineering”, *Wiley*, Hoboken, NJ, 2012, pp. 147-152. (Cited on page 81)

4

Fully woven textile integrated tags and antennas

Contents

This chapter includes the description of different fully woven textile integrated tags and antennas which have been developed using different technologies and work in different ranges of frequencies.

4.1 Low frequency tag with near-field RFID chip

4.1.1 Introduction

The ever growing interest in textile integrated devices has recently drawn attention to the areas of wearable identification, information storage and tracking systems. Due to the technological advances and decreased costs, the number of radiofrequency identification (RFID) based applications has dramatically increased, specially in the context of the Internet of Things (IoT). These applications have driven improvements in specific aspects of the technology, such as the range or working distance between reader and tag, or the data management capacity, which are closely linked to the operating frequency.

For instance, RFID technology is widely used nowadays in inventory tracking and item location, due to its advantages in comparison to barcode technology, including unattended reading and increased range, among many others. RFID technology is regulated by different standardisation bodies, although the oldest established is ISO (International Standards Organisation). Several standards have been defined to regulate different aspects of RFID technology. As an example, ISO 18000-V3 defines the radio interface for RFID systems working at 13.56 MHz. In addition, when working at 13.56 MHz, ISO 14443 defines the specifications for the use of RFID proximity cards for identity, security or payment applications, whereas ISO 15693 defines characteristics of the vicinity cards, which can be read from a larger distance than proximity cards. Vicinity cards are normally used in applications such as physical access.

When working at a frequency of 13.56 MHz, as will be the case, an RFID antenna would be enormous. For this reason, low frequency RFID standards have not been developed for their use with antennas, but inductors. The transmission is no longer realised through wave propagation using antennas but through inductive coupling between coils. For this reason, even though the frequency is very low, the read range is dramatically reduced and limited by the inductive coupling between the reader and the tag.

Several technologies have been used to develop both antenna and inductor based RFID tags: from the ultra thin RFID tags embedded in paper, to the ink-jet printed tags in plastic substrates [1–5]. With the aim of integrating the RFID tags into the textile, some solutions have been presented. One of the proposed textile based RFID tags which can be found in the literature is based on an embroidery technique [6–10], although these tags are not as industrially competitive as the conventional ones, due to the difficulty of manufacturing them at a large scale.

Moreover, the embroidery technique is not suitable for multilayered designs, and consequently, the number of possible design alternatives is reduced. For this reason, a woven RFID tag is presented [11]. The proposed tag has been designed to be used in contactless applications, in particular, for stock identification during inventory, data storage and anti-imitation of clothing. Moreover, the prototype has been designed to be totally hidden from touch, then it can not be easily identified in the fabric.

4.1.2 Structure of the tag

The tag is designed to operate according to ISO 15693 standard, for its use at a frequency of 13.56 MHz. The communication at this frequency is realised through inductive coupling between the tag and the interrogator device, as has been previously mentioned. This means that the tag inductance has to be designed to resonate together with the tag chip at 13.56 MHz. For the present design, a

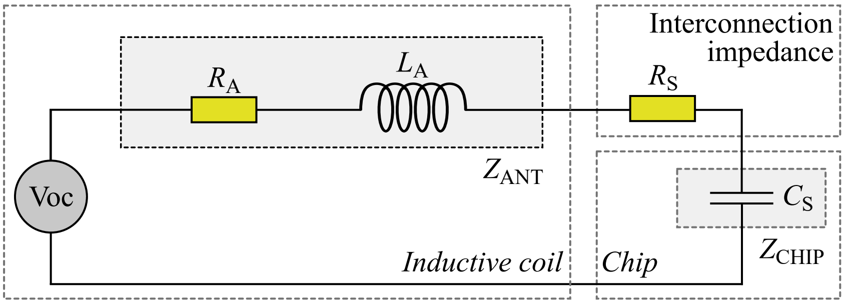

Figure 4.1: Ideal equivalent electrical circuit of the proposed tag.

NXP chip from the ICODE SLIX family has been chosen, presenting an input capacitance of $C_S = 23.5$ pF [12].

Figure 4.1 depicts the ideal equivalent electrical parameters of the proposed tag. On the left hand side of the circuit, the inductive part of the tag, L_A, is presented. On the right hand side of the circuit, the capacitance C_S is included. The ohmic losses of the inductive coil and the interconnection impedance between the coil and the chip are given by R_A and R_S, respectively. The inductive part of the circuit can be achieved using a planar coil as the one depicted in Figure 4.2.

The ideal equivalent circuit is modelled by a series resonant circuit whose input impedance is given by the addition of the real and imaginary impedances previously defined. The resonant, or working, frequency is found at the frequency for which the imaginary part of the input impedance is equal to zero or, equivalently, the phase of the input impedance is equal to zero. At the working frequency, f_o, L_A and C_S must fulfil (4.1).

$$L_A C_S (2\pi f_o)^2 = 1 \tag{4.1}$$

Using the EM simulation software ADS, the equivalent electrical circuit of the proposed tag can be simulated, substituting the conventional inductor by a planar square loop coil model. This ADS library model is defined by the number of turns of the coil, the dimensions of the conductive material cross section, the distance between turns and the dimensions of the biggest turn, as well as the electrical conductivity.

Although an infinite number of combinations of the beforementioned parameters can be used to achieve the desired inductance, not all these combinations

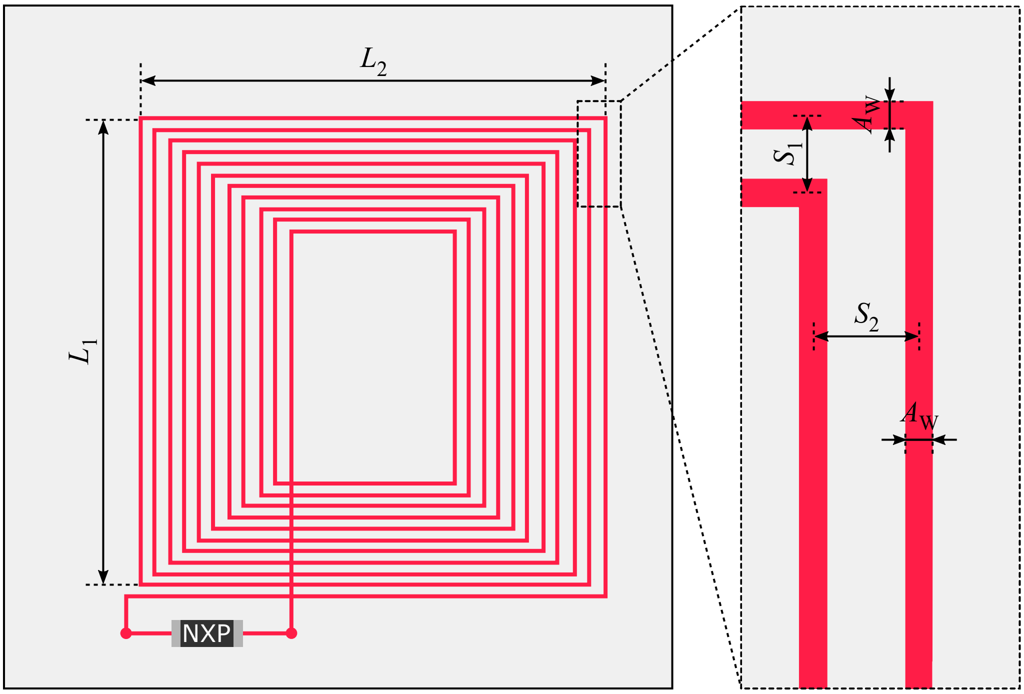

Figure 4.2: Schematic drawing of the proposed RFID tag and magnification.

can then be translated into a woven prototype. For this reason, the dimensions of the threads and the weaving loom limitations are taken into account in the design.

4.1.3 Design of the woven prototype

For the conductive parts of the coil, *Shieldex 117f17 HC+B 1-ply* threads have been used. When these threads are in the woven structure, they present a Pierce's cross section. Consequently, this cross section is an ellipse whose major and minor axes are $A_\mathrm{W} = 0.26$ mm and $A_\mathrm{H} = 0.13$ mm, respectively. Therefore, the width of the conductive strips of the tag is approximated by A_W as depicted in Figure 4.2.

With the aim of avoiding undesired short circuits, due to the existence of small filaments in the multifilament conductive threads, a sufficient separation between them must be adopted. Therefore, a distance of $S_1 = 1.5$ mm between the centres of the conductive threads in one of the directions, and a distance of $S_2 = 2$ mm in the perpendicular direction have been chosen.

When the beforementioned parameters S_1 and S_2 are different, there is not a predefined schematic model in ADS to simulate the behaviour of the planar coil, therefore, ADS Momentum has been employed for the design and simulation. By using 12 turns and being $L_1 = L_2 = 55$ mm, the external dimensions of the coil, the desired working frequency, $f_{\mathrm{o}} = 13.56$ MHz, was achieved.

To translate the square loop of the tag into a textile prototype, a woven structure composed of three layers has been designed. The top layer is composed of dielectric warp and weft threads, except in certain positions where the warp threads have been substituted by conductive *Shieldex* yarns. These positions correspond to twenty-three warp threads divided in two groups of 11 and 12 threads, respectively. The bottom layer is composed of dielectric warp and weft threads, except in certain positions where the weft threads have been substituted by conductive *Shieldex* yarns. These positions correspond to twenty-two weft threads divided in two groups of 11 threads each. The before mentioned top and bottom layers are independent and electrically isolated from each other by an additional dielectric layer which is woven between them, giving rise to a total thickness of the woven structure of $T_{\mathrm{S}} = 0.35$ mm.

The conductive warp and weft yarns in the top and bottom layers must be interconnected at specific locations, in order to configure the desired coil-shaped current path, as shown in Figure 4.3. The interconnections are realised by bringing the desired conductive weft yarn from the bottom layer vertically up, across the intermediate dielectric layer, weaving it around the corresponding warp yarn in the top layer, and taking it back to the bottom layer to continue its normal weaving pattern. This direct contact between conductive threads produces the required electrical connection. As the woven structure is tightened, the electrical connection is guaranteed.

Figure 4.3a depicts the bottom view of the RFID tag, where the dielectric threads have not been represented for simplification. Conductive warp threads corresponding to the top layer are grey colored, whereas the conductive weft threads which correspond to the bottom layer are red colored. The electrical connection between the conductive threads and the connection of the chip are blue and green colored, respectively. Figure 4.3b depicts a magnification where the layers to which each conductive thread belongs is indicated. Figure 4.3c represents a magnification of the chip interconnection.

In addition, conventional multifilament polyester threads have been employed for the dielectric parts of the design. For the warp and weft threads, 0.07 mm and 0.35 mm diameter yarns have been employed, leading to the substrate depicted in

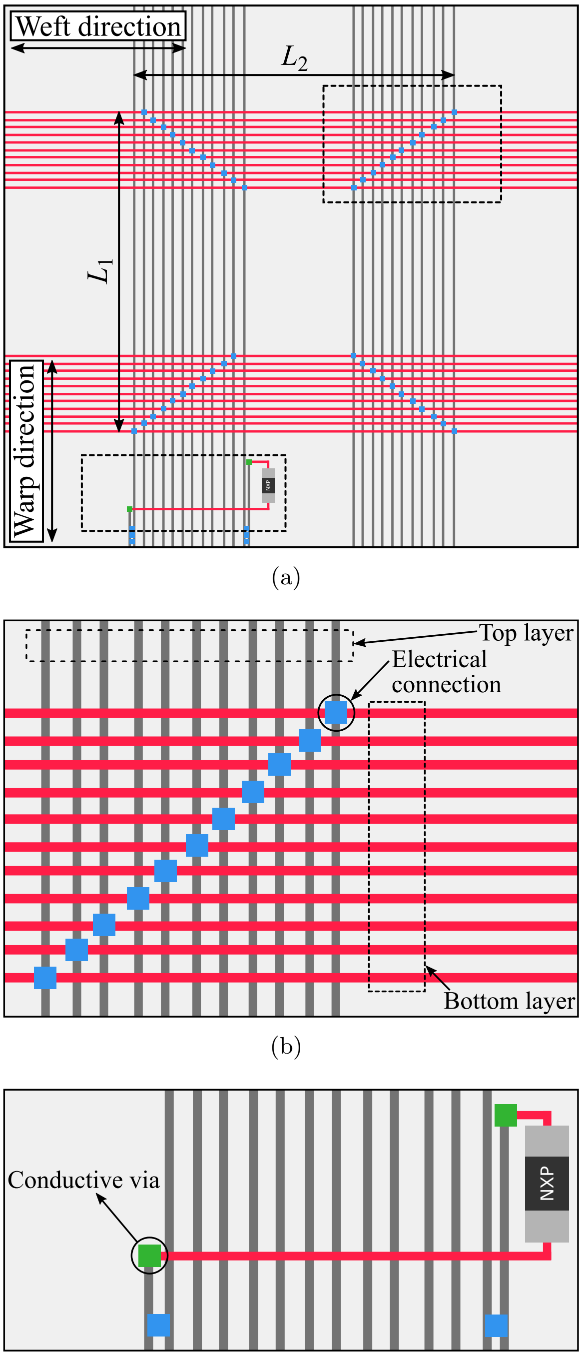

(a)

(b)

(c)

Figure 4.3: Overview of the RFID tag design and magnifications (bottom view). (a) General view of the tag. (b) Magnification of the electrical connections. (c) Magnification of the chip interconnection.

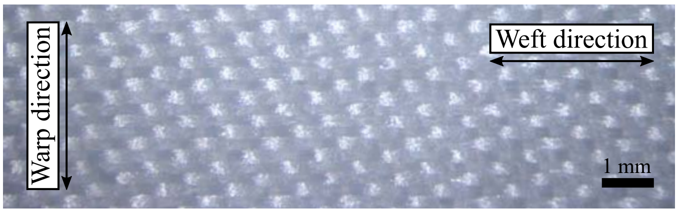

Figure 4.4: Overview of the woven substrate.

Figure 4.4. The substrate has been characterised using an Agilent Technologies 85072A Split Cylinder Resonator and its relative dielectric permittivity and loss tangent have been found to be $\varepsilon_{\mathrm{subs}} = 1.5$ and $\tan(\delta)_{\mathrm{subs}} = 0.0025$, respectively.

4.1.4 Simulations

The ideal equivalent electrical parameters of the tag have been simulated using ADS, without taking into account the possible existence of parasitic capacitive effects in the coil. Consequently, the ideal circuit depicted in Figure 4.1 has been simulated. With the aim of achieving a resonant frequency of 13.56 MHz, L_{A} has been found to be 5.86 µH.

By measuring the lengths of all the conductive threads required to conform the coil in the Momentum model, and multiplying the total length by the resistance of the *Shieldex* thread, 3 Ω/cm, a total resistance R_{A} of 440 Ωhas been estimated. The interconnection resistance is given by the conductive paths between the terminals of the coil and the terminals of the chip. Considering a length of 3 centimetres for these conductive paths, an interconnection resistance of 9 Ωis calculated.

Simulating the ideal equivalent electrical model and calculating the imaginary part and the phase of the input impedance, Z_{IN}, the graphs of Figure 4.5 are obtained. As can be observed, a resonance frequency corresponding with the zero crossing of the graphs is achieved for 13.56 MHz.

4.1.5 Fabrication process

Once the textile coil has been designed, the woven prototype can be manufactured following two steps. First, the textile coil needs to be woven and secondly, the chip must be integrated in the woven structure. The textile coil has been manufactured using an industrial MüGrip loom.

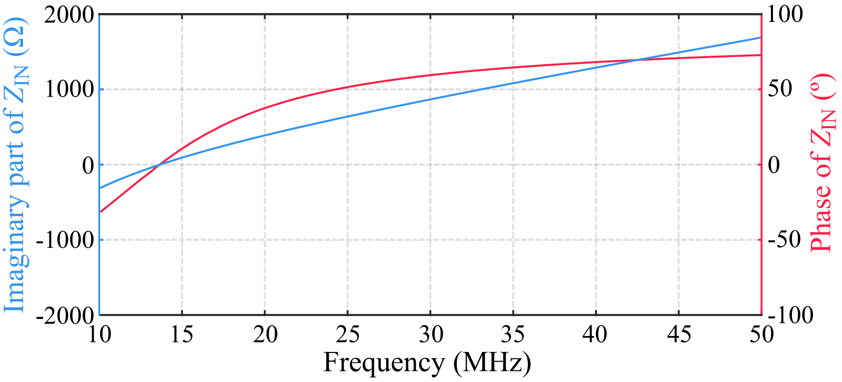

Figure 4.5: Simulated imaginary part and phase of the input impedance of the tag using the ideal equivalent model.

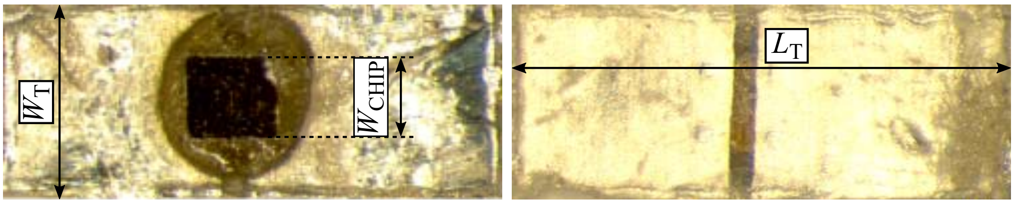

(a)

(b)

Figure 4.6: Overview of the NXP chip and dimensions. (a) Top view. (b) Bottom view.

With the aim of integrating the NXP chip in the woven coil, Figure 4.6 depicts the dimensions of the chip and its contacts, $W_{\mathrm{CHIP}} = 0.47$ mm, $W_{\mathrm{T}} = 1.09$ mm and $L_{\mathrm{T}} = 2.84$ mm. Due to the fact that the distance between the woven coil terminals is larger than the distance between the contacts of the chip, an adapting path is required, avoiding undesired short-circuits.

With the aim of integrating the chip in the woven coil while avoiding the undesired short circuits, several alternatives have been analysed. Isolating the conductive warp threads from the adapting path by the use of a dielectric paste has been discarded, since the textile would acquire a different texture, and this would not be interesting when trying to hide the tag.

Therefore, with the aim of solving this problem, two different alternatives, based on electrically conductive vias, are presented, with the novelty of connecting the chip in the bottom layer of the woven coil. The first proposed method to integrate the NXP chip in the tag is based on using a single *Shieldex* thread

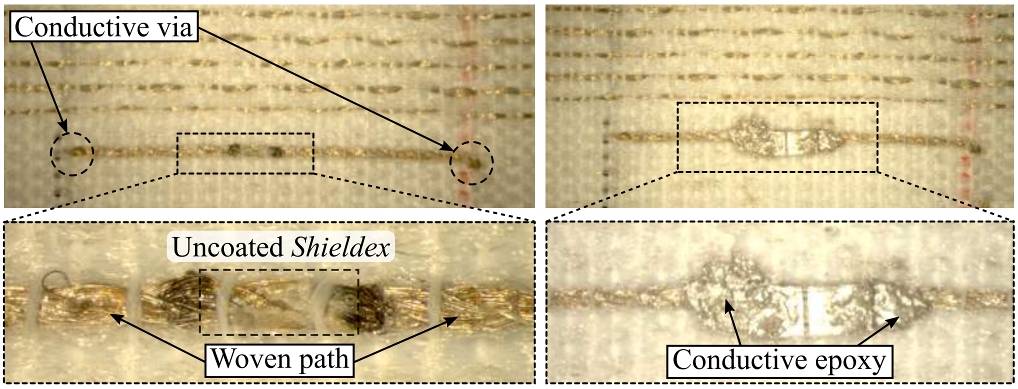

(a) (b)

Figure 4.7: Process of the chip integration by treating the *Shieldex* thread and using epoxy glue. (a) Conductive vias and magnification of the woven path. (b) Integrated chip and magnification of the epoxy connections.

which has been uncoated at the place where the chip will be mounted and corresponding to the footprint of the chip. This thread is a new warp thread which is electrically connected to both terminals of the woven coil in the top layer. The *Shieldex* thread crosses the prototype, from the top to the bottom layer, by using conductive vias as depicted in Figure 4.7a. In the bottom layer, the *Shieldex* thread is isolated from the other conductive warp threads, then it is able to cross the layer. In the area where the *Shieldex* thread has been uncoated, the chip can be connected by the use of conductive epoxy adhesive as depicted in Figure 4.7b.

The second proposed alternative to integrate the chip in the tag is based on the use of two silver warp monofilaments. Each silver monofilament is electrically connected to each terminal of the coil as in the first method, an both silver monofilaments cross the prototype from the top layer to the bottom layer through conductive vias. Consequently, each silver monofilament can then be welded to each pad of the chip.

The second proposed alternative to integrate the chip has been found to be the most advisable option, due to the fact that the welding process is easier to automate than the uncoating process. Therefore, the second proposed method has been employed during the experimental validation.

The resultant textile prototype is depicted in Figure 4.8. Figure 4.8a represents the top view of the manufactured prototype and a magnification where

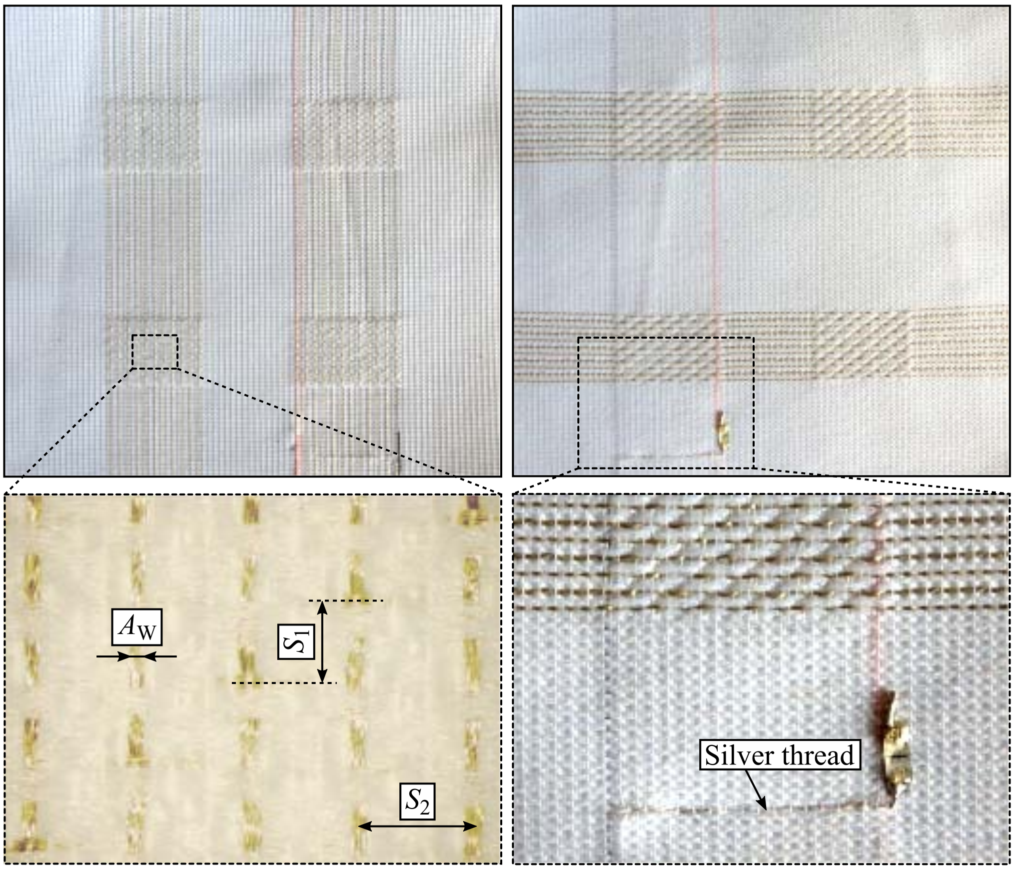

(a)

(b)

Figure 4.8: General overview of the manufactured prototype using the silver warp monofilament for the chip integration and magnifications. (a) Top view and detailed magnification of the dimensions. (b) Bottom view and corresponding magnification.

the dimensions of the conductive threads are detailed. Figure 4.8b depicts the bottom view of the manufactured prototype and a magnification where the chip is integrated using silver monofilaments.

4.1.6 Experimental validation

The experimental validation of the prototype has been carried out using a PNA-X N5247A vector network analyser from Agilent Technologies. For the direct current (DC) experimental characterisation, a Keysight Technologies U1252B multimeter has been used.

In order to have a more accurate model of the manufactured prototype, the experimental interconnection impedance $R_{\mathrm{S'}}$ has been measured and found to be 11.1 Ω. The input impedance of the coil in DC, $R_{\mathrm{A'}}$, without taking into account the interconnection has also been measured and found to be 444 Ω. Due to the existence of parasitic capacitive effects in the textile coil, the self resonance frequency (SRF) of the woven coil could be measured using a coaxial probe and was found to be 19.4 MHz, as depicted in Figure 4.9a (solid line).

Using the aforementioned experimental values and the SRF, a more accurate circuital model has been achieved by adjusting the parameters shown in Figure 4.10. The impedance $R_{\mathrm{A'}}$ has been divided into two impedances, $R_{\mathrm{A'1}}$ and $R_{\mathrm{A'2}}$, which have been found to be 160 Ω and 284 Ω, respectively. The new resonant components, $C_{\mathrm{A'}}$ and $L_{\mathrm{A'}}$, have been adjusted and are equal to 9 pF and 5.5 µH, respectively. Another impedance, R_{C}, in series with the parasitic capacitor has been required and is 35 Ω.

Figure 4.9a represents a comparison between the simulated and measured frequency response of the coil –before connecting the chip–, where the SRF can be identified at 19.4 MHz. Alternatively, Figure 4.9b depicts the comparison between the simulated and measured frequency response of the complete woven tag –which is composed of the woven coil and the chip–. A good agreement between the simulations and the measured results has been achieved.

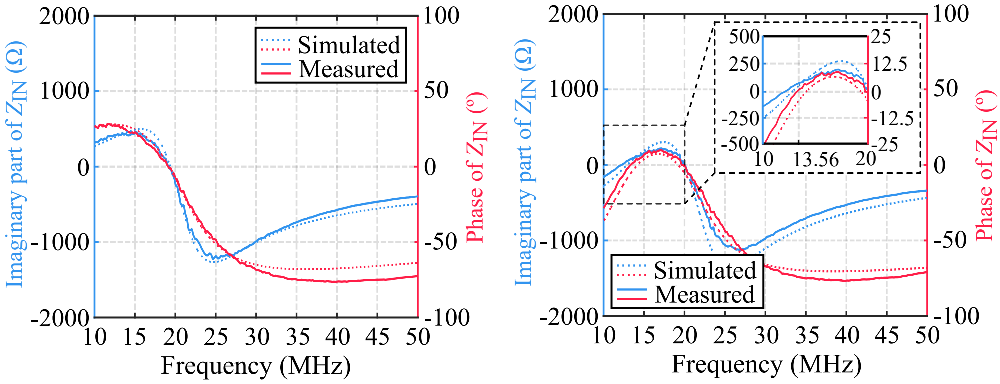

(a)

(b)

Figure 4.9: Imaginary part and phase of the input impedance of the coil and tag, respectively. (a) Frequency response of the coil: simulated (dotted lines) vs. measured (solid lines). (b) Frequency response of the complete tag: simulated (dotted lines) vs. measured (solid lines).

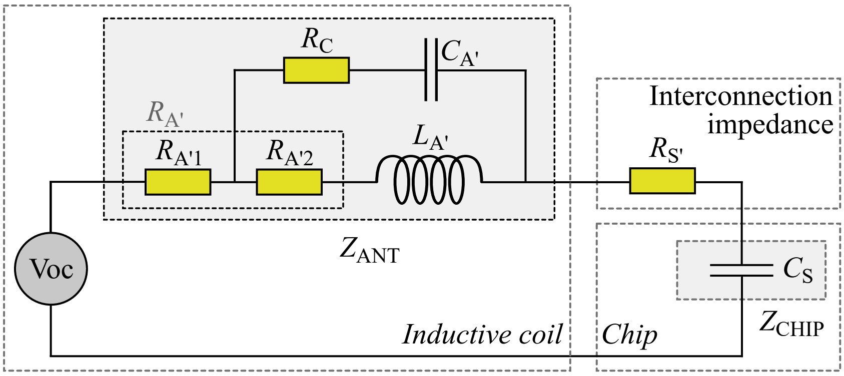

Figure 4.10: Equivalent electrical circuit of the proposed tag taking into account the self resonance.

After characterising the frequency response of the textile tag, the prototype has been tested using a smartphone as interrogator. As it could be anticipated taking into account the resistive loss of the conductive threads, the read range of the inductive RFID tag is a few centimetres, which are sufficient for the proposed applications.

Moreover, the tag has also been tested under different conditions. First, the tag has been bent in order to verify the performance of the electrical connections. As the electrical connections are achieved by the contact between conductive threads, the tag continues working properly after the bending test. Furthermore, the tag has also been tested after five washing cycles, obtaining a positive result.

4.1.7 Conclusion

A fully textile based tag for its use in clothing has been discussed. It presents several advantages in comparison with existing conventional RFID tags, including its potential for large scale production in comparison to other textile alternatives, or the possibility of integrating the tag in clothing, hiding it from sight and touch. Nevertheless, a pick and place mechanism is proposed to automatically connect the chip after manufacturing the woven coil.

Furthermore, the excess material around the woven coil can be mostly reduced, decreasing the dimensions of the final prototype. Consequently, the amount of conductive material required to manufacture the proposed tag is comparable to its analogous using embroidery procedures. However, weaving technology allows a level of large scale production which cannot be achieved with alternative embroidery techniques.

Thanks to the RFID chip, information regarding the product in which this tag has been located can be stored, not only for inventory or authentication, but also for customer information. This data could include information currently available in different uncomfortable labels attached to the clothing, or even purchase date details, avoiding the use of sales receipts. The introduction of RFID technology in clothing has an endless number of interesting applications which are the future of the textile industry.

Different alternatives for the design of the tag and the integration of the chip have been discussed and a final prototype has been proposed. The translation into a woven structure has been explained in detail, as well as the characteristics of the employed materials. An equivalent circuit of the proposed prototype has been presented and electromagnetic simulations and experimental results have been compared. A good agreement between simulations and experimental results has been achieved.

4.2 Microstrip-fed slot antenna for dedicated short-range communications

4.2.1 Introduction

As previously highlighted in Chapter 1, during the last years, there has been an overwhelming interest in wearable, flexible and textile integrated circuits and antennas. Antennas play an important role in wearables due to the number of different applications where they can be employed. For this reason, different approaches have been developed to integrate antennas into the textile.

The most translated antenna topology into textile is the patch antenna, due to its simplicity. For this reason, different alternatives have been employed to translate the patch antennas into their analogous textile prototypes. The dielectric substrate of the patch antennas has been usually implemented using either non-wovens such as ethylene vinyl acetate (EVA) [13], fleece, felt [14] or PF-4 foam [15], or conventional dielectric fabrics [16–18]. Alternatively, the conductive elements of the patch antennas have been implemented using conventional copper gauze [13], silver fabric [15] or commercial conductive fabrics such as *ShieldIt* or *Flectron* [14].

All the before mentioned antennas are not completely integrated in textile, therefore, they require several processes to be manufactured. In this section, a fully textile integrated microstrip-fed slot antenna is proposed [19].

Table 4.1: Dimensions of the radiating slot.

a_1 (mm)	a_2 (mm)	a_3 (mm)	b_1 (mm)	b_2 (mm)	b_3 (mm)
7	5	2	3	3	0.5

4.2.2 Structure of the antenna

A microstrip-fed slot antenna for dedicated short-range communications (DSCR) is proposed for its operation at 5.9 GHz with a 9.3 % bandwidth. The antenna is based on a microstrip line with a shorted port. The ground plane contains the radiating slot whose centre is placed at a distance of a quarter of the wavelength, $d_\mathrm{p} = 16.2$ mm, from the short circuit in order to constructively add the incident and reflected waves in the microstrip line, leading to a maximum of the magnitude of the electrical field in this position, as depicted in Figure 4.11a. The antenna is composed of three different layers as shown in Figure 4.11b.

The dimensions of the antenna are the width, $W_\mathrm{a} = 50$ mm, the length, $L_\mathrm{a} = 50$ mm, the substrate height, $H_\mathrm{ML} = 0.97$ mm (which will be imposed by the employed dielectric threads) and the width of the microstrip line, $W_\mathrm{ML} = 3.5$ mm (which will be essentially calculated from the values of H_ML and the equivalent permittivity of the substrate, ε_eq). The radiating slot has been optimised for bandwidth enhancement compared to a rectangular-shaped slot. Its dimensions are represented in the magnification of Figure 4.11a and detailed in Table 4.1.

The proposed antenna is fully integrated in textile, therefore, the conductive and dielectric parts are manufactured using different types of threads. Different materials have been employed for the design of the antenna, for both the weft and the warp directions. The weft direction coincides with the current direction, whereas the warp direction is perpendicular to the weft direction, as depicted in Figure 4.11a. In the following subsections, the employed materials will be analysed and the translation into a woven prototype will be explained.

4.2.3 Characterisation of the conductive materials

Electrically conductive *Shieldex 117f17 2-ply* yarns have been used for the weft threads. As will be explained later, these threads adopt the Pierce's elliptic cross section when they are in the woven structure. A single conductive *Shieldex 117f17 1-ply* warp yarn has also been used for the short-circuit of the antenna. This thread has been modelled keeping the circularly shaped cross section. The cross section approaches and corresponding dimensions of the different conductive

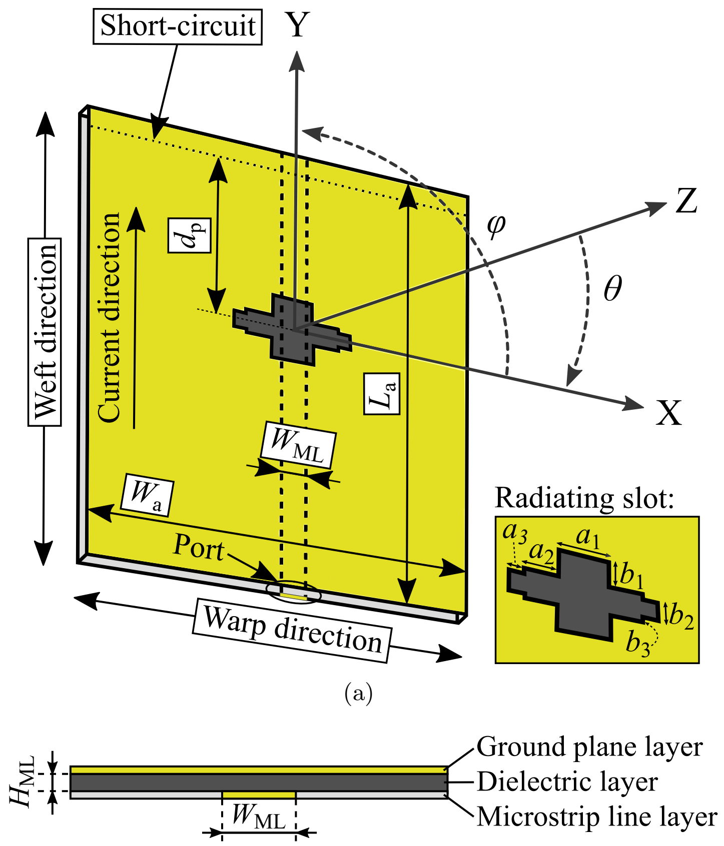

(a)

(b)

Figure 4.11: Schematic design of the proposed antenna. (a) General overview, reference coordinates system, dimensions and detail of the radiating slot. (b) Side view from the port plane, dimensions of the microstrip line and identification of the layers.

threads are summarised in Table 4.2, where the threads *Shieldex 117f17 2-ply* and *Shieldex 117f17 1-ply* have been denoted *Shx2p* and *Shx1p*, respectively for simplification. The thickness of the silver coating of each filament, for both types of threads, is given by $T_c = 0.5$ µm, whereas the total diameter of each filament is given by $D_f = 31$ µm, as it has been previously depicted in Figure 3.2.

Following the procedure described in section 2.1.2.2, both conductive threads must be translated into their analogous monofilaments. For this purpose, the analysis of the skin depth effect is discussed in this section. First, using the expression described in (2.1), where $\rho_{coat} = 1.59 \cdot 10^{-8}$ (Ωm) is the resistivity

Table 4.2: Dimensions of the cross sections of the conductive materials.

Thread	Thread direction	Cross section	Dimension	Notation	Value (mm)
Shx1p	Warp	Circular	Circumference radius	C_{R}	0.0125
Shx2p	Weft	Pierce	Horizontal semi-axis	H_{S}	0.1
			Vertical semi-axis	V_{S}	0.03

of the silver and f is the operating frequency of the design, $f = 5.9$ GHz, the skin depth is $\delta = 0.8262$ µm. As the thickness of the conductive coating of the filaments is less than the skin depth, the second part of the procedure is followed.

In order to employ the procedure described in section 2.1.2.2, some expressions must be particularised to the different cross sections of the *Shieldex* yarns. Using the expression (2.11), as the *Shx2p* threads and the *Shx1p* threads are composed of 34 and 17 filaments, respectively, the resistance per unit length of each thread is $(R/l)_{\mathrm{Shx1p}} = 9.7611\ \Omega/\mathrm{m}$ and $(R/l)_{\mathrm{Shx1p}} = 19.5222\ \Omega/\mathrm{m}$. As the threads are the same which have been already used in the previous chapter, these parameters remain the same. Nevertheless, the equivalent cross sections have been modified due to the forces the threads experiment in the different woven structure.

Particularising the expression in (2.6) for the Pierce's elliptic cross section, the areas of the equivalent conductive cross sections of the monofilament threads for the *Shx2p* and the *Shx1p* threads, S_{mon2} and S_{mon1}, can be expressed using, respectively, (4.2) and (4.3).

$$S_{\mathrm{mon2}} = \pi \cdot H_{\mathrm{S}} \cdot V_{\mathrm{S}} - \pi \cdot (H_{\mathrm{S}} - T_{\mathrm{R}}) \cdot (V_{\mathrm{S}} - T_{\mathrm{R}}) \tag{4.2}$$

$$S_{\mathrm{mon1}} = \pi \cdot {C_{\mathrm{R}}}^2 - \pi \cdot (C_{\mathrm{R}} - T_{\mathrm{R}})^2 \tag{4.3}$$

Once the expressions of the $S_{\mathrm{mon}i}$ are obtained, the resistances per unit length of the monofilament can be expressed particularising (2.7) for the Pierce's elliptic cross sections, as generically indicated in (4.4).

$$(R/l)_{\mathrm{mon}i} = \frac{1}{\sigma_{\mathrm{mon}i} \cdot \pi \cdot S_{\mathrm{mon}i}} \tag{4.4}$$

With the aim of achieving the same resistance per unit length in both the multifilament and the monofilamente threads, $(R/l)_{\mathrm{Shx2p}}$ must be equal to $(R/l)_{\mathrm{mon2}}$

and, equivalently, $(R/l)_{\mathrm{Shx1p}}$ must be equal to $(R/l)_{\mathrm{mon1}}$. As it has been thoroughly explained in section 2.1.2.2, the parameter T_{R} coincides with the skin depths, δ_{mon2} and δ_{mon1}, calculated using the equivalent electrical conductivities of the monofilaments, σ_{mon2} and σ_{mon1}, respectively, as previously expressed in (2.9). Solving the corresponding equations using numeric methods, the solutions have been found to be $\sigma_{\mathrm{mon2}} = 2.6311 \cdot 10^{36}$ Ω/m and $\sigma_{\mathrm{mon1}} = 9.96 \cdot 10^{9}$ Ω/m, respectively.

According to the procedure referenced in section 2.1.3.2 and the design of the woven patterns which will be described in section 4.2.5, the equivalent conductivity is given by $\sigma_{\mathrm{eq}} = 4.8 \cdot 10^{3}$ S/m. This low value of σ_{eq} is due to the fact that, in the woven design, there are no conductive threads in the warp direction to form the ground plane.

4.2.4 Characterisation of the dielectric materials

For the dielectric parts of the antenna, three different types of threads have been employed. For the weft threads, black PET 1670 dtex and uncoated PET 1530 dtex have been used. For the warp threads, high tenacity PES 550 dtex has been used. The characteristic parameters of the employed materials are summarised in Table 4.3 [20, 21].

For the PES warp yarns, denoted by PES_{warp}, the circular cross section has been kept due to their high tenacity. For the uncoated or white PET weft threads, denoted by $PET_{\mathrm{weft\_w}}$, the Pierce's elliptic cross section has been used, whereas for the black PET weft yarns, denoted by $PET_{\mathrm{weft\_b}}$, the circular cross section has been kept due to their rigidity. The dimensions of the cross section of each type of dielectric thread used in the proposed antenna are indicated in Table 4.4. According to the procedure referenced in section 2.1.2.1, the proportion of air in the multifilaments can be calculated, as summarised in Table 4.5.

According to the same procedure, the design of the woven structure is required. Due to the fact that the cross section of the $PET_{\mathrm{weft\_b}}$ is much bigger than

Table 4.3: Characteristic parameters of the dielectric materials.

Parameter	PET	PES
Relative permittivity	$\varepsilon_{\mathrm{fil\_PET}} = 3.7$	$\varepsilon_{\mathrm{fil\_PES}} = 3.4$
Loss tangent	$\tan(\delta)_{\mathrm{fil\_PET}} = 0.001$	$\tan(\delta)_{\mathrm{fil\_PES}} = 0.01$
Density (g/cm^3)	$\delta_{\mathrm{fil\_PET}} = 1.5$	$\delta_{\mathrm{fil\_PES}} = 1.5$

Table 4.4: Dimensions of the cross sections of the dielectric materials.

Thread	Thread direction	Cross section	Dimension	Value (mm)
PES_{warp}	Warp	Circular	Radius	0.0125
$PET_{\mathrm{weft\_w}}$	Weft	Pierce	Horizontal semi-axis	0.1
			Vertical semi-axis	0.03
$PET_{\mathrm{weft\_b}}$	Weft	Circular	Radius	0.46

Table 4.5: Parameters of the equivalent monofilaments.

Monofilament	% of air	Relative Permittivity	Loss Tangent
PES_{warp}	24%	$\varepsilon_{\mathrm{mon\_PESwarp}} = 1.72$	$\tan(\delta)_{\mathrm{mon\_PESwarp}} = 0.01$
$PET_{\mathrm{weft\_w}}$	15%	$\varepsilon_{\mathrm{mon\_PETweft\_w}} = 2.83$	$\tan(\delta)_{\mathrm{mon\_PETweft\_w}} = 0.001$
$PET_{\mathrm{weft\_b}}$	30%	$\varepsilon_{\mathrm{mon\_PETweft\_b}} = 2.11$	$\tan(\delta)_{\mathrm{mon\_PETweft\_b}} = 0.001$

the others, the weft threads will remain straight, whereas the warp threads will conform the woven structure around the weft threads. As $PET_{\mathrm{weft\_b}}$ yarns are much thicker than the other dielectric threads, the variation in the size of the air gaps between the threads mainly depends on the *epi* parameter associated to the $PET_{\mathrm{weft\_b}}$ yarns. This *epi* parameter is equal to 24 ends per inch or, equivalently, there is a 1.1 mm distance between centres of $PET_{\mathrm{weft\_b}}$ yarns. Although the MM represents an anisotropic structure, this woven density leads to a scalar equivalent relative permittivity of the structure of $\varepsilon_{\mathrm{eq}} = 1.1$. This is due to the single polarisation of the antenna and the fact that the current is mostly in the same direction as the propagation direction of the waveguide used in the modelling. Moreover, the equivalent loss tangent has also been calculated and it has been found to be $\tan(\delta)_{\mathrm{eq}} = 0.01$, due to the influence of the *PES*.

4.2.5 Design of the woven antenna

A fully textile integrated microstrip-fed slot antenna using rigid weft threads is proposed to work at 5.9 Ghz. The ground plane layer is composed of conductive threads in the weft direction (*Shx2p*) and dielectric threads in the warp direction (PES_{warp}). The dielectric layer is composed of dielectric threads in both directions ($PET_{\mathrm{weft\_w}}$ and PES_{warp}), and the microstrip line layer is composed of conductive weft threads (*Shx2p*), dielectric weft threads ($PET_{\mathrm{weft\_w}}$) and dielectric warp threads (PES_{warp}). A single conductive warp thread (*Shx1p*) has been used to electrically connect the ground plane layer with the microstrip line layer to achieve the short-circuit.

Due to the fact that all the weft threads in the design have a Pierce's cross section or circular-shaped cross section, these sections have been modelled as ellipses (or turned into circumferences). As the weft threads, aligned in the current direction, have been found to be rigid threads, different warp patterns have been designed to create the microstrip antenna structure while connecting the different layers of the prototype through the already explained binder threads. For this reason, the paths of the warp threads have been found to be mathematically modelled as ellipse arcs and tangent lines. The proposed woven structure for the MM is depicted in detail in Figure 4.12. A side view magnification of the proposed antenna design, as seen from the port plane, is shown in Figure 4.12a, where the weft ends and the warp threads are represented. Figure 4.12b depicts the bottom view and magnification, where the microstrip line can be seen.

4.2.6 Simulations

The proposed design has been analysed using a 3D high frequency EM simulator with a Transient Solver. Figure 4.13 depicts the simulated magnitude of the reflection coefficient (dB) and bandwidth (shaded) of the LM. Figure 4.14 shows the definition of the E-plane and the H-plane of the proposed antenna, whereas Figure 4.15 represents the simulated normalised radiation patterns: E-plane and H-plane co-polar (CP) contributions.

The simulated values of the gain, directivity and radiation efficiency are $G_{\mathrm{S}} = -1.5$ dB, $D_{\mathrm{S}} = 5.1$ dB and $\varepsilon_{\mathrm{eff\_S}} = 22$ %, respectively. The negative value of the simulated gain is, essentially, due to the low value of the equivalent conductivity.

4.2.7 Fabrication process

A fully textile integrated antenna has been manufactured, as depicted in Figure 4.16, using two processes. First, an industrial loom has been used to fabricate the textile structure and, secondly, a prototyping laser machine has been employed to create the radiating slot. Finally, an SMA connector is mounted on the woven antenna.

An industrial loom MüGrip loom with a maximum density of 107 *epi* has been used for the manufacturing of the textile structure. First, the three layers

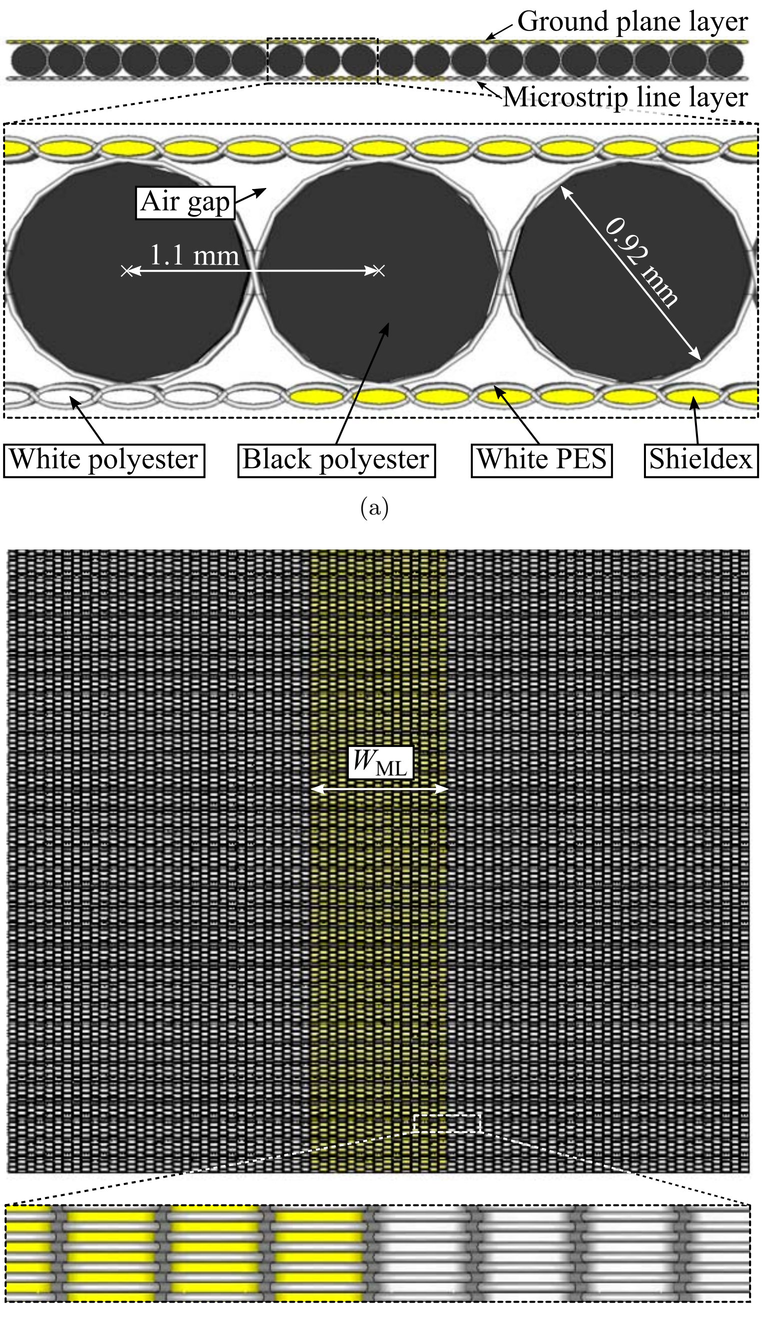

(a)

(b)

Figure 4.12: Schematic simulated monofilament model of the microstrip geometry. (a) Side view from the port plane, magnification and materials. (b) Bottom view and magnification.

of warp threads are assembled in the loom, except in the position corresponding to the short-circuit, where only one conductive thread is required to connect all the layers. Then, the weft yarns are successively inserted in the woven structure during the fabrication process. A finishing process is needed after removing the fabric from the loom in order to achieve the requirements, by the use of a stenter machine.

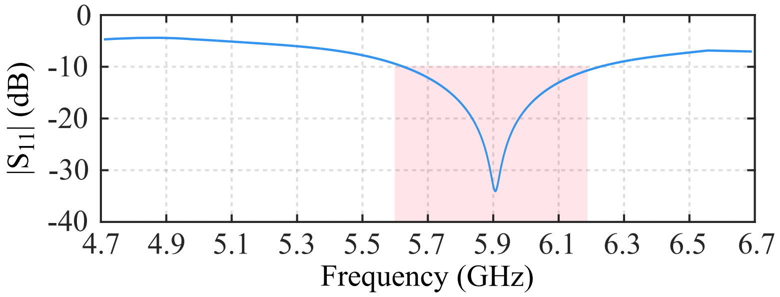

Figure 4.13: Simulated magnitude of the reflection coefficient (dB) and bandwidth (shaded).

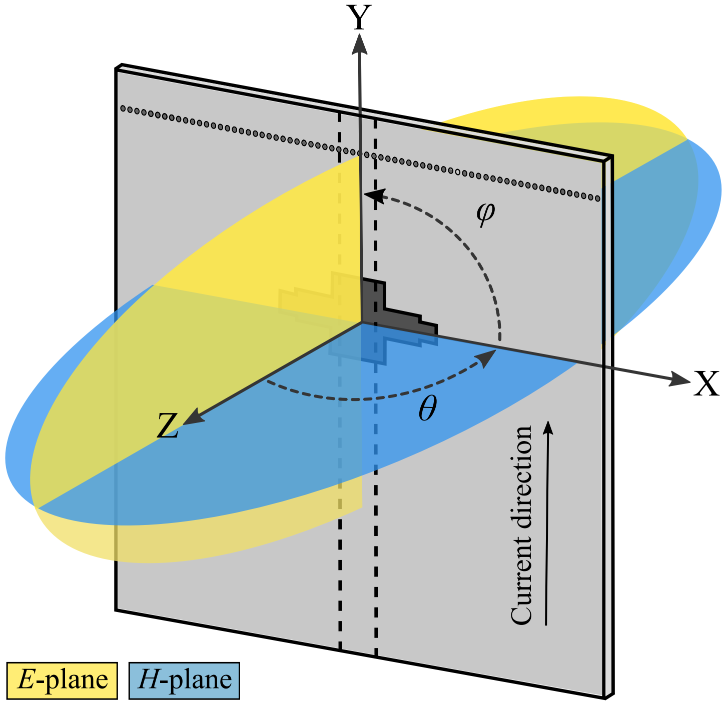

Figure 4.14: Definition of the E-plane and the H-plane.

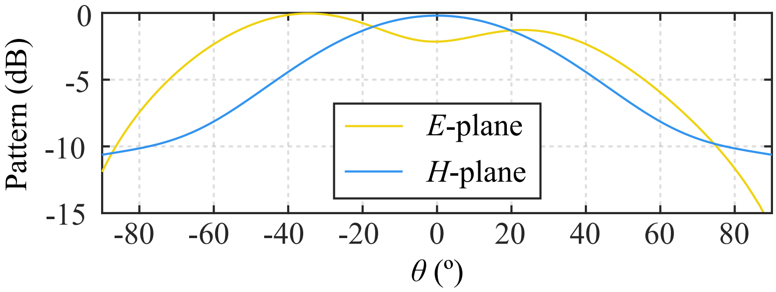

Figure 4.15: Simulated normalised radiation patterns: E-plane and H-plane CP contributions.

Figure 4.16a shows the top view of the antenna (slotted ground plane layer), whereas Figure 4.16b represents the bottom view of the antenna (microstrip line layer). In Figure 4.16c a side view from the port plane is shown, where the three layers of the prototype can be identified. Figure 4.16d shows a detailed view of the microstrip line and the conductive thread implementing the short-circuit.

A laser prototyping machine LPKF ProtoLaser has been used to structure the radiating slot in the ground layer of the prototype. The power level has been adjusted to structure only the ground plane layer of the antenna, avoiding the modification of the middle layer. Figure 4.17a represents the laser patterned slot, together with a magnification of the cut. Figure 4.17b shows the radiating slot after removing the leftover textile material: only the ground plane layer of the prototype has been cut even though the three layers remain connected through yarns.

An SMA connector has been installed in the woven prototype. Two shims of brass have been cut to size and placed on top of the microstrip line and under the ground plane, in order to provide the fabric with the necessary rigidity to install the connector as shown in Figure 4.16e and Figure 4.16f. The connector has been secured to the brass shims using conductive epoxy glue.

4.2.8 Experimental validation

In order to experimentally validate the prototype, the reflection coeffient has been measured using an Agilent N5247A PNA-X vector network analyser and compared with the simulations, as shown in Figure 4.18. The measured bandwidth has been found to be equal to 9.3 %.

The prototype has been measured at a spherical range in an anechoic chamber to characterise its radiation pattern, directivity, gain, and radiation efficiency.

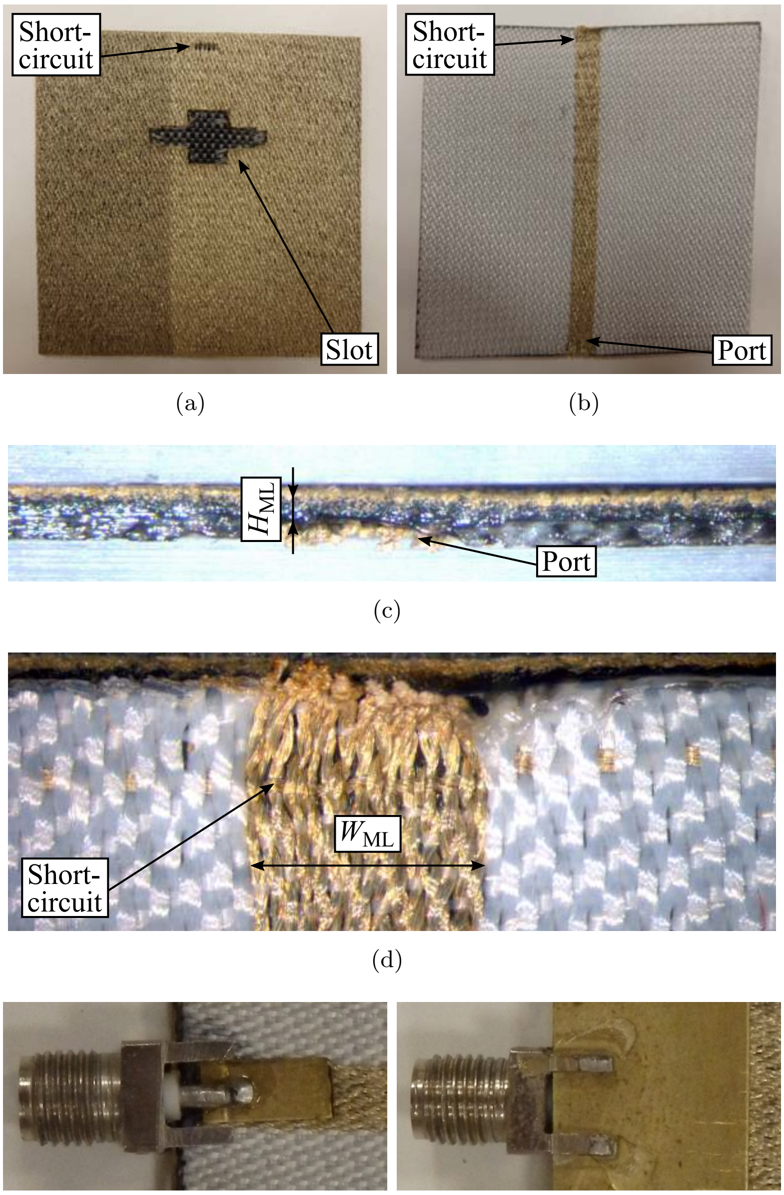

(a) (b) (c) (d) (e) (f)

Figure 4.16: Manufactured textile prototype without connector. (a) Top view. (b) Bottom view. (c) Side view from the port plane. (d) Microstrip line and short-circuit detail. (e) Connector view (microstrip line layer). (f) Connector detailed view (ground plane layer).

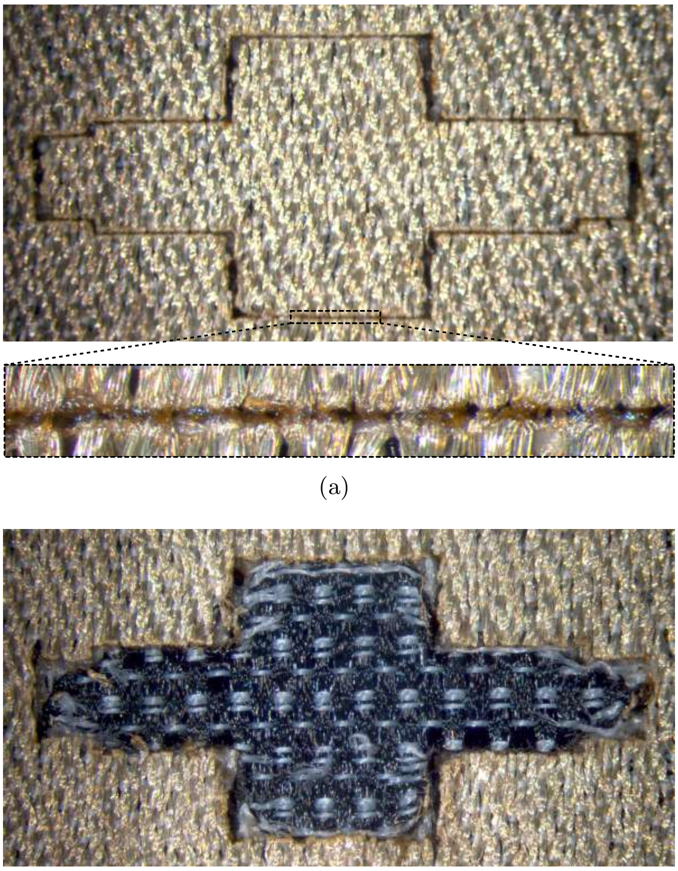

(a)

(b)

Figure 4.17: Detailed manufacturing process of the textile slot. (a) Before removing the leftover textile material and magnification of a cut area. (b) After removing the leftover textile material.

Measurements have been conducted at the frequency $f_o = 5.9$ GHz, which corresponds to the $|S_{11}|$ minimum (as observed in Figure 4.18).

The radiation pattern of the textile antenna under test (AUT) has been measured at the distance of $R = 5.4$ m, which is in the far field (FF) region. A picture of the measurement set-up at the spherical range in anechoic chamber is shown in Figure 4.19, where the AUT has been mounted in a foam platform and the probe antenna is a Narda 642 Standard Gain Horn (SGH) [22]. The E-plane and H-plane normalised radiation patterns of the AUT have been measured and compared with the simulated data, as depicted in Figure 4.20. A good agreement between simulated and measured CP components can be noticed (cross-polar,

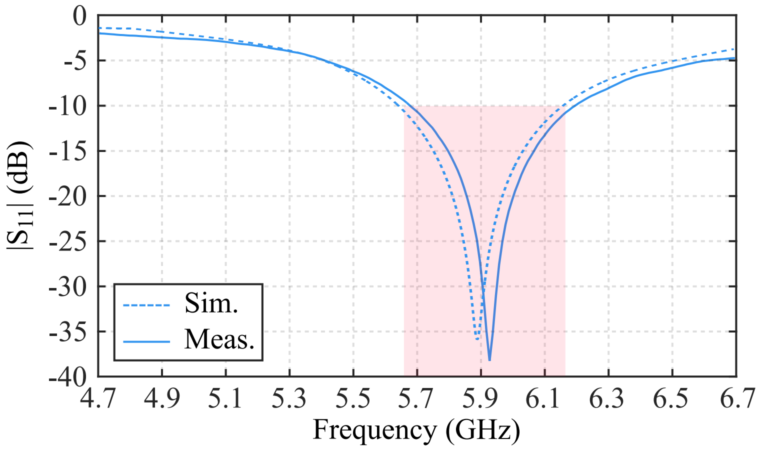

Figure 4.18: Simulated and measured magnitude of the reflection coefficient (dB) and bandwidth (shaded).

XP, component is below −40 dB in simulations).

The directivity has been calculated by integrating the measured AUT radiation pattern, yielding $D_{\mathrm{M}} = 4.9$ dB, which is in agreement with the low directivity of the AUT radiation pattern (as confirmed by the directive gain pattern depicted in Figure 4.21). This result is of great interest for automotive DSRC antennas, where antennas with low directivity are preferred [23, 24].

The AUT gain has been evaluated by means of the inter-comparison technique [25], resulting $G_{\mathrm{M}} = -2.75$ dB. Finally, given the AUT gain and directivity, the AUT radiation efficiency can be calculated: $\varepsilon_{\mathrm{eff\_M}} = 17.2$ %. A comparative between the simulated and the measured values of the gain, directivity and radiation efficiency is presented in Table 4.6. The low values of both gains can be justified due to the ohmic losses of the textile antenna conductive fibers. Moreover, the difference between the simulated and the measured gain values can be justified due to manufacturing errors in the connection between the textile antenna and the RF connector and the silver plated coating deterioration due to the wear out, which could be solved by the use of non-coated stainless steel threads.

A comparative between different microstrip textile antennas found in the literature has been summarised in Table 4.7 in terms of operating frequency, f, bandwidth, BW, gain, G, directivity, D, and radiation efficiency, $\varepsilon_{\mathrm{eff}}$. In the case a parameter has not been provided in the corresponding paper, NP has been indicated instead. The antennas described in [2, 13, 14] present higher radiation efficiencies, due to different reasons. First, their operating frequencies are lower,

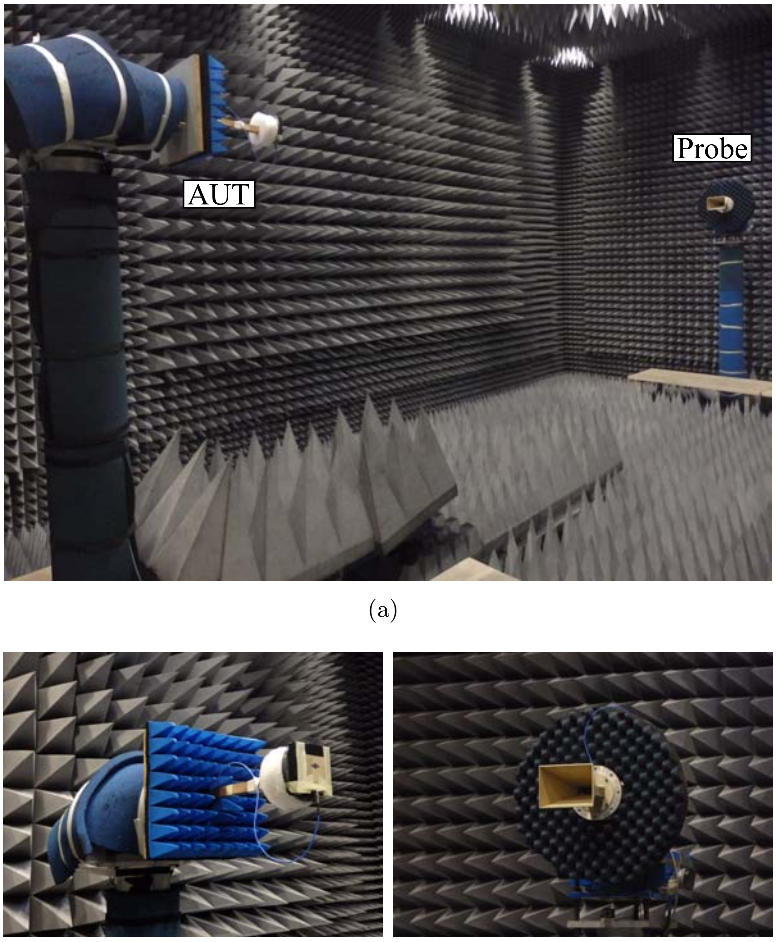

(a)

(b) (c)

Figure 4.19: Measurement set-up in anechoic chamber. (a) Overview of the setup. (b) Detailed antenna under test (AUT). (c) Detailed probe antenna.

Table 4.6: Comparative between simulations and measurements.

Parameter	Gain (dB)	Directivity (dB)	Radiation efficiency
Simulated	-1.5	5.1	22%
Measured	-2.75	4.9	17.2%

consequently, the losses are also lower, leading to higher efficiencies. Moreover, the different techniques used to provide the textile antennas with the conduc-

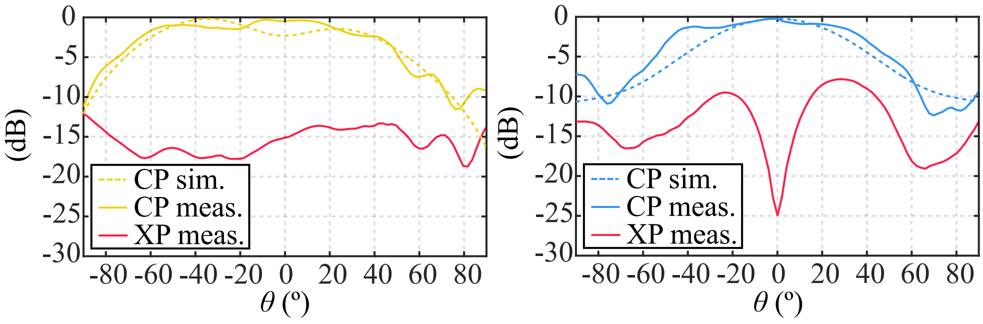

(a) (b)

Figure 4.20: Simulated and measured normalised radiation patterns (dB). (a) E-plane. (b) H-plane.

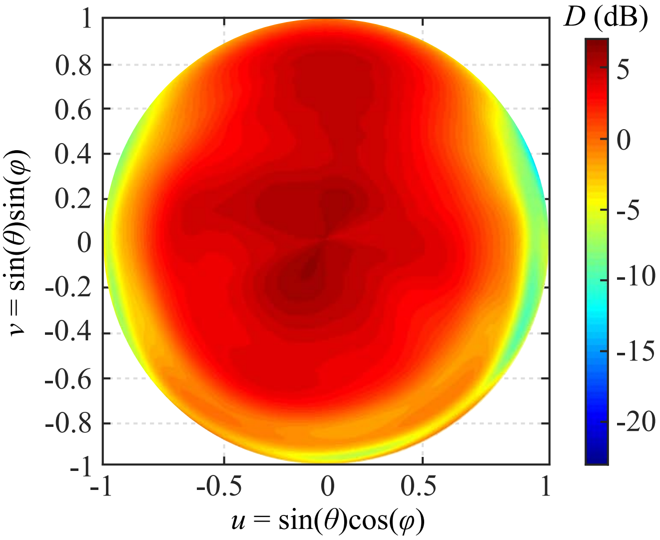

Figure 4.21: Directive gain pattern of the AUT. Directive gain at $\theta = 0°$, $\phi = 0°$ is 3.7 dB. Directivity $D = 4.9$ dB (at $\theta = 8°$, $\phi = 243°$).

tive elements, ink-jet printing, copper patches and copper plated nylon fabrics, respectively, do not allow a fully textile integration while avoiding subsequent post-treatments.

The antennas described in [16, 17] present higher gain values, although information regarding the radiation efficiency is not provided for comparative. The antennas presented in [15, 18] provide information regarding their radiation efficiencies, which is comparable to the radiation efficiency achieved in this work,

Table 4.7: Comparative between textile microstrip antennas in the literature.

Reference	f (GHz)	BW (%)	G (dB)	D (dB)	$\varepsilon_{\mathrm{eff}}$ (%)
[2]	0.43	5.2	2.41	NP	51
[13]	2.505	NP	5.98	8.72	53
[14]	2.45	6.04	9.1	NP	63
[16]	5.5	1.6	3.5	NP	NP
[17]	6.0	9.3	6.11-6.69	NP	NP
[18]	1.57542	3	1.2	NP	19
[15]	2.450	NP	4.09	NP	15.8
	4.725	NP	7.62	NP	38.9
	5.800	NP	6.73	NP	13.8
This work [19]	5.9	9.3	-2.75	4.9	17.2

although the conductive elements of the mentioned antennas are achieved by the use of copper patches and silver coated nylon fabric, respectively, leading to a lower textile integration level of the prototypes.

4.2.9 Conclusions

A novel fully textile-integrated microstrip-fed slot antenna for its use in DSRC for automobile upholsteries has been presented. First, a complete characterisation of the employed materials has been discussed. Then, the parametric modelling technique to simulate textile structures based on the reduction of the computational complexity of the problem has been applied to the antenna. To validate the design, a prototype has been manufactured and experimentally characterised.

A good agreement between simulations and measurements has been achieved, consequently the theoretically predicted behaviour of the textile structure has been experimentally verified. Nevertheless, in order to improve the measured gain of the antenna it is proposed to use conductive threads with a lower resistance and to use an electrically conductive epoxy with higher conductivity.

The manufactured prototype reveals the potential of the woven technology applied to microstrip designs working at microwave frequencies, opening a new field of research. This prototype represents a first step in TIC technology and demonstrates the possibility of fully integration of antennas in woven structures.

This antenna has been manufactured using a laser prototyping machine to implement the radiating slot, although this could have been avoided using a weaving loom provided with an automatic cutting mechanism in the warp and weft directions. Nevertheless, this weaving loom has not been available during the elaboration of the Thesis.

4.3 Mixed embroidered and woven coaxial-fed cavity-backed slot antenna for wireless body area network applications

4.3.1 Introduction

With the aim of improving the performance of the antenna presented in the previous section, avoiding the backwards radiation resulting from the microstrip structure, a novel antenna is presented in this section, whose topology is based on a SIW cavity-backed slot antenna. Although in the literature some approaches to develop textile integrated SIW antennas have already been proposed, they have been manufactured using previously fabricated conductive fabrics [26–33].

Not only the textile SIW antennas presented in the literature have been manufactured using prefabricated conductive fabrics, but also the conductive vias have been implemented using brass eyelets [26,27,30,32,33], avoiding the complete integration into textile. In order to achieve the goal of a complete integration of the antenna into the textile, a mixed embroidered and woven coaxial-fed cavity-backed slot antenna for wireless body area network applications is proposed in this section.

4.3.2 Structure of the antenna

A mixed embroidered and woven coaxial-fed cavity-backed slot antenna for wireless body area network applications is proposed for its operation at 5 GHz with a 20 % bandwidth. The antenna is based on the SIW technology, for this reason, the structure is divided into three layers: the slotted layer which corresponds to the top cover, the dielectric layer whose thickness is H, and ground layer which corresponds to the bottom cover of the SIW, as schematically depicted in Figure 4.22, together with the employed coordinate system.

In order to achieve a cavity structure, one of the ports of the square-shaped SIW whose length is given by L_{S}, is short-circuited. The short-circuit is achieved using identical extra conductive vias whose diameter are denoted by D and which

Table 4.8: Dimensions of the antenna.

Dimensions (mm)							
L_{A}	H	D	S	d_{F}	d_{S}	L_{S}	W_{S}
28	0.36	0.2	0.4	13	13	17	2.8

are separated S between centres. The antenna is fed using a coaxial cable which is connectorised through the ground layer (or bottom layer) of the SIW using a SMA connector. This connector is placed at a distance d_{F} from the short-circuit as depicted in Figure 4.22a.

The radiating slot, which is placed in the top layer of the SIW, is a rectangle-shaped slot whose dimensions are L_{S} and W_{S}, respectively. With the aim of achieving the required 5 GHz resonant frequency, the slot is placed at a distance d_{S} from the other port of the SIW, as depicted in Figure 4.22b. The beforementioned dimensions are summarised in Table 4.8.

The proposed antenna is fully integrated in textile and the different layers of the SIW structure are achieved using weaving technology. For this reason, the structure of the woven layers corresponds to a TIW topology, already presented in Chapter 3. Likewise, the conductive vias of the TIW are implemented in textile technology, although in this case they are embroidered. Both the conductive and dielectric elements of the antenna are threads, which are divided into the two already known directions, the weft and the warp directions. The employed materials are analysed in the following subsection.

4.3.3 Characterisation of the employed materials

As previously mentioned, the proposed antenna has been designed using two different techniques. On the one hand, the textile structure composed of three layers has been woven. On the other hand, the conductive vias which connect the different layers have been implemented using an embroidery technique.

The woven structure employed in this antenna has been provided from a sample of the woven structure required in the TIW thoroughly discussed in section 3.1. However, while the woven structure of the TIW presented conductive threads in both the warp and the weft directions, the woven structure employed in this antenna belongs to a part of the sample where the conductive warp threads have been replaced with dielectric warp threads. For this reason, it is expected that the gain of the antenna is not very high.

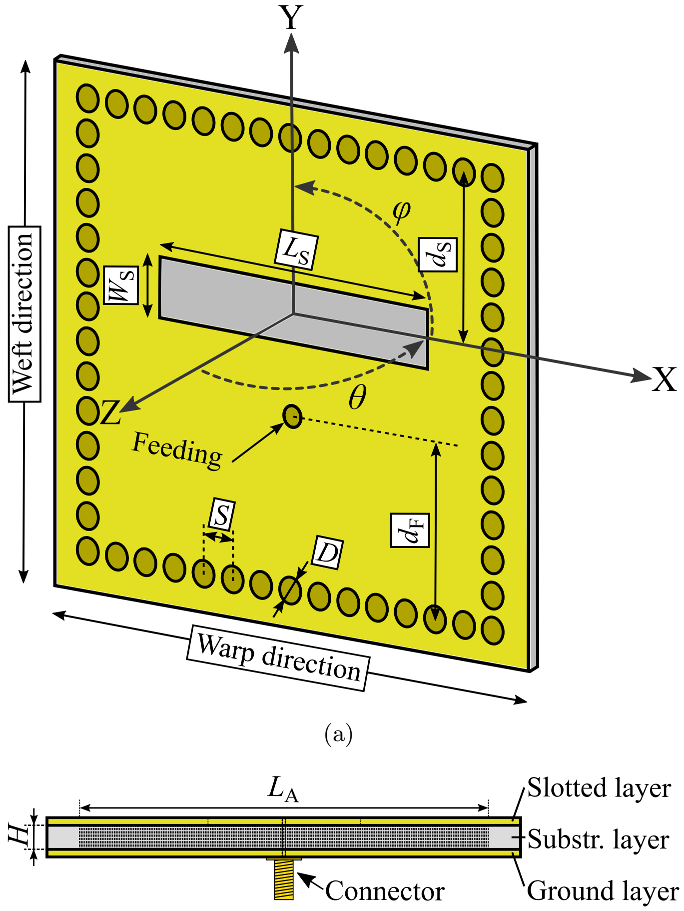

(a)

(b)

Figure 4.22: Schematic design of the proposed antenna: conductive and dielectric materials are yellow and grey colored, respectively. (a) General overview, reference coordinates system, dimensions and detail of the radiating slot. (b) Side view from the port plane, dimensions and identification of the layers.

Although the equivalent relative permittivity of the substrate has already been discussed in section 3.1 and found to be $\varepsilon_{\text{eq}} = 1.55$, the operating frequency of the herein presented antenna is much lower. Consequently, in this work, the equivalent relative dielectric permittivity of the proposed structure may increase due to the air gaps are larger with respect to the associated wavelength. With the aim of experimentally characterise this value, a TIW provided with a pair of TIW to coaxial transitions has been manufactured and measured using the same textile structure as the antenna. The measurements have been compared

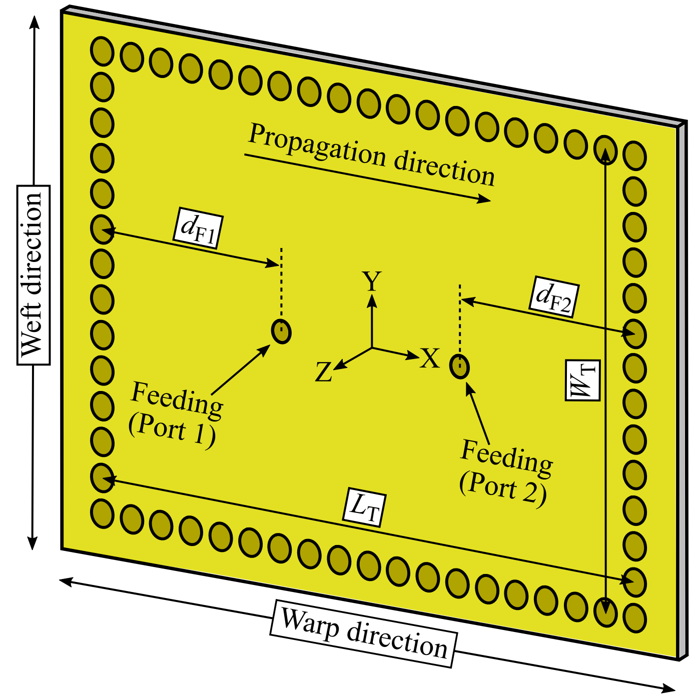

Figure 4.23: Schematic design of the TIW provided with a pair of TIW to coaxial transitions.

to the corresponding simulations of the LM, while sweeping the value of the ε_{eq} parameter.

Figure 4.23 schematically depicts the TIW provided with the aforementioned transitions. Both feeding points are located at a distance d_{F1} and d_{F2}, respectively, from the shortcircuiting vias. Both distances are $d_{F1} = d_{F2} = 12$ mm, while the length and width of the waveguide are $L_T = 30$ mm and $W_T = 28$ mm, respectively. The dimensions of the conductive vias and their separation are analogous as in the previously described design of the antenna.

The TIW has been manufactured and connectorised as depicted in Figure 4.24, and then measured using an Agilent N5247A PNA-X vector network analyser. A narrow-band performance of the TIW could be anticipated due to the design of the transitions. However, the main goal is finding the central frequency of the manufactured TIW bandpass, which has been found to be $f_{cBP} = 5.6$ GHz.

Different versions of the LM associated to the TIW have been simulated sweeping the value of the ε_{eq} parameter. Eventually, $\varepsilon_{eq} = 2.2$ has been found to be the value of the equivalent relative permittivity which makes the simu-

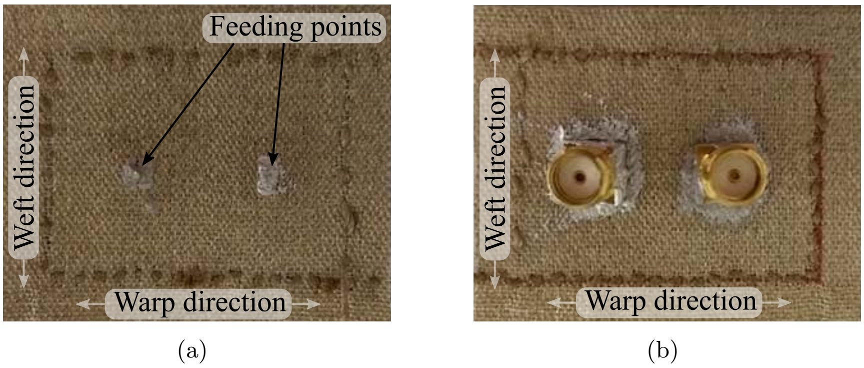

(a) (b)

Figure 4.24: Manufactured TIW provided with a pair of TIW to coaxial transitions. (a) Top view. (b) Bottom view.

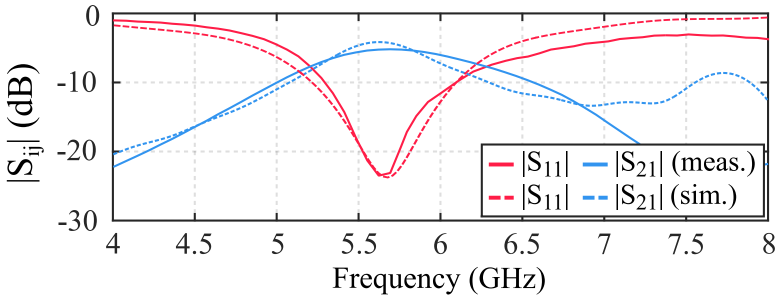

Figure 4.25: Simulated and measured scattering parameters of the TIW and corresponding transitions to coaxial.

lations and measurements coincide, as depicted in Figure 4.25. Consequently, as predicted, the equivalent relative permittivity has increased. Employing the same procedure, the equivalent electrical conductivity has been found to be $\sigma_{\text{eq}} = 2 \cdot 10^4$ S/m.

4.3.4 Simulations

Once the materials have been characterised, the mixed embroidered and woven cavity-backed slot antenna has been designed and simulated. The proposed design has been analysed using a 3D high frequency EM simulator with a Transient Solver. Figure 4.26 depicts the simulated magnitude of the reflection coefficient (dB) and bandwidth (shaded) using the LM. Figure 4.27 represents the definition of the E–plane and the H–plane of the proposed antenna, whereas Figure

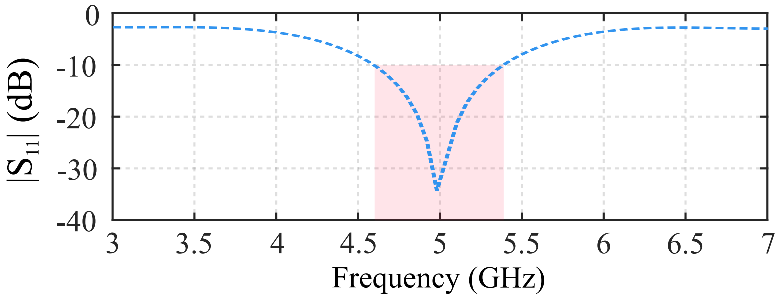

Figure 4.26: Simulated magnitude of the reflection coefficient (dB) and bandwidth (shaded) of the antenna.

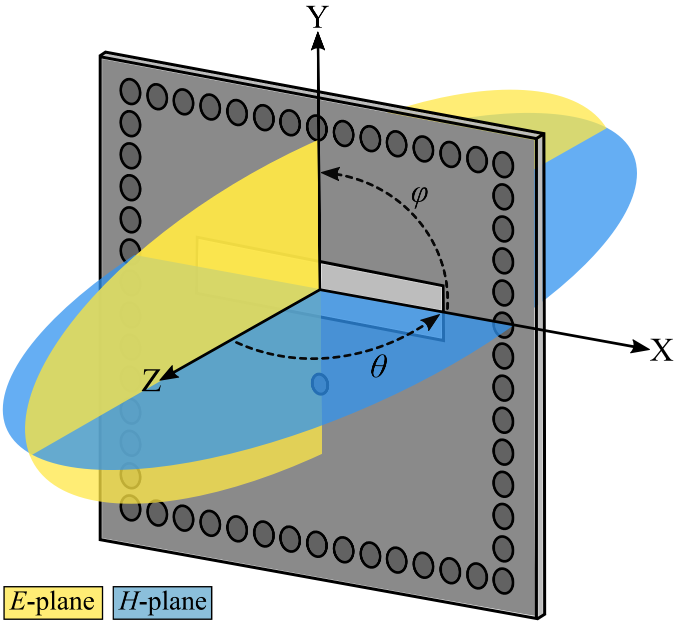

Figure 4.27: Definition of the E–plane and the H–plane.

4.28 depicts the simulated normalised radiation patterns: E–plane and H–plane, including both CP and XP contributions.

The simulated values of the gain, directivity and radiation efficiency are $G_{\mathrm{S}} = -5.1$ dB, $D_{\mathrm{S}} = 6.3$ dB and $\varepsilon_{\mathrm{eff\_S}} = 7.2$ %, respectively. The negative value of the simulated gain is, essentially, due to the low value of the equivalent conductivity. This low value is the result of using conductive material only for the warp threads, instead of for the warp and the weft threads.

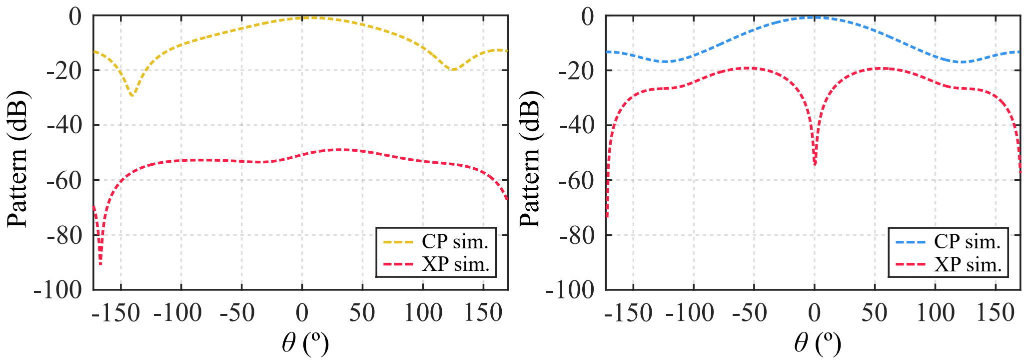

(a)

(b)

Figure 4.28: Simulated normalised radiation patterns of the antenna. (a) E–plane. (b) H–plane.

4.3.5 Fabrication process

A fully textile integrated antenna has been manufactured using three processes. First, the woven structure composed of three layers has been manufactured using an industrial loom. Secondly, an embroidery process has been employed to manufacture the conductive vias. Finally, a cutting process has been required to fabricate the radiating slot. Once the antenna is fabricated, it is connectorised using a SMA connector which is glued to the textile prototype employing conductive epoxy glue.

The woven structure is composed of three layers. The middle layer is completely dielectric, however, the conductive covers of the TIW structure have been manufactured using conductive weft threads and dielectric warp threads. This is due to the the woven structure employed to fabricate the proposed antenna has previously designed and employed for another purpose. Figure 4.29 depicts several schematic drawings of the woven structure.

In Figure 4.29a, a side view of the woven structure is presented, where the warp ends and the weft threads are depicted. Figure 4.29b represents the side view of the woven structure after cutting the threads belonging to the radiating slot using a laser prototyping machine LPKF ProtoLaser. To avoid the presence of loose threads after the cutting process, the woven structure has been manufactured using dielectric binders, as depicted in Figure 4.29c.

Cutting the radiating slot using a laser prototyping machine has been decided due to the unavailability to use a weaving loom provided with an automatic cutting mechanism and an auxiliary layer.

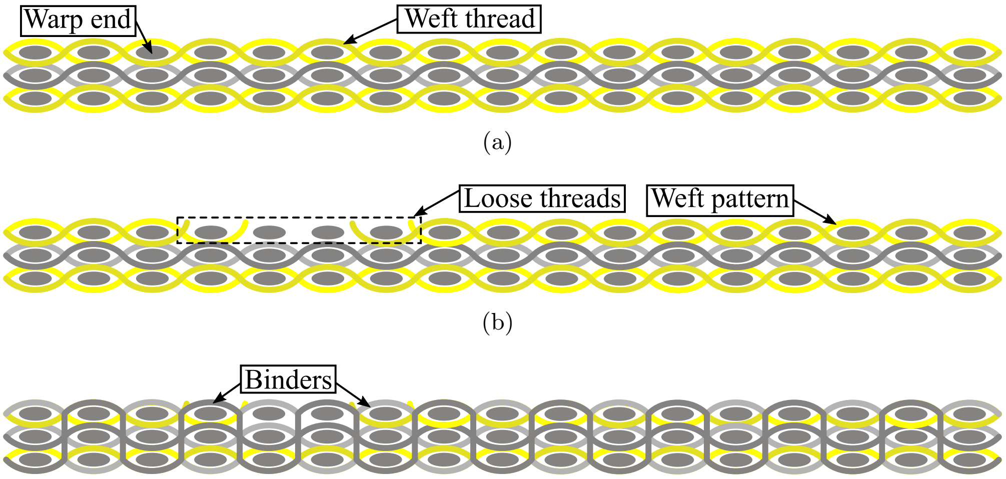

(a)

(b)

(c)

Figure 4.29: Schematic drawing of the woven structure. (a) Side view. (b) Side view after cutting the threads belonging to the radiating slot. (c) Side view using binders to avoid the loose threads.

The conductive vias of the prototype are achieved using an embroidery procedure with a Brother Innovis NV2600 embroidery machine. As a result, Figure 4.30 depicts the manufactured prototype. Figure 4.30a and Figure 4.30b represent, respectively, the top and bottom views of the prototype before its connectorisation. Analogously, Figure 4.30c and Figure 4.30d depict the top and bottom views of the manufactured prototype after the connectorisation.

Figure 4.31 depicts detailed views of the manufactured prototype and corresponding magnifications. In Figure 4.31a, the conductive cover of the woven SIW structure is depicted, in which the conductive warp threads and the dielectric weft threads can be identified. Figure 4.31b represents the woven substrate, whereas Figure 4.31c depicts a side view of the prototype where the three layers can be easily identified.

4.3.6 Experimental validation

With the aim of experimentally validating the prototype, the reflection coefficient has been measured using an Agilent N5247A PNA-X vector network analyser with the set-up presented in Figure 4.32. The measured reflection coefficient has been compared with the simulations, as depicted in Figure 4.33.

The manufactured antenna operates at a central frequency of 5 GHz and the measured bandwidth has been found to be equal to 20 %.

The manufactured prototype has been measured in a spherical range in anechoic chamber in order to characterise its radiation pattern, directivity, gain and radiation efficiency. The measurements have been conducted at the frequency f_o = 5 GHz, which corresponds to the $|S_{11}|$ minimum, as observed in Figure 4.33.

The radiation pattern of the textile AUT has been measured at the distance of R = 5.4 m, which is in the FF region. Figure 4.34a represents the measurement set-up at the spherical range in anechoic chamber, where the AUT has been mounted in a cardboard and plastic platform as detailed shown in Figure 4.34b, and the probe antenna is a Narda 643 SGH [22]. The E-plane and H-plane normalised radiation patterns of the AUT have been measured. The measurements have been processed using ANCAN software [34, 35] and compared with

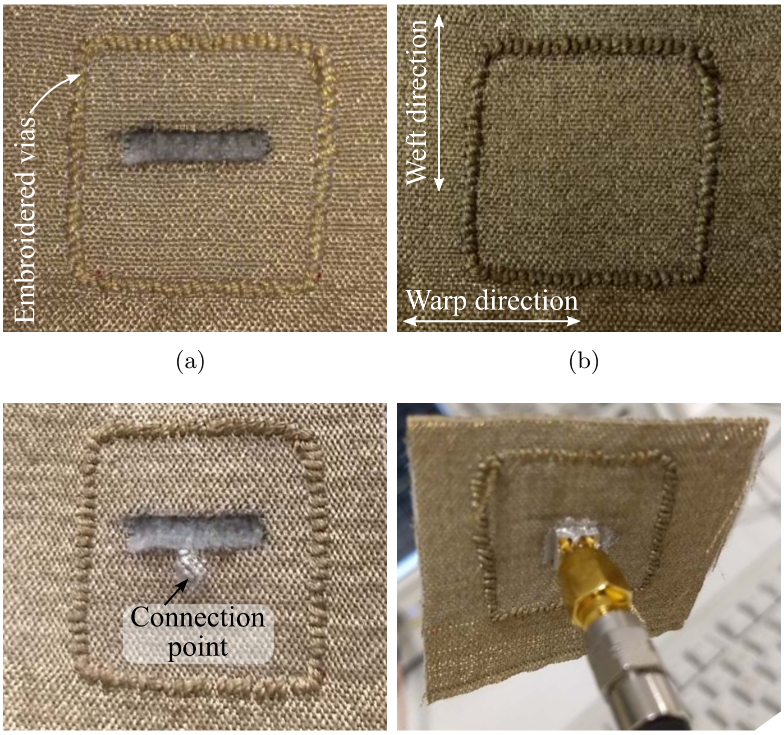

(a) (b)

(c) (d)

Figure 4.30: Manufactured prototype. (a) Top view before connectorising. (b) Bottom view after connectorising. (c) Top view after connectorising. (d) Bottom view after connectorising.

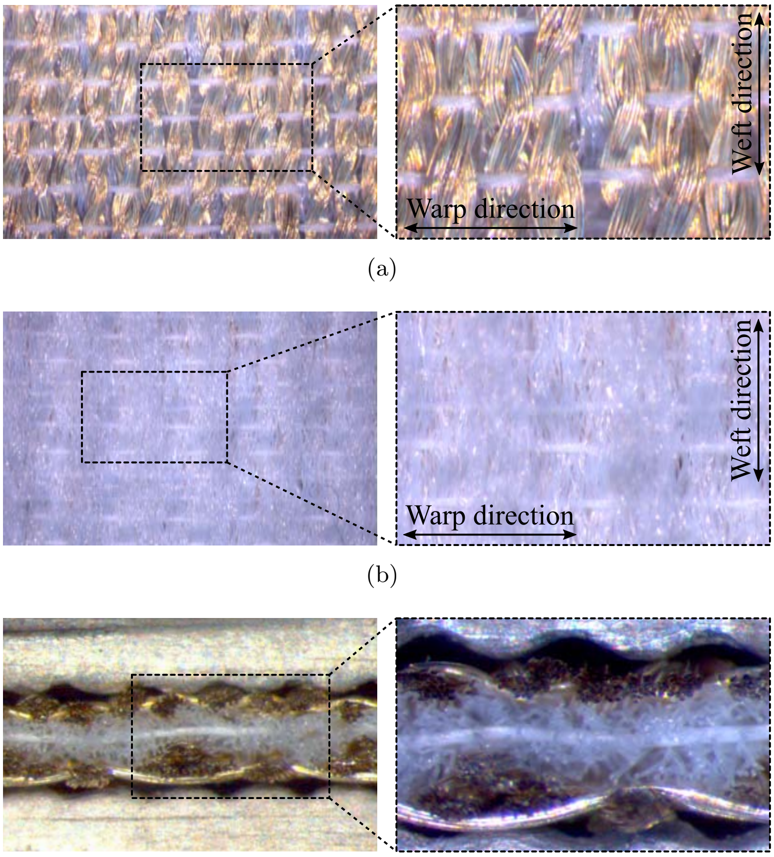

(a)

(b)

(c)

Figure 4.31: Detailed views of the manufactured prototype and magnifications. (a) Conductive cover of the TIW structure. (b) Substrate. (c) Side view.

the simulated data, as depicted in Figure 4.35.

A good agreement between simulated and measured CP components can be noticed. The difference between the simulated and measured CP components of the E-plane can be due to a fabrication defect in the slot, which is not exactly rectangle-shaped as required, as it can be perceived in Figure 4.30a and Figure 4.30c. However, in both E-plane and H-plane measured radiating patterns, the backward radiation is reduced in comparison to the simulations. The measured XP components present higher levels in comparison to simulations, especially in the E-plane, and may be due to the XP component of the probe antenna.

Directivity has been calculated by integrating the measured AUT radiation pattern, yielding to $D_{\mathrm{M}} = 7.49$ dB, which is in agreement with the low direc-

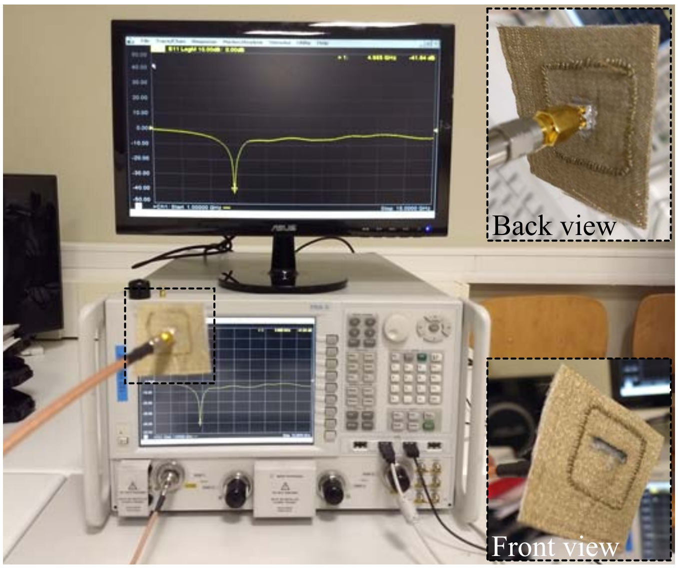

Figure 4.32: Measurement set-up with PNA-X and magnifications of prototype under test.

tivity of the AUT radiation pattern (as confirmed by the normalised directive gain pattern depicted in Figure 4.36a). Analogously, Figure 4.36b depicts the measured normalised gain pattern in the backward direction.

AUT gain has been calculated by means of the inter-comparison technique [25], leading to $G_{\mathrm{M}} = -4.9$ dB. Finally, given the AUT gain and directivity, the AUT radiation efficiency can be calculated: $\varepsilon_{\mathrm{eff\_M}} = 5.77$ %. A comparative between the simulated and the measured values of the gain, directivity and radiation efficiency is summarised in Table 4.9.

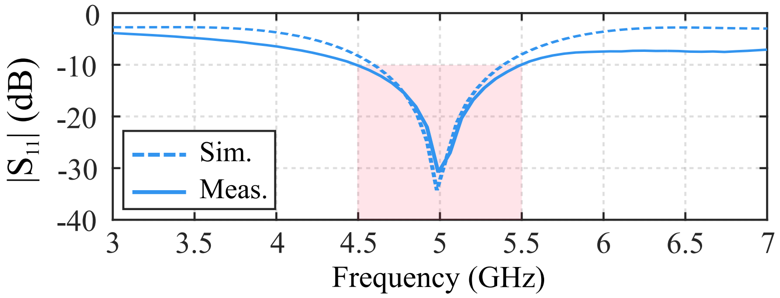

Figure 4.33: Simulated and measured magnitude of the reflection coefficient (dB) and bandwidth (shaded).

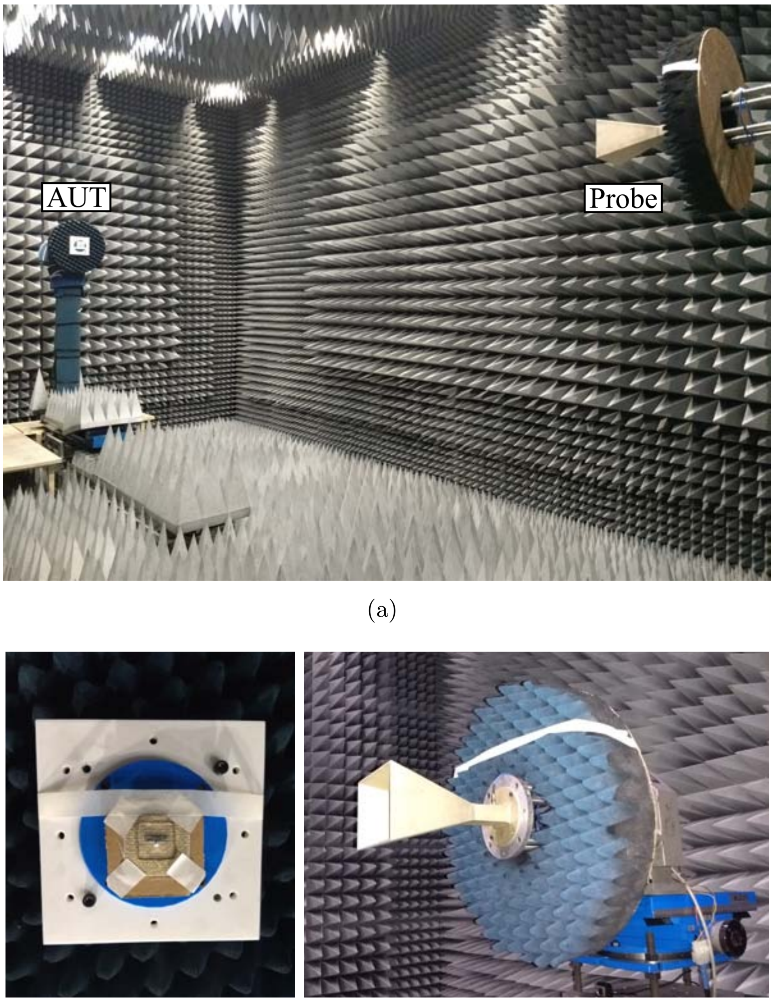

(a)

(b) (c)

Figure 4.34: Measurement set-up in anechoic chamber. (a) Overview of the set-up. (b) Detailed antenna under test (AUT). (c) Detailed probe antenna.

Table 4.9: Comparative between simulations and measurements.

Parameter	Gain (dB)	Directivity (dB)	Radiation efficiency
Simulated	-5.1	6.3	7.2%
Measured	-4.9	7.49	5.77%

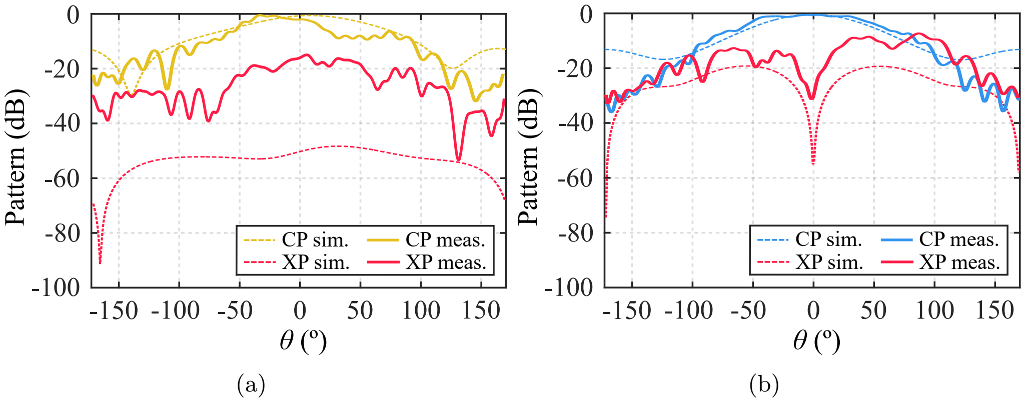

Figure 4.35: Simulated and measured normalised radiation patterns. (a) E–plane. (b) H–plane.

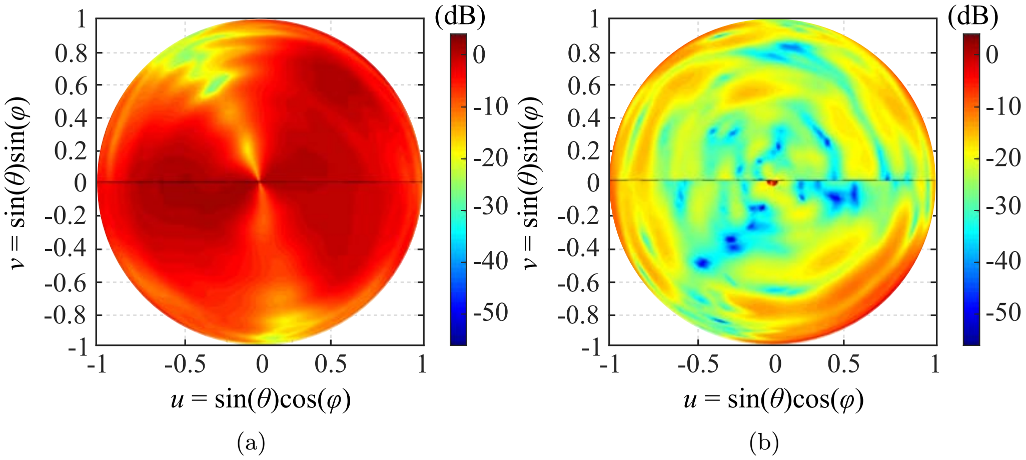

Figure 4.36: Measured normalised gain pattern. (a) Forwards. (b) Backwards.

A comparative between different textile SIW antennas found in the literature has been summarised in Table 4.10 in terms of the operating frequency, f, bandwidth, BW, gain, G, directivity, D, and radiation efficiency, ε_{eff}. In the case a parameter has not been provided in the corresponding paper, NP has been indicated instead. The antennas presented in [26, 27, 30–32] present higher radiation efficiencies for several reasons. The main reason is due to they operate at lower frequencies than the antenna proposed in this section. Moreover, in the beforementioned references, the conductive covers of the SIW structure of the antennas are achieved using different conductive fabrics (*ShieldIT Super* from *LessEMF Inc.* in [30], electrotextile in [26, 31], conductive copper plated Taffeta fabric in [27, 33]), instead of woven patterns. In [29], even though two different values of the gain are presented, for each frequency band, neither the directivity nor the radiation efficiency are provided, consequently, the antenna is not completely characterised.

In [32], a SIW antenna has been presented which is based on the same topology as the antenna presented in this section. However, although the antenna presented in [32] has been fabricated using copper-plated taffeta electro-textile, it is not fully integrated into textile for several reasons. Firstly, the employed substrate is cork and, secondly, the conductive vias are achieved using brass eyelets. Moreover, the conductive taffeta and the cork substrate require an additional adhesive procedure to achieve a compact prototype.

4.3.7 Conclusions

A novel mixed embroidery and woven coaxial-fed cavity-backed slot antenna for its use in wireless body area network applications has been presented. First, a complete characterisation of the employed textile materials has been explained. Then, a translation from a conventional SIW antenna into an embroidery and woven prototype has been presented. To validate the design, a prototype has been manufactured and experimentally characterised. The simulations have been compared to the measurements and a good agreement has been achieved.

Nevertheless, the antenna presents a low gain, as it has been predicted by the simulations, due to the use of conductive threads only in one direction. In order to improve the performance of the antenna, using conductive threads in both directions is proposed, as well as employing conductive threads with higher conductivity.

Table 4.10: Comparative between textile SIW antennas in the literature.

Reference	f (GHz)	BW (%)	G (dB)	D (dB)	ε_{eff} (%)
[30]	2.45	6.12	5.35	NP	74.3
[28]	5.8	4.3	3.12	NP	37.7
[29]	2.45	6.4	2.9	NP	NP
	5.5	12.1	5	NP	NP
[26]	2.45	4.9	5.9	NP	74
[27]	2.45	12.2	6.5	NP	73
[31]	2.4	16.2	4.7	NP	67
[32]	5.15-5.85	23.7	4.3	NP	85
[33]	2.45	NP	5	NP	89
	2.53	NP	5	NP	93
	2.65	NP	5	NP	92
This work	5	20	-4.9	7.49	5.77

Bibliography

[1] V. Lakafosis *et al.*, “Progress towards the first wireless sensor networks consisting on ink-jet printed, paper-based RFID-enabled sensor tags”, *Proceedings of the IEEE*, vol. 98, no. 9, pp. 1601-1609, Sep. 2010. (Cited on page 109)

[2] W. G. Whittow *et al.*, “Inkjet-printed microstrip patch antennas realized on textile for wearable applications”, in *IEEE Antennas and Wireless Propag. Lett.*, vol. 13, pp. 71-74, 2014. (Cited on pages 109, 132, and 135)

[3] S. Dey and N. C. Karmakar, “Design and analysis of a novel low cost high data capacity chipless RFID tag on plastic substrate”, presented in *46th European Microw. Conf.*, London, UK, Sep. 2016. (Cited on page 109)

[4] M. Akbari *et al.*, “Implementation and performance evaluation of graphene-based passive UHF RFID textile tags”, presented in *Int. Symp. Electromagnetic Theory*, Espoo, Finland, Aug. 14-18, 2016. (Cited on page 109)

[5] M. L. Scarpello *et al.*, “Stability and efficiency of screen-printed wearable and washable antennas”, *IEEE Antennas Wireless Propag. Lett.*, vol. 11, pp. 838-841, July, 2012. (Cited on page 109)

[6] G. Ginestet *et al.*, “Embroidered antenna-microchip interconnections and contour antennas in passive UHF RFID textile tags”, in *IEEE Antennas and Wireless Propag. Lett.*, vol. 16, pp. 1205-1208, 2017. (Cited on page 109)

[7] A. Paraskevopoulos *et al.*, “Higher-mode textile patch antenna with embroidered vias for on-body communication”, in *IET Microw. Antennas and Propag.*, vol. 10, no. 7, pp. 802-807, May 2016. (Cited on page 109)

[8] T. Acti *et al.*, “Embroidered wire dipole antennas using novel copper yarns”, in *IEEE Antennas Wireless Propag. Lett.*, vol. 14, pp. 638-641, Nov. 2015. (Cited on page 109)

[9] A. Kiourti, C. Lee and J. L. Volakis, "Fabrication of textile antennas and circuits with 0.1 mm precision", *IEEE Antennas Wireless Propag. Lett.*, vol. 15, pp. 151-153, May 2016. (Cited on page 109)

[10] Z. Wang *et al.*, "Embroidered conductive fibers on polymer composite for conformal antennas", in *IEEE Trans. Antennas Propag.*, no. 9, pp. 4141-4147, Sep. 2012. (Cited on page 109)

[11] L. Alonso-González *et al.*, "Multifunctional fully textile integrated RFID tag to revolutionise the Internet of Things in clothing", in *IEEE Antennas Propag. Mag.*, [under review.] (Cited on page 109)

[12] NXP Icode Slix Product family datasheet, HF-RFID. [Online]. Available: https://www.nxp.com/docs/en/brochure/75016918.pdf (Cited on page 110)

[13] H. Wang, Z. Zhang, Y. Li and Z. Feng, "A dual-resonant shorted patch antenna for wearable application in 430 MHz band," *IEEE Trans. Antennas Propag.*, vol. 61, no. 12, pp. 6195-6200, Dec. 2013. (Cited on pages 120, 132, and 135)

[14] C. Hertleer *et al.*, "Aperture-coupled patch antenna for integration into wearable textile systems," *IEEE Antennas Wireless Propag. Lett.*, vol. 6, pp. 392-395, 2007. (Cited on pages 120, 132, and 135)

[15] S. J. Chen, T. Kaufmann and C. Fumeaux, "Wearable textile microstrip patch antenna for multiple ISM band communications," presented in IEEE Int. Symp. on Antennas and Propag. (APSURSI), Orlando, FL, July 7–13, 2013. (Cited on pages 120, 134, and 135)

[16] S. Ha, S. Lee, H. J. Yoo and C. Jung, "Compact textile patch antenna for wearable fabric applications," presented in Asia-Pacific Microwave Conf., Yokohama, Japan, Dec. 7–10, 2010. (Cited on pages 120, 134, and 135)

[17] S. J. Ha and C. W. Jung, "Reconfigurable beam steering using a microstrip patch antenna with a U-slot for wearable fabric applications," *IEEE Antennas Wireless Propag. Lett.*, vol. 10, pp. 1228-1231, 2011. (Cited on pages 120, 134, and 135)

[18] I. Gil and R. Fernández-García, "Wearable GPS patch antenna on jeans fabric," presented in Progress in Electromagnetic Research Symp. (PIERS), Shanghai, China, Aug. 8–11, 2016. (Cited on pages 120, 134, and 135)

[19] L. Alonso-González *et al.*, "Fully textile-integrated microstrip-fed slot antenna for dedicated short-range communications", in *IEEE Trans. Antennas Propag.*, vol. 66, no. 5, pp. 2262-2270, May 2018. (Cited on pages 120 and 135)

[20] L. Chao *et al.*, "Dielectric permittivity measurements of thin films at microwave and terahertz frequencies", presented in *European Microw. Conf.*, Manchester, UK, Oct. 10–13, 2011. (Cited on page 124)

[21] B. C. Steele, "Electronic ceramics", *Elsevier Applied Science*, London, UK, USA, 1991, pp. 140. (Cited on page 124)

[22] Narda. Standard Gain Horns, datasheet [accessed September 7, 2017]. Available at: https://nardamiteq.com/docs/WAVEGUIDEHORNANTENNAS_STANDARD_GAIN_HORNS_2.60_TO_40_GHZ.PDF (Cited on pages 131 and 144)

[23] A. Malarky, G. Z. Rafi, S. Safavi-Naeini and L. Delgrossi, "A Planar Dual Band GPS and DSRC Antenna for Road Vehicles", presented at the IEEE 66th Vehicular Technol. Conf., Baltimore, MD, 2007, pp. 2096-2100. (Cited on page 132)

[24] C. Y. Liou, S. G. Mao, T. C. Chiang and C. T. Tsai, "Compact and low-profile conical antenna for automotive DSRC application", IEEE Int. Symp. on Antennas and Propag. (APSURSI), Fajardo, Puerto Rico, 2016, pp. 117-118. (Cited on page 132)

[25] IEEE Standard test procedures for antennas, ANSI/IEEE Std 149-1979. (Cited on pages 132 and 146)

[26] R. Moro *et al.*, "Textile microwave components in substrate integrated waveguide technology," *IEEE Trans. Microw. Theory and Techn.*, vol. 63, no. 2, pp. 422-432, Feb. 2015. (Cited on pages 136, 149, and 150)

[27] R. Moro *et al.*, "Circularly-polarised cavity-backed wearable antenna in SIW technology," *IET Microw. Antennas Propag.*, vol. 12, no. 1, pp. 127-131, Oct. 2018. (Cited on pages 136, 149, and 150)

[28] Y. Hong, J. Tak and J. Choi, "An all-textile SIW cavity-backed circular ring-slot antenna for WBAN applications," *IEEE Antennas Wireless Propag. Lett.*, vol. 15, pp. 1995-1999, 2016. (Cited on pages 136 and 150)

[29] S. Yan, P. J. Soh and G. A. E. Vandenbosch, "Dual-band textile MIMO antenna based on substrate-integrated waveguide (SIW) technology," *IEEE Trans. Antennas Propag.*, vol. 63, no. 11, pp. 4640-4647, Nov. 2015. (Cited on pages 136, 149, and 150)

[30] M. E. Lajevardi and M. Kamyab, "Ultraminiaturized metamaterial-inspired SIW textile antenna for off-body applications," in *IEEE Antennas Wireless Propag. Lett.*, vol. 16, pp. 3155-3158, 2017. (Cited on pages 136, 149, and 150)

[31] S. Agneessens, "Coupled eighth-mode substrate integrated waveguide antenna: small and wideband with high-body antenna isolation," in *IEEE Access*, vol. 6, pp. 1595-1602, 2018. (Cited on pages 136, 149, and 150)

[32] O. Caytan *et al.*, "Half-mode substrate-integrated-waveguide cavity-backed slot antenna on cork substrate," in *IEEE Antennas Wireless Propag. Lett.*, vol. 15, pp. 162-165, 2016. (Cited on pages 136, 149, and 150)

[33] S. Lemey, F. Declercq and H. Rogier, "Dual-band substrate integrated waveguide textile antenna with integrated solar harvester," in *IEEE Antennas Wireless Propag. Lett.*, vol. 13, pp. 269-272, 2014. (Cited on pages 136, 149, and 150)

[34] Y. Alvarez and F. Las-Heras, "ANCAN: an integrated software tool for the analysis and characterization of antenna arrays," in *IEEE Antennas Propag. Mag.*, vol. 49, no. 6, pp. 156-164, Dec. 2007. (Cited on page 144)

[35] Y. Alvarez and F. Las-Heras, "Software tool for antenna array simulation as educational support in telecommunication engineering," in *IEEE Antennas Propag. Soc. Int. Symp.*, Albuquerque, NM, July 9-14, 2006. (Cited on page 144)

5

Fully woven frequency selective surfaces

Contents

This chapter includes the description of fully woven textile integrated frequency selective surfaces (FSS) achieving a bandstop behaviour.

5.1 Narrow-band FSS

5.1.1 Introduction

During the last few years, there has been an overwhelming interest in FSS due to the wide number of applications in which they can be used [1], such as absorbers [2], artificial magnetic conductors [3, 4], electromagnetic shielding, among others. The electromagnetic shielding can be achieved thanks to the bandpass [5,6] or bandstop [7,8] responses of the FSS, depending on the periodic structure.

Different approaches have been used to develop FSS, from conventional designs based on resonators implemented over rigid substrates [9–11], FSS based on 3D printing [12], the use of high permittivity ceramic materials in order to avoid conductive materials [13], thicker multiband designs based on SIW technology [14] or multilayered designs [15]. The before mentioned alternatives present different advantages, such as the possibility of achieving high precision details in the fabricated prototypes. Nevertheless, none of them are flexible or washable through industrial processes, and their dimensions are constrained by the prototyping machine or 3D printer, leading to a limited number of unit cells in the manufactured design.

In order to solve these problems, there has been an increasing interest in flexible FSS manufactured using different technologies applied to textiles, such as embroidery [16], ink-jet printing [17] or screen printing [18]. However, these solutions still present the disadvantages thoroughly explained in Chapter 1. Therefore, with the aim of achieving a large, flexible and washable FSS completely integrated into textile, a narrow-band FSS implemented in a woven structure is proposed [19].

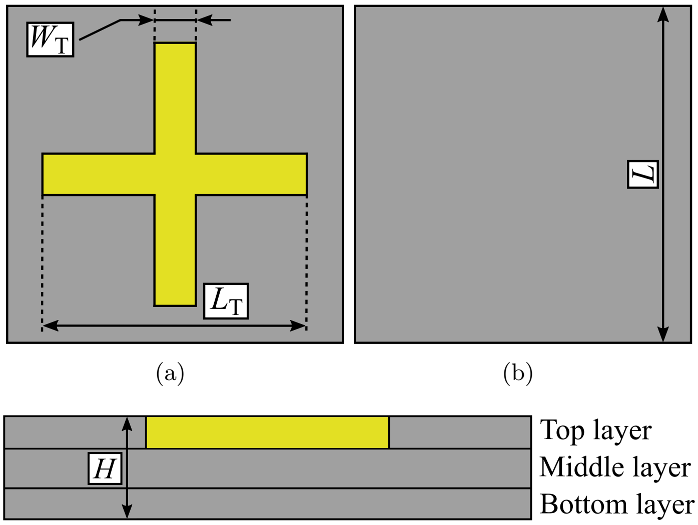

(a)

(b)

(c)

Figure 5.1: Schematic drawing of the unit cell and corresponding dimensions. (a) Top layer: $W_T = 5$ mm and $L_T = 35$ mm. (b) Middle or bottom layer: $L = 45$ mm. (c) Side view and its layers: $H = 1$ mm.

5.1.2 Structure of the FSS

A bandstop FSS is proposed to work at 3.75 GHz with a 0.8 GHz bandwidth. The FSS has been designed from a unit cell. Figure 5.1a and Figure 5.1b represent, respectively, the top and bottom views of the unit cell. The unit cell is composed of three layers, leading to a total height denoted by H as depicted in Figure 5.1c, where the middle and bottom layers are identical and completely dielectric. The top layer of the unit cell is composed of a cross-shaped resonator, whose geometric parameters are L_T and W_T, respectively. The total length of the square-shaped unit cell is L.

5.1.3 Description of the employed materials

Different materials have been employed for the design of the FSS, for both the weft and the warp directions. In the proposed FSS, the warp direction coincides with the direction of the Y–axis. Consequently, the weft direction is oriented in the X–axis direction.

Electrically conductive *Shieldex 117f17 2-ply* yarns have been used for the conductive warp and weft threads. The diameter of the *Shieldex 117f17 2-ply*

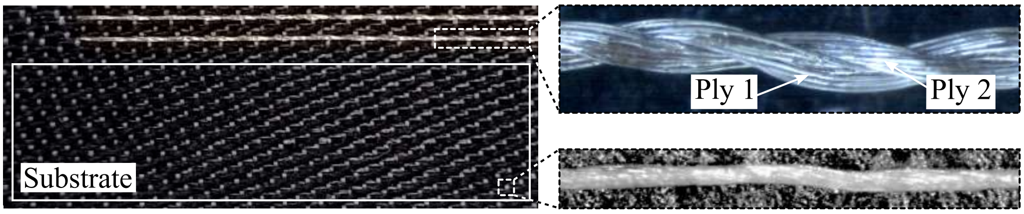

Figure 5.2: Woven substrate with two conductive threads and magnifications: a *Shieldex* thread and a dielectric *PET* warp thread.

yarns has been aproximated to $d_{\text{Shieldex}} = 0.3$ mm. In the upper right corner of the Figure 5.2 a sample of a *Shieldex 117f17 2-ply* yarn is depicted.

For the dielectric parts of the FSS two different types of threads have been used. One the one hand, high tenacity black polyethersulfone (commonly known as PES) 550 dtex, formed by 28 filaments, has been employed for the weft threads. The diameter of the *PES* yarns is $d_{\text{PES}} = 0.3$ mm. One the other hand, for the warp threads, white polyethylene-terephthalate (commonly known as PET or polyester) $76f24$, which means that it is composed of 76 filaments with 24 dtex, has been used. The diameter of the *PET* yarns has been approximated to $d_{\text{PET}} = 0.1$ mm. Figure 5.2 depicts a sample of the woven substrate, where the black *PES* is depicted, and a magnification of a warp *PET* yarn is detailed in the bottom right corner.

5.1.4 Design of the woven FSS

A layer-to-layer angle interlock 3D woven bandstop FSS is proposed. The FSS has been designed from a unit cell to which perfect boundary conditions (PBC) have been applied, leading to an ideal infinite FSS. Nevertheless, a finite version composed of 8 × 8 unit cells has also been simulated to be able to compare the simulations with the measurements.

The substrate of the FSS is a multilayered fabric composed of three layers of weft *PES* threads interwoven using warp *PET* yarns, leading to a satin woven structure. Due to the air gaps between the threads, a sample of the substrate has been manufactured and electromagnetically characterised using an Agilent Technologies 85072A Split Cylinder Resonator. Consequently, its relative dielectric permittivity and loss tangent have been found to be $\varepsilon_{\text{subs}} = 1.75$ and $\tan(\delta)_{\text{subs}} = 0.0037$, respectively. Figure 5.2 represents the top view of a sample of the woven substrate.

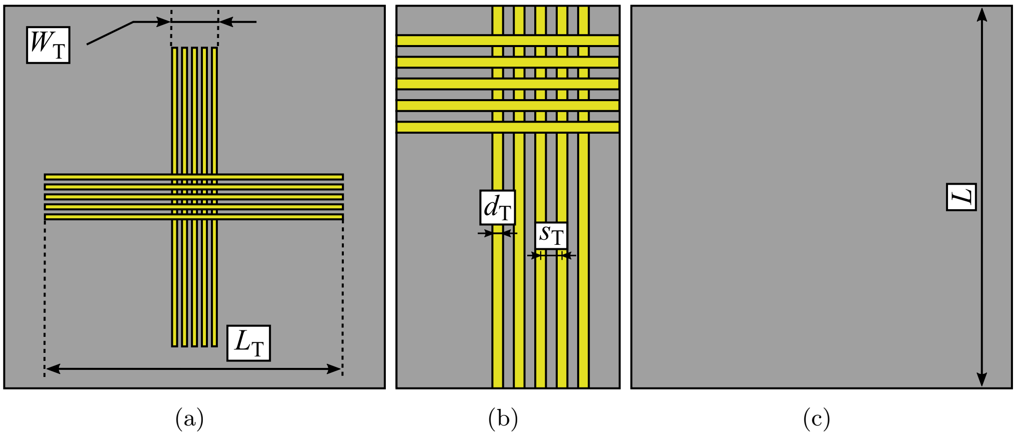

(a) (b) (c)

Figure 5.3: Schematic drawing of the proposed unit cell and its dimensions. The dimensions are summarised in Table 5.1. (a) Top view. (b) Detailed view of the dimensions (top view). (c) Bottom view.

As previously mentioned, the woven prototype is composed of three layers: the top layer is a dielectric layer in which the conductive cross-shaped resonators are inserted, and the middle and bottom layers are identical and completely dielectric layers. Two dielectric layers have been used due to the already mounted warp threads in the employed weaving machine. Nevertheless, the use of an additional dielectric layer (the bottom layer) does not suppose any modification in the EM behaviour of the FSS. Consequently, the three layers are identical, except for the positions where the dielectric threads have been substituted by conductive threads to implement the resonators.

Due to the dimensions of the unit cell, the simulation of the complete woven structure is not possible with the available resources. Consequently, the conductive resonators placed in the top layer are translated into 5 *Shieldex* threads as shown in Figure 5.3a, which will be simulated as 5 conductive strips, separated a distance s_T between centres and whose widths are $d_T = d_{\text{Shieldex}}$, as it can be

Table 5.1: Dimensions (mm) of the top layer and the unit cell of the FSS.

Top layer				Unit cell	
L_T	W_T	d_T	s_T	L	H
35	5	0.3	1.2	45	1

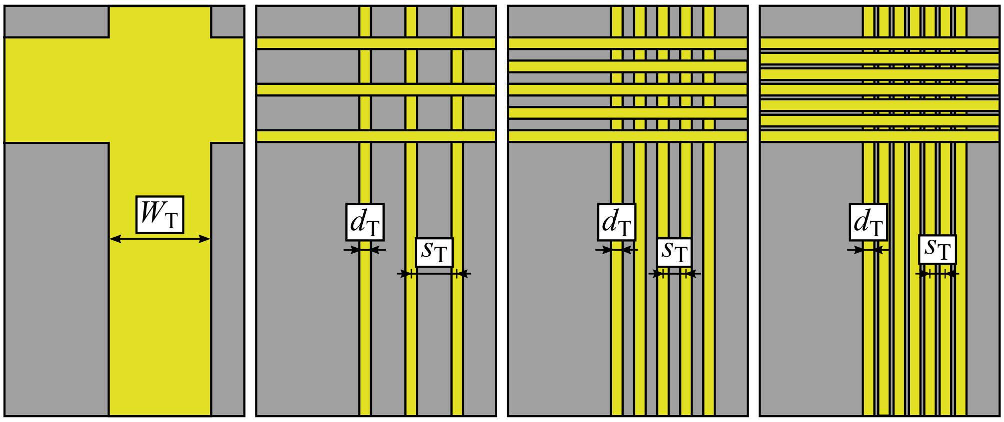

(a) (b) (c) (d)

Figure 5.4: Detailed schematic drawing of the different versions of the proposed unit cell and its dimensions. (a) Uniform . (b) Three strips. (c) Five strips. (d) Nine strips.

Table 5.2: Dimensions (mm) of the different versions of the translation into a woven prototype.

Figure 5.4a		Figure 5.4b		Figure 5.4c		Figure 5.4d	
W_T	s_T	d_T	s_T	d_T	s_T	d_T	s_T
5	0	0.3	2.4	0.3	1.2	0.3	0.6

seen in Figure 5.3b. The middle and bottom layers are completely dielectric as depicted in Figure 5.3c. All the beforementioned dimensions are summarised in Table 5.1.

Nevertheless, Figure 5.4 depicts different detailed versions of the translation of the unit cell into a woven prototype. Figure 5.4a represents the detailed uniform cross-shaped resonator which would be structured in a conventional rigid substrate. Figure 5.4b, Figure 5.4c and Figure 5.4d represent, respectively, a detailed view of the unit cell translated using 3, 5 and 9 strips corresponding to 3, 5 and 9 conductive threads. While the dimension denoted by d_T remains constant in the non-uniform resonators, the distance s_T is modified as summarised in Table 5.2. In section 5.1.5, the different electromagnetic behaviours of the presented versions are explained.

5.1.5 Simulations

The proposed design has been analysed using the 3D full–wave HFSS software. Figure 5.5 depicts an overview of the unit cell to which PBC have been applied. The tangential component of the magnetic field, H_T, in the two boundaries which are parallel to the YZ–plane fulfils $H_\mathrm{T} = \vec{H} \cdot \hat{n}_\mathrm{Y} = H_\mathrm{Y} = 0$. Alternatively, the tangential component of the electric field, E_T, in the two boundaries which are parallel to the XZ–plane fulfils $E_\mathrm{T} = \vec{E} \cdot \hat{n}_\mathrm{X} = E_\mathrm{X} = 0$, being $\hat{n}_\mathrm{Y}$ and $\hat{n}_\mathrm{X}$ the unit vectors in Y and X direction, respectively. These two conditions lead to a PBC environment. The unit cell has been illuminated with a plane wave, whose polarisation axis is vertically oriented (Y–axis), propagating in the $\hat{\mathrm{k}}$ direction from port 1 to port 2, so that the S_{21} parameter can be calculated.

First, different versions of the translation into a woven prototype have been simulated as depicted in Figure 5.6. These versions have been simulated as infinite FSS using the set-up presented in Figure 5.5, with two ports at a distance of $D/2 = 0.75$ m from each side of the FSS. Consequently, the more strips employed in the translation, the higher attenuation achieved. Nevertheless, instead of using the translation proposed in Figure 5.4d with 9 strips, the translation depicted in Figure 5.4c with 5 strips has been employed. This decision has been made due to manufacturing specifications.

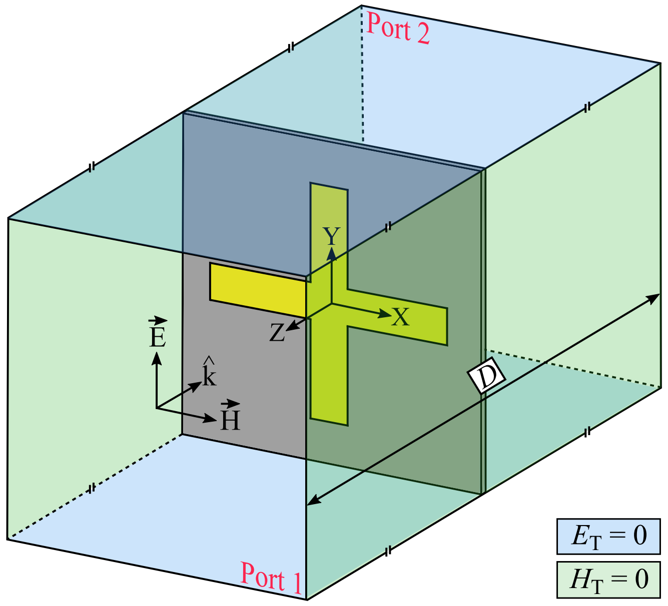

Figure 5.5: Overview of the unit cell with the boundary conditions.

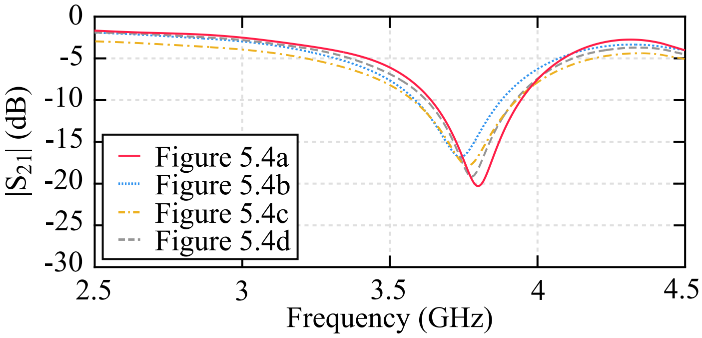

Figure 5.6: Simulated $|S_{21}|$ parameter for the different versions of the unit cell proposed in Figure 5.4 using the infinite FSS (set-up in Figure 5.5).

Table 5.3: Characteristics of the employed horn antennas.

Narda Standard Gain Horns		
Model	644	643
Notation	N644SGH	N643SGH
Low Frequency (GHz)	2.6	3.95
High Frequency (GHz)	3.95	5.9
Waveguide dimensions	WR-284	WR-187

Then, an infinite array of resonators has been simulated and compared to a finite version 8×8 unit-cell. For the finite FSS, two horn antennas are simulated at a distance of $D/2$ from each side of the FSS in order to illuminate the FSS emulating the real set-up. Two pairs of different horn antennas are required for the simulations and characterisation of the FSS in order to guarantee the single-mode operation in the complete range of frequencies.

Consequently, a pair of Narda 644 SGH antennas and a pair of Narda 643 SGH antennas have been employed, whose characteristics are summarised in Table 5.3 [20]. For this reason, the non-shaded and the shaded range of frequencies represent, respectively, the frequencies in which a single-mode operation of each different horn is guaranteed, and this is applicable for the all of the following graphics.

The simulated set-up for the finite FSS is depicted in Figure 5.7a. The simulated S_{21} parameter, normalised by the response in the absence of the FSS, is shown in Figure 5.7b. The dimensions of the simulated horns are identical to the dimensions of the real horns employed for the validation.

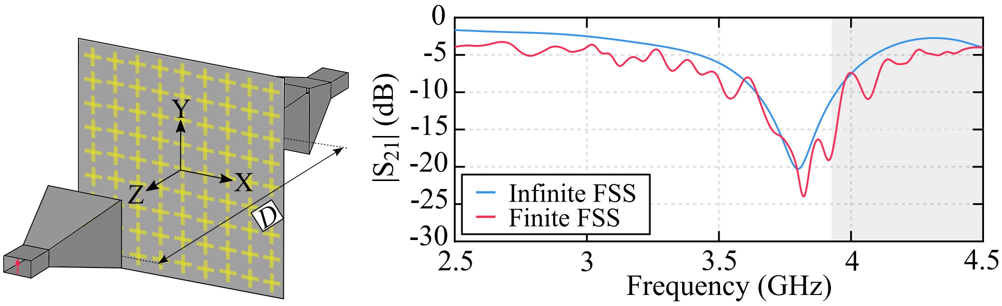

(a) (b)

Figure 5.7: Normal incidence. (a) Schematic drawing of the simulated set-up ($D = 1.5$ m). (b) Simulated $|S_{21}|$ parameter for an infinite FSS (set-up in Figure 5.1a) and for a finite FSS.

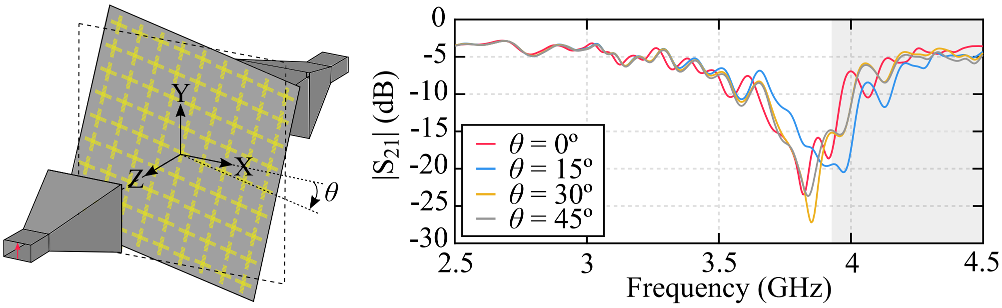

(a) (b)

Figure 5.8: Set-up and performance in terms of angle θ. (a) Schematic drawing of the simulated set-up. (b) Simulated $|S_{21}|$ parameter and the influence of the angle θ on the finite FSS performance.

The behaviour of the designed FSS in terms of the angle θ formed by the electric field, $\vec{E}$, and the resonators when rotating the FSS around the Z-axis has been studied. For this purpose, the FSS has been simulated from $\theta = 0°$ to $\theta = 45°$ as depicted in Figure 5.8a. The simulated $|S_{21}|$ parameter for the different angles θ is shown in Figure 5.8b. The minimum value of the $|S_{21}|$ parameter is modified with the angle θ, however the attenuation level remains over 10 dB in the studied cases. Consequently, the FSS presents an stable performance in terms of the angle θ.

To study the behaviour of the designed FSS in terms of the angle of incidence, the FSS has been simulated rotating it around its Y–axis, from $\phi = 0°$ to $\phi = 45°$

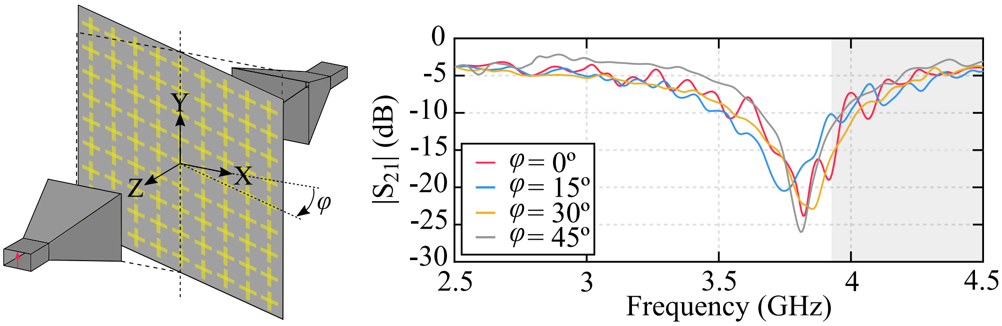

(a)

(b)

Figure 5.9: Set-up and performance in terms of the angle of incidence. (a) Schematic drawing of the simulated set-up. (b) Simulated $|S_{21}|$ parameter and the influence of the angle of incidence on the finite FSS performance.

as depicted in Figure 5.9a. The simulated $|S_{21}|$ parameter for the different angles of incidence is shown in Figure 5.9b. Although the minimum value of the $|S_{21}|$ has been shifted, the simulated FSS presents a stable performance in terms of the angle of incidence.

5.1.6 Fabrication process

A finite 8×8 unit cells FSS has been manufactured using an industrial MüGrip loom. The manufacturing process has been based on satin weaving. The conductive warp yarns are previously mounted in the loom and the conductive weft threads are inserted in the fabric during the fabrication process leading to a conductive lattice in the top layer of the fabric, instead of the required cross-shaped resonators, thanks to an auxiliary layer as depicted in Figure 5.10a.

In Figure 5.10a, the red and blue colored segments of conductive thread correspond, respectively, to the segments of warp and weft conductive threads which are interwoven in the auxiliary layer. In Figure 5.10b, a schematic drawing of the woven structure after the cutting process is depicted, in which the leftover conductive segments have been removed and the cross-shaped resonators are represented.

With the aim of translating the schematic drawing in Figure 5.10 into woven patterns, Figure 5.11 is presented. Figure 5.11a represents the front view of the weft threads and the side view of the warp patterns. In the segment which corresponds to the separation between two adjacent resonators the conductive threads must be interrupted in order to avoid a shortcircuit. For this reason,

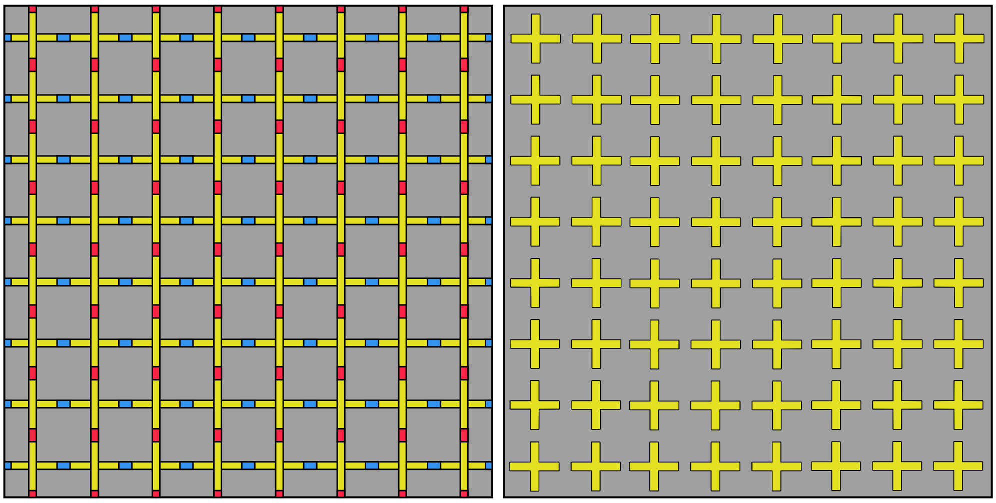

(a)

(b)

Figure 5.10: Schematic drawing of the woven structure before and after the cutting process. (a) Top layer before the cutting process. Red and blue colored segments represent, respectively, warp and weft segments of threads which have been left unwoven from the main fabric for the subsequent cutting procedure. (b) Top layer after the cutting process.

along this segment, the conductive warp threads are interwoven in the auxiliary layer and, subsequently, interwoven again in the main fabric. An analogous process is required for the undesired segments of the weft threads.

An automatic cutting process is then required to remove the auxiliary layer, leading to the representation depicted in Figure 5.11b. In this representation, the weft threads corresponding to the positions of the top layer beneath the auxiliary layer have been left loose, after the cutting process.

The described woven patterns lead to a layer-to-layer angle interlock weaving [21–24], due to the individually woven layers of weft threads through undulated warp threads. In order to, not only connect the different layers to create a multilayered structure, but also avoid the presence of loose weft threads after the cutting process, binders must be employed. Binders are threads which, instead of present a woven pattern in an individual layer, they connect different layers to conform a compact woven structure, as depicted in Figure 5.11c. These threads must be dielectric, in order to achieve the separation between the conductive resonators avoiding the shortcircuits. Due to the necessity of using these binders also between the conductive threads, 5 conductive strips have been employed,

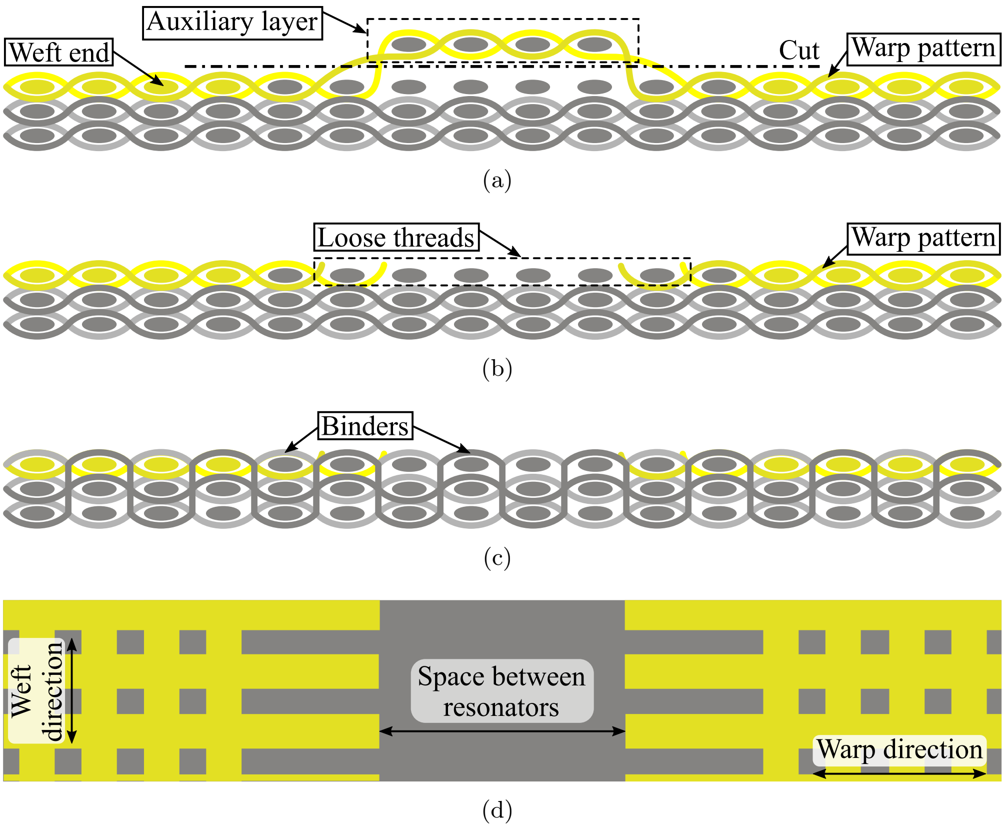

Figure 5.11: Schematic drawing of the woven structure based on a layer-to-layer angle interlock 3D fabric. (a) Side view of the woven structure with using an auxiliary layer. (b) Side view of the woven structure with the loose threads, after cutting the auxiliary layer. (c) Side view of the woven structure using binders to avoid the loose threads. (d) Top view equivalence.

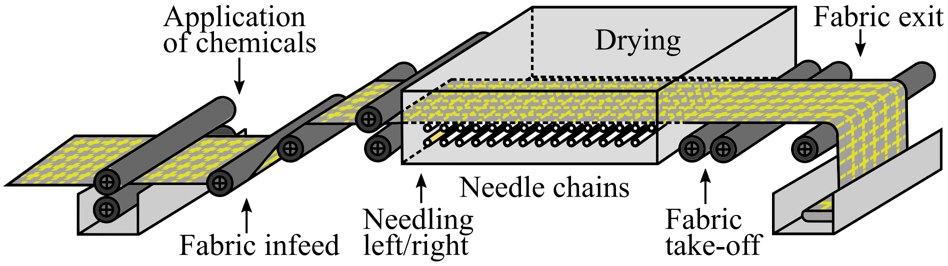

Figure 5.12: Schematic drawing of the finishing process using a stenter machine.

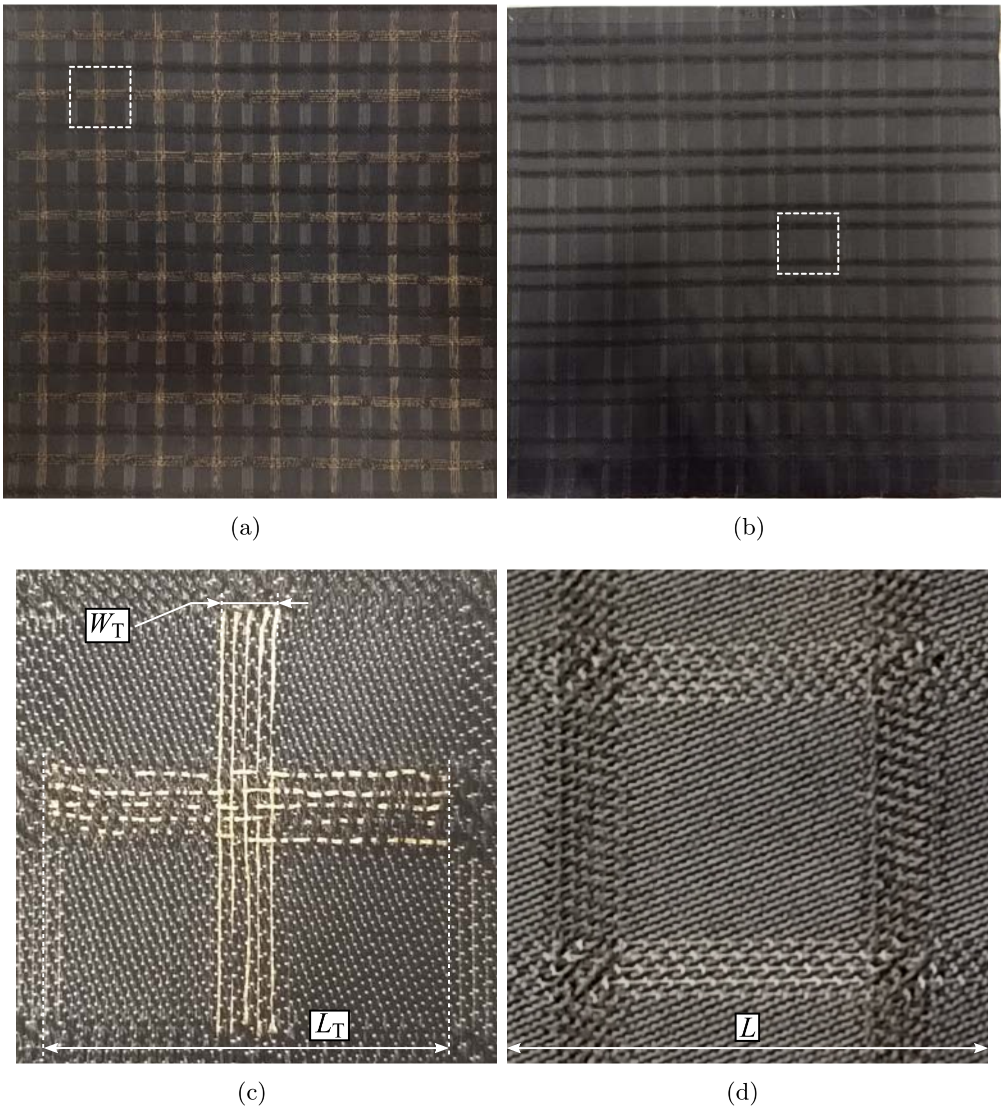

(a) (b) (c) (d)

Figure 5.13: Manufactured prototype and magnification of a unit cell. (a) Top view of the prototype. (b) Bottom view of the prototype. (c) Magnification and dimensions of the top view of the unit cell. (d) Magnification and dimensions of the bottom view of the unit cell.

instead of 9, in the translation into the woven prototype. By the use of the auxiliary layer and the binders, the different cross-shaped resonators can be achieved as schematically depicted in Figure 5.11d.

A finishing process is required after removing the fabric from the loom in order to achieve the requirements. Figure 5.12 depicts a generic finishing process which starts with the insertion of the fabric in liquid chemicals, then needling the fabric and finally applying heat to dry it. The manufactured FSS has been heated at 185° on the frame of the stenter machine. The top view of the manufacture prototype can be seen in Figure 5.13a, whereas the bottom view is depicted in Figure 5.13b. A magnification of a unit cell from the top layer is shown in Figure 5.13c, whereas its analogous bottom view is depicted in Figure 5.13d. The white woven lines in the beforementioned figures are due to the binders.

5.1.7 Experimental validation

The prototype has been experimentally validated using different set-ups and employing the two beforementioned horn antennas, horn N644SGH and horn N643SGH, respectively, which are depicted in Figure 5.14, together with their dimensions in centimetres. All the set-ups are composed of a wooden frame, in which the prototype has been assembled and allows the required movements for the validation under different angles of incidence, two different pairs of horn antennas mounted on rotary platforms for the validation of the different values of the angle θ and a vector network analyser. The S_{21} parameter between the horn antennas, for each set-up, calibrated by using the response between the antennas without the FSS, has been measured using an Agilent N5247A PNA-X vector network analyser and compared with the simulations.

The FSS has been experimentally validated under normal incidence conditions using the set-up shown in Figure 5.15a. The comparison between simulations and measurements can be seen in Figure 5.15b. The manufactured FSS presents a bandstop behaviour, $|S_{21}| < -10$ dB, which provides a 0.6 GHz stopband centered at 3.75 GHz, with a 10 dB minimum attenuation and a 27 dB maximum attenuation. The predicted simulated data agree with the measurements, although the differences may be due to the approximations taken into account in the simulations. In the simulations, conductive flat strips are employed for the resonators, whereas the manufactured conductive woven paths are slightly longer due to the weaving curves. For this reason, the measured range of working frequencies has been slightly shifted to lower values, although the bandwidth has been enhanced.

The FSS has been experimentally validated for different values of the angle $\theta \in [0°, 45°]$, using the set-up shown in Figure 5.16a in which the antennas have been mounted on the rotary platforms. The comparison between simulations

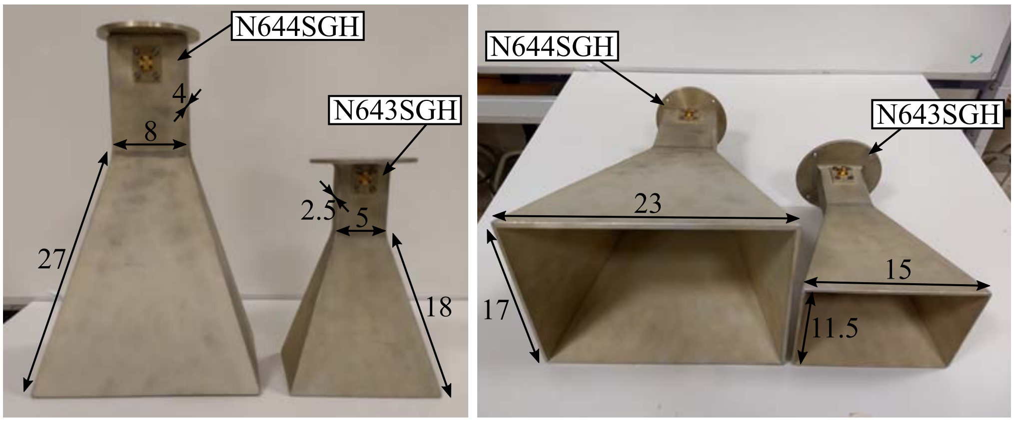

(a)

(b)

Figure 5.14: Horn antennas employed for the measurements and their dimensions in centimetres. (a) Top view. (b) Overview.

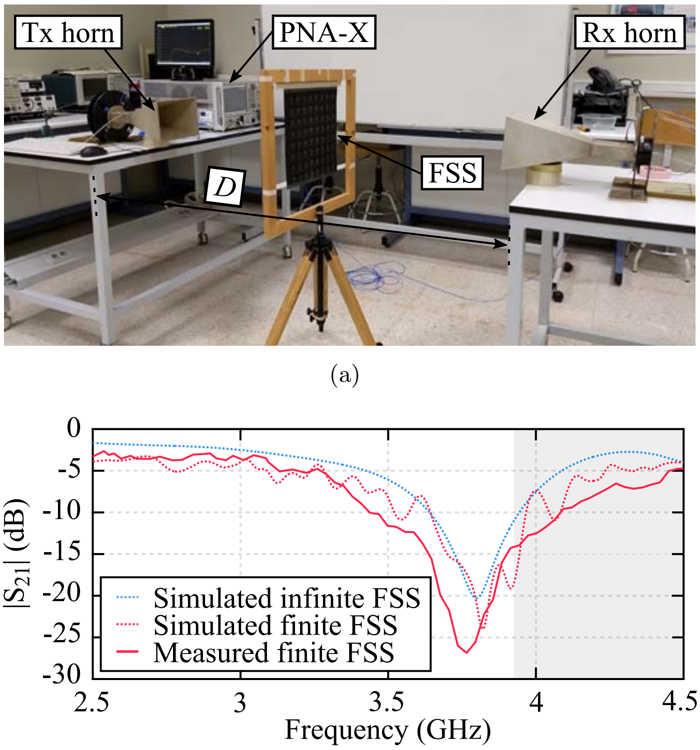

(a)

(b)

Figure 5.15: Normal incidence. (a) Measurement set-up using horn N644SGH ($D = 1.5$ m). (b) Measured vs. simulated $|S_{21}|$ parameter.

and measurements is depicted in Figure 5.16b. The manufactured FSS presents a bandstop behaviour, consequently, the FSS exhibits a stable performance in terms of the angle θ. This represents an interesting point for the potential use of the proposed FSS as a wall cover or curtain to filter undesired frequencies.

The FSS has also been experimentally validated for different angles of incidence, $\phi \in [0°, 45°]$, using the set-up shown in Figure 5.17a. The comparison between simulations and measurements is shown in Figure 5.17b. As predicted, the manufactured FSS also exhibits a stable performance in terms of the angle of incidence, reinforcing its applicability in the aforementioned wall covering.

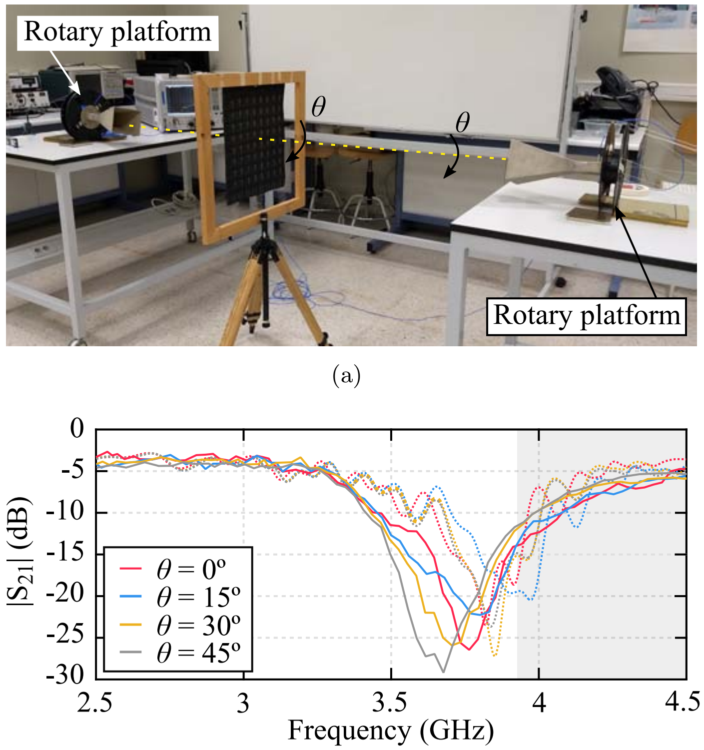

(a)

(b)

Figure 5.16: Performance in terms of the angle θ. (a) Measurement set-up using horn N643SGH. (b) Measured (solid line) vs. simulated (dashed line) $|S_{21}|$ parameter and the influence of the angle θ on the finite FSS performance.

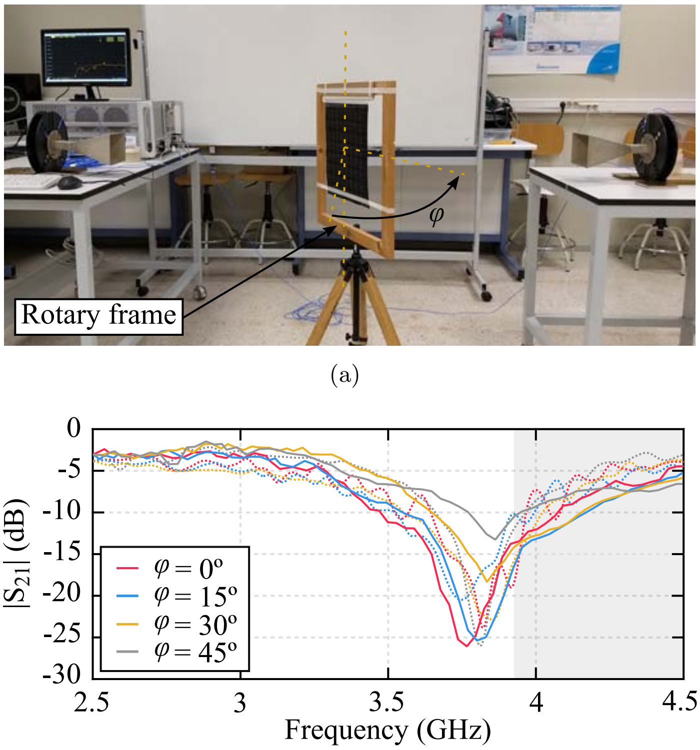

(a)

(b)

Figure 5.17: Angle of incidence. (a) Measurement set-up using horn N643SGH. (b) Measured (solid line) vs. simulated (dashed line) $|S_{21}|$ parameter and the influence of the angle of incidence on the finite FSS performance.

5.1.8 Conclusions

A novel flexible fully textile-integrated bandstop FSS has been presented. A methodology to implement a layer-to-layer angle interlock 3D woven structure and its subsequent cutting procedure to achieve the independent resonators have been throughly explained.

To validate the design, a 8×8 unit–cell prototype has been manufactured and experimentally characterised under different conditions, including different angles of polarisation and angles of incidence. A good agreement between simulations and measurements has been achieved, experimentally verifying the theoretically predicted behaviour of the textile structure. Therefore, the manufactured FSS exhibits a stable performance in terms of the angle of polarisation and the angle of incidence.

The manufacturing procedure using industrial textile machinery provides the possibility of manufacturing flexible and large FSS, as opposed to other alternatives based in conventional substrates, solving the fabrication problems of large shielding surfaces.

5.2 Wideband FSS

5.2.1 Introduction

With the aim of enhancing the bandstop FSS presented in the previous section, in terms of the bandwidth, a broadband FSS is proposed. For this purpose, two isolated layers of resonators are implemented in the woven structure, whose individual resonant frequencies are 3.4 GHz and 5.1 GHz, respectively, leading to a more complex layer-to-layer angle interlock 3D woven structure.

A broadband bandstop behaviour is achieved as a result of the coupling phenomenon between both layers of resonators. In contrast to the FSS presented in the previous section, this FSS is implemented using square-ring resonators instead of cross-shaped resonators [25].

5.2.2 Structure of the FSS

The broadband bandstop FSS is designed to opertate at 5 GHz with a 1.8 GHz bandwidth. For this purpose, first, the FSS has been designed from a unit cell to which PBC have been applied, leading to an ideal infinite FSS. Figure 5.18a represents an overview of the unit cell and the boundary conditions, which are analogous as the conditions explained in the previous section.

Figure 5.18b depicts a side view of the unit cell and its layers. The unit cell is composed of three layers, the top and the bottom layers which are separated by an insulating layer (middle layer), leading to a total height of the unit cell denoted by H. The top layer of the unit cell is composed of a square-shaped ring resonator, whose side and width are L_{T} and W_{T}, respectively, as it can be seen in Figure 5.18c. Similarly, the bottom layer of the unit cell is composed of a square-shaped ring resonator, whose side and width are L_{B} and W_{B}, respectively, as it can be seen in Figure 5.18d. The total length of the square-shaped unit cell is L. All the mentioned dimensions are summarised in Table 5.4.

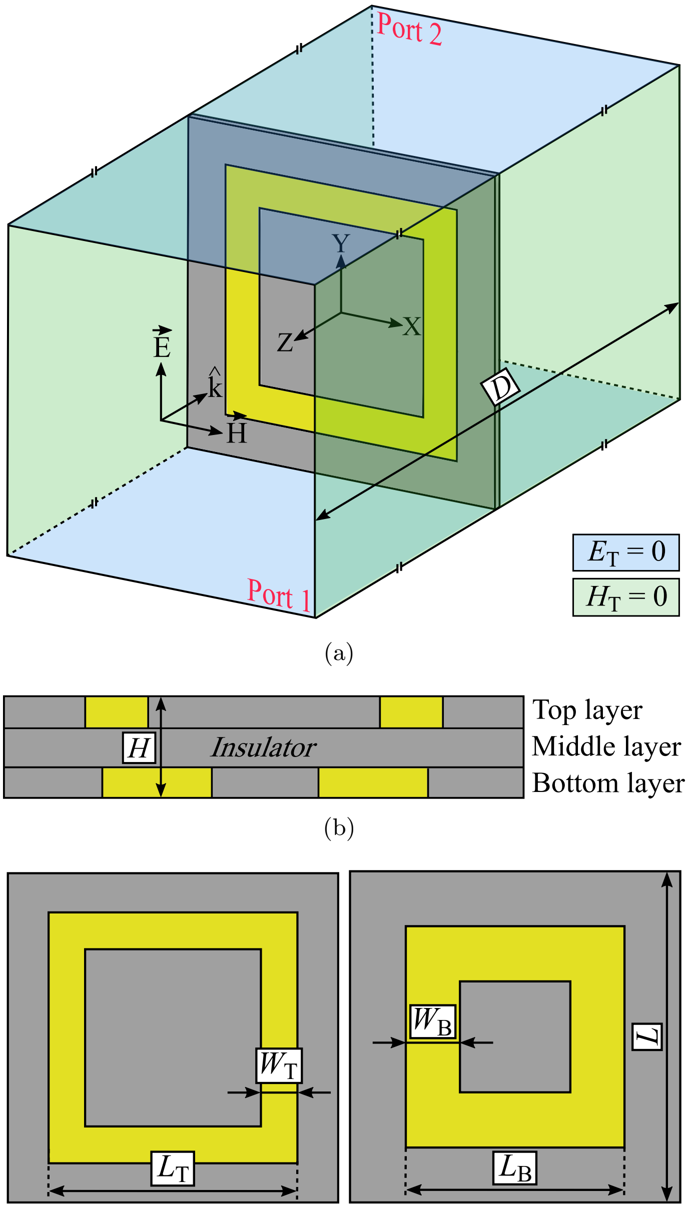

Figure 5.18: Schematic drawing of the unit cell and dimensions. (a) Overview of the unit cell and PBC. (b) Side view. (c) Top layer. (d) Bottom layer.

5.2.3 Description of the employed materials

The proposed FSS is completely integrated in textile, therefore, different materials have been employed for the warp and weft threads during its fabrication. In the proposed FSS, the warp and weft directions coincide with the directions of the Y–axis and X–axis, respectively.

Electrically conductive *Shieldex 117f17 2-ply* yarns have been used for the conductive warp and weft threads. The equivalent diameter of the *Shieldex 117f17 2-ply* yarns is $d_{\text{Shieldex}} = 0.3$ mm. For the dielectric parts of the FSS two different types of threads have been used. For the weft threads, high tenacity white PES 550 dtex has been employed. The diameter of the *PES* yarns is $d_{\text{PES}} = 0.3$ mm. Alternatively, for the warp threads, white PET $76f24$, which means that it is composed of 76 filaments with 24 dtex, has been used. The diameter of the *PET* yarns is $d_{\text{PET}} = 0.1$ mm. Figure 5.19 depicts a comparison between the employed dielectric materials.

5.2.4 Design of the woven FSS

The FSS has been designed from a unit cell to which PBC have been applied, leading to an ideal infinite FSS, as previously explained. Nevertheless, a finite version composed of 9 × 9 unit cells has also been simulated to compare the simulations with the measurements. First, a sample of the dielectric substrate has been manufactured and electromagnetically characterised in order to design the FSS and, therefore, translate it into a woven prototype.

The substrate of the FSS is a multilayered fabric composed of three layers of weft *PES* threads interwoven using warp *PET* yarns, leading to a satin woven structure, which has been manufactured and electromagnetically characterised using an Agilent Technologies 85072A Split Cylinder Resonator. Its relative dielectric permittivity and loss tangent have been found to be $\varepsilon_{\text{subs}} = 1.7$ and $\tan(\delta)_{\text{subs}} = 0.00362$, respectively. Figure 5.20 shows a side view of the woven substrate.

Table 5.4: Dimensions (mm) of the FSS.

Top layer		Bottom layer		Unit cell	
L_{T}	W_{T}	L_{B}	W_{B}	L	H
34	5	30	7.5	45	1

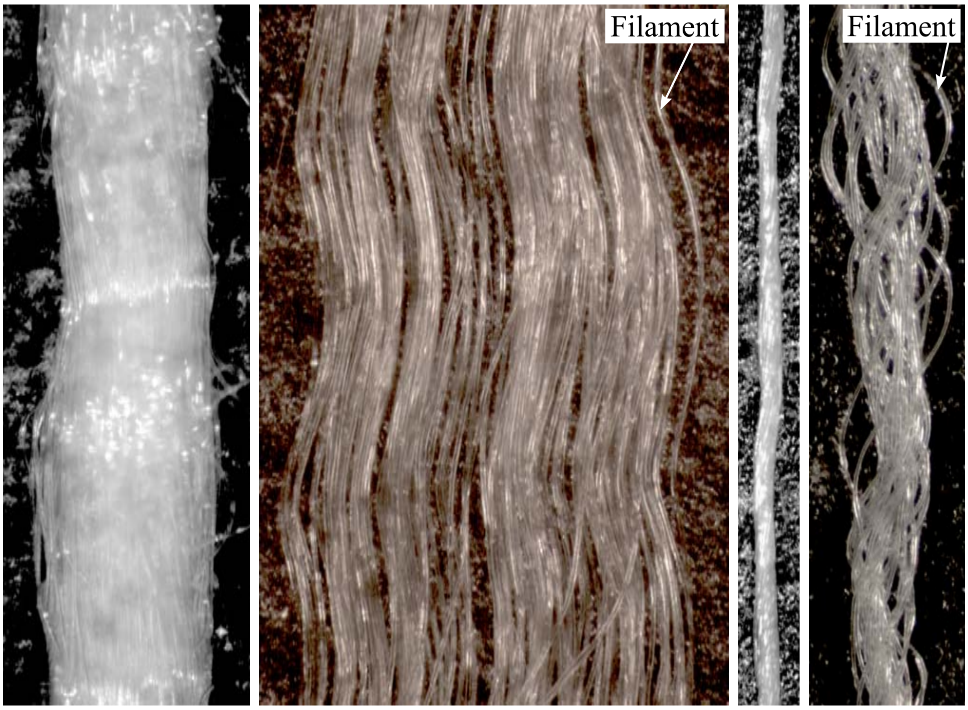

(a) (b) (c) (d)

Figure 5.19: Employed dielectric weft and warp thread. (a) High tenacity PES 550 dtex weft thread sample. (b) Unraveled filaments from (a). (c) PET $76f24$ dtex thread warp sample. (d) Unraveled filaments from (c).

The woven prototype is composed of three layers, as the FSS presented in the previous section: two dielectric layers in which the conductive square-rings are inserted, separated by the insulating layer. The three layers are identical, except for the positions where the dielectric threads have been substituted by conductive threads to implement the square-ring resonators. The conductive square rings placed in the top layer are translated into 5 *Shieldex* threads as shown in Figure 5.21a, which will be simulated as 5 conductive strips, separated a distance s_T between centres and whose widths are $d_\mathrm{T} = d_\mathrm{Shieldex}$, as it can be seen in Figure 5.21c. The conductive square rings placed in the bottom layer are translated into 7 *Shieldex* threads as shown in Figure 5.21b, which will be simulated as 7 conductive strips, separated a distance s_B between centres and whose widths are $d_\mathrm{B} = d_\mathrm{Shieldex}$, as it can be seen in Figure 5.21d. The mentioned dimensions are summarised in Table 5.5.

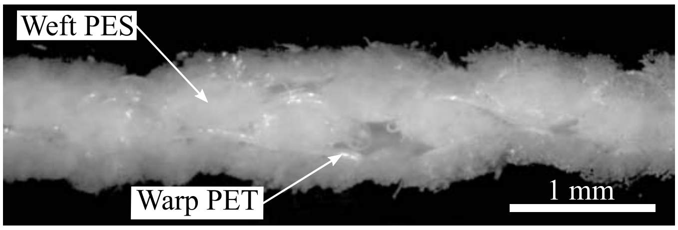

Figure 5.20: Side view of the woven substrate.

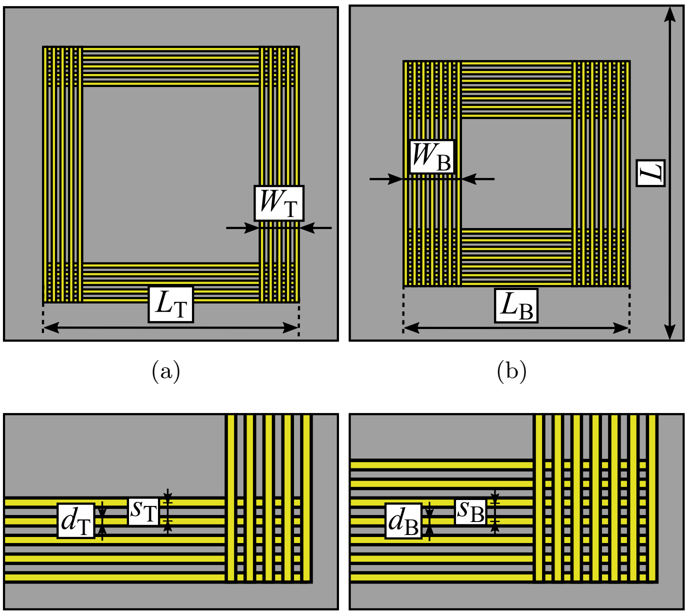

(a) (b)

(c) (d)

Figure 5.21: Schematic drawing of the proposed unit cell and its dimensions. (a) Top view. (b) Bottom view. (c) Detailed view of the dimensions (top view). (d) Detailed view of the dimensions (bottom view).

5.2.5 Simulations

The proposed design has been analysed using HFSS software. First, an infinite FSS modelled as one unit cell with PBC have been simulated under normal incidence conditions. Then, the result has been compared with the simulation of a finite structure. Afterwards, the behaviour of the finite FSS in terms of the angle θ formed by the electric field, $\vec{E}$, and the resonators, the angle of incidence and the radius of curvature.

Table 5.5: Dimensions (mm) of the woven FSS.

Top layer				Bottom layer				Unit cell	
L_T	W_T	d_T	s_T	L_B	W_B	d_B	s_B	L	H
34	5	0.3	1.175	30	7.5	0.3	1.2	45	1

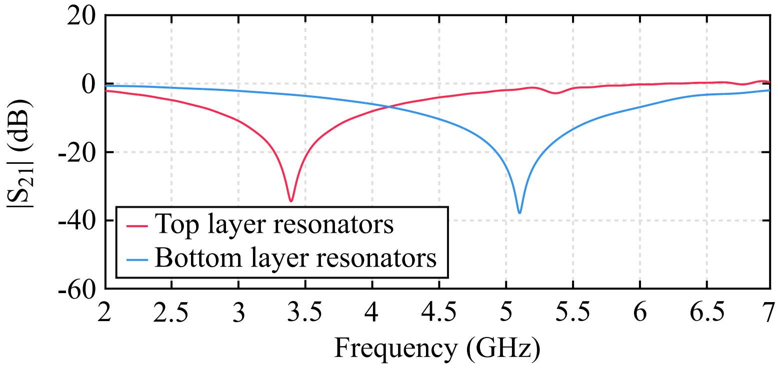

Figure 5.22: Simulated individual behaviour of the resonators in the top and bottom layers using the PCB conditions.

Two infinite arrays of resonators have been simulated applying PBC to a unit cell placing two ports at a distance of $D/2 = 0.75$ m from each side of the FSS, respectively, as previously illustrated in Figure 5.18a. In Figure 5.22, the individual behaviour of the resonators in the top and bottom layers, respectively, is represented. The resonators in the top and bottom layers present a bandstop behaviour at a central frequency of 3.4 GHz and 5.1 GHz, respectively.

The simulated individual behaviour of the electric field is depicted in Figure 5.23. Figure 5.23a represents the electric field at 5.1 GHz for a unit cell with PBC composed only of the top layer resonators, whereas Figure 5.23b represents its behaviour at 3.4 GHz. As predicted, the resonance phenomenon is produced in Figure 5.23b. Figure 5.23c represents the electric field at 3.4 GHz for a unit cell with PBC composed only of the bottom layer resonators, whereas Figure 5.23d represents its behaviour at 5.1 GHz. Analogously, the structure resonates at the highest frequency.

An infinite FSS (using both arrays of resonators) has been simulated, leading to a broadband bandstop behaviour of the complete FSS, as a result of the coupling phenomenon between the two layers of resonators. A finite version 9×9 unit–cells has also been simulated in the middle of two horn antennas separated

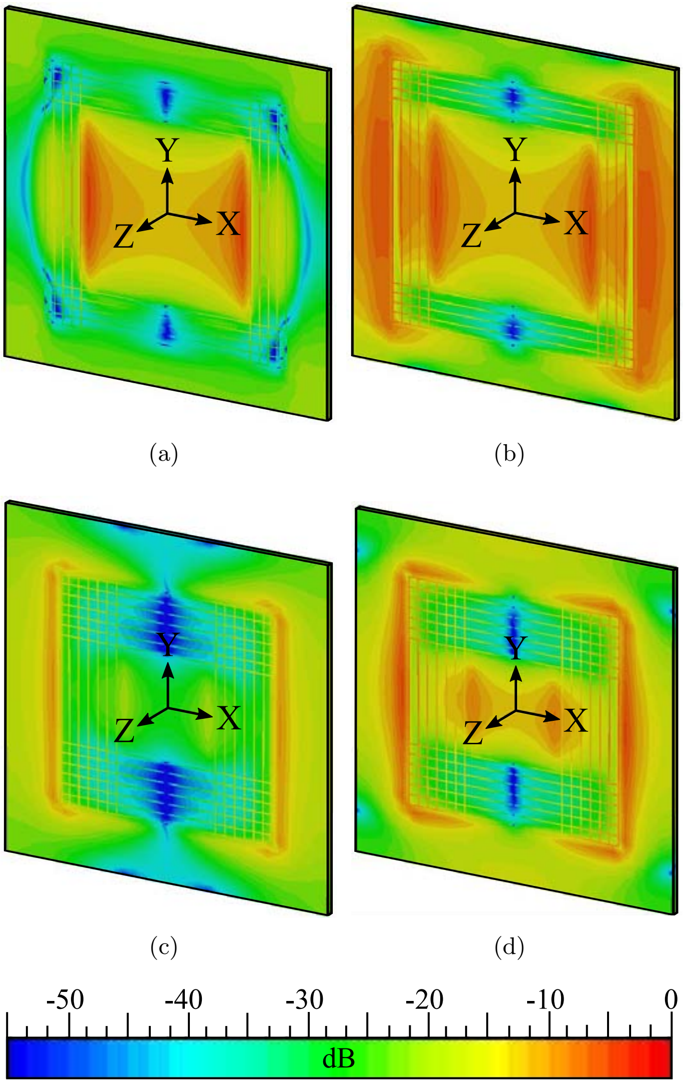

(a) (b)

(c) (d)

(e)

Figure 5.23: Simulated individual behaviour of the normalised electric field (PBC). (a) Resonators in the top layer at 5.1 GHz. (b) Resonators in the top layer at 3.4 GHz. (c) Resonators in the bottom layer at 3.4 GHz. (d) Resonators in the bottom layer at 5.1 GHz. (e) Common scale for (a) to (d) representations.

a distance $D = 1.5$ m, as depicted in Figure 5.24a. The simulated S_{21} parameter, normalised by the response in the absence of the FSS, is shown in Figure 5.24b. The dimensions of the simulated horns are identical to the dimensions of the

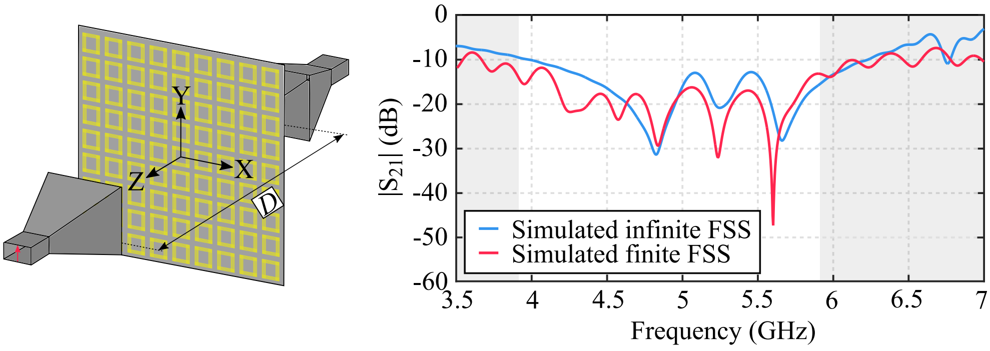

(a) (b)

Figure 5.24: Normal incidence. (a) Schematic drawing of the simulated set-up ($D = 1.5$ m). (b) Simulated $|S_{21}|$ parameter for an infinite FSS (set-up in Figure 5.18a) and for a finite FSS.

real horns which have been used for the experimental validation, which are the denoted as horn N643SGH and described in Table 5.3 in the previous section. The comparison between the simulation of both $|S_{21}|$ parameters can be seen in Figure 5.24b. The non-shaded range of frequencies represents the frequencies in which a single-mode operation of the horns is guaranteed.

To study the behaviour of the designed FSS in terms of the angle θ, the FSS has been simulated rotating it around the Z–axis, from $\theta = 0°$ to $\theta = 45°$ as depicted in Figure 5.25a. The simulated $|S_{21}|$ parameter for the different angles θ is shown in Figure 5.25b. Although the minimum value of the $|S_{21}|$ parameter is modified with the angle θ, the attenuation level remains over 10 dB in the non–shaded region. Consequently, the FSS presents an stable performance in terms of the angle θ.

To study the behaviour of the designed FSS in terms of the angle of incidence, the FSS has been simulated rotating it around the Y–axis, from $\phi = 0°$ to $\phi = 45°$ as depicted in Figure 5.26a. The simulated $|S_{21}|$ parameter for the different angles of incidence is shown in Figure 5.26b. The simulated FSS presents a stable performance in terms of the angle of incidence.

The performance of the FSS has also been studied in terms of the radius of curvature, bending it around a cylinder whose axis is parallel to the X–axis, with a radius varying from $R = 600$ mm to $R = 400$ mm, as depicted in Figure 5.27a. The minimum distance between the FSS and the transmitter horn is $D/2$. The simulated $|S_{21}|$ parameter for the different radii of curvature is shown in

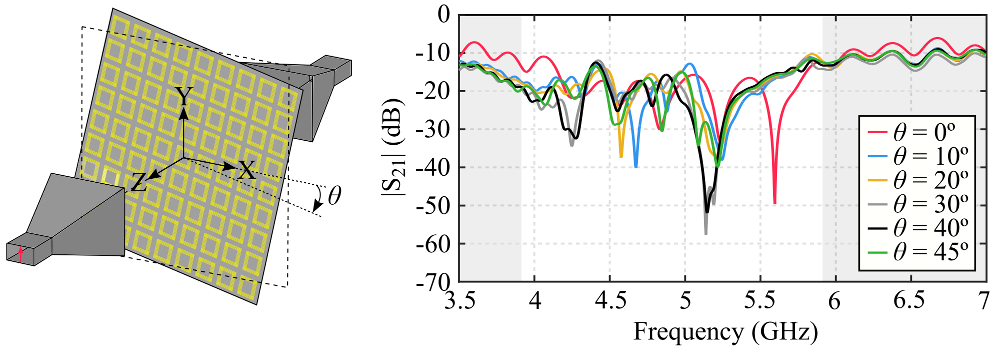

(a) (b)

Figure 5.25: Set-up and performance in terms of angle θ. (a) Schematic drawing of the simulated set-up. (b) Simulated $|S_{21}|$ parameter and the influence of the angle θ on the finite FSS performance.

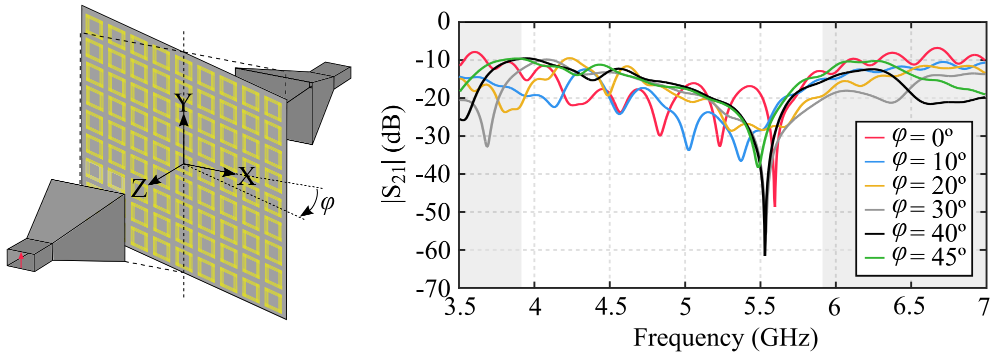

(a) (b)

Figure 5.26: Set-up and performance in terms of the angle of incidence. (a) Schematic drawing of the simulated set-up. (b) Simulated $|S_{21}|$ parameter and the influence of the angle of incidence on the finite FSS performance.

Figure 5.27b. Although the minimum value of the $|S_{21}|$ parameter is modified with the radius of curvature, the attenuation level remains over 10 dB in the non–shaded region. Consequently, the FSS presents an stable performance in terms of the radius of curvature.

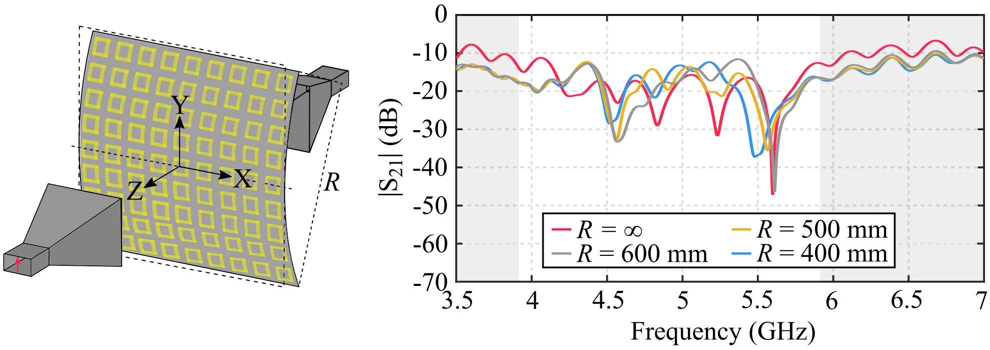

(a) (b)

Figure 5.27: Set-up and performance in terms of radius of curvature. (a) Schematic drawing of the simulated set-up. (b) Simulated $|S_{21}|$ parameter and the influence of the radius of curvature on the finite FSS performance.

5.2.6 Fabrication process

A finite 9 × 9 unit cells FSS has been manufactured using an industrial MüGrip loom. The manufacturing process is based on satin weaving and leading to a layer-to-layer angle interlock 3D woven structure. For this purpose, the conductive warp yarns are previously mounted in the loom and the conductive weft threads are inserted in the fabric during the fabrication process leading to two conductive lattices in either side of the fabric, instead of the required square-rings, as depicted in Figure 5.28. In Figure 5.28a, the lattice which corresponds to the top layer is presented, where the red and blue colored segments represent, respectively, the warp and the weft segments of the conductive threads which have been left unwoven from the main fabric for the subsequent cutting process. Consequently, Figure 5.28b depicts the top layer after the cutting procedure where the square-shaped resonators can be identified. Alternatively, Figure 5.28c and Figure 5.28d represent the analogous concept applied to the bottom layer of the design.

As already thoroughly explained for the FSS presented in the previous section, the weaving procedure employed to create a layer of individual resonators requires an auxiliary layer. This procedure is summarised in Figure 5.29. In contrast to the FSS previously presented, this FSS requires two auxiliary layers, and consequently, each auxiliary layer corresponds to each layer of resonators. Figure 5.29a depicts both auxiliary layers before the cutting procedure, whereas Figure

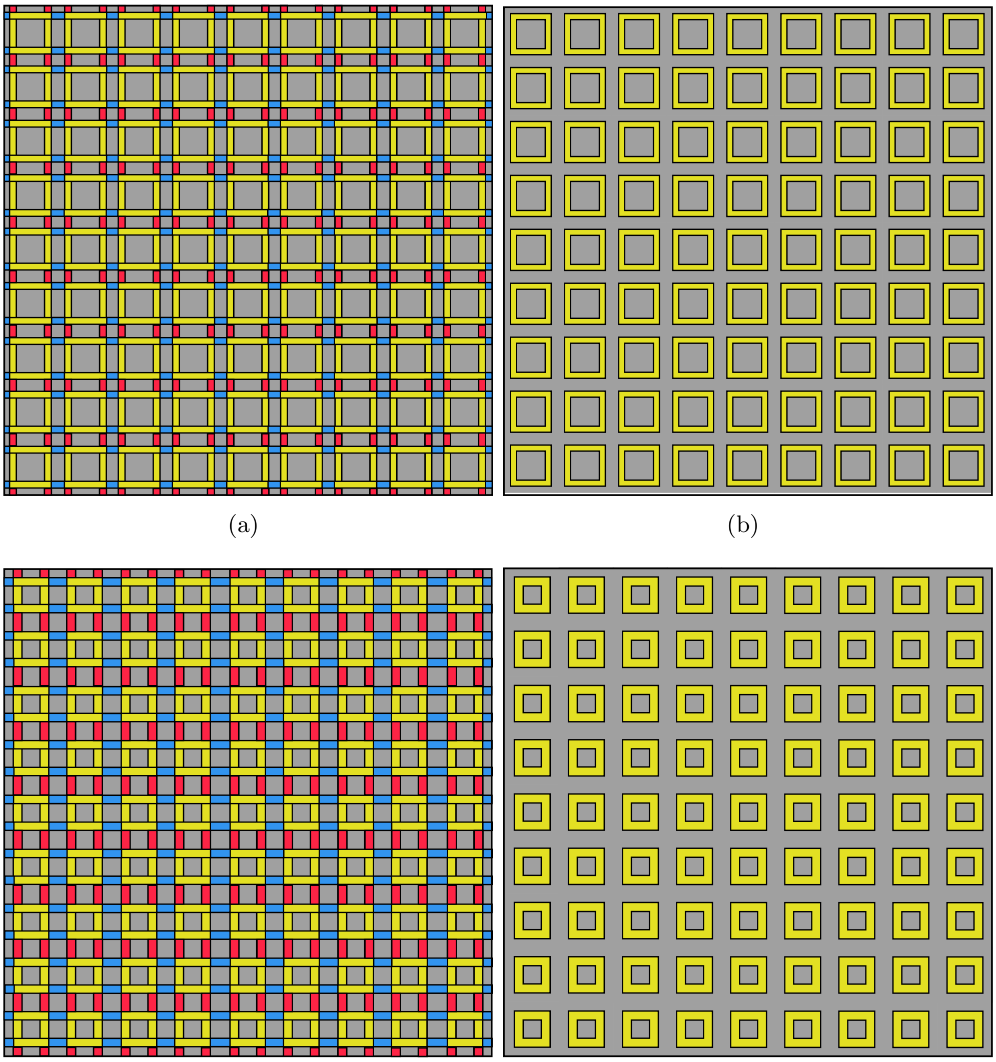

(a) (b)

(c) (d)

Figure 5.28: Schematic drawing of the woven structure before and after the cutting process. (a) Top layer before the cutting process. (b) Top layer after the cutting process. (c) Bottom layer before the cutting process. (d) Bottom layer after the cutting process.

5.29b represents the loose threads after the cutting procedure if binders had not been employed. As explained in the previous section, dielectric binders are required to provide the prototype with compactness, avoiding the presence of the before mentioned loose threads. A schematic drawing of the binders is depicted in

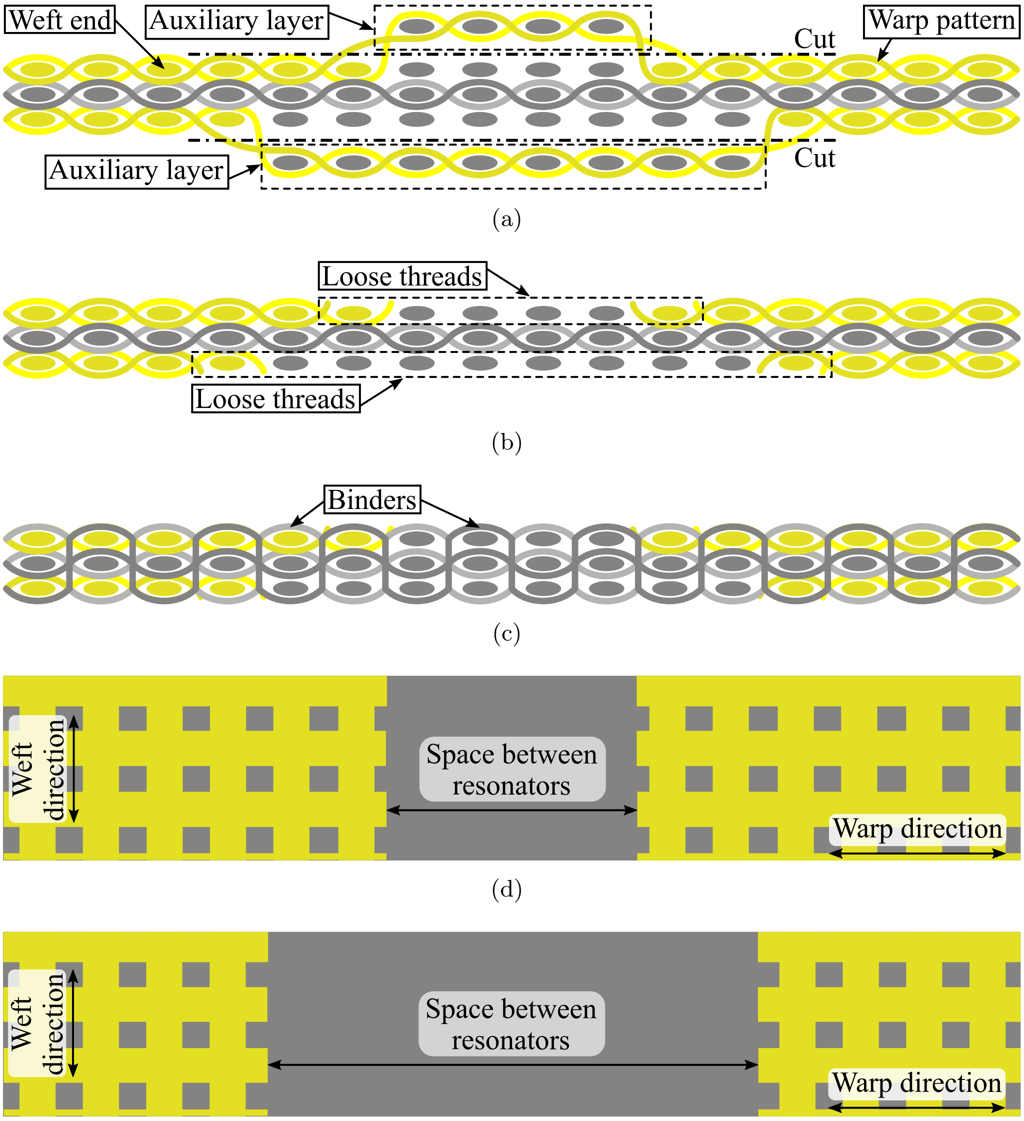

Figure 5.29: Schematic drawing of the woven structure based on a layer-to-layer angle interlock 3D fabric. (a) Side view of the woven structure with using two auxiliary layers. (b) Side view of the woven structure with the loose threads, after cutting the auxiliary layers. (c) Side view of the woven structure using binders to avoid the loose threads. (d) Top view equivalence. (e) Bottom view equivalence.

Figure 5.29c. Using these auxiliary layers and the binders, the required structure is achieved, which is represented in Figure 5.29e (top layer) and in Figure 5.29e (bottom layer). A finishing process has been required after removing the fabric from the loom, as explained in the previous FSS, using the same stenter machine.

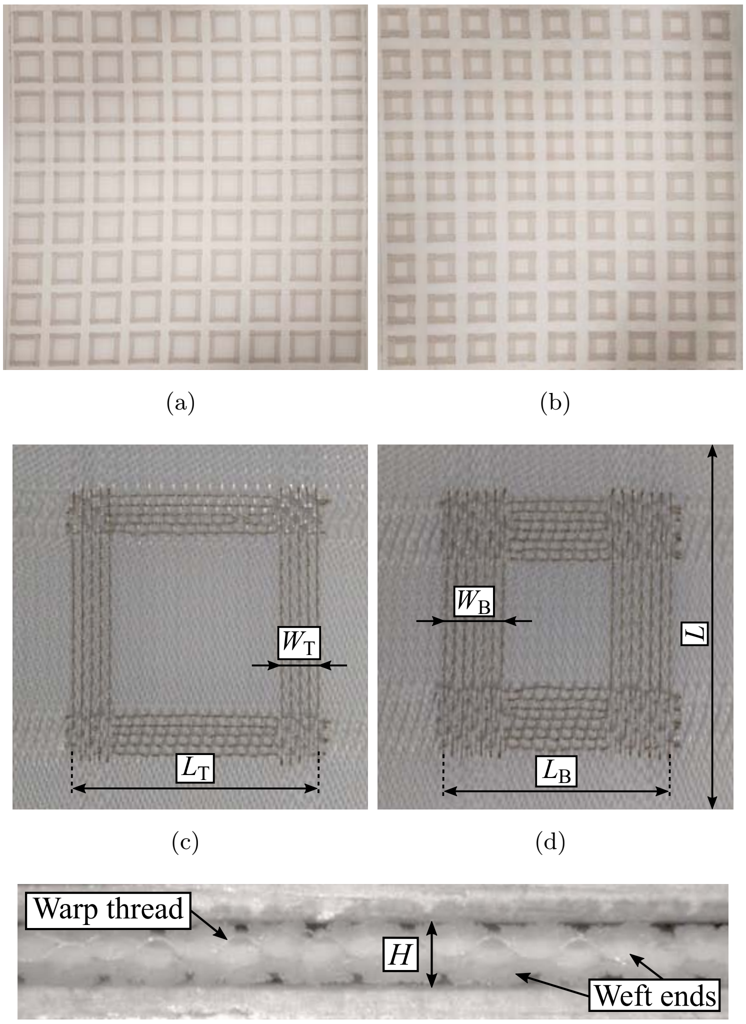

(a) (b)

(c) (d)

(e)

Figure 5.30: Manufactured prototype. (a) Top view. (b) Bottom view. (c) Magnification of a unit cell from the top layer. (d) Magnification of a unit cell from the bottom layer. (e) Side view of the prototype compressed between two metallic sheets.

The top and bottom views of the manufactured prototype can be seen in Figure 5.30a and Figure 5.30b, whereas a magnification of the unit cells from the top and bottom layers are shown in Figure 5.30c and d, respectively. A side view of the manufactured prototype is depicted in Figure 5.30e.

5.2.7 Experimental validation

The prototype has been experimentally validated using the set-ups presented in the following paragraphs. These set-ups are composed of the same wooden frame employed in the previous section, two horn antennas (horn N643SGH in Figure 5.14) mounted on rotary platforms and a vector network analyser. The S_{21} parameter between the horn antennas, for each set–up, calibrated by using the response between the antennas without the FSS, has been measured using an Agilent N5247A PNA-X vector network analyser and compared with the simulations.

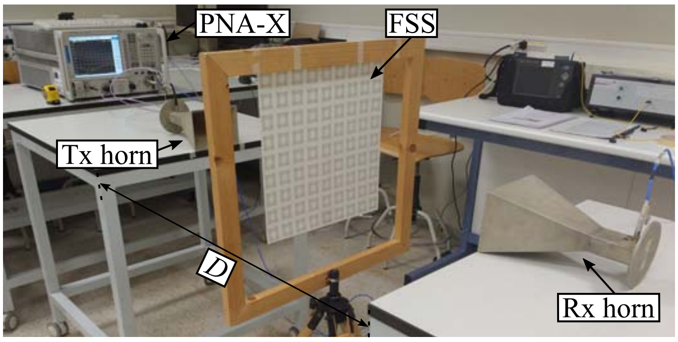

(a)

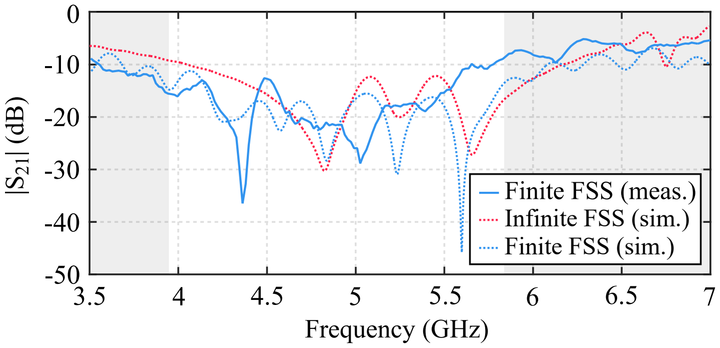

(b)

Figure 5.31: Normal incidence. (a) Measurement set-up ($D = 1.5$ m). (b) Measured vs. simulated $|S_{21}|$ parameter.

The FSS has been experimentally validated under normal incidence conditions using the set-up shown in Figure 5.31a. The comparison between simulations and measurements can be seen in Figure 5.31b. In the nominal frequency band of the horn antennas, the manufactured FSS provides a bandstop behaviour, with a minimum 10 dB attenuation over a 1.8 GHz bandwidth centered around 5 GHz. There is a good agreement between the simulations and measurements, although the differences might be due to the approximations employed in the simulations. While the manufactured conductive paths are curved due to the weaving process, they are slightly longer than their analogous simualted flat strips. For this reason, the measured range of working frequencies is slightly shifted to lower frequencies.

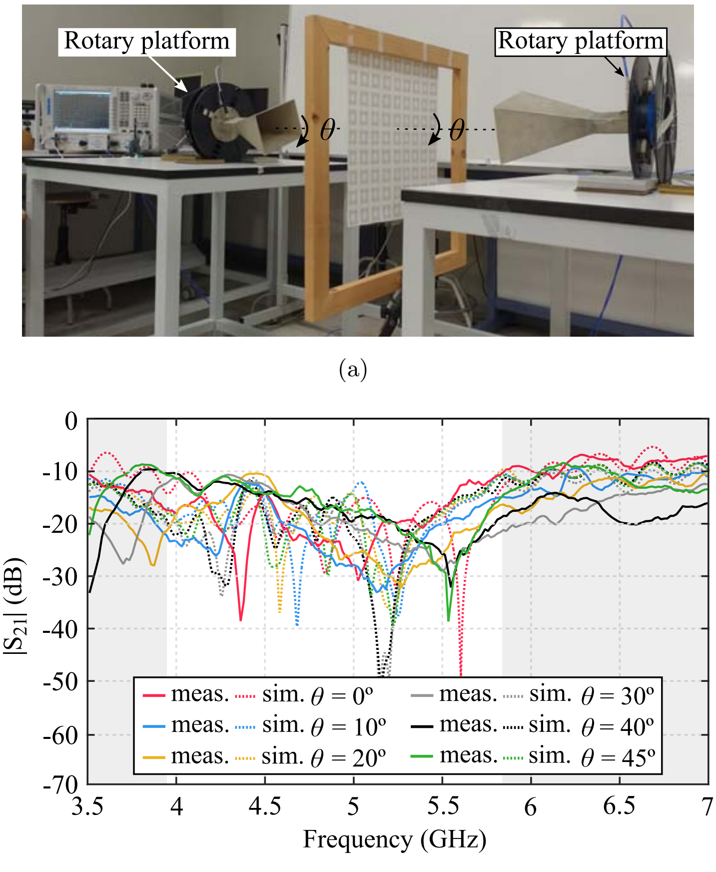

(a)

(b)

Figure 5.32: Performance in terms of the angle θ. (a) Measurement set-up. (b) Measured vs. simulated $|S_{21}|$ parameter and the influence of the angle θ on the finite FSS performance.

The FSS has been experimentally validated for different values of the angle θ using the set-up shown in Figure 5.32a in which the antennas have been mounted on the rotary platforms. The comparison between simulations and measurements is depicted in Figure 5.32b. In the single mode frequency range of the antennas, represented as the non-shaded part of the figure, the manufactured FSS has a bandstop behaviour.

Consequently, the FSS exhibits a stable performance in terms of the angle θ. This represents an interesting point for the potential use of the proposed FSS as a wall cover or curtain to filter undesired frequencies.

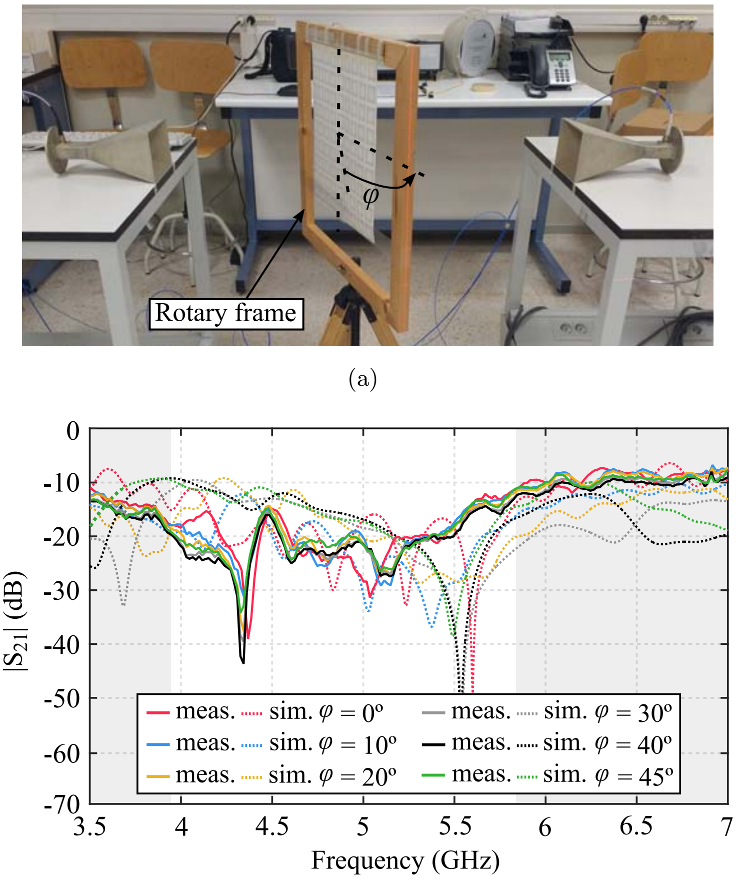

(a)

(b)

Figure 5.33: Angle of incidence. (a) Measurement set-up. (b) Measured vs. simulated $|S_{21}|$ parameter and the influence of the angle of incidence on the finite FSS performance.

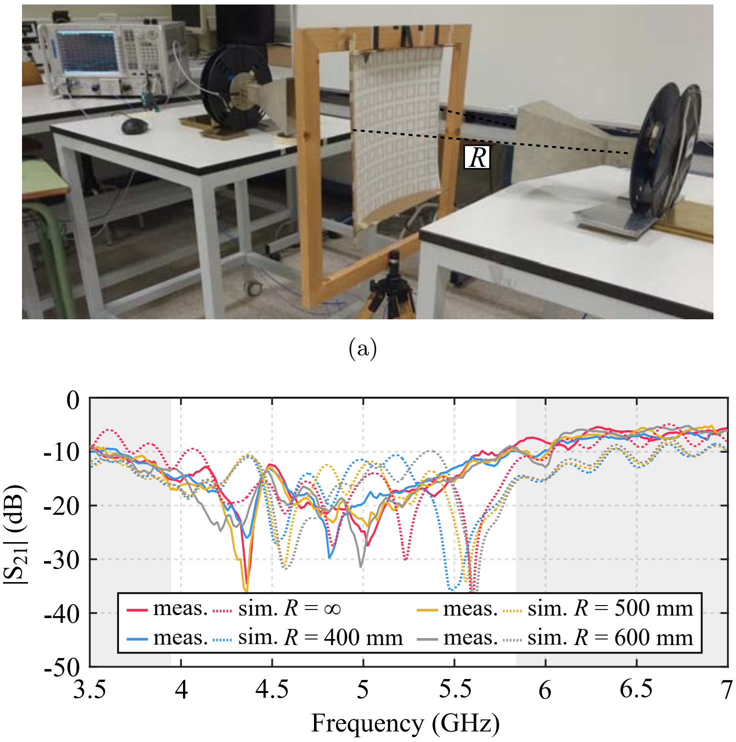

(a)

(b)

Figure 5.34: Radius of curvature. (a) Measurement set-up. (b) Measured vs. simulated $|S_{21}|$ parameter and the influence of the radius of curvature on the finite FSS performance.

The FSS has been experimentally validated for different angles of incidence using the set-up shown in Figure 5.33a with a rotary canvas. The comparison between simulations and measurements can be seen in Figure 5.33b. In the single mode frequency range of the antennas, the manufactured FSS has a bandstop behaviour. Consequently, the FSS exhibits a stable performance in terms of the angle of incidence, reinforcing its applicability in the aforementioned wall covering.

Due to its high flexibility, this FSS has been experimentally validated for different radii of curvature using the set-up shown in Figure 5.34a. The FSS has been bent around different cardboard pieces to achieve the required radius of curvature. The comparison between simulations and measurements is shown in Figure 5.34b. The manufactured FSS presents a bandstop behaviour leading to a stable performance in terms of the radius of curvature. This fact is of great interest for the beforementioned application of covering walls. For this purpose, it is not necessary to attach the woven FSS to the wall, as it works properly under bent conditions. Consequently, the FSS can be used as a curtain, leading to an easily removable filter.

5.2.8 Conclusions

A novel broadband flexible fully textile-integrated bandstop FSS has been presented. To validate the design, a 9×9 unit–cell prototype has been manufactured and experimentally characterised under different conditions, including different angles of polarisation, angles of incidence or radius of curvature. A good agreement between simulations and measurements has been achieved, experimentally verifying the theoretically predicted behaviour of the textile structure. Therefore, the manufactured FSS exhibits a stable performance in terms of the angle of polarisation, the angle of incidence and the radius of curvature.

The manufacturing procedure using industrial textile machinery provides the possibility of manufacturing flexible and very large FSS with sizes up to 5 metres wide and hundres of metres long without the need of unions, as opposed to other alternatives based in conventional substrates, solving the fabrication problems of large shielding surfaces.

Bibliography

[1] B. A. Munk, *Frequency selective surfaces: Theory and design.* USA, Wiley-Interscience Publication, 2000, pp. 1-25. (Cited on page 156)

[2] J. Tak and J. Choi, "A wearable metamaterial microwave absorber", in *IEEE Antennas Wireless Propag. Lett.*, vol. 16, pp. 784-787, Aug., 2016. (Cited on page 156)

[3] S. M. Rouzegar, A. Alighanbari and O. M. Ramahi, "Wideband uniplanar artificial magnetic conductors based on curved coupled microstrip line resonators," in *IEEE Microw. Wirel. Compon. Lett.*, vol. 27, no. 4, pp. 326-328, Apr. 2017. (Cited on page 156)

[4] F. M. Monavar and N. Komjani, "Bandwidth enhancement of microstrip patch antenna using Jerusalem Cross-shaped frequency selective surfaces by invasive weed optimization approach," in *Progress In Electromagnetics Research*, vol. 121, pp. 103-120, 2011. (Cited on page 156)

[5] J. C. Zhang, Y. Z. Yin, and J. P. Ma, "Design of narrow band-pass frequency selective surfaces for millimeter wave applications," in *Progress In Electromagnetics Research*, vol. 96, pp. 287-298, 2009. (Cited on page 156)

[6] W. Fu1 *et al.*, "Polarization insensitive wide-angle triple-band metamaterial bandpass filter", presented in *Progress in Electromagnetic Research Symposium (PIERS)*, Shanghai, China, Aug., 8–11, 2016. (Cited on page 156)

[7] C. Xu *et al.*, "A novel dual-stop-band FSS for infrared stealth applications", presented in *Int. Applied Computational Electromagnetics Soc. Symp. (ACES)*, Suzhou, China, Aug., 1–4, 2017. (Cited on page 156)

[8] M. Nauman and W. T. Khan, "A miniaturized dual-band stop frequency selective surface for 900 MHz and 1800 MHz bands shielding", presented

in *11th European Conf. on Antennas and Propag. (EUCAP)*, Paris, France, Mar., 19–24, 2017. (Cited on page 156)

[9] X. Xiong *et al.*, "WiFi band-stop FSS for increased privacy protection in smart building", presented in *IEEE 6th Int. Symp. on Microw. Antenna Propag. and EMC Technol. (MAPE)*, Shanghai, China, Oct., 28–30, 2015, pp. 826-828. (Cited on page 156)

[10] N. Liu *et al.*, "A Design Method for Synthesizing Wideband Band-Stop FSS via Its Equivalent Circuit Model", in *IEEE Antennas and Wireless Propag. Lett.*, vol. 16, pp. 2721-2725, Aug., 2017. (Cited on page 156)

[11] M. Yan *et al.*, "A novel miniaturized dual-stop-band FSS for Wi-Fi application", presented in *Progress in Electromagnetic Research Symp. (PIERS)*, Shanghai, China, Aug., 8–11, 2016. (Cited on page 156)

[12] M. H. Nisanci *et al.*, "Experimental validation of a 3D FSS designed by periodic conductive fibers part-2: band-stop filter characteristic", in *IEEE Trans. on Electromagnetic Compatibility*, vol. 59, no. 6, pp. 1835-1840, Jun. 2017. (Cited on page 156)

[13] L. Li *et al.*, "All-dielectric metamaterial band stop frequency selective surface via high-permittivity ceramics", presented in *Progress in Electromagnetic Research Symp. (PIERS)*, Shanghai, China, Aug., 8–11, 2016. (Cited on page 156)

[14] W. Fu *et al.*, "Polarization insensitive wide-angle triple-band metamaterial bandpass filter", in *Journal of Physics D: Applied Physics*, vol. 49, no. 28, 2016. (Cited on page 156)

[15] M. Fallah, A. Ghayekhloo and A. Abdolali, "Design of frequency selective band stop shield using analytical method", in *Journal of Microw., Optoelectronics and Electromagnetic Applications*, vol. 14, no. 2, Dec. 2015. (Cited on page 156)

[16] M. M. Tahseen and A. A. Kishk, "Flexible and portable textile-reflectarray backed by frequency selective surface", in *IEEE Antennas Wireless Propag. Lett.*, vol. 17, no. 1, pp. 46-49, Jan. 2018. (Cited on page 156)

[17] W. G. Whittow *et al.*, "Printed frequency selective surfaces on textiles", in *Electr. Lett.*, vol. 50, no. 13, pp. 916-917, June 19 2014. (Cited on page 156)

[18] M. Ghebrebrhan *et al.*, “Textile frequency selective surface”, in *IEEE Microw. Wireless Components Lett.*, vol. 27, no. 11, pp. 989-991, Nov. 2017. (Cited on page 156)

[19] L. Alonso-González *et al.*, “Layer-to-layer angle interlock 3D woven bandstop frequency selective surface”, in *Progress In Electromagnetics Research*, [under review.] (Cited on page 156)

[20] Narda. Standard Gain Horns, datasheet [accessed September 7, 2017]. Available at: https://nardamiteq.com/docs/WAVEGUIDEHORNANTENNAS_STANDARD_GAIN_HORNS_2.60_TO_40_GHZ.PDF (Cited on page 162)

[21] B. Yu *et al.*, “2D and 3D imaging of fatigue failure mechanisms of 3D woven composites”, in *Composites Part A: Applied Science and Manufacturing*, vol. 77, pp. 37-49, Oct. 2015. (Cited on page 165)

[22] L. Jin *et al.*, “Tension-tension fatigue behaviour of layer-to-layer 3-D angle-interlock woven composites”, in *Materials Chemistry and Physics*, vol. 140, pp. 183-190, June 2013. (Cited on page 165)

[23] A. C. Long and L. P. Brown, *Composite reinforcements for optimum performance: Modelling the geometry of textile reinforcements for composites: TexGen*, Woodhead Publishing Ltd, 2011, ISBN: 978-1-84569-965-9. [Online]. Available: www.woodheadpublishing.com/en/book.aspx?bookID=2233. (Cited on page 165)

[24] H. Lin, L. P. Brown, and A. C. Long, “Modelling and simulating textile structures using TexGen” in *Advanced Materials Research*, vol. 331, 2011. (Cited on page 165)

[25] L. Alonso-González *et al.*, “Broadband flexible fully textile-integrated bandstop frequency selective surface”, in *IEEE Trans. Antennas Propag.*, [under review.] (Cited on page 172)

6

General conclusions

In this Doctoral Thesis, the design, simulation and manufacturing techniques to develop fully textile integrated circuits and antennas operating at the microwave range of frequencies have been presented. Although several approaches to develop circuits and antennas based on textile have been previously discussed in the bibliography, none of them present, simultaneously, three important characteristics: complete integration in textile, possibility of achieving multilayered designs and large-scale production. For this reason, weaving technology has been found to be the appropriate alternative.

First, with the aim of simplifying the design and simulation of woven structures, a novel modelling technique based on three steps has been developed. These three steps correspond, respectively, to three different, although electromagnetically equivalent, models of a woven structure. The first model, denoted by filament model, emulates the real composition of the employed materials –multifilament threads–, whereas the second and simpler model, the monofilament model, transform them into monofilaments. Finally, the layers model emulates the conventional topologies employed to simulate circuits and antennas using homogeneous substrates. As a result, the translation between the models allows the reduction of the computational complexity of the simulations.

With the aim of demonstrating the validity of the modelling, the beforementioned technique has been first employed in the development of two textile integrated waveguides working, respectively, in the millimetre-wave and microwave ranges of frequencies. As a result, a good agreement between the simulations and the measurements has been achieved and the propagation of a signal through a woven structure has been demonstrated.

Once the modelling has been has been experimentally validated, different prototypes have been designed based on the beforementioned technique. First, a woven near-field radiofrequency identification tag provided with a commercial chip has been discussed and different alternatives to connect the chip have been proposed. Nevertheless, with the aim of developing radiating structures working in the far field region, two different antennas have been implemented. First, a microstrip-fed slotted antenna has been presented, although, with the aim of suppressing the backward radiation, a coaxial-fed cavity backed slotted antenna has been also proposed. Both antennas have been validated in an anechoic chamber presenting good agreement between simulations and measurements.

In addition, two different frequency selective surfaces have also been proposed taking advantage of the large-scale production capabilities of the weaving technology. For this purpose, first, a frequency selective surface based on a layer of periodic cross-shaped resonators has been proposed. Nevertheless, with the aim of increasing the bandwidth, a new frequency selective surface based on two isolated layers of periodic squared-ring resonators has been proposed. Consequently, not only the large-scale production capabilities have been employed, but also, this last prototype represents an example of a completely textile integrated multilayered design, satisfying the aforementioned three important characteristics which a textile integrated circuit should accomplish.

A

List of publications

A.1 International journals

This section presents the main information regarding the publications related to this Doctoral Thesis. Three works (I-III) have been published in journals indexed in the Journal Citation Reports (JCR). Moreover, three works, (IV-VI), have also been considered for publication, although they are still under the peer review process. The complete references of the journals wherein the works have been or are susceptible to be published can be found in Table A.1. The main metrics defined by the JCR are summarised in Table A.2.

(I) **L. Alonso-González**, S. Ver-Hoeye, C. Vázquez-Antuña, M. Fernández-García, and F. L. H. Andrés, "On the techniques to develop millimeter-wave textile integrated waveguides using rigid warp threads", in *IEEE Transactions on Microwave Theory and Techniques*, vol. 66, no. 2, pp. 751–761, Feb. 2018.

(II) **L. Alonso-González**, S. Ver-Hoeye, M. Fernández-García, Y. Álvarez-López, C. Vázquez-Antuña, and F. L. H. Andrés, "Fully textile-integrated microstrip-fed slot antenna for dedicated short-range communications", in *IEEE Transactions on Antennas and Propagation*, vol. 66, no. 5, pp. 2262-2270, May 2018.

(III) **L. Alonso-González**, S. Ver-Hoeye, M. Fernández-García, and F. Las-Heras, “Three-dimensional fully interlaced woven microstrip-fed substrate integrated waveguide”, in *Progress In Electromagnetics Research*, [accepted for publication].

A.1.1 International journals under review

(IV) **L. Alonso-González**, S. Ver-Hoeye, C. Vázquez-Antuña, M. Fernández-García, and F. L. H. Andrés, “Multifunctional fully textile integrated RFID tag to revolutionise the Internet of Things in clothing”, in *IEEE Antennas and Propagation Magazine*, [under review].

(V) **L. Alonso-González**, S. Ver-Hoeye, M. Fernández-García, C. Vázquez-Antuña, and F. L. H. Andrés, “Broadband flexible fully textile-integrated bandstop frequency selective surface”, in *IEEE Transactions on Antennas and Propagation*, [under review].

(VI) **L. Alonso-González**, S. Ver-Hoeye, M. Fernández-García, and F. Las-Heras, “Layer-to-layer angle interlock 3D woven bandstop frequency selective surface”, in *Progress In Electromagnetics Research*, [under review].

Table A.1: Complete references of the journals with published works.

Work	Journal title (abbreviation)	Publisher	ISSN	Periodicity
(I)	Transactions on Microwave Theory and Techniques (TMTT)	IEEE	0018-9480	Monthly
(II, V)	Transactions on Antennas and Propagation (TAP)	IEEE	0018-926X	Monthly
(III, VI)	Progress In Electromagnetics Research (PIER)	PIER	1559-8985	Monthly
(IV)	Antennas and Propagation Magazine (APM)	IEEE	1045-9243	Bimonthly

Table A.2: JCR Metrics and rank in the *Engineering, Electrical and Electronic* category.

Journal	Rank	Quartile	Total cites	Impact factor
TMTT	67/262	Q2	21060	2.897
TAP	61/262	Q1	29239	2.332
PIER	94/262	Q2	3719	2.404
APM	122/262	Q2	2522	1.747

A.2 Conference papers

This section presents the main information regarding the works which correspond to oral presentations in international (i-ii) and national (iii) conferences. Table A.3 summarises the main information about the conferences and corresponding International Standard Book Number (ISBN) of the proceedings.

(i) **L. Alonso**, S. Ver Hoeye, M. Fernández, C. Vázquez, R. Camblor, G. Hotopan, A. Hadarig, and F. Las-Heras, “Millimetre wave textile integrated waveguide beamforming antenna for radar applications”, presented in *Global Symposium on Millimeter-Waves (GSMM)*, Montreal, QC, May 25–27, 2015, pp. 1–3.

(ii) **L. Alonso-González**, S. Ver Hoeye, C. Vázquez, M. Fernández, A. Hadarig and F. Las-Heras, “Novel parametric electromagnetic modelling to simulate Textile Integrated Circuits”, presented in *2017 IEEE MTT-S International Conference on Numerical Electromagnetic and Multiphysics Modeling and Optimization for RF, Microwave, and Terahertz Applications (NEMO)*, Seville, Spain, May 17–19, 2017, pp. 67–69.

A.2.1 National conference papers

(iii) **L. Alonso-González**, S. Ver Hoeye, C. Vázquez, M. Fernández, A. Hadarig and F. Las-Heras, “Textile integrated waveguide cavity–backed slot antenna for 5G wearable applications”, presented in *XXXI Simposium Nacional de la Unión Científica Internacional de Radio*, Madrid, Spain, Sep. 5–7, 2016[1].

---

[1] Young Scientist Best Paper Award.

Table A.3: Conferences information.

<table>
<tr><th>Work</th><th colspan="4">Conference</th></tr>
<tr><td rowspan="3">(i)</td><td colspan="4">2015 8th Global Symposium on Millimeter-Waves (GSMM 2015)</td></tr>
<tr><td>Proceedings publisher</td><td>ISBN</td><td>Periodicity</td><td>Venue & date</td></tr>
<tr><td>IEEE</td><td>978-1-4673-8063-8</td><td>Annual</td><td>Montreal, Canada, May 25-27, 2015</td></tr>
<tr><td rowspan="3">(ii)</td><td colspan="4">2017 IEEE MTT-S International Conference on Numerical Electromagnetic and Multiphysics Modeling and Optimization for RF, Microwave, and Terahertz Applications (NEMO 2017)</td></tr>
<tr><td>Proceedings publisher</td><td>ISBN</td><td>Periodicity</td><td>Venue & date</td></tr>
<tr><td>IEEE</td><td>978-1-5090-4837-3</td><td>Annual</td><td>Seville, Spain, May 17-19, 2017</td></tr>
<tr><td rowspan="3">(iii)</td><td colspan="4">2016 XXXI Simposium Nacional de la Unión Científica Internacional de Radio (URSI 2016)</td></tr>
<tr><td>Proceedings publisher</td><td>ISBN</td><td>Periodicity</td><td>Venue & date</td></tr>
<tr><td>J. Córcoles *et al.*</td><td>978-84-608-9674-6</td><td>Annual</td><td>Madrid, Spain, September 5-7, 2016</td></tr>
</table>

B

Other works related to the Doctoral Thesis

B.1 International research stay

During the development of the Doctoral Thesis, the author carried out a research stay in the George Green Institute for Electromagnetics Research at The University of Nottingham.

- Stay under supervision of Dr. Steve Greedy.
- Duration: from September 13th, 2017 to December 12th, 2017.
- Funding: Ayudas económicas de movilidad de excelencia para docentes e investigadores de la Universidad de Oviedo.

As a result, there has been a research collaboration with the Future Composites Manufacturing Research Hub through The University of Manchester. This collaboration is related to the manufacturing of complex woven structures under the supervision of Prof. Prasad Potluri, principal investigator in the Hub.

B.2 Technology transfer through research projects

During the development of the Doctoral Thesis, a Eurostars project proposal has been accepted. Therefore, the research group in which the author of this Doctoral Thesis works has been subcontracted. The main information related to the project is the following.

- Project: Fully integrated textile electronic tags for the next generation RFID uses in the fashion sector.
- Project ID: 11802[1].
- Abbreviation: FITex-ID.
- Reference: E! 11802 FITex-ID
- Start date: July 1st, 2018.
- Duration: 24 months.
- Technological area: electronic engineering.
- Market area: clothing and shoe stores.
- Project costs: 1.552.240 €.
- Main partners:
    - 3D Weaving[2] (Belgium)
    - Primo1D[3] (France)
    - Wearable Technologies SL[4] (Spain)

---

[1] www.eurostars-eureka.eu/project/id/11802

[2] www.3dweaving.com/

[3] www.primo1d.com/

[4] http://wetech.es/es/home/